RESPONSE COVARIANCE-BASED MULTI-SENSING DAMAGE DETECTION OF CIVIL STRUCTURES

LIN JIANFU

PhD

The Hong Kong Polytechnic University

2018

The Hong Kong Polytechnic University
Department of Civil and Environmental Engineering

RESPONSE COVARIANCE-BASED MULTI-SENSING DAMAGE DETECTION OF CIVIL STRUCTURES

LIN Jianfu

A thesis submitted in partial fulfillment of the requirements

for the Degree of Doctor of Philosophy

June 2018

CERTIFICATE OF ORIGINALITY

I hereby declare that this thesis is my own work and that, to the best of my knowledge and belief, it reproduces no material previously published or written, nor material that has been accepted for the award of any other degree or diploma, except where due acknowledgment has been made in the text.

_______________________(Signed)

__LIN Jianfu____(Name of student)

To my family

for their love and support

ABSTRACT

Structural deterioration with time is inevitable once civil structures are built, for they are subjected to harsh environment and extreme events, such as strong winds and severe earthquakes. The functionality and safety of civil structures during their service time become a vital issue. Therefore, structural health monitoring (SHM) techniques have been developed to monitor structural deterioration and detect structural damage, if any, for the functionality and safety of structures. Vibration-based structural damage detection methods, as a significant part of SHM, have been developed accordingly in past decades. However, when they are applied to civil structures, vibration-based damage detection methods encounter a few major difficulties, such as the less sensitivity of damage index, uncertainties in modelling and measurement, the number and type of sensors and their spatial location, and damage detection algorithm and procedure.

Many damage indexes used in vibration-based damage detection methods, such as natural frequencies, are not sensitive to local damage of a civil structure. Different types of sensors are often used in an SHM system for a civil structure to measure both global and local structural responses, but multi-sensing information has not been used effectively for local damage detection. This thesis thus proposes a response covariance-based multi-sensing damage index in the time-domain and the associated sensitivity-based damage detection method. The feasibility and accuracy of the proposed damage index and damage detection method are investigated through numerical studies on an overhanging beam model. The results show that the proposed damage index is sensitive to structural parameter change but insensitive to measurement noise and that the proposed damage detection method can effectively use multi-sensing information for local damage detection.

A civil structure often consists of hundreds of structural members and joints, but the number of sensors installed in the structure is always limited. It is quite possible

that the local damage may not be covered by the deployed sensors and its location may even not be accessible. Therefore, sensors shall be optimally placed in a structure so that the sensing information from the sensors can be used for effective damage detection. This thesis first proposes a response covariance-based optimal sensor placement method with a single objective function and a single type of sensors. The single objective function is actually formed by using a weighting factor to combine the two objective functions of response covariance sensitivity and response independence. Numerical studies are conducted to investigate the feasibility and effectiveness of the proposed method via a five bays three-dimensional frame structure. It is found that the acceleration responses often contain higher kinetic energy in higher-order vibrational modes for global structure information, displacement responses contain more kinetic energy in lower-order vibrational modes for global structure information, and strain responses are only sensitive to local damage only near the sensor locations. Therefore, a structural damage detection-oriented multi-type sensor placement method with multi-objective optimization is further developed in this thesis. The multi-objective optimization problem is formed by directly using the two covariance-related objective functions, and the non-dominated sorting genetic algorithm (NSGA)-II is adopted to find the solution for the optimal multi-type sensor placement to achieve the best structural damage detection. The proposed method is finally applied to a nine-bay three-dimensional frame structure numerically and experimentally. Both numerical and experimental studies show that the optimal multi-type sensor placement determined by the proposed method can avoid redundant sensors and provide satisfactory results for structural damage detection.

When the proposed covariance-based multi-type sensor placement method and the associated damage detection methods are applied to a large and complex civil structure, the obstacles exhibit. The global stiffness matrix, modal parameters, and dynamic responses are less sensitive to local damage of a large structure compared with a small structure. The one-stage damage detection is inaccurate and sometimes impossible due to too many unknown damage parameters and seriously ill-conditioned inversed problem for a large structure. Therefore, a covariance-based multi-stage damage detection strategy incorporating with a multi-scale finite element (FE) model is proposed for the damage detection of a large structure. In a multi-scale FE model, local detailed FE models using shell/solid elements and a global FE model using beam elements are integrated. The multi-stage damage detection is characterized by a few stages of different damage detection levels. For instance, the first stage is to detect the existence of damage and/or the location of damage, the second stage is to detect the damage-affected members in the identified damage location, and the final stage is to identify the damage source and quantify the damage severity. The proposed covariance-based multi-stage damage detection method is numerically and experimentally examined for its feasibility and effectiveness by using a testbed model of a high-voltage power transmission tower. Both numerical and experimental results manifest that the multi-stage detection method can effectively identify the damage in a joint due to bolt loosening and can even provide information deep down to the damage of bolts when a local detailed FE model is incorporated.

The damage index and damage detection methods, including the response covariance-based multi-sensing damage index, the response covariance-based multi-objective single-type and/or multi-type optimal sensor placements for damage detection, and the multi-stage damage detection strategy, presented in this thesis could conquer some obstacles, if not all, in the damage identification of large civil structures.

PUBLICATIONS ARISING FROM THE THESIS

Journal papers

Lin, J. F., Xu, Y. L., "Two-stage covariance-based multisensing damage detection method", *Journal of Engineering Mechanics*, ASCE, 2017:143, B4016003, https://doi.org/10.1061/(ASCE)EM.1943-7889.0001053.

Lin, J. F., Xu, Y.L., "Response covariance-based sensor placement for structural damage detection", *Structure and Infrastructure Engineering*, 2017: 1-14. https://doi.org/10.1080/15732479.2017.1402067.

Lin, J. F. , Xu, Y.L., Law, S.S. "Structural damage detection-oriented multi-type sensor placement with multi-objective optimization", *Journal of Sound and Vibration,* 2018: 420: 1-22. https://doi.org/10.1016/j.jsv.2018.01.047.

Lin, J. F. , Xu, Y.L., Zhan, S. "Experimental investigation on multi-objective multi-type sensor optimal placement for structural damage detection", *Structural Health Monitoring - An International Journal*, 2018, 1-20. https://doi.org/10.1177/1475921718785182.

Xu, Y.L., **Lin, J.F.**, Zhan, S., Wang, F.Y. "Multi-stage damage detection of a transmission tower: numerical investigation and experimental validation", *Structural Control and Health Monitoring* (Submitted).

Conference papers and presentations

Lin, J. F., Xu, Y. L. "Multi-sensing structural condition assessment using normalized covariance-based damage detection vector", in: *The 6th International Conference on Structural Health Monitoring of Intelligent Infrastructure (SHMII-6),* Hong Kong, December 9-11, 2013.

Lin, J. F., Xu, Y. L."Two-stage covariance-based multi-sensing damage detection method under white noise excitation", in*: Proceedings of the ASCE Engineering Mechanics Institute International Conference (EMI 2015)*, Hong Kong, January 7-9, 2015.

Lin, J. F., Xu, Y. L. "Experimental studies of two-stage covariance-based multi-sensing damage detection method", in : *The Joint 6th International Conference on Advances in Experimental Structural Engineering (6AESE) and 11th International Workshop on Advanced Smart Materials and Smart Structures Technology (11ANCRiSST),* University of Illinois , Urbana-Champaign , USA, August 1-2, 2015.

Lin, J. F., and Xu, Y.L. "Response covariance-based multi-objective multi-type sensor placement for structural damage detection", in: *The 7th World Conference on Structural Control and Monitoring (7WCSCM)*, Qingdao, China, July 22-25, 2018.

ACKNOWLEDGMENTS

Foremost, I would like to express my sincere gratitude to my chief supervisor, Prof. You-Lin Xu, for his time, patience, contribution and continuous support throughout my PhD study at The Hong Kong Polytechnic University (PolyU), which is a great challenge and achievement in my life. I deeply appreciate not only for Prof. Xu's insightful guidance, invaluable suggestion and financial support for my research but also for providing me with a versatile platform in which I can learn advanced academic knowledge. Under the supervision and encouragement of Prof. Xu, I have learned and achieved much more than what constitutes this thesis during the past five years.

I gratefully acknowledge the financial support received from the one-year top-up studentship program of the Department of Civil and Environment Engineering of PolyU and Prof. Xu's research project of the Hong Kong Research Grant Council (RGC) for my first three years PhD study. I would also thank for Prof. Xu's generous financial support from his research projects for a part-time research assistant position during my last two years of study.

Especially, I wish to express my appreciation to my group member and research fellow Mr. ZHAN Sheng for his great contribution for all my experimental work during my PhD program, in which his insightful experience, good guidance and assistance are very important to complete my research. Moreover, I want to thank the senior technical staffs at the Structural Dynamics Laboratory of PolyU: Mr. Liu Chi-shing, Mr. Kwan Wing-hong, Mr. Cheung Chi-fai, and Mr. Lai Yu-man for their professional assistance and useful help in my experimental studies. I also want to thank the staffs at the departmental general office and the university research office for their kind assistance.

My thanks also go to past and current members of Prof. Xu's research groups: Dr. Zhang Chao-dong, Dr. Wang Feng-yang, Dr. Lin Jing-hua, Dr. Zhu Qing, Dr. Zheng

Yue, Dr. Peng Yi-xin, Dr. Zhang Xiao-hua, Mr. Hu Rong-pan, Mr. Wang Zhi-lu, Miss. Tan Zhong-xu, Dr. He Jia, and Dr. Hu Liang. Their positive attitude, grateful suggestion, valuable experience, and kindly help always inspired me in time of difficulty.

Besides, I would like to express my profound appreciation to my former master-degree chief supervisor Dr. Huang Jian-liang, and former co-supervisor Prof. Chen Shu-hui at Zhong Shan University (SYSU), and Prof. Law Siu-seong, Prof. Xia Yong, Dr. Zhu Song-ye and Dr. Dong You of PolyU for their care and encouragement during the last five years.

Getting through my PhD study required more than academic support, I would like to sincerely thank all the peoples who accompanied me over these years in Hong Kong and specially express my gratitude to my dear friends: Dr. Wang Jun-fang, Dr. Tang Yi-qun, Dr. Wang You-wu, Dr. Liu Kun, Dr. Li Jun, Dr. Feng Wei-qiang, Mr. Chen Wen-bo, Mr. Chen Jun-bo, and Mr. Su Jun-biao.

Finally, and most importantly, I am very grateful to my parents and my younger sister for their patience, unconditional love and support all the time.

CONTENTS

LIST OF FIGURES

LIST OF TABLES

LIST OF NOTATIONS

$\mathbf{A}_c$ and $\mathbf{B}_c$	The continuous state matrix and input matrix
$A(\mathrm{m}^2)$	Sectional area
A_i and A_i^d	The cross-sectional areas of the i^{th} element in the intact and damaged states
A_1, A_2 and A_3	The corresponding sectional areas of the three segments of the beam
$\overline{A}_d$ and $\overline{I}_d$	A uniform equivalent sectional area and equivalent moment inertia
$\mathbf{B}$	The strain-displacement relationship matrix
b	Width of the beam element
$\mathbf{C}_c$ and $\mathbf{D}_c$	The output matrix and transmission matrix
$C_{\mathrm{pq}}(\tau)$	The cross-covariance function
$\hat{C}_{\mathrm{pq}}(\tau)$	The normalized cross-covariance function
$\tilde{C}_{\mathrm{pq}}(\tau)$	The normalized cross-covariance function considering measurement noise
${c_{ij}}^2$	The covariance of excitations between f_i and f_j
${c_{jj}}^2$	The variance of the excitation f_j
d_{pq}	The Euclidean distance
D_0 and d_0	The outer and inner diameter of the alloy steel tube
E (Pa)	The Young modulus
$\mathrm{E_P}$	The noise level

$E[\bullet]$	The expectation operation
$\mathbf{f}(t)$	The excitation force vector
f_s	The sampling ratio
f_{SA}	The first objective function in terms of response covariance sensitivity
f_{CA}	The second objective function in terms of response independence
$\hat{f}_{\mathrm{SA}}(\boldsymbol{\theta})$ and $\hat{f}_{\mathrm{CA}}(\boldsymbol{\theta})$	The non-dimensional objective functions normalized by their maximum values $\max f_{\mathrm{SA}}(\boldsymbol{\theta})$ and $\max f_{\mathrm{CA}}(\boldsymbol{\theta})$
F and M	The tensile force and bending moment
$\mathbf{F}(\boldsymbol{\theta})$	The multi-objective function for OSP
$\mathbf{G}$	The coordinate transformation matrix from the global coordinate to the local coordinate
H	The entropy information for a selected sensor configuration
H_0	The entropy information for the reference sensor configuration
h	Thickness of the beam element
$\ddot{\mathbf{h}}(t)$, $\dot{\mathbf{h}}(t)$, and $\mathbf{h}(t)$	Denote the unit impulse response (UIR) vector of acceleration, velocity, and displacement
$\ddot{h}_{p,f_i}$ and $\ddot{h}_{q,f_j}$	The UIRs of acceleration at the locations p and q corresponding to f_i and f_j
$\mathbf{I}_\varepsilon$	The identity matrix
$I_y\,(\mathrm{m}^4)$, $I_z\,(\mathrm{m}^4)$, and $I_p\,(\mathrm{m}^4)$	Moment of inertias
I_1, I_2 and I_3	Moment of inertias of three segments of a beam

I_{SCA}	The SCA index developed for optimal sensor placement
$I_{\mathrm{SCA}}(\boldsymbol{\theta}_{\mathrm{Pa}})$	Denotes the utility function for OSP
J_1 and J_2	The objective functions in the first and second step of model updating, respectively
$\mathbf{K_d}$ and $\mathbf{M_d}$	The system stiffness matrix and mass matrix for a damaged structure
$\mathbf{K}_i$ and $\mathbf{M}_i$	The i^{th} elemental stiffness and mass matrix of the structure in its intact state
$\mathbf{K}^{\mathrm{d}}$ ($\mathbf{K}^{\mathrm{u}}$)	Denotes the global stiffness matrix of the damaged (undamaged) tower structure
$\hat{\mathbf{K}}_r^{\mathrm{u,sup}}$	Represents the stiffness matrix of the undamaged r^{th} super-element (joint)
$\mathbf{K}_h^{\mathrm{u,ele}}$	The stiffness matrix for the h^{th} beam element
$\mathbf{K}^{\mathrm{d,hybrid}}$ ($\mathbf{K}^{\mathrm{u,hybrid}}$)	Denotes a hybrid global stiffness matrix in damaged (undamaged) state
$\bar{\mathbf{K}}_n^{\mathrm{u,bol}}$	The global stiffness matrix contributed by the n^{th} set of bolts in undamaged state
k	The iteration number
$\mathbf{L}_{\mathrm{d}}$	The selection matrix matching the nodal displacements for strain computation
$\mathbf{L}_{\mathrm{f}}$	The mapping matrix relating the excitation forces to the corresponding dofs of the structure
l	Length of the beam element
Δl	The equal increment of a tensile length
l_i, A_i and I_i	The length, sectional area and moment inertia of i^{th} segment of the damaged beam

$\mathbf{M}$, $\mathbf{C}$ and $\mathbf{K}$	The $N \times N$ mass, damping and stiffness matrices of the structure
$\mathbf{M}^e$ and $\mathbf{K}^e$	The consistent element mass and stiffness matrix
n	The total data number used for covariance computation
ne	The element number of a structure
np	The number of the damaged parameters for each element
$\mathbf{N}_{\text{oise}}$	A standard normal distribution vector with zero mean and unit standard deviation
N_p	The initial number of candidate sensor locations
N_o	The number of optimal placement sensors
N_a	The number of the estimated parameters
N_{oi}	The number of sensors of the i^{th} type
N_{oi}^L, N_{oi}^U	The lower and upper bounds of sensor number for the i^{th} type
Nr	The total number of suspicious super-elements
Nc	The total set number of the suspected bolts
$\mathrm{P}_\eta(\Delta\boldsymbol{\alpha})$	The penalty term for the regularization method
$\mathbf{P}(\boldsymbol{\theta})^0$	Denotes a collection of chromosomes in the NSGA-II method
$\mathbf{Q}(\boldsymbol{\theta})$	Denotes a new population in the NSGA-II method
$\mathbf{q}(t)$, $\dot{\mathbf{q}}(t)$ and $\ddot{\mathbf{q}}(t)$	The modal displacement, velocity and acceleration of the structure
$\mathbf{R}$	The correlation coefficient matrix
r_{pq}	The correlation coefficient

$r_{\mathrm{p}_l \mathrm{q}_k}$	The correlation coefficient computed from the responses recorded by the sensors p_l and q_k.
$\mathbf{S}$	The sensitivity matrix of the CBMS index vector to the fractional stiffness change vector
T	Denotes the transpose of a matrix
$\mathbf{V}_{\mathrm{pq}}$	The covariance-based multi-sensing (CBMS) damage detection index vector
$\mathbf{V}_{\mathrm{pq}}{}^{m}$	The CBMS vector computed from the measured responses
$\mathbf{V}_{\mathrm{pq}}{}^{c}$	The CBMS vector computed through the responses from the finite element model
$\Delta\mathbf{V}_{\mathrm{pq}}$	The variance between the $\mathbf{V}_{\mathrm{pq}}{}^{m}$ and $\mathbf{V}_{\mathrm{pq}}{}^{c}$
w_{SCA}	The weighting factor for the response covariance-based OSP method
$\mathbf{y}_{measured}$ and $\mathbf{y}_{calculated}$	The vectors of polluted measurement response and calculated response
$\mathbf{y}(t)$	The vector for the structural responses collected from different type of sensors
y_p and y_q	The structural response recorded by the sensor p and q
$\mathbf{y}_i^a$ and $\mathbf{y}_i^m$	The analytical and measured responses from the i^{th} sensor
$\hat{\mathbf{y}}_p$	The normalized structural response of sensor p
$\mathbf{z}(t)$, $\dot{\mathbf{z}}(t)$, and $\ddot{\mathbf{z}}(t)$	The displacement, velocity and acceleration response vectors of the structure at time t
$\ddot{z}_p$ and $\ddot{\mathrm{z}}_q$	The acceleration response of the structure at location p and q

$\{\boldsymbol{\alpha}\}$	The coefficient matrix of the structural parameters
$\alpha_{k,i}$	The coefficient of the k^{th} parameter for the i^{th} element
$\alpha_{1,i}$ and $\alpha_{2,i}$	The coefficients of the i^{th} elemental stiffness and mass matrix
$\Delta\boldsymbol{\alpha}$	The fractional stiffness change parameter or the least-squares solution of damage detection
$\Delta\boldsymbol{\alpha}_{\varepsilon}$	The least-squares solution for damage detection considering the random error from measurement and/or modeling errors
$\Delta\boldsymbol{\alpha}^{\text{sup}}$	The equivalent damage parameter vector
$\Delta\alpha_r^{\text{sup}}$	The equivalent damage parameter assigned to the r^{th} super-element
$\Delta\alpha_h^{\text{ele}}$	The stiffness reduction factor for the h^{th} beam element
$\Delta\alpha_n^{\text{bol}}$	Defined as a stiffness reduction factor assigned to the n^{th} set bolts
α_t and α_b	The equivalent stiffness reduction in terms of fractional change of tensile stiffness and the bending stiffness
$\alpha^{k,*}$ and $(\boldsymbol{\alpha}^{\text{sup}})^{k,*}$	The adaptive adjustment factor for the adaptive Tikhonov regularization method
β and γ	The time variable for the Duhamel's integral
$\boldsymbol{\delta}(t)$	The Dirac delta function
Δ_{err}	The covariance matrix of the estimation error

$\boldsymbol{\varepsilon}$	The random error vector which is assumed to obey zero-mean normal distribution with a variance of σ_{ε}^{2}.
$\left[\boldsymbol{\varepsilon}\boldsymbol{\varepsilon}^{\mathrm{T}}\right]$	The covariance matrix of the random error vector
$\boldsymbol{\varepsilon}(t)$	The strain response of the structure
η	A tuning parameter in the elastic net method
$\boldsymbol{\theta}$	Denotes the optimal sensor configuration
$\boldsymbol{\theta}_{\mathrm{Pa}}$	The Pareto solution with respect to an OSP
λ	The regularization parameter
μ_p and μ_q	The mean values of the normalized structural responses recorded by the sensors p and q
$v_p(t)$ and $v_q(t+\tau)$	The measurement noise in the structural responses recorded by the sensors p and q
ν	Poisson ratio
$\boldsymbol{\xi}$ and $\boldsymbol{\omega}$	The diagonal matrices of damping ratios and the natural frequencies of structure
ξ_1 and ξ_2	The first two damping ratios of a structure
$\rho(Kg/\mathrm{m}^3)$	Denotes the density of the material
σ_p^0	The standard deviation of y_p
τ	The time lag
$\boldsymbol{\Phi}$	Denotes the mode shape matrix
$\boldsymbol{\Phi}_i$ and ω_i	The i^{th} mode shape and natural frequency
$\boldsymbol{\Psi}$	The matrix of strain mode shapes
ω_i^a and ω_i^m	The i^{th} analytical and measured natural frequency

LIST OF ABBREVIATIONS

FRF	Frequency response function
MPC	Multi-point constraint
BSI	British standard institution
BSSP	Backward sequential sensor placement
CBMS	Covariance-based multi-sensing
DOFs	Degrees-of-freedom
FE	Finite element
EfI	Effective independence
EI	The effective independence matrix
HVPT	High-voltage power transmission
IE	Information entropy
NSGA-II	Non-dominated sorting genetic algorithm-II
OSP	Optimal sensor placement
RMS	The root-mean-square
SCA	Sensitivity and correlation analyses
SGCC	State grid corporation of China
SHM	Structural health monitoring
SNR	Signal-to-noise ratio
std	Standard deviation
UIR	Unit impulse response

CHAPTER 1

INTRODUCTION

1.1 Research Motivation

Owing to the rapid development of economy and the high demand of modern infrastructure from our community, numerous large-scale and complex civil structures, such as long-span bridges, tall buildings and high-voltage power transmission towers have been built around the world. Most of these structures are slender structures characterized with low natural frequencies and structural damping ratios. They often suffer from large structural deformation (Chan et al. 2006) and excessive structural vibration, when they are subjected to harsh environments such as strong winds and severe earthquakes. Therefore, many challenges are presented to professionals and researchers on how to ensure that these structures function properly during their long service lives and how to prevent them from destructive failure.

The structural health monitoring (SHM) technology has been recently developed as a cutting-edge technology to provide a better solution for the above problems concerned (Aktan et al. 1998; Aktan et al. 2000; Farrar and Worden 2007; Worden et al. 2007; Xu and Xia 2012). Currently, SHM systems are mainly implemented in large-scale landmark civil structures including large-span bridges and skyscrapers, such as Tsing Ma Bridge (Xu and Xia 2012) and Canton Tower (Ni et al. 2009) , and a great deal of research work has been dedicated to those structures. In contrast, applications of SHM for high power transmission towers have obtained less attention. However, numerous high power transmission towers have been built for high-voltage power transmission (HVPT) and an increasing amount of funding is being invested in this area because of dramatically increasing demand of energy in recent years. On the other hand, being exposed to natural hazards, these HVPT towers may experience structural failures more frequently than long-span bridges or tall buildings. Therefore, more research efforts should be paid for the SHM of HVPT towers.

As indicated and demonstrated in the literature (Xu and Xia 2012), robust damage detection on these slender structures, as the core task of SHM, is actually still in their infancy at the present stage, although SHM systems have found certain practical applications in monitoring loading and environmental effects, verifying the design criteria and guiding the timely inspection and maintenance on large civil structures. In the past decades, many vibration-based damage detection methods have been developed (Doebling et al. 1998; Sohn et al. 2002; Fan and Qiao 2011) for detecting, localizing and quantifying defects in structures by using the measured vibration responses. However, there are still five major difficult problems identified and insufficiently solved for damage detection of large civil structures.

1. Many damage indexes used in vibration-based damage detection methods, such as natural frequencies and mode shapes, are not sensitive to local damage of a civil structure. Different types of sensors are often used in an SHM system for a civil structure to measure various types of global and local structural responses, but multi-sensing information has not been used effectively for local damage detection.

2. Considering budget constraints and measurement inaccessibility, the number of sensors installed for capturing the structural responses of a large civil structure is always limited compared with the substantial structural components. Therefore, sensors may not directly monitor the locations of structural defects, and optimal sensor placement is important to ensure that the damage-induced structural information is effectively captured. Most of the optimal sensor placement (OSP) methods only use a single optimal objective function or consider different optimal objectives separately. The combination of multiple objective functions for OSP may lead to more accurate assessment for the structures. As indicated by some researchers (Meo and Zumpano 2005) single objective OSP algorithm can optimize the design objective, but may go

against another significant objective. However, the OSP problem with multiple objectives is more challenging than the OSP with only a single objective. Therefore, how to develop multiple OSP objectives for damage detection and how to implement multi-objective OSP are desirable for investigation.

3. Different merits and limitations of multi-type sensors often lead to the requirement of multi-objective functions in the optimization. In multi-type sensor and multi-objective OSP problems, conflicted objectives are very common because of the limited number of sensors and the complex nature of problem. Therefore, the investigation of structural damage detection-oriented multi-type sensor placement with multi-objective optimization is demanded. The simultaneous optimization of the conflicting objectives may lead to a set of compromised solutions known as the non-dominated or Pareto-optimal solutions, and these non-dominated solutions represent the trade-offs amongst different objectives. Thus, the development of a way how to select a most optimal sensor placement from the Pareto solutions is also worthy of attention.

4. A large-scale civil structure is usually a complex structure comprising tens of thousands of structural components of different sizes that are connected to one another in different ways. Local damage often does not significantly affect the global responses of these structures, thus traditional one-stage damage detection methods are inaccurate and sometimes are impossible for practical application. Therefore, the multi-stage strategy incorporating with a multi-scale finite element (FE) model may facilitate the damage detection of large civil structures.

5. Most studies of OSP and damage detection of large structures are theoretical or numerical studies, but experimental studies are important in the sense that new OSP methods and damage detection algorithms should be validated through the experiments before they are applied to real structures. However, the experimental exploration of multi-objective multi-type sensor optimal placement for damage

detection has not been found yet. Moreover, the experimental studies of multi-stage damage detection with multi-scale damage detection model for large structure are also rarely sought.

1.2 Research Objectives

This thesis develops a response covariance-based multi-sensing damage detection method, a damage detection oriented multi-type sensor optimal placement with multi-objection optimization, and the multi-stage damage detection strategy for large civil structures. The findings will improve the existing damage detection technologies for enhancing the ability to ensure the functionality and safety of slender structures. The major research objectives are specifically described as follows:

1. To develop a sensitive damage index to fuse data from multiple types of sensors, a new response covariance-based damage detection index and a multi-sensing damage detection method will be proposed. Heterogeneous data are normalized and integrated in a united multi-sensing damage detection index, and thus the corresponding sensitivity-based damage identification formulations can include both global and local responses.

2. To comprehensively consider different requirement for optimal sensor placement in damage detection, a response covariance-based sensor placement method for structural damage detection will be proposed with two optimization objectives in terms of the response covariance sensitivity and the response independence. The two objectives are analytically derived and then combined as one integrated objective function by using the weighted-sum method for application.

3. To extend the proposed two OSP objectives in the multi-objective optimization framework, the non-dominated sorting genetic algorithm (NSGA)-II will be adopted to directly find the solution for the optimal multi-type sensor placement to achieve the

best structural damage detection.

4. To experimentally verify the feasibility and efficiency of the proposed multi-sensing damage detection method and multi-objective multi-type sensor optimal placement method, damage detection will be performed on a nine-bay three-dimensional frame structure in the laboratory under multiple damage scenarios.

5. To extend the proposed response covariance-based multi-sensing damage detection method a large and complex structure, a multi-stage damage detection strategy incorporating with a multi-scale FE model will be proposed for the damage detection of a large structure. A finite element model of an HVPT tower is built and numerical damage detection study is performed to demonstrate the feasibility of the proposed method for a large civil structure.

6. To examine the accuracy of the numerical results, a laboratory-based testbed for the structural damage detection of a scaled HVPT tower will be established. The proposed multi-stage damage detection method will be implemented to the HVPT tower with multi-type sensor optimal placement. The experimental study on the laboratory-based testbed for this HVPT tower model will be conducted to demonstrate the numerical results obtained under objective 5.

1.3 Assumptions and Limitations

The development and application of a response covariance-based multi-sensing damage detection method, damage detection oriented multi-type sensor optimal placement with multi-objection optimization, and multi-stage damage detection strategy for large structures proposed in this thesis are subject to the following assumptions and limitations:

1. Assume that a structure is in static equilibrium initially and that the external excitations acting on the structure are mutual-independent Gaussian white noise excitations with zero means for damage detection.

2. Assume that the excitations are narrow banded and can be measured for damage detection. In experimental damage detection studies, the excitations are generated by exciters.

3. In experimental damage detection studies, the structural damage can be modeled as a degradation of the stiffness for the damaged region, such as grinding away a layer of material from the surface of the damaged beam in the middle segment for the three-dimensional frame structure and totally loosening one set of bolts in one connected beam for the damaged joint in the HVPT tower testbed for laboratory test. The main reason is that the severity of the above-mentioned damage can be more easily controlled and quantified accurately.

4. The structure is supposed to behave linearly and operate under the same working conditions before and after the occurrence of damage.

5. Considering extensive computation required in the damage detection of the full HVPT tower, only the damage-prone joints in 1/4 tower are selected for the demonstration of the proposed multi-stage damage detection.

1.4 Outline and Scope

This thesis covers various topics to achieve the aforementioned objectives, which includes 9 chapters and is organized as follows:

Chapter 1 introduces the problem, motivation, objectives, assumptions, and scope of this work.

Chapter 2 presents literature review on relevant topics, including the vibration-based damage detection methods and data fusion of multi-type structural responses; the optimal sensor placement methods and multi-objective optimization approaches; multi-scale modeling techniques, and multi-stages damage detection strategy.

Chapter 3 first proposes a covariance-based multi-sensing (CBMS) damage detection method in the time domain in terms of a CBMS vector as a new damage index and then a sensitivity study is conducted for damage detection. Numerical studies are finally performed to investigate the feasibility and accuracy of the proposed framework using an overhanging beam with two damage scenarios.

Chapter 4 presents a response covariance-based sensor placement method for structural damage detection with two objective functions for optimization. The relationship between the covariance of acceleration responses and the covariance of unit impulse responses of a structure subjected to multiple white noise excitations is first derived. The response covariance-based damage detection method is then presented. Two objective functions based on the response covariance sensitivity and the response independence are, respectively, formulated and finally integrated into a single objective function for optimal sensor placement. Numerical studies are conducted to investigate the feasibility and effectiveness of the proposed OSP in a three-dimensional frame structure by using the proposed response covariance-based damage detection method.

Chapter 5 develops a structural damage detection-oriented multi-type sensor placement method with multi-objective optimization. The multi-objective optimization problem is formed by using the two objective functions in Chapter 4, and the non-dominated sorting genetic algorithm (NSGA)-II is adopted to find the solution for the optimal multi-type sensor placement to achieve the best damage detection. The proposed method is finally applied to a nine-bay three-dimensional frame structure.

The selection of a most optimal sensor placement from the Pareto solutions via the utility function and the knee point method is demonstrated in the case study.

Chapter 6 experimentally examines the proposed response covariance-based damage detection method and the structural damage detection-oriented multi-objective multi-type sensor optimal placement method in a nine-bay three-dimensional frame structure. The multi-type sensors are optimally installed on the frame structure, and different damage scenarios are generated on the frame structure to validate the effectiveness of the proposed methods.

Chapter 7 proposes a multi-stage damage detection strategy incorporating with a multi-scale FE model for the damage detection of large structures. For the problem concerned in this thesis, the three-stage damage detection strategy is used. The first stage is to detect the existence of damaged joints and the locations of damaged joints based on the traditional beam model of the tower. The second stage is to detect the possibly damaged members with loosened bolts in the identified damaged joint based on the traditional beam model of the tower. The final stage is to identify the loosened bolts and quantify the damage severity based on the multi-scale FE model of the tower. Finally, the proposed multi-stage damage detection with optimal sensor placement (OSP) is numerically validated for their feasibility and effectiveness by using a 5.05m height testbed model of a scaled high-voltage power transmission (HVPT) tower.

Chapter 8 is an extension for the numerical study in Chapter 7 and an experimental investigation will be conducted in this chapter to validate the numerical study. Before this method can be applied to real transmission towers, this chapter aims to experimentally examine the effectiveness of the proposed multi-stage damage detection strategy incorporating with a multi-scale FE model for identifying the damage due to bolts loosen in a transmission tower testbed in laboratory.

Chapter 9 summarizes the contributions, findings, and conclusions of this thesis. The limitations of this study are discussed and some recommendations for future study are provided.

CHAPTER 2

LITERATURE REVIEW

As mentioned in Chapter 1, this thesis focuses on vibration-based damage detection of civil structures with the new developments of a sensitive damage detection index, multi-objective optimal sensor placement, optimal multi-type sensor placement, and multi-stage damage detection. The relevant topics and the most up-to-date research in the areas concerned will be reviewed in this chapter so that the problems and the needs for the new developments can be clearly identified. The overview of the relevant topics and the new developments targeted in this study is illustrated in Fig.2.1.

2.1 Structural Health Monitoring

Economic and life-safety issues are the primary driving force behind the development of structural health monitoring (SHM) technology. Comparing with the traditional visual inspection and maintenance approaches requiring one's expertise experience, the SHM technology is one kind of approaches which can continuously and automatically provide structural state information to the management team, so that the early stage structural problems may be identified quickly and the timely decisions can possibly be made by the authority in emergent situations.

SHM as a cutting-edge technology has been extensively investigated in different disciplines. Doebling et al.(1998) and Sohn et al.(2002) made a comprehensive review on advances of SHM. Specifically, an SHM system often includes five major subsystems: (a) sensor system; (b) data acquisition and transmission system; (c) data processing and control system; (d) data management system; (e) structural evaluation system, as shown in Fig.2.2. The major objectives of the SHM (Xu and Xia 2012) are to monitor the environmental condition of the structure, assess its performance in service, update the structural state and the relative FE model, verify or revise the rules used in its design stage, detect its damage or deterioration and fatigue after long time service, and guide its inspection and maintenance.

Structural damage detection, as a significant part of SHM, has thus been developed accordingly in past decades. Structural damage detection is an inverse problem for structural condition assessment. Two popular and important structural damage detection techniques in the field of SHM are wave-propagation-based techniques (Raghavan and Cesnik 2007) and vibration-based techniques (Fan and Qiao 2011). All the structural damage identification can be divided into a few stages of different damage detection levels as shown in Fig. 2.3: (1) detecting the existence of the damage on the infrastructure; (2) locating the damage; (3) identifying the types of damage and quantifying the severity of the damage; and (4) damage prognosis and useful life estimation. Increasing difficulty level often requires the knowledge of previous stages for the description of structural damage state.

Some experience of structural damage detection has been also summarized (Worden et al. 2007) as follows: (1) the assessment of damage requires a comparison between two system states in terms of healthy and damaged states; (2) identifying the existence and location and/or severity of damage can be done in an unsupervised learning mode, but identifying the type of damage present can generally be done in a supervised learning mode; and (3) sensors cannot measure damage directly, thus feature extraction through signal processing and statistical classification is necessary to convert sensor data into damage information.

2.2 Vibration-Based Damage Detection Methods

Research in vibration-based damage identification methods has been rapidly expanding over the last few decades (Doebling et al. 1996; Farrar and Doebling 1997; Doebling et al. 1998; Farrar et al. 2001; Fan and Qiao 2010; Farrar and Worden 2012). These vibration-based damage detection methods can be categorized as model-based and model-free methods. Model-based methods assume that the structural response can be accurately computed by using a finite element model and the damaged state of the real structure can be achieved by model updating technologies. Model-free methods are data-driven approaches which entirely rely on the measurement data to extract the damage sensitive features and establish classification schemes to identify the occurrence of structural damage. These two kinds of damage detection methods will be reviewed in the following two sections.

2.2.1 The Model-Based Damage Detection Methods

Significant efforts have been dedicated to vibration-based methods for model updating and damage detection in the past few decades. The basic idea behind these efforts is that a change in the physical properties is associated with changes in the modal properties which may be detected. Natural frequencies and mode shapes were taken as the measured modal properties to identify local damages in the early work of Cawley and Adams (1979) and others.

Nevertheless, Farrar et al. (1994) showed that the change of natural frequencies was not sufficiently sensitive to detect local damage. Mode shape-based damage detection methods also have similar difficulties for general application (Chance et al. 1994). Hence, there is some research on model updating and damage detection by directly using structural dynamic responses without the need of modal extractions. Cattarius and Inman (1997) used the phase shift in the time history of structural dynamic response to identify the presence of local anomalies in a structure. Choi and Stubbs (2004) formed the damage index directly from the time response to locate and quantify local anomalies in a structure. Similarly, those early works of the time domain damage detection methods mainly aimed to illustrate the proposed procedure and theoretically guide the subsequent experimental validation. The effect of not having noise or with slight noise was considered in the simulations study but still was not explicitly considered for the laboratory experiments.

Regarding to the measurement noise and/or modeling uncertainties in the practical application, statistic-based structural damage detection index may be more preferable to extract the slight change in the time-domain information. Some researchers notice that successful damage detection for practical application remarkably depended on the high signal-to-noise ratio (SNR) of information. Therefore, some statistic techniques may help filter the interruption and precisely extract the principal component from the measurement. Moreover, some researchers suggested to develop some statistic-based model or stochastic model to better represent the real structural condition, such as Zhu et al (2007) and Wong et al (2007). This thesis focuses on the techniques of developing statistic damage index for vibration-based structural damage detection, and many researchers have dedicated to this approach. Bendat and Piersol (1993) summarized the time-domain methods based on the covariance computation and showed advanced features of using covariance function in reducing random noise impact. Sun and Chang (2006) proposed a covariance-driven wavelet packet signature as a new index for health monitoring of structures under random ambient excitation. Both numerical and experimental results illustrated that their proposed technique could provide an accurate assessment on the damage locations, but the accuracy of the assessment of damage severity was low. Zhang et al. (2008) developed a new statistical moment-based structural damage detection method; its efficiency and effectiveness in sensitivity to structural damage but insensitivity to measurement noise have been numerically and experimentally demonstrated. When the target structure with a large number of unknown identification parameters, this statistical moment-based index may face a challenge of insufficient components after the statistical computation for damage identification. Further development in this context is the work of Li and Law (2010) and Law et al. (2012): a new covariance of covariance (CoC) matrix was formed from auto/cross-correlation functions of structural acceleration responses, in which the correlation of acceleration responses is the function of time lag. The components of the CoC matrix were found to be more sensitive to local stiffness reduction than using modal frequencies and mode shapes. The previous works often used acceleration responses for structural damage detection because acceleration responses contain better global information of a structure such as natural frequencies and mode shapes. However, this may not be consistent with the fact that damage is a local phenomenon and that using only a single type of sensor such as an accelerometer has its limitations for damage detection.

2.2.2 The Model-Free Damage Detection Methods

The model-free damage detection methods have been characterized by the use of purely data-based algorithms that do not depend on the physical descriptions of the structures, which is desirable in dealing with damage detection of large and complex structures in the practical application. The model-free damage detection mainly consists of three steps. First, the damage features should be extracted by using an extensive collection of vibration data, which are conducted based on signal processing technologies, such as the empirical mode decomposition (EMD), principal component analysis (PCA), and wavelet transformation (WT). Second, the base-line on the health state of the structure and the damage classification library should be built upon extensive measurement data from long-term monitoring. Finally, damage detection is conducted by using pattern recognition technologies, such as machine learning, deep learning and others, in which the condition of the damaged structure can be interpreted by using the collected data.

Many research works have been contributed to the vibration-based model-free damage detection methods (Farrar and Worden 2012). Fugate et al. (2001) applied statistical process control methods in terms of “control charts” to vibration-based damage detection, which can be conducted in an unsupervised learning mode to use the vibration test data. To detect structural damage in the presence of operational and environmental variations, Figueiredo and his colleges (Figueiredo et al. 2010; Figueiredo et al. 2011; Figueiredo et al. 2012) investigated and compared different machine learning algorithms based on the auto-associative neural network, factor analysis, Mahalanobis distance, and singular value decomposition. To enhance the performance of the statistical methods, Yao et al. (2012) developed an autoregressive statistical pattern recognition algorithms for damage detection of civil structures by using model spectra, residual auto-correlation, and resampling-based threshold construction methods. By using Fast Fourier Transform (FFT) and continuous wavelet transform (CWT) to extract the damage sensitive features, a signal-based pattern-recognition approach was used for structural damage diagnosis (Long et al. 2012). The previous model-free damage detection methods depend on the pattern recognition algorithms. Another kind of popular approach is the Bayesian-based damage detection method. Sohn and Law (1997) developed a Bayesian probabilistic approach for structural damage detection. A Markov-chain Monte Carlo based Bayesian approach (Figueiredo et al. 2014) was proposed for damage detection of bridges under unknown sources of variability. More recently, a model-free ANN-based approach combing the Bayes' theorem was proposed for the damage detection of a railway bridge (Neves et al. 2017). Latest, Wang et al. (2018) proposed a Bayesian probabilistic approach for acoustic emission-based rail condition assessment by using experimental data, which was effective for damage localization and quantification. However, the model-free damage detection methods often encounter a few obstacles in practical application. When comparing with the model-based damage detection methods, the model-free damage detection methods have difficulty in establishing an explicit relationship between the damage parameters and the dynamic responses. Moreover, the model-free methods require a dense sensor network for damage localization, and the severity quantification is usually very difficult or directly impossible. Further, most of the civil structures are unique and only limited amount of data on the damaged structures in the real-world scenarios is available, thus establishing a damage classification library for pattern recognition of civil structures is very challenging or unsuitable.

2.3 Damage Detection Using Multi-Type Sensors

Structural acceleration responses seem to be preferred measured responses because accelerometers are relatively reliable sensors with high signal-to-noise ratio, and acceleration responses usually contain better global information of a structure. However, using only accelerometers has its limitations for local damage detection. Therefore, the concept of using multi-sensing (multi-type sensors) measurements for damage detection and structural condition assessment has been sought. Studer and Peters (2004) presented a strategy using multi-metric data of strain, integrated strains and gradients measured from optical fiber sensors for damage identification. Law et al. (2005) used a wavelet-based approach to combine acceleration and strain response for damage identification and achieved better damage detection results than using the two measurements separately. Chan et al. (2006) proposed an integrated GPS-accelerometer data processing technique for improving the accuracy of measurement data. Zhang et al. (2011) suggested an integrated optimal sensor placement of displacement transducer and strain gauges for better response reconstruction. Sim et al. (2011) presented a flexibility-based method combining acceleration and strain responses for structural damage detection. More recently, Lee et al. (2013) developed a modified GDM (global-deviation method) which can be effectively utilized in detecting damage based on the mixed measurements of accelerometers and strain gauges. For some extent, these one-step approaches by using multi-type sensing data can show great potential to improve the quality of damage identification, but criteria of how to select the kind of sensors and their arrangement are not explicitly and systematically considered for practical engineering application yet. Huang et al. (2012) proposed a probabilistic damage detection approach using vibration-based nondestructive testing through multiple steps to move the accelerometers closing the damage candidates and got satisfactory fining results at the end, but the multiple steps with sensor location adjustment may be still not easy for practical engineering application. Sung et al. (2014) found that the damage metric estimated from acceleration measurement is insensitive to damage near the hinged support of a real bridge, and therefore they proposed a multi-scale sensing and diagnosis system for bridge health monitoring based on a two-step improvement approach using accelerometers and gyroscopes. It seems that the two-stage and multi-sensing approach is not only a concise and easy implement method, but also it is a more desirable and flexible scheme for data combination and fusion. This is regarded as a method that may achieve more accurate and reliable results for structural damage detection. However, there is still not much literature found for a detail discussion of a standard and unified framework for two-stage and multi-sensing structural damage detection and condition assessment (Lin and Xu 2017).

2.4 Optimal Sensor Placement Methods

A civil structure often consists of hundreds of structural members and joints, but the number of sensors installed in the structure is always limited. It is quite possible that the local damage may not be covered by the deployed sensors and its location may even not be accessible. Therefore, sensors shall be optimally placed in a structure so that the sensing information from the sensors can be used for effective damage detection. Previous studies have revealed that arbitrary sensor placement could lead to false damage identification (Santi et al. 2005; Huston 2010). Significant efforts have been spent on optimal sensor placement (OSP) in the last few decades, and many OSP methods have been proposed for various purposes including damage detection (Meo and Zumpano 2005; Barthorpe and Worden 2009; Yi and Li 2012). However, most of the OSP methods are applied for single-type sensors only. Although the design can be carried out independently for each type of sensors, the final sensor configuration by combining the individual designs could not avoid redundant measurement and exhibit holistically optimal performance (Zhang et al. 2011; Zhu et al. 2013; Yuen and Kuok 2015; Lu et al. 2016).

The proper selection, installation and use of multi-type sensors become important for the SHM of structures (Ni et al. 2009; Sim et al. 2011; Sung et al. 2014; Xu et al. 2016; Zhang and Xu 2016). Various types of sensors (e.g., accelerometer, displacement transducer and strain gauge) are installed in a structure to measure multi-type structural responses. Acceleration responses can be easily measured with a high signal-to-noise ratio and contain higher kinetic energy in higher-order vibrational modes. By contrast, displacement responses contain more kinetic energy in lower-order vibrational modes. Strain or stress responses are sensitive to local changes closer to the sensors but not sensitive to local changes far away from the sensors. Because of the different merits and limitations of these sensors, the joint use of multi-type sensors complicates the optimal sensor placement for structural damage detection.

Some efforts have been devoted to optimizing the performance of multi-type sensors in a unified framework. Zhang et al. (2011) suggested an extended EfI OSP method for two types of sensors, in which the displacement transducers are integrated with the strain gauges for better response estimation. Zhu et al. (2013) and Xu et al. (2016) carried out further studies on multi-type sensor optimal placement for response reconstruction in terms of the Kalman filter. This method was later extended to the situations with the reconstruction of unknown external excitation (Zhang and Xu 2015) and applied for damage detection of an overhanging beam structure (Zhang and Xu 2016). Yuen and Kuok (2015) proposed a Bayesian sequential sensor placement algorithm for multi-type sensors optimization based on robust information entropy such that the overall performance of various types of sensors can be assessed. Recently, a data correlation analysis-based OSP method combined with a bone energy algorithm (Lu et al. 2016) was studied with different types of sensors deployed for less redundant measured information in a large spherical lattice dome-like structure. However, all the above works were based on the optimization of a single objective function with a unique optimal sensor configuration.

Different merits and limitations of multi-type sensors often lead to the requirement of multi-objective functions in the optimization. In multi-type sensor and multi-objective OSP problems, conflicted objectives are very common because of the limited number of sensors and the complex nature of the problem (Coello 1999; Deb 2001). The simultaneous optimization of the conflicting objectives may lead to a set of compromised solutions known as the non-dominated or Pareto-optimal solutions, and these non-dominated solutions represent the trade-offs amongst different objectives. An efficient Pareto sequential sensor placement (PA-SSP) algorithm with multi-objective functions (Papadimitriou 2005) was developed for model updating. This algorithm was proved to be more efficient than the strength Pareto evolutionary algorithm (SPEA). The non-dominated sorted genetic algorithm-II (NSGA-II) was used for the optimal contaminant sensor network design in (Preis and Ostfeld 2008) and the optimal sensor configuration design of water distribution networks in (Yoo et al. 2015). Also, Kim et al. (2008) used the NSGA-II to tackle a surveillance sensor placement problem. Moreover, Mathakari et al. (2007) proposed the reliability-based optimal design of electrical transmission towers using multi-objective genetic algorithms. For active control systems of buildings, Cha and his colleagues (Cha et al. 2012; Cha et al. 2013; Cha et al. 2013) investigated the optimal placement of both actuators and sensors by developing a novel multi-objective genetic algorithm (NS2-IRR GA) through the integration of the NSGA-II and the implicit redundant presentation (IRR) GA. To enhance the capability of structural damage detection, optimal accelerometer placement with multiple objectives in terms of information entropies computed by multiple mode-shapes was reported in (Ye and Ni 2012). Additionally, the damage detection was investigated in (Cha and Buyukozturk 2015) by adopting an advanced multi-objective optimization algorithm with two objectives in terms of the differences of two sets of modal strain energy (MSE) before and after damage occurring although the single type sensor of accelerometers is not optimally placed. However, the exploration of multi-type sensor optimal placement with multiple objectives for structural damage detection is still rarely found.

2.5 Challenges in Damage Detection of Large Structures

As mention before, the vibration-based damage detection methods (Doebling et al. 1998; Sohn et al. 2002; Fan and Qiao 2011; Xu and Xia 2012) are widely used in the field of SHM. Although many vibration-based damage detection methods succeed in identifying damage in small structures. However, successful damage detection of a large civil structure is still rarely found. Specifically, damage detection of large structure encounters a few major difficulties: (1) a larger number of damage parameters (unknowns) for the identification which is in contrast to the small number of sensors installed in the structure in practice; (2) the change of global stiffness matrix, modal parameters, and the dynamic responses are less sensitive to the local damage;

(3) many damage indexes used are not sensitive to local damage of a civil structure; (4) structural damage detection of large structure is inherently a severely ill-conditioned inverse problem, in which the numerical difficulty to achieve computation convergence increases dramatically. Some research efforts to deal with these problems will be reviewed in the following three paragraphs.

To reduce the number of unknowns in a large structure, two-stage damage detection strategy and/or substructure-based approaches are popular for damage detection. When the number of sensors is limited, one-step damage detection method sometimes may not be workable in the practical application. Some researchers (Xiang and Liang 2012; Sung et al. 2014; Lin and Xu 2017) proposed to use two-stage damage detection, in which some suspicious areas including both the real damage locations and some false alarms were first located and then damage refinement was conducted in the narrowed areas by excluding the unsuspicious locations. This is a simple two-stage strategy that can reduce the identification parameters step by step for better damage detection accuracy, but success in the first stage is usually too difficult for a large structure because of too many identification parameters at the very beginning. For large structures, damage detection is very difficult and the accuracy of the parameter estimation is rarely reliable. The substructure-based identification is a desirable strategy to divide the structure into substructures such that the number of unknown parameters is manageable for each substructure. Accordingly, substructure-based damage identification can be performed more efficiently. Therefore, application of the substructure-based damage detection methods in both frequency domain and time domain has attracted considerable interest. Koh et al. (1991) proposed a substructure-based method by using the extended Kalman filter to estimate the structural stiffness and damping coefficients from measured dynamic responses. Yun and his colleagues (Yun and Lee 1997; Yun and Bahng 2000) proposed a substructural identification method for local damage estimation which incorporated with an auto-regressive and moving average with stochastic input model or the backpropagation neural network. Later, Koh et al. (2003) developed a GA-based substructural and progressive parameter identification method, in which only measurements within the substructure of concern and at interface ends were used when identifying the substructure parameters. Various substructural identification approaches need to know interface responses, which are treated as input to the concern substructures. In practice, however, it is not always possible to obtain interface measurements, such as rotational response for beam/frame structures. Furthermore, Koh et al. (2003) proposed a substructural identification method which can release the interface measurement. More recently, Law et al. (2010) proposed a method to identify the coupling forces between substructures from the acceleration response of a structure under support excitation, and the local structural damage was then detected from the identified coupling forces based on dynamic sensitivity analysis. Also, Law and Ding (2011) compared two substructural identification methods in terms of an accurate finite element model of the whole structure that is assumed known and only the finite element model of the concerned substructure is needed. The numerical study shows that the second approach is better because the target substructure for updating consists of a significantly reduced number of components and the identification problem is more efficient. Later, the substructural damage identification approaches without the information of responses and forces at the interface degrees-of-freedom are developed (Li et al. 2012; Li and Law 2012; Li and Law 2012), in which the response and force reconstruction are based on the transmissibility matrix. On the other hand, the substructure technique is popularly used to reduce the number of unknowns for damage detection, in which the targeted structure is divided into a few numbers of substructures and each substructure has an equivalent damage parameter. For instance, some researchers (Yin et al. 2009; Lam and Yin 2011) proposed a substructure-based damage detection of transmission tower utilizing ambient vibration data, which identified damaged substructure by estimating the equivalent stiffness reduction and was validated by numerical and experimental studies. Noted that this damage detection method was to estimate the equivalent stiffness reduction of substructures, but cannot identify the reduction in stiffness of individual members. However, damage could possibly occur inside the substructure and different members of the substructure may bear different damage extents. Differently, Zhang and his colleague (Zhang and Xu 2017; Xu et al. 2018) developed a two-level damage identification with response reconstruction to identify damage in both substructure level and individual element level. The method was investigated through numerical and experimental studies by using a simply-supported overhanging steel beam model and a testbed model of the Tsing Ma Suspension (TMS) bridge, which can identify the suspicious substructures in stage one and identify the location and severity of damaged beam elements inside a suspicious substructure in stage two.

To comprehensively capture damage characteristic of the large structure, multi-type sensors are employed in many SHM system such that data fusion of different type of information attracts much attention. Therefore, multi-sensing structural damage detection (Studer and Peters 2004; Chan et al. 2006; Sim et al. 2011; Sung et al. 2014; Lin and Xu 2017) has been sought based on fusing global and local measured information since the last decade. Considering the budget constraint and measurement inaccessibility, the number of sensors is always limited for capturing the structural responses of large civil structures when compared with the substantial structural components. In other words, sensors may not directly monitor the locations of structural defects. Zhang and his colleagues proposed to optimally reconstruct those unmeasured responses for damage detection (Zhang and Xu 2015; Xu et al. 2016; Hu et al. 2018), especially for a large structure. Moreover, optimal sensor placement is particularly important to ensure that the damage-induced structural information is effectively captured. To effectively use both the global and local measurement information, multi-type sensor optimal placement has gained much attention for applications in parameters identification (Yuen and Kuok 2015) and structural health monitoring (Lu et al. 2016). Different merits and limitations of multi-type sensors often lead to the requirement of multi-objective functions in the optimization. Therefore, some researchers devoted to the simultaneous optimization of the conflicting objectives for the single-type and/or multi-type sensor optimal placement problem in structural damage detection (Ye and Ni 2012; Guo et al. 2016; Lin and Xu 2017; Lin et al. 2018).

The aforementioned methods, namely two-stage strategy and/or substructure technique, data fusion, response reconstruction, or multi-objective multi-type sensor optimal placement, have potential to alleviate the problems in damage detection of large structures. However, most of these methods were validated by using small structures other than large and complex structures, and the combination of these ideas was not sufficiently investigated yet. Besides, some attention should be paid to the behavior in local details because the damage is typically a local phenomenon (Doebling et al. 1998; Farrar et al. 2001). Some research indicated (Li et al. 2007; Li et al. 2012; Castro-Triguero et al. 2017; Wang et al. 2017) that accurate modeling of local structural components is critical for local failure or vulnerability analysis of large structures. However, a detailed model of a local damaged structure is still rarely applied for more accurate identification no matter in small or large structures.

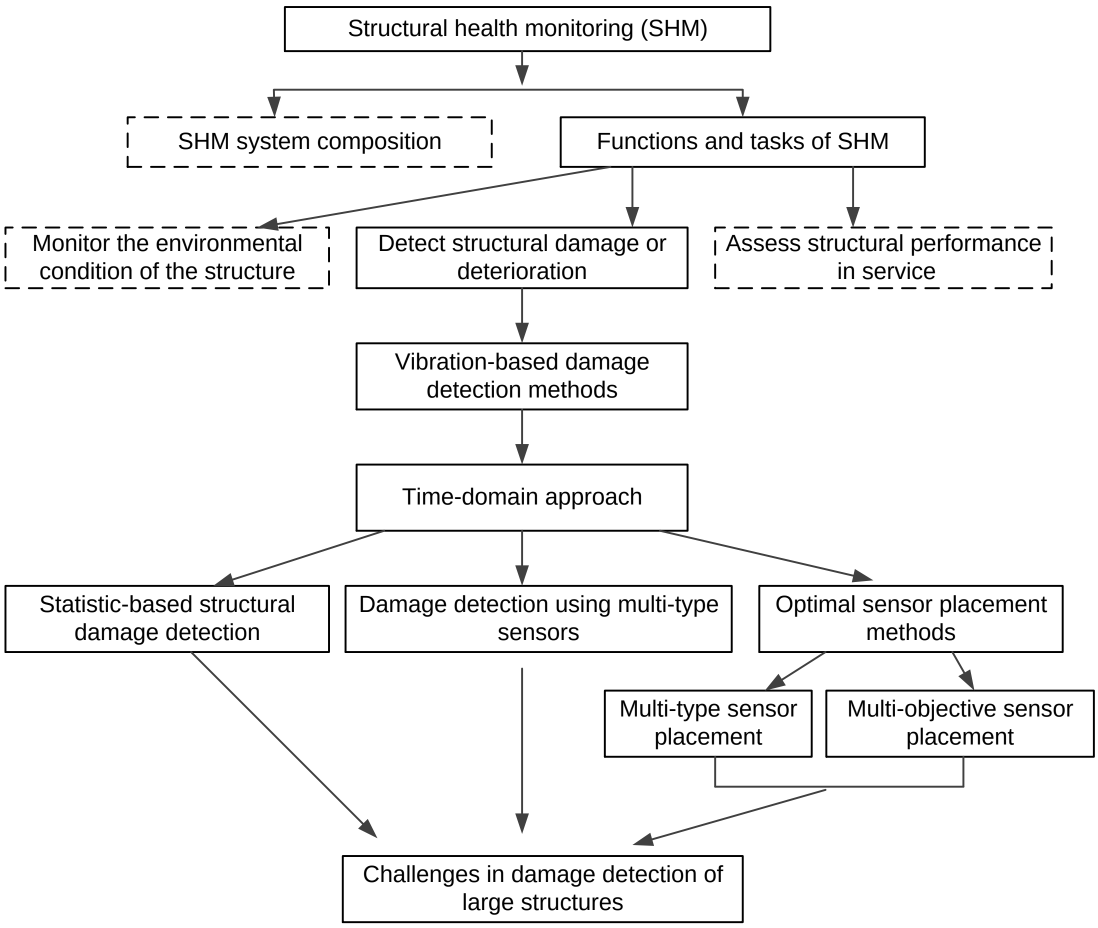

Fig. 2.1 The overview of the literature review and the new developments in the thesis

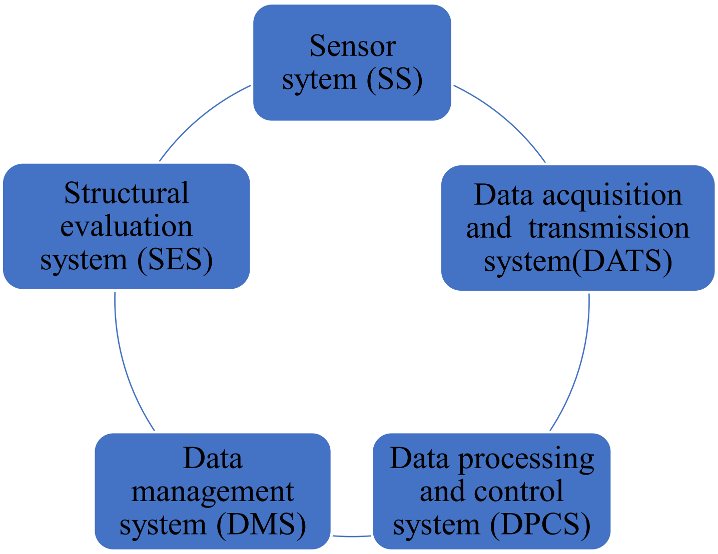

Fig. 2.2 Basic components of SHM system

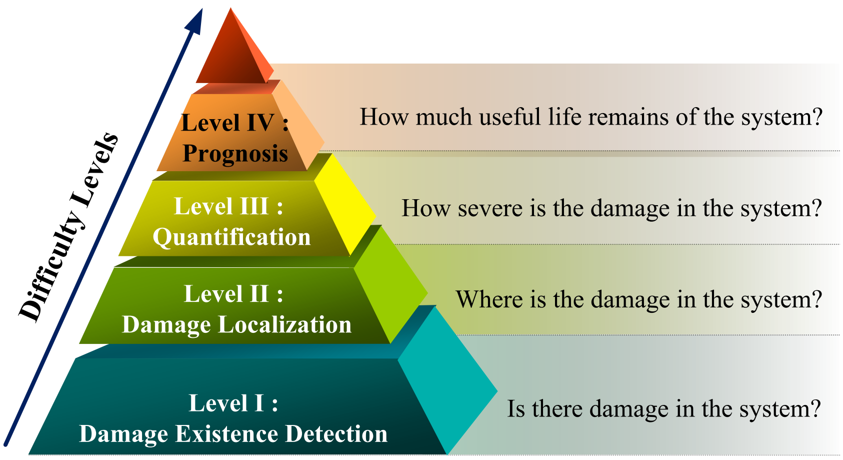

Fig. 2.3 Four-step process of the description of structural damage state

CHAPTER 3

RESPONSE COVARIANCE-BASED MULTI-SENSING DAMAGE DETECTION METHOD

3.1 Introduction

Many damage indexes used in vibration-based damage detection methods, such as natural frequencies, are not sensitive to local damage of a civil structure. Different types of sensors are often used in a structural health monitoring (SHM) system for a civil structure to measure both global and local structural responses, but multi-sensing information has not been used effectively for local damage detection. This chapter aims at developing a new response covariance-based multi-sensing damage detection method. This method features the structural damage detection method that can fuse the normalized data collected from different types of sensors and reduce the adverse impact of measurement noise in structural responses. The cross-covariance functions are employed to assimilate heterogeneous data from different types of sensors and combine various structural responses together to form a multi-sensing data set. A normalized cross-covariance matrix is then formed and the covariance-based multi-sensing (CBMS) vector is defined as a new damage index. The sensitivity-based method is then used to derive the formulations for the CBMS damage detection method. A numerical study is finally performed to investigate the feasibility and accuracy of the proposed method using an overhanging beam with multiple damage scenario. It shall be pointed out that the response covariance-based multi-sensing damage detection method proposed in this chapter is a general framework only and the key issues for implementing this method for a civil structure as well as the validation of the proposed method will be discussed in the subsequent chapters.

3.2 Methodology

3.2.1 Equation of Motion

The equation of motion of a linear-elastic structural system with N degrees-of-freedom (DOFs) can be written as

$$\mathbf{M}\ddot{\mathbf{z}}(t)+\mathbf{C}\dot{\mathbf{z}}(t)+\mathbf{K}\mathbf{z}(t)=\mathbf{L}_{\mathrm{f}}\mathbf{f}(t) \tag{3.1}$$

where $\mathbf{M}$, $\mathbf{C}$ and $\mathbf{K}$ are, respectively, the $N\times N$ mass, damping and stiffness matrices of the structure; $\mathbf{z}(t)$, $\dot{\mathbf{z}}(t)$, and $\ddot{\mathbf{z}}(t)$ are, respectively, the displacement, velocity and acceleration response vectors of the structure at time t; $\mathbf{f}(t)$ is the excitation force vector; and $\mathbf{L}_{\mathrm{f}}$ is the mapping matrix relating the excitation forces to the corresponding DOFs of the structure.

Eq. (3.1) can be decoupled using the coordinate transformation $\mathbf{z}=\mathbf{\Phi}\mathbf{q}(t)$. After pre-multiplying both sides with $\mathbf{\Phi}^{\mathrm{T}}$, the equation of motion in the modal coordinate can be expressed as

$$\ddot{\mathbf{q}}(t)+2\boldsymbol{\xi}\boldsymbol{\omega}\dot{\mathbf{q}}(t)+\boldsymbol{\omega}^{2}\mathbf{q}(t)=\mathbf{\Phi}^{\mathrm{T}}\mathbf{L}_{\mathrm{f}}\mathbf{f}(t) \tag{3.2}$$

where $\mathbf{q}(t)$, $\dot{\mathbf{q}}(t)$ and $\ddot{\mathbf{q}}(t)$ are, respectively, the modal displacement, velocity and acceleration of the structure; $\mathbf{\Phi}$ denotes the mode shape matrix and the superscript T denotes the transpose of a matrix; $\boldsymbol{\xi}$ and $\boldsymbol{\omega}$ are, respectively, the diagonal matrices of damping ratios and the natural frequencies of structure.

According to the strain-displacement relationship, the strain response can be expressed in modal coordinates as

$$\boldsymbol{\varepsilon}(t)=\mathbf{BGL}_{\mathrm{d}}\mathbf{z}(t)=(\mathbf{BGL}_{\mathrm{d}}\mathbf{\Phi})\mathbf{q}(t)=\mathbf{\Psi}\mathbf{q}(t) \tag{3.3}$$

where $\boldsymbol{\varepsilon}(t)$ is the strain response of the structure; the matrix $\mathbf{\Psi}=\mathbf{BGL}_{\mathrm{d}}\mathbf{\Phi}$ is the matrix of strain mode shapes; $\mathbf{L}_{\mathrm{d}}$ is the selection matrix matching the nodal displacements for strain computation; the matrix $\mathbf{G}$ is the coordinate transformation matrix from the global coordinate to the local coordinate; and the vector $\mathbf{B}$ defines the local strain-displacement relationship (Ottosen et al. 1992).

The equation of motion can then be rewritten in the state space with the state vector $\mathbf{x} = [\mathbf{q}, \dot{\mathbf{q}}]^{\mathrm{T}}$ as

$$\dot{\mathbf{x}}(t) = \mathbf{A}_c\mathbf{x}(t) + \mathbf{B}_c\mathbf{f}(t) \tag{3.4}$$

with

$$\mathbf{A}_c = \begin{bmatrix} \mathbf{0} & \mathbf{I} \\ -\boldsymbol{\omega}^2 & -2\boldsymbol{\xi\omega} \end{bmatrix};\ \mathbf{B}_c = \begin{bmatrix} \mathbf{0} \\ \boldsymbol{\Phi}^{\mathrm{T}}\mathbf{L}_{\mathbf{f}} \end{bmatrix}; \tag{3.5}$$

where $\mathbf{A}_c$ and $\mathbf{B}_c$ are the continuous state matrix and input matrix, respectively.

Three types of sensors are considered here: strain gauge, displacement transducer and accelerometer. The structural responses collected from the sensors are included in the observation vector as $\mathbf{y}(t) = [\boldsymbol{\varepsilon}(t), \mathbf{z}(t), \ddot{\mathbf{z}}(t)]^{\mathrm{T}}$. On the other hand, the structural responses $\mathbf{y}(t)$ calculated from the finite element model of the structure can be explicitly written as

$$\mathbf{y}(t) = \mathbf{C}_c\mathbf{x}(t) + \mathbf{D}_c\mathbf{f}(t) \tag{3.6}$$

with

$$\mathbf{C}_c = \begin{bmatrix} \boldsymbol{\Psi} & \mathbf{0} \\ \boldsymbol{\Phi} & \mathbf{0} \\ -\boldsymbol{\Phi\omega}^2 & -2\boldsymbol{\Phi\xi\omega} \end{bmatrix};\ \mathbf{D}_c = \begin{bmatrix} \mathbf{0} \\ \mathbf{0} \\ \boldsymbol{\Phi\Phi}^{\mathrm{T}}\mathbf{L}_{\mathbf{f}} \end{bmatrix}; \tag{3.7}$$

where $\mathbf{C}_c$ and $\mathbf{D}_c$ are the output matrix and transmission matrix, respectively.

3.2.2 Response Covariance-Based Damage Index

Strain, displacement, and acceleration responses have different units and orders of magnitudes. They need to be normalized before they can be used in the subsequent analysis.

$$\hat{y}_p(t) = \frac{y_p(t)}{\sigma_p^0} \tag{3.8}$$

where y_p is the structural response recorded by the sensor p; $\hat{y}_p$ is the normalized structural response; and σ_p^0 is the standard deviation of y_p and the superscript 0 denotes the response recorded from the intact structure.

To fully utilize multi-sensing information and significantly reduce the adverse impact of measurement noise, the cross-covariance function (Bendat and Piersol 1993) of the two normalized stationary time responses, $y_p(t)$ and $y_q(t)$, of a linear structure under stationary excitations is considered here.

$$\hat{C}_{\mathrm{pq}}(\tau) = E[\{\hat{y}_p(t) - \mu_p\} \cdot \{\hat{y}_q(t+\tau) - \mu_q\}] = \lim_{n\to\infty} \frac{1}{n} \cdot \sum_{j=1}^{n} \{\hat{y}_p(t_j) - \mu_p\} \cdot \{\hat{y}_q(t_j+\tau) - \mu_q\}$$

(3.9)

where $E[\bullet]$ is the expectation operation; n is the total data number used for covariance computation; μ_p and μ_q are the mean values of the normalized structural responses recorded by the sensors p and q, respectively; and τ is the time lag.

When measurement noise is taken into consideration and expressed in an explicit form, Eq. (3.9) becomes:

$$\tilde{C}_{\mathrm{pq}}(\tau) = E[\{\hat{y}_p(t) - \mu_p + v_p(t)\} \cdot \{\hat{y}_q(t+\tau) - \mu_q + v_q(t+\tau)\}] \tag{3.10}$$

where $v_p(t)$ and $v_q(t+\tau)$ are the measurement noise in the structural responses recorded by the sensors p and q, respectively. The measurement noise is assumed to be a white noise Gaussian process with $E(v_p) = E(v_q) = 0$. The measurement noise is also assumed to be uncorrelated with each other as well as with measured responses. Consequently, Eq. (3.10) can be further expressed as:

$$\begin{aligned} \tilde{C}_{\mathrm{pq}}(\tau) =& E[\{\hat{y}_p(t) - \mu_p\} \cdot \{\hat{y}_q(t+\tau) - \mu_q\}] + E[\{\hat{y}_p(t) - \mu_p\}] \cdot E[v_q(t+\tau)] \\ &+ E[v_p(t)] \cdot E[\{\hat{y}_q(t+\tau) - \mu_q\}] + E[v_p(t)] \cdot E[v_q(t+\tau)] \\ &\approx E[\{\hat{y}_p(t) - \mu_p\} \cdot \{\hat{y}_q(t+\tau) - \mu_q\}] \end{aligned} \tag{3.11}$$

It is noted that when the data number $n \to \infty$, $\tilde{C}_{\mathrm{pq}}(\tau) \to C_{\mathrm{pq}}(\tau)$, which indicates that sufficiently long measured data can ensure that the use of covariance computation can reduce the impact of measurement noise significantly.

When $\mu_p = \mu_q = 0$, the normalized cross-covariance function becomes the normalized cross-correlation function, and it is simplified as

$$\hat{C}_{\mathrm{pq}}(\tau)=E[\hat{y}_p(t)\hat{y}_q(t+\tau)]=E\left[\left(\frac{y_p(t)}{\sigma_p^0}\right)\left(\frac{y_q(t+\tau)}{\sigma_q^0}\right)\right] \tag{3.12}$$

The components of the covariance-based multi-sensing (CBMS) damage detection index vector $\mathbf{V}_{\mathrm{pq}}$ (Lin and Xu 2017) are computed by using Eq. (3.12), and the CBMS index vector $\mathbf{V}_{\mathrm{pq}}$ is written as

$$\begin{aligned}\mathbf{V}_{\mathrm{pq}}=&[\hat{C}_{\mathrm{p_1q_1}}(\tau_0),\hat{C}_{\mathrm{p_1q_2}}(\tau_0),\cdots,\hat{C}_{\mathrm{p}_i\mathrm{q}_j}(\tau_0),\cdots,\hat{C}_{\mathrm{p}_s\mathrm{q}_s}(\tau_0),\cdots,\hat{C}_{\mathrm{p_1q_1}}(\tau_1),\hat{C}_{\mathrm{p_1q_2}}(\tau_1),\cdots,\\&\hat{C}_{\mathrm{p}_i\mathrm{q}_j}(\tau_1),\cdots,\hat{C}_{\mathrm{p}_s\mathrm{q}_s}(\tau_1),\cdots,\hat{C}_{\mathrm{p_1q_1}}(\tau_{\mathrm{nt}-1}),\hat{C}_{\mathrm{p_1q_2}}(\tau_{\mathrm{nt}-1}),\cdots,\hat{C}_{\mathrm{p}_i\mathrm{q}_j}(\tau_{\mathrm{nt}-1}),\cdots,\hat{C}_{\mathrm{p}_s\mathrm{q}_s}(\tau_{\mathrm{nt}-1})]^{\mathrm{T}}\end{aligned} \tag{3.13}$$

where $\mathrm{p}_i\in[\mathrm{p}_1,\mathrm{p}_s]$ and $\mathrm{q}_j\in[\mathrm{q}_1,\mathrm{q}_s]$, and the subscript s denotes the total number of selected sensors; the nt is the time lags number selected for the subsequent study; and the superscript T denotes the transpose operation of a vector. Because the normalized cross-covariance function $\hat{C}_{\mathrm{pq}}(\tau)$ in Eq. (3.12) is a decay function (Bendat and Piersol 2010), its value gradually reduces as the time lag τ increases and at the same time the covariance of the measurement white noise is a constant with the prescribed number of measurement data. By taking this feature into account, only the first nt time lags in $\hat{C}_{\mathrm{pq}}(\tau)$ are selected in Eq. (3.12) to avoid using the values of $\hat{C}_{\mathrm{pq}}(\tau)$ smaller than the covariance of the measurement white noise for damage detection.

It is worth pointing out that the proposed CBMS damage index has some advantages for damage detection. The first advantage is that the CBMS index can flexibly combine different types of responses into the same damage detection index. The second advantage is that the proposed CBMS index is sensitive to local damage because both the global and local responses are used together for damage detection. For example, the strain responses are local responses, which are very sensitive to local damages. Moreover, the proposed CBMS index is insensitive to the measurement noise, when sufficient number of data is used for the computation of response covariance. In other words, the signal-to-noise-ratio (SNR) of the CBMS index depends on the measurement time duration of the dynamic responses.

3.2.3 Damage Model and Damage Detection Equation

The proposed damage detection method is based on the fact that any change in the physical property of a structure will alter its dynamic responses as well as response covariance (Lu and Law 2007). Denote the matrix $\{\boldsymbol{\alpha}\}$ shown in Eq. (3.14) as the coefficient matrix of the structural parameters and its values are directly related to the fractional changes in the parameters of the structure. For a finite element model of the structure with ne sets of unknowns and each set of unknowns with np parameters for the identification, the total number of unknown fractional changes of the structure is $\mathrm{ne}\times\mathrm{np}$. Hence, at least $\mathrm{ne}\times\mathrm{np}$ equations are needed to find all the unknown fractional changes.

$$\{\boldsymbol{\alpha}\} = \left[\boldsymbol{\alpha}_1, \boldsymbol{\alpha}_2, \cdots, \boldsymbol{\alpha}_k, \cdots, \boldsymbol{\alpha}_{\mathrm{np}}\right]^T = \begin{bmatrix} \alpha_{1,1} & \alpha_{2,1} & \cdots & \alpha_{k,1} & \cdots & \alpha_{\mathrm{np},1} \\ \alpha_{1,2} & \alpha_{2,2} & \cdots & \alpha_{k,2} & \cdots & \alpha_{\mathrm{np},2} \\ \vdots & \vdots & \ddots & \vdots & \vdots & \vdots \\ \alpha_{1,i} & \alpha_{2,i} & \vdots & \alpha_{k,i} & \vdots & \alpha_{\mathrm{np},i} \\ \vdots & \vdots & \vdots & \vdots & \ddots & \vdots \\ \alpha_{1,\mathrm{ne}} & \alpha_{2,\mathrm{ne}} & \cdots & \alpha_{k,\mathrm{ne}} & \cdots & \alpha_{\mathrm{np},\mathrm{ne}} \end{bmatrix}^T \in \mathbb{R}^{\mathrm{ne}\times\mathrm{np}} \tag{3.14}$$

subject to: $k \in [1, \mathrm{np}]; i \in [1, \mathrm{ne}];$

where $\alpha_{k,i}$ is the coefficient of the k^{th} parameter for the i^{th} element with the unit value representing the intact state and other values the damage state. The changes in the structural parameters will cause the changes in structural dynamic responses and accordingly response covariance. Therefore, the CBMS damage index vector is a function of the coefficient matrix $\boldsymbol{\alpha}$, which can be expressed as:

$$\mathbf{V}_{\mathrm{pq}}(\boldsymbol{\alpha}) = f(\boldsymbol{\alpha}_1, \boldsymbol{\alpha}_2 \cdots, \boldsymbol{\alpha}_k, \cdots \boldsymbol{\alpha}_{\mathrm{np}}) \tag{3.15}$$

The parameter changes and their damage models for a civil structure often refer to the changes in structural stiffness, mass and damping (Cattarius and Inman 1997). The changes in structural stiffness and mass after damage occurrence are considered in this study as they are most common damage scenarios. The Rayleigh damping model is used in this study, and accordingly the change in structural damping depends on the change in the structural stiffness and mass. A linear damage model is adopted in this study for the changes in both structural stiffness and mass, and the structural connectivity is assumed to be maintained after damage. The system stiffness matrix $\mathbf{K_d}$ and mass matrix $\mathbf{M_d}$ for a damaged structure can then be expressed as:

$$\begin{cases} \mathbf{K_d} = \sum_{i=1}^{\mathrm{ne}} \alpha_{1,i} \cdot \mathbf{K}_i = \sum_{i=1}^{\mathrm{ne}} (1+\Delta\alpha_{1,i}) \cdot \mathbf{K}_i \\ \mathbf{M_d} = \sum_{i=1}^{\mathrm{ne}} \alpha_{2,i} \cdot \mathbf{M}_i = \sum_{i=1}^{\mathrm{ne}} (1+\Delta\alpha_{2,i}) \cdot \mathbf{M}_i \end{cases} \tag{3.16}$$

$$\text{subject to: } \alpha_{1,i}\ ,\ \alpha_{2,i} \in \boldsymbol{\alpha};\ 0 \le \alpha_{1,i}\ ,\ \alpha_{2,i} \le 1$$

where $\mathbf{K}_i$ and $\mathbf{M}_i$ are respectively the i^{th} elemental stiffness and mass matrix of the structure in its intact state in a global structural coordinate system; $\alpha_{1,i}$ and $\alpha_{2,i}$ are respectively the coefficients of the i^{th} elemental stiffness and mass matrix; $\Delta\alpha_{1,i} = \alpha_{1,i} - 1$ and $\Delta\alpha_{2,i} = \alpha_{2,i} - 1$ are the fractional changes (damage) in the i^{th} elemental stiffness and mass matrix, respectively. To simplify the damage detection problem, the cross-sections of the beam elements in the example structure are assumed to be rectangular and the damage of the element is represented by reducing the width of the beam element symmetrically (see Appendix A). In such a case, only the stiffness and mass changes are considered in the damage detection and the fractional change of both the element stiffness and mass matrices is the same, i.e., $\Delta\alpha_{1,i} = \Delta\alpha_{2,i}$. As a result, the computed fractional change represents the fractional change of both stiffness and mass in the subsequent discussions of this chapter without further statement. Besides, it is worth pointing out that both the reductions of stiffness and mass are only selected for the numerical study in Chapter 3 for a demonstration. The selection of unknown damage detection parameters should consider the real damage scene as well as the physical meaning for a specific damage case, such as a structural component is broken in which damage is only accompanied with stiffness loss but without mass loss.

A sensitivity-based damage detection method in the time-domain is adopted for structural damage detection using the CBMS index vector. The CBMS vector computed from the measured responses, $\mathbf{V}_{\mathrm{pq}}{}^{m}$, can be expressed in a first-order Taylor expansion as

$$\mathbf{V}_{\mathrm{pq}}{}^{m} = \mathbf{V}_{\mathrm{pq}}{}^{c} + \frac{\partial \mathbf{V}_{\mathrm{pq}}{}^{c}}{\partial \boldsymbol{\alpha}} \Delta\boldsymbol{\alpha} \tag{3.17}$$

Eq. (3.17) can be further rewritten as a linear damage identification equation integrated with the iterative Gaussian-Newton algorithm as

$$\Delta\mathbf{V}_{\mathrm{pq}}{}^{k} = \mathbf{S}^{k} \Delta\boldsymbol{\alpha}^{k+1}; \quad (k = 0,1,2\cdots) \tag{3.18}$$

with
$$\Delta\mathbf{V}_{\mathrm{pq}} = \mathbf{V}_{\mathrm{pq}}{}^{m} - \mathbf{V}_{\mathrm{pq}}{}^{c} \tag{3.19}$$

and
$$\mathbf{S} = \frac{\partial \mathbf{V}_{\mathrm{pq}}{}^{c}}{\partial \boldsymbol{\alpha}} = \left[\frac{\partial \mathbf{V}_{\mathrm{pq}}{}^{c}}{\partial \alpha_1}, \frac{\partial \mathbf{V}_{\mathrm{pq}}{}^{c}}{\partial \alpha_2}, \cdots \frac{\partial \mathbf{V}_{\mathrm{pq}}{}^{c}}{\partial \alpha_i} \cdots, \frac{\partial \mathbf{V}_{\mathrm{pq}}{}^{c}}{\partial \alpha_{\mathrm{ne}}} \right] \tag{3.20}$$

where $\mathbf{V}_{\mathrm{pq}}{}^{c}$ is the CBMS vector computed through the responses from the finite element model; the vector $\Delta\mathbf{V}_{\mathrm{pq}}$ is the difference between $\mathbf{V}_{\mathrm{pq}}{}^{m}$ and $\mathbf{V}_{\mathrm{pq}}{}^{c}$; $\Delta\boldsymbol{\alpha}$ denotes the vector of the fractional stiffness changes in the damage elements; $\Delta\alpha_i \in \Delta\boldsymbol{\alpha}$ ($-1 \le \Delta\alpha_i \le 0$) is the fractional change of the stiffness in the i^{th} damaged element of a structure; and $\mathbf{S}$ is the sensitivity matrix of the CBMS index vector to the fractional stiffness change vector, which is computed using the finite difference method ; and the superscript k is the iteration number.

3.2.4 Regularization-Based Damage Detection

Regularization methods are usually used to find the solution of inverse problems expressed by Eq. (3.18). One of the effective regularization methods for damage detection is the adaptive Tikhonov regularization (Li and Law 2010). The adaptive Tikhonov regularization employs a squared norm (L_2-norm) optimization objective function, but this objective function cannot produce a sparsity solution when the measurement noise is taken into consideration, for it tends to keep all the signals including measurement noise in the optimization solution. If a structure with a large number of components, the damage detection methods using the L_2-norm optimization objective function often require extensive computation time to find the solution or simply could not find the solution. This is because in reality, there are only a few local damages in a structure, the number of measurement sensors is limited, and the measurement noise is inevitable. On the other hand, the regularization methods including an L_1-norm penalizing term in the optimization can enforce sparsity for the solution (Donoho 2006). Zou and Hastie (2005) proposed an elastic net method including an L_1-norm penalizing term to produce a sparse solution. The elastic net method can give a sparsity result of shrinkage of the unknown identification variables into a smaller subset in terms of potential damage locations, whereas the adaptive Tikhonov regularization method can conduct an iterative improvement for identified damage severities within the subset of potential damage locations.

In order to combine the advantage of the two regularization methods, the two types of objective functions mentioned above will be used successively in this study and can be expressed by Eq. (3. 21) in terms of a tuning parameter η.

$$J(\Delta\boldsymbol{\alpha},\lambda,\beta)=\arg\min_{\Delta\boldsymbol{\alpha}}\left[\left\|\mathbf{S}\cdot\Delta\boldsymbol{\alpha}-\Delta\mathbf{V}_{\mathrm{pq}}\right\|_2^2+\lambda^2\cdot\mathrm{P}_\beta(\Delta\boldsymbol{\alpha})\right]$$

$$=\begin{cases}\arg\min\limits_{\Delta\boldsymbol{\alpha}}\left[\left\|\mathbf{S}\cdot\Delta\boldsymbol{\alpha}-\Delta\mathbf{V}_{\mathrm{pq}}\right\|_2^2+\lambda^2\cdot\left((1-\beta)\cdot\left\|\Delta\boldsymbol{\alpha}\right\|_2^2+\eta\cdot\left\|\Delta\boldsymbol{\alpha}\right\|_1\right)\right]; & if\ (0.0<\eta\le 1.0)\\ \arg\min\limits_{\Delta\boldsymbol{\alpha}^{k+1}}\left[\|\mathbf{S}^k\cdot\Delta\boldsymbol{\alpha}^{k+1}-\Delta\mathbf{V}_{\mathrm{pq}}{}^k\|_2^2+\lambda^2\cdot\|\Delta\boldsymbol{\alpha}^{k+1}+\sum_{r=1}^{k}\Delta\boldsymbol{\alpha}^r-\boldsymbol{\alpha}^{k,*}\|_2^2\right]; & if\ (\eta=0)\end{cases}$$

(3.22)

where $\mathrm{P}_\eta(\Delta\boldsymbol{\alpha})$ is a penalty term; λ is the regularization parameter that governs the contribution of the two errors between $\left\|\mathbf{S}\cdot\Delta\boldsymbol{\alpha}-\Delta\mathbf{V}_{\mathrm{pq}}\right\|_2^2$ and $\mathrm{P}_\eta(\Delta\boldsymbol{\alpha})$; $\left\|\Delta\boldsymbol{\alpha}\right\|_1$ is the sparsity-inducing term (Zou and Hastie 2005; Donoho 2006); the superscript k denotes the current iteration number and the term $\alpha^{k,*}$ is an adaptive adjustment factor (Li and Law 2010); and $\eta\in\left[0,1\right]$ is a tuning parameter that adjusts the weighting to employ a sparse solution. The objective function with $\eta\in(0,1]$ is called the hybrid objective function in this study and the objective function with $\eta = 0$ is called the L_2-norm optimization objective function. How to use the two objective functions in the two-stage covariance-based multi-sensing damage detection method will be discussed in the next section.

For a large civil structure, the number of sensors is always limited compared with the number of degrees-of-freedom of the structure. In such cases, the use of the combined elastic net method and Tikhonov regularization method becomes necessary by taking their respective advantages. The elastic net method including an L_1-norm penalizing term in the optimization can enforce sparsity for the solution, which is especially suitable to identify the sparse locations of damage when the number of sensors is relatively small. On the other hand, the Tikhonov regularization method has an explicit solution for detecting both damage locations and severities through iteration. Consequently, the elastic net method is used for detecting potential damage locations while the Tikhonov regularization method is used to refine the detection of both damage locations and severities in this study.

The covariance-based multi-sensing damage detection proposed in this study is divided into two stages. The first stage aims to find potential damage locations by using the hybrid objective function for regularization. The tuning parameter is selected between $0.0 < \eta \le 1.0$ in this stage and the penalty term $\mathrm{P}_{\eta}(\Delta\boldsymbol{\alpha})$ thus varies linearly between the L1-norm and L2-norm of $\Delta\boldsymbol{\alpha}$. The regularized solution in this stage uses the elastic net method with a non-zero η and its regularization parameter λ is determined by the K-fold cross-validation method (Kohavi 1995). $\eta = 1$ denotes that the optimization for the solution is enforced with the largest sparsity. By using the hybrid objective function, the first stage can narrow down the damage search area without iterations, but there are some false alarms in damage locations. With additional sensors installed in the most possible damage locations, the second stage of the covariance-based multi-sensing damage detection method aims to find the true damage locations with accurate damage severities by using the L_2-norm objective function. In this stage, the tuning parameter η is set to zero and the previous damage identification results are used as the initial condition of the second stage. The Adaptive Tikhonov regularization method is employed and the regularization parameter λ is determined by the L-curve method (Hansen and O'Leary 1993). The flowchart for implementing the two-stage covariance-based multi-sensing damage detection method is shown in Fig. 3.1.

3.3 Numerical Study

An overhanging steel beam shown in Fig.2 is employed in the numerical study to examine the feasibility and accuracy of the proposed new method for damage detection. The FE model of the beam consists of 41 nodes and 40 equal-length beam elements. The first fourteen natural frequencies of the beam are list in Table 3.1. The structural damping is assumed to be Rayleigh damping with the first two damping ratios $\xi_1 = 0.01$ and $\xi_2 = 0.01$. In this study, the first two damping ratios are assumed to remain unchanged before and after damage. Other higher order damping ratios are computed by $\xi_i = \dfrac{\mathbf{\Phi}_i^T \mathbf{C} \mathbf{\Phi}_i}{2\omega_i}$, where $\mathbf{\Phi}_i$ and ω_i are the i^{th} mode shape and natural frequency, respectively. It is noted that other damping model is not exclusive. The beam is subjected to external white noise excitation with a standard deviation $100N$ at the node 24. For the beam and loading given in the numerical example, the maximum peak values of stress and strain responses occur in the middle span of the beam or nearby. Therefore, elements 20 and 22 are selected as damage elements in damage scenario one. The elements close to the supports also suffer relatively large stress and strain responses. Thus, elements 12 and 22 are selected as damage elements in damage scenario two, in which one damage element close to the support and the other in the middle span are selected. Two damage elements are assumed to have both stiffness and mass reductions. Damage scenario one is shown in Fig. 3.2 (a): the element 20 with a 10% stiffness and mass reduction, and the element 22 with a 5%

stiffness and mass reduction; Damage scenario two is shown in Fig. 3.2 (b): the element 12 with a 10% stiffness and mass reduction, and the element 22 with a 5% stiffness and mass reduction. Measurement noise is simulated as a normally distributed random component which will be added to the calculated structural responses at the sensor locations. As a result, the measured structural response is obtained by the following equation.

$$\mathbf{y}_{measured} = \mathbf{y}_{calculated} + \mathrm{E_P} \cdot \mathbf{N}_{\mathrm{oise}} \cdot \mathrm{std}(\mathbf{y}_{calculated}) \tag{3.23}$$

where $\mathbf{y}_{measured}$ and $\mathbf{y}_{calculated}$ are the vectors of polluted measurement response and calculated response of the damaged beam, respectively; $\mathrm{E_P}$ is the noise level; $\mathbf{N}_{\mathrm{oise}}$ is a standard normal distribution vector with zero mean and unit standard deviation; and $\mathrm{std}(\bullet)$ is the standard deviation operator. The sampling rate used in this study is $f_s = 1000\mathrm{Hz}$.

The tuning parameter for the elastic net method is $\eta = 0.9$ in this study. The convergence criteria for iteration used in the adaptive Tikhonov regularization are as follows:

$$\begin{aligned} &\mathrm{Toler1}(k) = \frac{\| \mathbf{V}_{\mathrm{pq}}{}^{m} - \mathbf{V}_{\mathrm{pq}}{}^{c}(\boldsymbol{\alpha}^k) \|_2}{\| \mathbf{V}_{\mathrm{pq}}{}^{m} \|_2} \times 100(\%) \le \mathrm{toler1}; \quad \text{or} \\ &\mathrm{Toler2}(k) = \frac{\| \Delta\boldsymbol{\alpha}^k - \Delta\boldsymbol{\alpha}^{k-1} \|_2}{\| \sum_{i=1}^{k} \Delta\boldsymbol{\alpha}^i \|_2} \times 100(\%) \le \mathrm{toler2}; \end{aligned} \tag{3.24}$$

where the tolerance limit in Eq. (3.18) is set as 1.0×10^{-4} for toler1 and toler2. The maximum iteration number is set to 30 for the cases with measurement noise.

The current method is proposed as a general method, aiming to fuse the responses from accelerometer, displacement transducer and strain gauge for multi-sensing damage detection. To apply this method, the prerequisite is to find the optimal placements of three types of sensors. However, there are no sophisticated optimal multi-type sensor placement methods available for the two-stage multi-sensing damage detection method proposed in this study. Therefore, in the numerical example, the widely-used Effective Independence (EfI) method is adopted for the optimal placement of a single type sensor, accelerometer, in consideration that the acceleration response is regarded as a global dynamic response and it is popular for structural damage detection. The stage one of the proposed two-stage multi-sensing damage detection method is then conducted to find the potential damage locations first. Once the potential damage locations are identified, the strain gauges are then installed in the potential damage locations because strain responses are sensitive to local damage. The stage two of the proposed two-stage multi-sensing damaged detection method is finally performed to find both damage locations and severities. Consequently, the displacement responses are not included in the numerical study in this chapter.

3.3.1 Effective-Independence-Based Optimal Sensor Placement

Because of cost consideration, only a small number of sensors can be placed on a structure for system identification or damage detection. Especially for the structure with a large number of components, the sensors must be placed in an optimal fashion so that the modal characteristics of the structure or the damage locations as well as severities can be identified as accurately as possible. The effective independence (EfI) technique is an efficient method presented to place sensors for modal identification of a large space structure (Kammer 1991; Yao et al. 1992). Based on the FE model, a set of target modes is selected for identification. The EfI method casts the linear independence problem in the form of a target mode response estimation problem. The sensor locations that produce the best target mode response estimate also produce linearly independent target mode shape partitions.

With the aim of maximizing the data information so that structural dynamic behavior can be fully characterized, the EfI method is employed for optimal sensor placement in this study. The first four modes make major contributions to the dynamic responses. Therefore, at least four sensors are needed. In this numerical study, four sensors are selected and their types and locations are discussed as follows. Since the acceleration responses are global responses, the four accelerometers are used for damage localization in the first stage of the proposed two-stage covariance-based damage detection method. The white noise excitation acts at node 24 in the vertical direction such that only vertical acceleration responses are considered. The locations at the nodes 11 and 31 are eliminated, which are the locations of two supports and where the acceleration is equal to zero. On the other hand, the locations at nodes 1 and 41 are eliminated because they are the free ends of the overhanging beam. Thus, the initial candidate set of sensor locations includes 37 candidates which are all the nodes except the nodes 1, 11, 31 and 41. The approach then ranks the candidate locations based on their contributions to the linear independence of the corresponding FE model target mode partitions. Locations that do not contribute are removed from the candidate set. In an iterative manner, the initial candidate set of sensor locations is reduced to the target number of sensors of 4. The optimal sensor locations of the 4 accelerometers are shown in Fig. 3.3.

3.3.2 Signal to Noise Ratio (SNR) Analysis

A study on the SNR is conducted in this section to examine the denoising capability of the CBMS vector of the dynamic responses of the beam to the white noise excitation. The normalized acceleration response from the node 17 and the normalized strain response from the mid-point of the element 20 are respectively computed for 50s (1000Hz×50s=50000 data points) and 200s (1000Hz×200s=200000 data points) with and without measurement noise included. These normalized responses are then used to calculate their auto-covariance and cross-covariance. The effect of noise on the covariance is evaluated in terms of the difference between the covariance with measurement noise and the covariance without measurement noise. The measurement noise level is set as 10% of the standard deviation of the response. The time lag number is set as 600 for the covariance computation. The SNR analysis results are shown in Figs. 3.4 and 3.5 for the response duration of 50s and 200s, respectively. Fig. 3.4 (a) displays the auto-covariance of acceleration response at the node 17 with and without measurement noise as well as the difference in the two auto-covariances for the response duration of 50s. It can be seen that there is a very small difference in the two auto-covariances of acceleration responses. The maximum auto-covariance of acceleration response without measurement noise effect, $\max\left\|\mathbf{C}_{\mathrm{pq}}\right\|$, is 0.9812 and the maximum difference between the two auto-covariances, $\max\left\|\Delta\mathbf{C}_{\mathrm{pq}}{}^{noise}\right\|$, is 0.0033, as listed in Table 2. The maximum difference between the two auto-covariance reflects the maximum effect of measurement noise. The ratio of the maximum difference between the two auto-covariances to the maximum auto-covariance, $\dfrac{\max\left\|\Delta\mathbf{C}_{\mathrm{pq}}{}^{noise}\right\|}{\max\left\|\mathbf{C}_{\mathrm{pq}}\right\|}$, is 0.0034 only. However, the ratio of the maximum difference between the two acceleration responses due to measurement noise to the maximum acceleration response without measurement noise is about 0.1. The comparison of 0.0034 with 0.1 demonstrates that the CBMS vector can filter the measurement noise effect significantly. The comparison is also carried out on the auto-covariance of the normalized strain response in the element 20 as well as the cross-covariance between the normalized acceleration response at the node 17 and the normalized strain response in the element 20. Similar observations can be made from Figs. 3.4 (b) and 3.4 (c) as well as Table 3.2: the auto-covariance of strain response and the cross-covariance between acceleration and strain responses can also filter the measurement noise effect significantly.

It is noted from Eq. (3.9) that longer measurement data used in covariance computation can reduce more measurement noise effect. To examine this point, the duration of the normalized responses is increased from 50s to 200s. Similar comparison is carried out on the auto-covariance of the normalized acceleration and strain response as well as the cross-covariance between the normalized acceleration and strain response. The computation results are shown in Figs. 3.5(a), 3.5(b) and 3.5(c). The maximum auto-covariance, the maximum covariance difference, and the ratio of the maximum covariance difference to the maximum covariance all are listed in Table 3.2. By comparing Fig. 3.5 with Fig. 3.4, it is noted that the covariance difference becomes smaller if the responses of 200s duration are used. Table 3.2 shows that although the maximum values of auto-covariance and cross-covariance of the responses of 200s duration are similar to those of 50s duration, the maximum covariance difference and the ratio of the maximum covariance difference to the maximum covariance using the responses of 200s duration become smaller compared with those of 50s duration. This confirms that longer measurement data used in covariance computation can reduce more measurement noise effect. According to the SNR analysis results, the response measurement duration of 200s is thought to have sufficient data number (1000Hz×200s=200000 data points) for noise suppression in the covariance computation and this value will be used for the subsequent studies.

Figs. 3.4 and 3.5 also show that the auto-covariance of acceleration has the fastest attenuation of amplitude, while the auto-covariance of strain has the slowest attenuation of amplitude. On the other hand, the amplitude of the covariance difference caused by noise varies within a certain level without attenuation trend. Therefore, the time lag number shall be selected appropriately for the subsequent damage detection. If the time lag number is selected too large, the noise level may be close to the auto-covariance of acceleration response, the quality of covariance-based multi-sensing damage detection will be affected. vector expressed by Eq. (3.13) is also small, which will affect the quality of damage detection results. Through a careful inspection of the auto-covariance of acceleration responses as well as the acceleration covariance differences, the number of time lag used in the subsequent covariance computation for damage detection is set as 200 other than 600.

3.3.3 Damage Localization

Many existing damage detection methods can find accurate results under the condition that the measurement noise is not considered or only very small measurement noise is included in the measured responses. The measurement noise is inevitable in practice and the noise level is assumed in this numerical study as 10% in all the measurement dynamic responses to demonstrate the advantage of the proposed damaged detection method. The structural damage identification results can be sought by solving Eq. (18) in the sensitivity-based damage detection methods. It is noted that the adaptive Tikhonov regularization is one of the currently used methods to find the solution from the ill-condition damage identification function with noise interruption. The elastic net method with the hybrid objective function is also one of the methods to find the solution efficiently without requiring any iteration. These two methods are adopted for initial damage localization as the first stage of damage detection in this study.

The damage localization is investigated using the initial optimal sensor configuration with 4 accelerometers, as shown in Fig. 3.3. For the damage scenario one, the damage localization using the adaptive Tikhonov regularization method and the elastic net method are compared and the results are shown in Fig. 3.6 (a). Using the adaptive Tikhonov regularization for damage location identification, the true damage in elements 20 and 22 are respectively identified but with only 5.29% and 2.36% fractional change for both stiffness and mass: the identified damage severities are far away from their true values of 10% and 5% respectively. There are also some false alarms in elements 12, 19, 21, 23 and 29. The maximum false alarm occurs in element 21 with 4.82% fractional change for both stiffness and mass. By contrast, the use of the elastic net method for damage localization yields more satisfactory results. It is noted from Fig. 3.6 (a) that the true damage in elements 20 and 22 are respectively identified with 12.29% and 4.14% fractional change for both stiffness and mass, which are quite close to the true damage severities of 10% and 5% respectively. It is noted that there are more false alarms in elements 7, 8, 9, 13, 14, 15, 19, 21, 29 and 32. However, the maximum false alarm occurs in element 13 with 2.58% fractional change only for stiffness and mass. Moreover, the computation time for damage localization using the elastic net method and the adaptive Tikhonov regularization is about 134s and 3665s, respectively. The elastic net method only takes 3.66% (134s/3665s*100%) computation time of its counterpart. The adaptive Tikhonov regularization method can identify damage locations with less number of false alarms, but the true damage severity are not prominent in the subset of potential damage candidates. It is also noted that the elastic net method can give more accurate and desirable damage severity results but with more number of false alarms. Moreover, it is found that the elastics net method needs much less computation time to find the solution than the adaptive Tikhonov regularization method in this study. This is because for a structure with limited number of sensor and a few damage locations, the elastic net method can effectively converge to the sparse solution to find the potential sparse damage locations without iteration; while the adaptive Tikhonov regularization method tends to achieve a more evenly distributed solution, so it needs extensive iteration to converge to the sparse damage locations. By considering all the factors, the first stage of damage detection in this study only uses the elastic net method for damage localization. The further refinement for damage detection will be conducted in the second stage to reach more accurate and reliable damage detection results by using the adaptive Tikhonov regularization method with the L_2-norm objective function in an iterative manner.

Similar comparison of damage localization is conducted in the damage scenario two using the adaptive Tikhonov regularization method and the elastic net method and the results are shown in Fig. 3.6 (b). Using the adaptive Tikhonov regularization for damage location identification, the true damages in elements 12 and 22 are respectively identified but with only 6.64% and 3.09% fractional change for both stiffness and mass, meanwhile there are some false alarms in elements 11, 13, 21, 23 and 29. By contrast, using the elastic net method for damage localization, the true damages in elements 12 and 22 are respectively identified with 10.18% and 4.78% fractional change for both stiffness and mass, meanwhile there are some false alarms in elements 5, 13, 19, 20 and 33. It is noted that the elastic net method for damage localization can give more satisfactory results, which are similar to those observations from the damage scenario one.

3.3.4 Damage Severity Identification

When the number of sensors is limited, one step damage detection method sometimes may not be workable in the practical application, as demonstrated in the last section. Xiang et al.(2012) and Sung et al.(2014) among others found that a two-stage approach may be helpful. Under the conditions of limited sensors, they prefer to focus on the damage localization in the first stage to narrow down the potential damage areas. The two-stage damage detection approach is also adopted in this study. By using the Effective Independence (EfI) method, four accelerometers are selected for the first stage damage detection, as shown in the Fig. 3.3. The first stage damage detection results for two damage scenarios are shown in Fig. 3.6. It can be seen from Fig. 3.6 that the damage detection results are not satisfactory. However, potential damage locations can be identified according to damage severities. Therefore, the second-stage damage detection is required by adding strain gauges to the potential damage locations because strain responses are sensitive to local damage.

Following what has been found in the last section for the damage scenario one, all the locations with non-zero value of fractional change in elements 7, 8, 9, 13, 14, 15, 16, 18, 19, 20, 21, 22, 29, 32 and 33, identified by using the elastic net method, are selected as the potential damage candidates. The adaptive Tikhonov regularization with L_2-norm objective function in the iterative manner is used for initial damage identification refinement and the results are shown in Fig. 3.7 (a). It is noted from Fig. 3.7 (a) that the identified fractional changes in the damage elements as well as in the elements with false alarms are improved to some extent. However, the number of the potential damage candidate is not reduced obviously. It seems that the limited number and information from the current sensors are insufficient. Extra sensors shall be supplemented in the second stage to improve the damage identification results from the previous potential subset of damage candidate. The selection of additional sensor numbers and their locations depends on the potential damage locations identified in the stage one. Since the potential damage locations identified in the stage one with obviously large damage severities is two, only two accelerometers or two strain gauges are added in the two potential damage locations in the second-stage damage detection.

Based on the initial refinement results of the potential damage candidate locations, two new sets of sensor configuration with two additional sensors for damage refinement in stage two are shown in Fig. 3.8 (a) and Fig. 3.8 (b), respectively. In Fig. 3.8(a), two additional accelerometers are installed at the nodes close to the two most possible damaged elements, and in Fig. 3.8(b) two strain gauges are installed on the two most possible damaged elements. Clearly, the sensor configuration shown in Fig.3.8(a) is based on single-type sensor but that shown in Fig. 3.8(b) is based on dual-type sensors. The adaptive Tikhonov regularization with L_2-norm objective function in the iterative manner is now applied to the beam with the single- and dual-type sensor configurations, respectively, and the results are shown in Fig. 3.9 (a).

The identification results from the single-type six accelerometers show a little change compared with the initial refinement results using four accelerometers only. There is only minor improvement for damage severity identification but the number of false alarms does not reduce. Comparatively, the identification results from the dual-type sensor configuration (two strain gauges and four accelerometers) show that both the damage locations and severities are perfectly identified and nearly all the false damage alarms occurring in stage one are eliminated. It is noted that strain gauges directly installed on the most potential damage elements can enhance the accuracy of damage identification significantly. Nevertheless, the strain gauge often has a limitation for its local effective range for damage detection and the strain gauges are expected to install as close as possible to the damaged elements. Therefore, the damage localization conducted in the first stage is very important to narrow down the number of potential damage candidates. The initial damage detection refinement using the adaptive Tikhonov regularization with L_2-norm objective function is also important so that only the small number of strain gauges is needed to add to the beam for the final damage detection.

The damage refinement study for damage scenario two is also investigated. The first stage damage location identification is conducted using the same initial optimal sensor configuration as shown in Fig. 3.3, and the potential damage candidates are selected in the stage one by the elastic method. In the stage two, the damage identification is initially improved by the adaptive Tikhonov method as shown in Fig. 3.7 (b). After adding two accelerometers or two strain gauges as shown in Fig. 3.8 (c) and (d), the refinement results for damage identification are compared as shown in Fig. 3.9 (b). It is found that both cases with additional sensors show some improvement, and the dual type sensor configuration with two additional strain gauges can identify the damage perfectly. The studies of damage scenarios one and two show similar observations that the second-stage damage detection does improve damage detection quality and give actual damage locations as well as severities. This confirms the effectiveness of using the proposed two-stage CBMS damage detection method.

3.3.5 Discussions

Then, what is the reason why the two strain gauges added to the two most potential damage elements can produce nearly perfect identification results for both damage locations and severities even with 10% measurement noise included in the stage two? By taking the damage scenario one as example, Fig. 3.10 presents the profiles of the norm of sensitivity of the CBMS vector to the elemental stiffness and mass change for the first sensor configuration shown in Fig. 3.3 and the second and third sensor configurations shown in Fig. 3.8 (a) and Fig. 3.8(b) respectively. The elemental sensitivity is obtained from each column of the sensitivity matrix in Eq. (3.20) for the corresponding element. Compared with the first sensor configuration, the elemental damage sensitivities are increased for the second sensor configuration, which is the major reason for the improvement of the damage identification results. For the third sensor configuration with dual-type sensors, the elemental damage sensitivities are increased globally and there are also two sharp peaks in the sensitivity profile occurring at the two elements placed with strain gauges. This is why the two strain gauges added to the two most potential damage elements can produce nearly perfect identification results for both damage locations and severities even with 10% measurement noise included in the stage two. Strain gauges are so sensitive to the damage occurring at the elements on which they are installed and those elements nearby. Nevertheless, these sharp peaks cover very limited region and further research is needed to find the effective region of strain gauges in general.

3.4 Summary

A response covariance-based multi-sensing (CBMS) damage detection method has been presented in this chapter. Instead of using the heterogeneous measurement data separately, the new method can assimilate and normalize the heterogeneous data simultaneously, define the CBMS vector as a new damage index in terms of the normalized cross-covariance matrix, and work together with the sensitivity approach for damage detection. In the proposed method, the elastic net method with a hybrid objective function is used for damage localization in the first stage, and the adaptive Tikhonov regularization with L_2-norm objective function in the iterative manner is employed together with additional strain gauges for damage identification refinement. The feasibility and accuracy of the new method have been confirmed through the numerical study using an overhanging beam with multiple damaged elements. It can come to the conclusions that the CBMS vector is relatively insensitive to the measurement noise but sensitive to damage, and that the dual-type sensor configuration is better for damage detection with higher accuracy. Both the damage locations and severities are perfectly identified and nearly all the false damage alarms occurring in stage one are eliminated even with 10% measurement noise considered.

Although a general framework of the response covariance-based damage detection method has been presented in this chapter, there is no optimal multi-type sensor placement method available for multi-sensing damage detection. The currently-used Effective Independence (EfI) method has to be adopted in the numerical study for the optimal placement of accelerometer in stage one in this chapter. After finding the suspicious elements, the strain gausses were directly installed on these possible damaged locations for the refinement of damage identification in stage two. Clearly, the optimal multi-type sensor placement method to ensure the sensitivity of the structural responses measured by the sensors and at the same time to reduce the redundant sensors should be considered for the implementation of the response covariance-based multi-sensing damage detection method proposed in this chapter.

Table 3.1 Natural frequencies of the overhanging beam

Mode No.	Frequency (Hz)	Mode No.	Frequency (Hz)
1	5.06	9	198.66
2	8.37	10	213.12
3	17.40	11	259.49
4	43.06	12	347.00
5	64.57	13	405.63
6	72.77	14	426.20
7	101.21	15	426.36
8	158.32	16	491.00

Table 3.2 The maximum absolute values of covariance and covariance difference

Type of covariance	$\max\left\Vert \mathbf{C}_{\mathrm{pq}} \right\Vert$		$\max\left\Vert \Delta\mathbf{C}_{\mathrm{pq}}^{noise} \right\Vert$		$\dfrac{\max\left\Vert \Delta\mathbf{C}_{\mathrm{pq}}^{noise} \right\Vert}{\max\left\Vert \mathbf{C}_{\mathrm{pq}} \right\Vert}$	
	50s	200s	50s	200s	50s	200s
$\mathrm{cov}(\ddot{\mathrm{z}},\ddot{\mathrm{z}})$	0.9812	0.9878	0.0033	0.0013	0.0034	0.0013
$\mathrm{cov}(\ddot{z},\varepsilon)$	0.8525	0.8327	0.0043	0.0017	0.0050	0.0020
$\mathrm{cov}(\varepsilon,\varepsilon)$	2.5249	2.4416	0.0041	0.0014	0.0016	0.00057

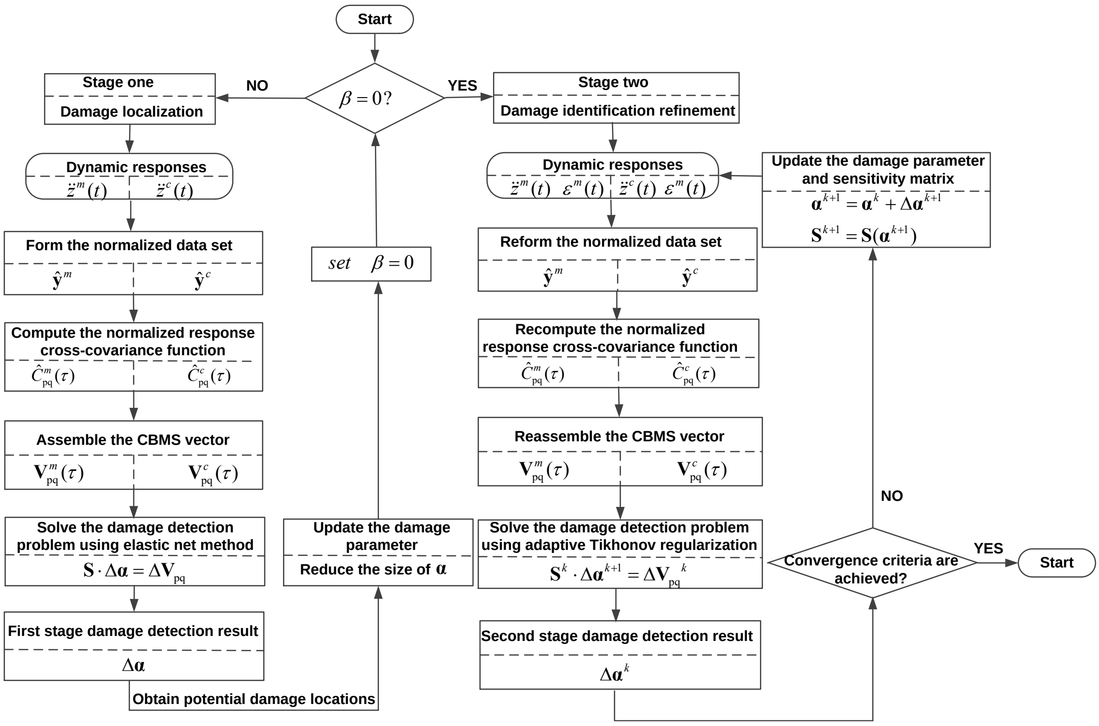

Fig. 3.1 Flowchart of the proposed two-stage damage identification

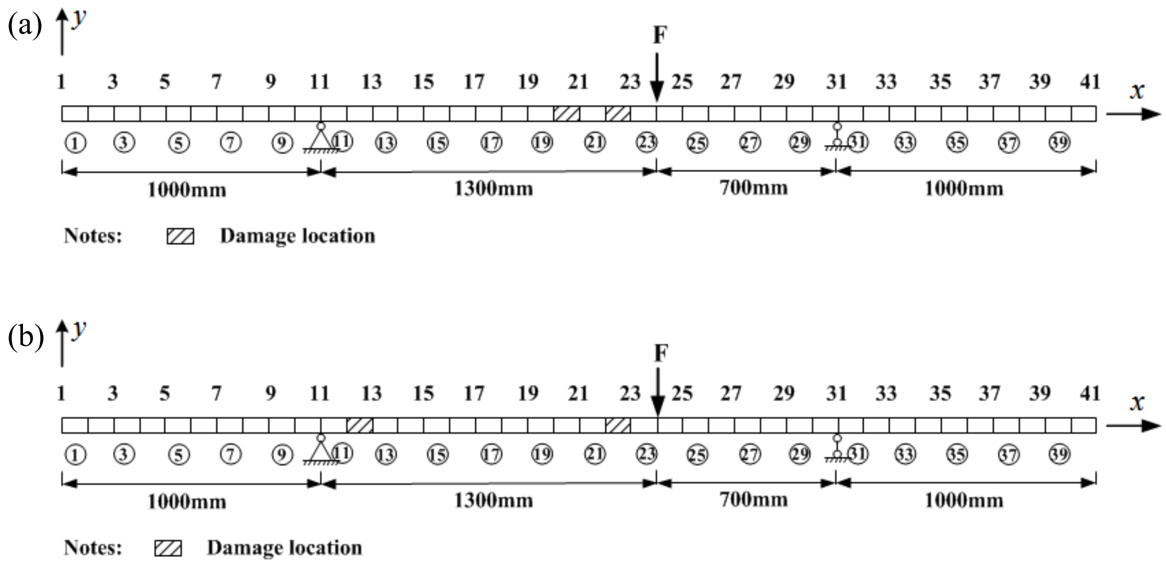

Fig. 3.2 Finite element model of an overhanging steel beam and damage locations: (a) Damage scenario 1;(b)Damage scenario 2.

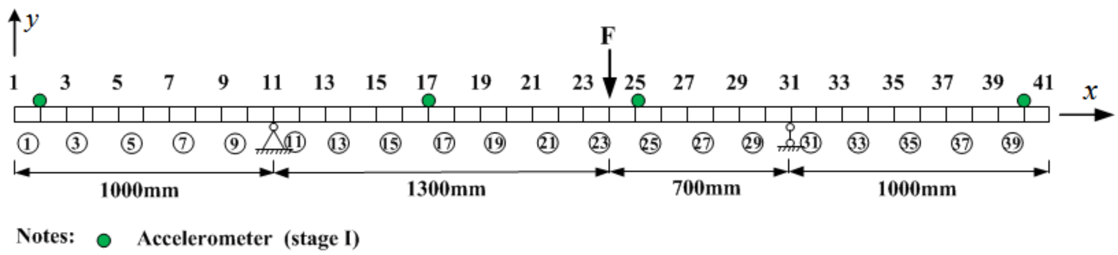

Fig. 3.3 The initial optimal sensor configuration

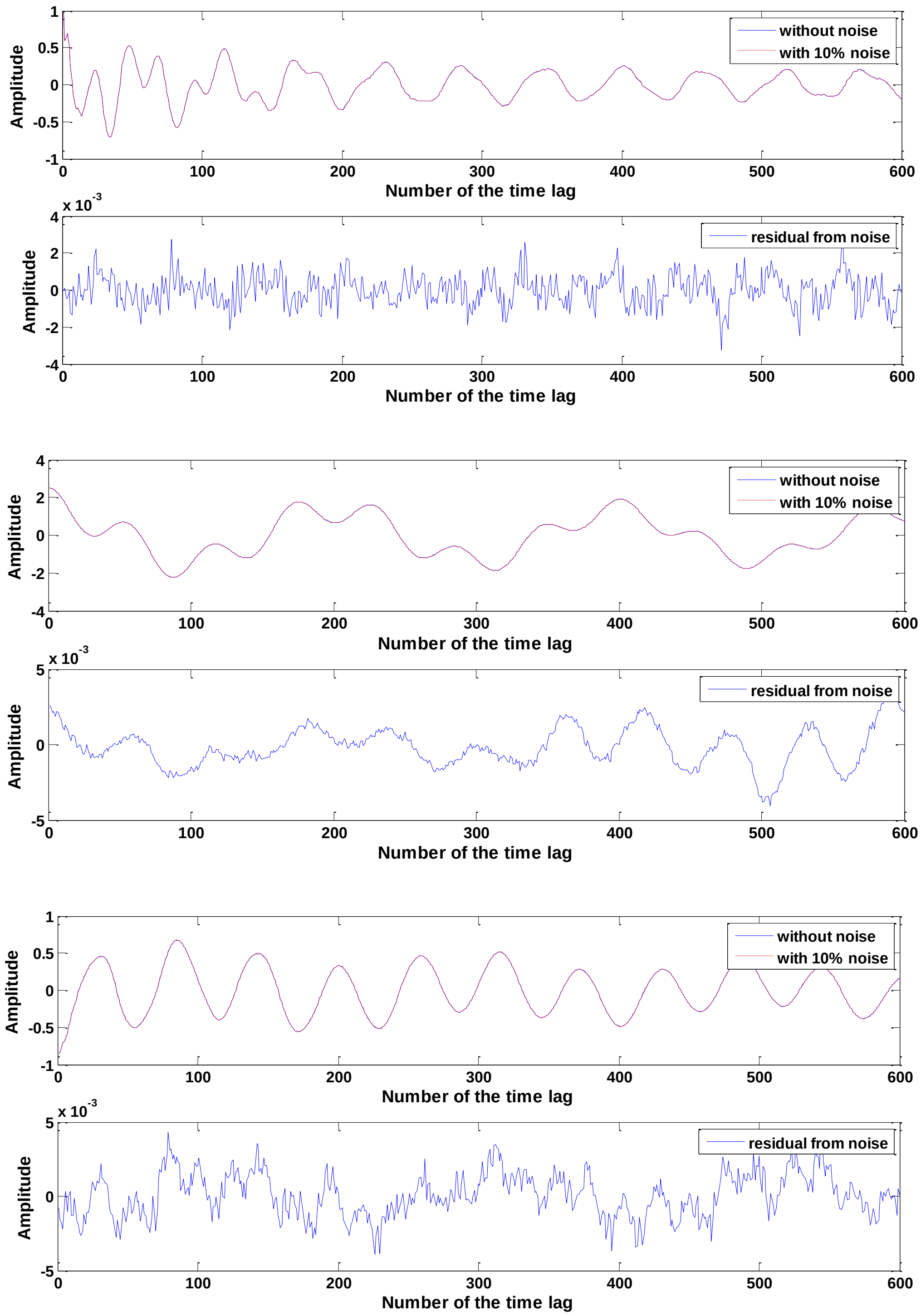

Fig. 3.4 SNR analysis of the CBMS vectors computed from acceleration and strain (50s): (a) Auto-covariance of normalized acceleration response at node 17; (b) Auto-covariance of normalized strain response at element 20; (c) Cross-covariance of acceleration at node 17 and strain responses at element 20.

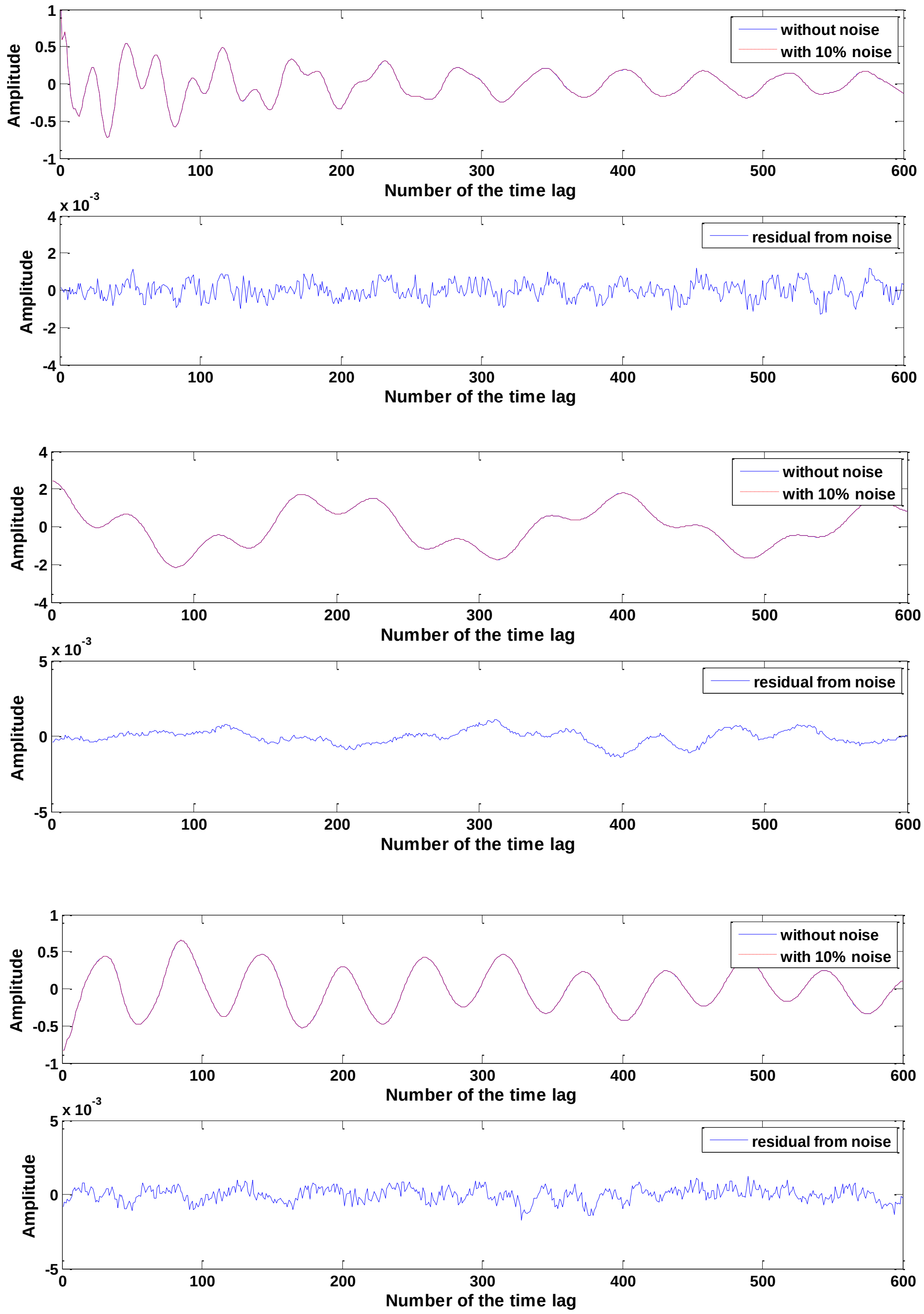

Fig. 3.5 SNR analysis of the CBMS vectors computed from acceleration and strain(200s): (a)Auto-covariance of normalized acceleration response at node 17; (b)Auto-covariance of normalized strain response at element 20; (c)Cross-covariance of acceleration at node 17 and strain responses at element 20.

(a)

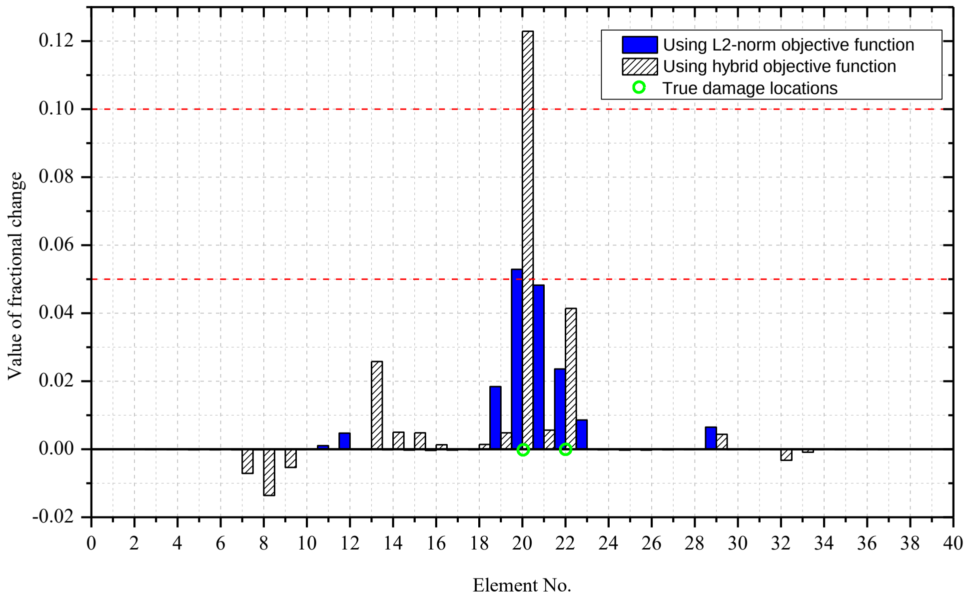

(b)

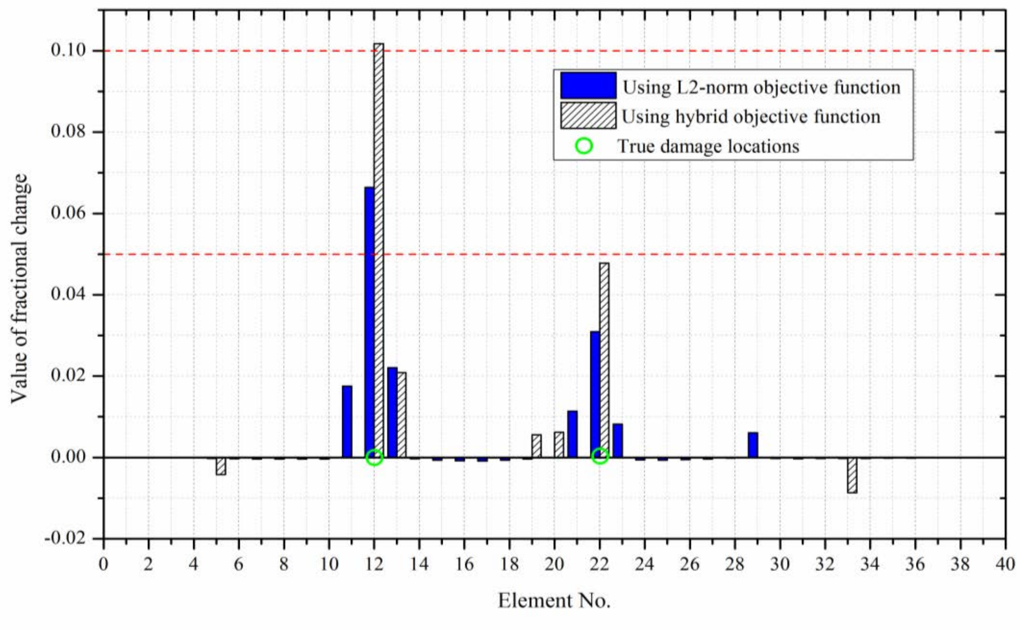

Fig. 3.6 The damage localization using two objective functions with 10% measurement noise: (a) For the damage scenario 1; (b) For the damage scenario 2.

(a)

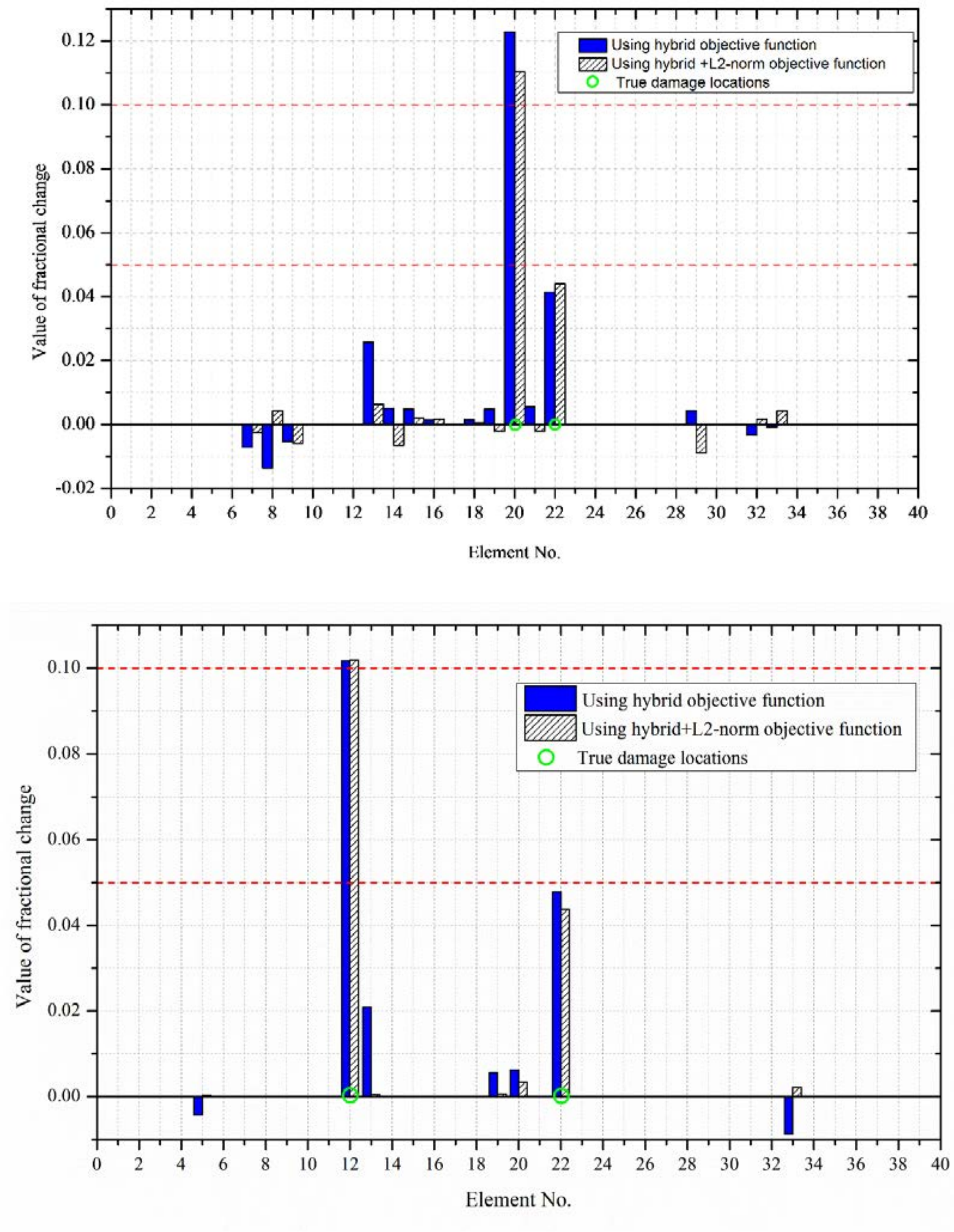

(b)

Fig. 3.7 Damage refinement within the narrowed subset of damage candidate: (a) For the damage scenario 1; (b) For the damage scenario 2.

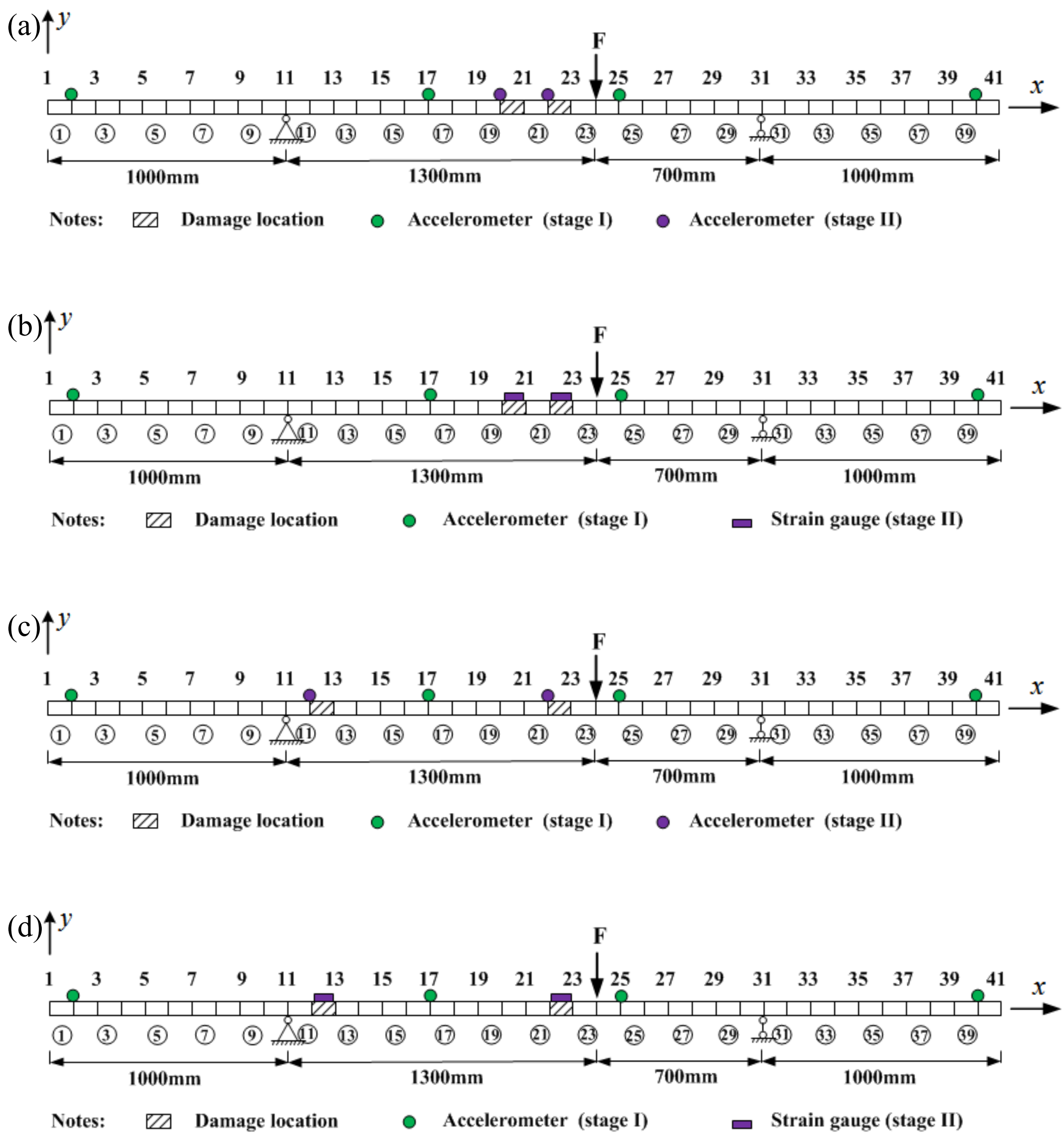

Fig. 3.8 Stage two senor configurations for damage refinement with different additional sensors: (a) Damage scenario 1: sensor configuration added 2 accelerometers; (b) Damage scenario 1:sensor configuration added 2 strain gauges; (c) Damage scenario 2: sensor configuration added 2 accelerometers; (d) Damage scenario 2:Sensor configuration added 2 strain gauges.

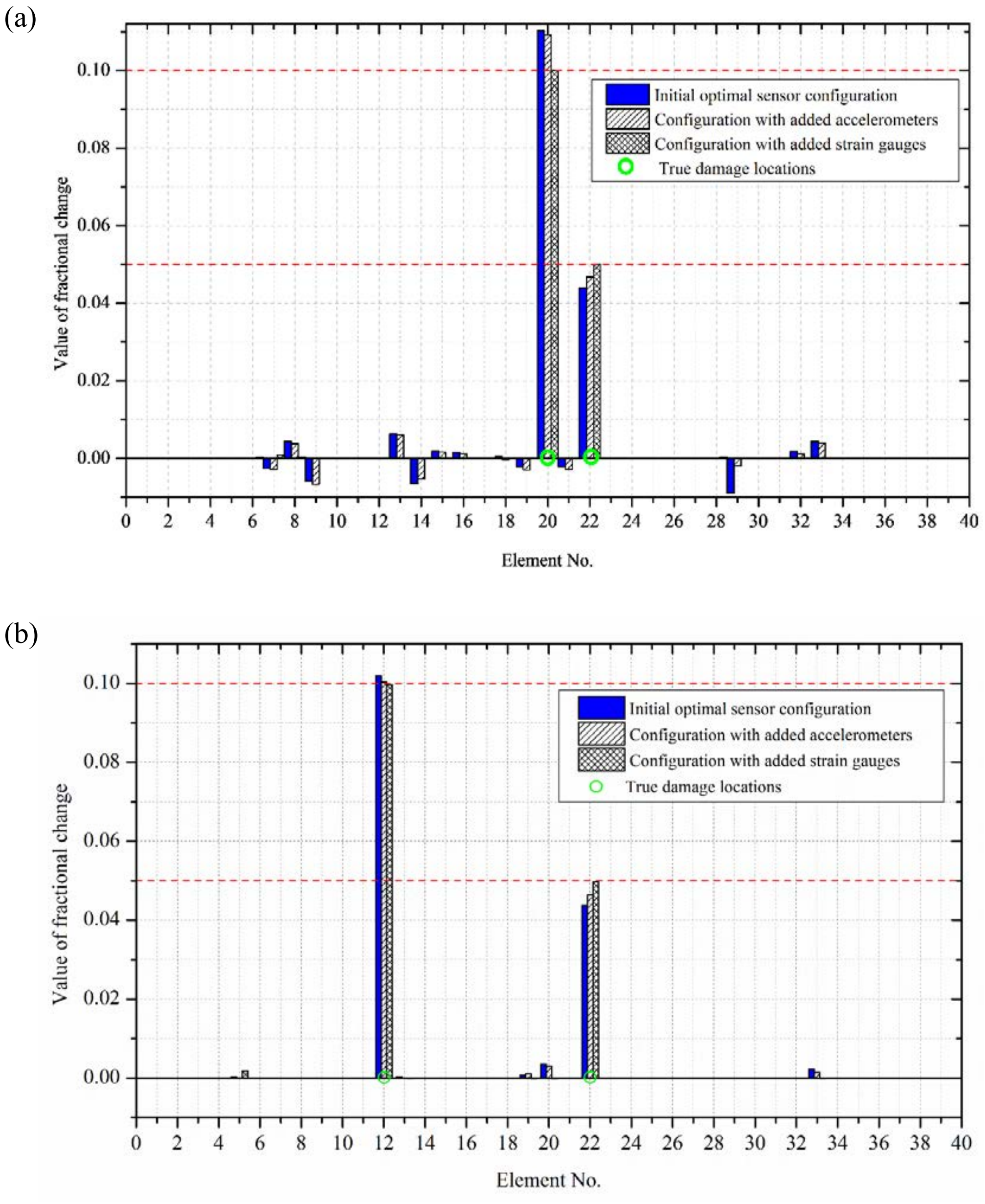

Fig. 3.9 Comparison of single- and dual-type sensor damage refinement with added sensors: (a)Comparison for damage scenario 1; (b)Comparison for damage scenario 2.

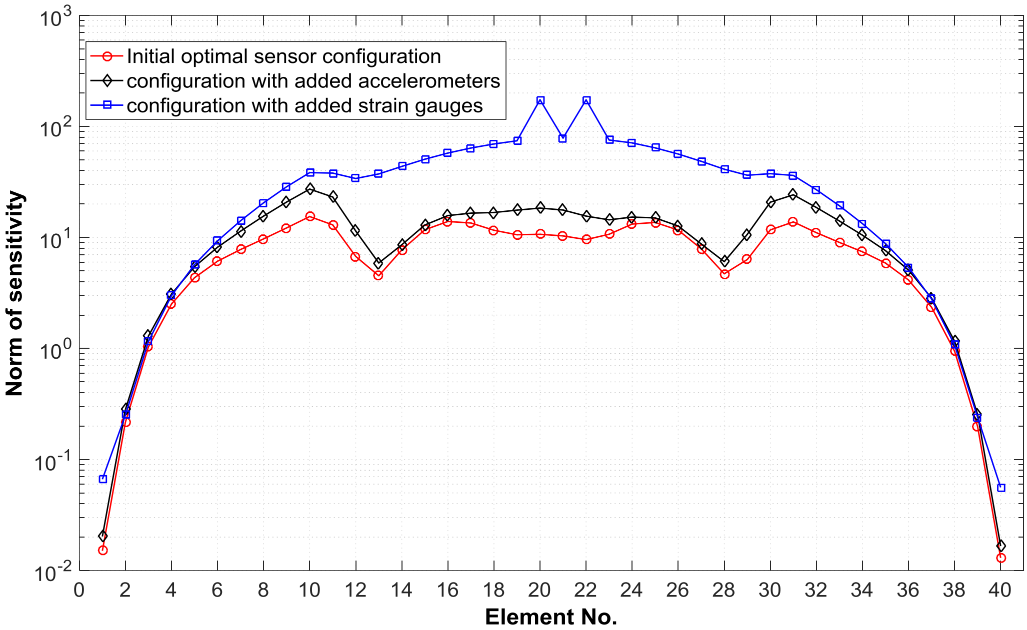

Fig. 3.10 Elemental damage sensitivity analysis for three sets of sensor configuration

CHAPTER 4

RESPONSE COVARIANCE-BASED SENSOR PLACEMENT FOR STRUCTURAL DAMAGE DETECTION

4.1 Introduction

In Chapter 3, the response covariance-based multi-sensing damage detection method was proposed and implemented in two stages of damage localization and damage severity refinement. The accelerometers installed in the first stage were optimally placed by using the EfI method. The strain gausses were then installed on the identified damage locations in the second stage. It is noted that the sensor placement will affect the quality of damage detection and that the EfI OSP method does not directly target at damage detection, particularly response covariance-based damage detection.

This chapter will therefore propose a response covariance-based optimal sensor placement method to facilitate the proposed damage detection method to achieve better damage identification. The accelerometers are probably the most popular sensors for damage detection, and this chapter will thus start from the exploration of the OSP objective functions and the associated OSP method for accelerometer optimal placement in Section 4.2. First, the relationship between the covariance of acceleration responses and the covariance of unit impulse responses of a structure subjected to multiple white noise excitations will be derived. Second, the optimal sensor placement objectives in terms of the response covariance sensitivity and the response independence will be developed. The two OSP objectives aim to enhance the damage sensitivity of the structural responses measured by the sensors and to reduce redundant sensors. Finally, an integrated single objective function is formed by using a weighting factor to combine the two objective functions. In Section 4.3, a numerical study will be performed to investigate the feasibility and effectiveness of the proposed sensor placement method for damage detection through a five-bay three-dimensional frame structure. A summary of the works presented in this chapter is given in Section 4.4.

4.2 Methodology

4.2.1 Unit Impulse Response and Response Covariance

The dynamic responses of the structure to unit impulse excitations $\boldsymbol{\delta}(t)$ at the locations of the external excitations can be computed as follows:

$$\mathbf{M}\ddot{\mathbf{h}}(t)+\mathbf{C}\dot{\mathbf{h}}(t)+\mathbf{K}\mathbf{h}(t)=\mathbf{L_f}\boldsymbol{\delta}(t) \tag{4.1}$$

where $\boldsymbol{\delta}(t)$ is the Dirac delta function vector; $\ddot{\mathbf{h}}(t)$, $\dot{\mathbf{h}}(t)$, and $\mathbf{h}(t)$ denote the unit impulse response (UIR) vector of acceleration, velocity, and displacement, respectively.

The acceleration response $\ddot{z}_p(t)$ of the structure at location p under multiple external excitations can be expressed by the Duhamel's integral as

$$\ddot{z}_p(t)=\sum_{i=1}^{m}\int_0^{\infty}\ddot{h}_{p,f_i}(\gamma)f_i(t-\gamma)d\gamma \tag{4.2}$$

where the subscript i is the excitation index; γ is the time variable for the Duhamel's integral; and $\ddot{h}_{p,f_i}$ is the acceleration UIR at the location p to the excitation f_i.

By substituting $\ddot{z}_p(t)$ and $\ddot{z}_q(t)$ computed by the Duhamel's integral into Eq. (4.2), the $C_{\mathrm{pq}}(\tau)$ can be expressed as (Bendat and Piersol 2010)

$$\begin{aligned}C_{\mathrm{pq}}(\tau)&=E\left[\ddot{z}_p(t)\ddot{z}_q(t+\tau)\right]\\&=\sum_{i}^{m}\sum_{j}^{m}\left\{\int_0^{\infty}\int_0^{\infty}\ddot{h}_{p,f_i}(\gamma)\ddot{h}_{q,f_j}(\beta)E\left[f_i(t-\gamma)f_j(t+\tau-\beta)\right]d\gamma d\beta\right\}\end{aligned} \tag{4.3}$$

where the subscript i and j denote the i^{th} and j^{th} excitation, respectively; $\ddot{h}_{p,f_i}$ and $\ddot{h}_{q,f_j}$ are the UIRs of acceleration at the locations p and q corresponding to

f_i and f_j, respectively; γ and β are the time variables for the Duhamel's integral.

The excitations are assumed as the mutual-independent Gaussian white noise excitations with zero means in this study. As a result, the expectation term in Eq. (4.3) can be written as

$$E\left[f_i(t-\gamma)f_j(t+\tau-\beta)\right]=c_{ij}^{\;2}\delta(i-j)\delta(\gamma-\beta+\tau)=\begin{cases}c_{jj}^{\;2}, & (i=j \text{ and } \beta=\gamma+\tau)\\ 0, & (i\neq j \text{ or } \beta\neq\gamma+\tau)\end{cases} \tag{4.4}$$

where $c_{ij}^{\;2}$ is the covariance of excitations between f_i and f_j; $\delta(\bullet)$ is the Dirac delta function; and $c_{jj}=\sigma_{f_j}$ is the standard deviation of the excitation f_j. As a result, Eq. (4.3) can be simplified as

$$C_{\mathrm{pq}}(\tau)=\sum_{j=1}^{m}\left\{c_{jj}^{\;2}\int_0^{\infty}\ddot{h}_{p,f_j}(\gamma)\ddot{h}_{q,f_j}(\gamma+\tau)\,d\gamma\right\}=\sum_{j=1}^{m}c_{jj}^{\;2}[\ddot{\mathbf{h}}_{p,f_j}(\gamma)^{\mathrm{T}}\ddot{\mathbf{h}}_{q,f_j}(\gamma+\tau)] \tag{4.5}$$

where $c_{jj}^{\;2}$ is the variance of the excitation f_j, indicating the contribution of the j^{th} excitation to the covariance of the two acceleration responses; and the superscript T denotes the transpose of a vector.

In this chapter, it is assumed that the standard deviation of the excitation c_{jj} can be estimated for the white noise excitations. Eq. (4.5) thus shows the relationship between the covariance of the two acceleration responses and the covariance of two corresponding acceleration UIRs for a structure subjected to multiple white noise excitations with mutual independence. This relationship indicates that the damage induced variation of response covariance $C_{\mathrm{pq}}(\tau)$ is only related to the UIRs, $\ddot{\mathbf{h}}_{p,f_j}(\gamma)$ and $\ddot{\mathbf{h}}_{q,f_j}(\gamma+\tau)$, with the input excitations expressed as a constant $c_{jj}^{\;2}$. In other words, $C_{\mathrm{pq}}(\tau)$ is related to the location of excitation but not to the amplitude of excitation. Therefore, the performance of the response covariance-based damage index and sensor placement indices is dependent on the acceleration UIRs only.

By substituting the normalized acceleration responses into Eq. (4.3), the normalized covariance function of two acceleration responses is obtained as

$$\hat{C}_{pq}(\tau) = E[\hat{\ddot{z}}_p(t)\hat{\ddot{z}}_q(t+\tau)] = \mathrm{E}\left[\left(\frac{\ddot{z}_p(t)}{\sigma_p^0}\right)\left(\frac{\ddot{z}_q(t+\tau)}{\sigma_q^0}\right)\right]$$
$$= \sum_{j=1}^{m} \frac{c_{ii}{}^2}{\sigma_p^0 \sigma_q^0} [\ddot{\mathbf{h}}_{p,f_j}(\gamma)^{\mathrm{T}} \ddot{\mathbf{h}}_{q,f_j}(\gamma+\tau)] \tag{4.6}$$

where σ_p^0 and σ_q^0 are the standard deviations of the acceleration responses $\ddot{z}_p$ and $\ddot{z}_q$ of the structure without any damage, respectively.

Accordingly, the sensitivity matrix $\mathbf{S}$ in Eq. (3.20) can be rewritten by using the UIR of acceleration as

$$\mathbf{S} = \frac{\partial \mathbf{V}_{pq}{}^c}{\partial \boldsymbol{\alpha}} = \sum_{j=1}^{m} \frac{c_{jj}{}^2}{\sigma_p^0 \sigma_q^0} \cdot \frac{\partial [\ddot{\mathbf{h}}_{p,f_j}(\gamma)^{\mathrm{T}} \ddot{\mathbf{h}}_{q,f_j}(\gamma+\tau)]}{\partial \boldsymbol{\alpha}} \tag{4.7}$$

Thus, the fractional stiffness change parameter $\Delta\boldsymbol{\alpha}$ can be obtained by solving the damage detection equation $\Delta\mathbf{V}_{\mathrm{pq}}{}^k = \mathbf{S}^k \Delta\boldsymbol{\alpha}^{k+1}$ in Eq. (3.18), and the least-squares solution (Shi et al. 2000) is

$$\Delta\boldsymbol{\alpha} = \left(\mathbf{S}^{\mathrm{T}}\mathbf{S}\right)^{-1} \mathbf{S}^{\mathrm{T}} \Delta\mathbf{V}_{\mathrm{pq}} \tag{4.8}$$

where the superscript “-1” denotes the matrix inverse operation.

When considering the random error from measurement and/or modeling errors, the least-squares solution $\Delta\boldsymbol{\alpha}_\varepsilon$ of Eq. (3.18) can be rewritten as

$$\Delta\boldsymbol{\alpha}_\varepsilon = \left(\mathbf{S}^T\mathbf{S}\right)^{-1} \mathbf{S}^{\mathrm{T}} \left[\Delta\mathbf{V}_{\mathrm{pq}} + \boldsymbol{\varepsilon}\right] \tag{4.9}$$

where $\boldsymbol{\varepsilon}$ is the random error vector, which is assumed to obey zero-mean normal distribution with a variance of σ_ε^2.

4.2.2 Optimal Sensor Placement with Two Objectives

Optimal sensor placement method can help obtain structural responses which may lead to higher accuracy in the estimated parameters (Shi et al. 2000). The estimation error for $\Delta\boldsymbol{\alpha}$ in this study can be computed by using Eqs. (4.8) and (4.9) as follows:

$$\Delta_{err} = E\left[\left(\Delta\boldsymbol{\alpha}_\varepsilon - \Delta\boldsymbol{\alpha}\right)\left(\Delta\boldsymbol{\alpha}_\varepsilon - \Delta\boldsymbol{\alpha}\right)^{\mathrm{T}}\right] = \left(\mathbf{S}^{\mathrm{T}}\mathbf{S}\right)^{-1} \mathbf{S}^{\mathrm{T}} E\left[\boldsymbol{\varepsilon}\boldsymbol{\varepsilon}^{\mathrm{T}}\right] \mathbf{S} \left(\mathbf{S}^{\mathrm{T}}\mathbf{S}\right)^{-1} \tag{4.10}$$

where Δ_{err} is the covariance matrix of the estimation error, and the matrix $\left[\boldsymbol{\varepsilon}\boldsymbol{\varepsilon}^{\mathrm{T}}\right]$ is the covariance matrix of the random error vector. Assume that the random errors on all the estimated parameters are independent and identically distributed with an equal variance of σ_{ε}^{2} and that they are not related to the measured responses. The parameter uncertainties mainly come from either measurement noise or modeling error. Most researchers assumed that they are independent-identically distributed Gaussian white noise processes (Au et al. 2013; Zhang et al. 2015). Some measurement data also support this assumption for measurement noise. The term $\left[\boldsymbol{\varepsilon}\boldsymbol{\varepsilon}^{\mathrm{T}}\right]$ can then be expressed as $\left[\sigma_{\varepsilon}^{2}\mathbf{I}_{\varepsilon}\right]$, where $\mathbf{I}_{\varepsilon}$ is the identity matrix. As a result, Eq. (4.10) can be simplified as

$$\Delta_{err}=\left(\mathbf{S}^{\mathrm{T}}\mathbf{S}\right)^{-1}\mathbf{S}^{\mathrm{T}}\left[\sigma_{\varepsilon}^{2}\mathbf{I}_{\varepsilon}\right]\mathbf{S}\left(\mathbf{S}^{\mathrm{T}}\mathbf{S}\right)^{-1}=\sigma_{\varepsilon}^{2}\left(\mathbf{S}^{\mathrm{T}}\mathbf{S}\right)^{-1} \tag{4.11}$$

It can be found from Eq. (4.11) that the estimation error of parameters, Δ_{err}, is inversely proportional to the Fisher information matrix $\mathbf{S}^{\mathrm{T}}\mathbf{S}$. To reduce the estimation error of parameters, Udwadia (1994) proposed to maximize the trace of the Fisher's information matrix. The first objective function of the optimal sensor placement for damage detection is thus taken based on the response covariance sensitivity as

$$f_{\mathrm{SA}}(\boldsymbol{\theta})=\frac{1}{\sqrt{\mathbf{trace}[\mathbf{S}^{\mathrm{T}}\mathbf{S}]}}=\frac{1}{\sqrt{\sum_{i=1}^{\mathrm{ne}}\left[\left(\frac{\partial\mathbf{V}_{\mathrm{pq}}{}^{c}}{\partial\alpha_{i}}\right)^{\mathrm{T}}\left(\frac{\partial\mathbf{V}_{\mathrm{pq}}{}^{c}}{\partial\alpha_{i}}\right)\right]}} \tag{4.12}$$

where the vector $\boldsymbol{\theta}$ denotes the optimal sensor configuration with respect to the optimal locations of sensors with prescribed number; and the sensitivity matrix $\mathbf{S}$ is computed by Eq. (4.7). According to the definition of the first objective function, the optimal sensor placement with the smallest f_{SA} shall be most sensitive to the fractional stiffness changes of the damaged elements.

The first objective function described above aims to find the maximum increment of the response covariance with respect to the fractional stiffness change. The sensor placement based on this objective function may have the selected sensors clustered around some parts of the structure with similar sensitivity to local damage, and accordingly information from some of them may overlap. On the other hand, correlation analysis can help to reduce such overlapped information by collecting more independent structural responses (Khawsuk and Pao 2002). Response independence can potentially improve the quality of damage detection results. In this regard, the second objective aims to obtain independent acceleration responses through correlation analysis. For two different normalized acceleration responses, such as $\hat{\ddot{z}}_p$ and $\hat{\ddot{z}}_q$, the correlation coefficient at $\tau = 0$ is given by

$$r_{\mathrm{pq}} = E\left[\hat{\ddot{z}}_p(t)\hat{\ddot{z}}_q(t)\right] = \sum_{j=1}^{m} \frac{c_{jj}{}^2}{\sigma_p^0 \sigma_q^0} [\ddot{\mathbf{h}}^{\mathrm{T}}_{p,f_j}\ \ddot{\mathbf{h}}_{q,f_j}]; \qquad r_{pq} \in [-1,1] \tag{4.13}$$

The correlation coefficient r_{pq} is a scalar value according to its definition in statistics. The independence of two acceleration time series $\hat{\ddot{z}}_p(t)$ and $\hat{\ddot{z}}_q(t)$ should be measured from different installation locations but not from different time delays τ. Thus, the correlation coefficient at $\tau = 0$ is used, which explicitly shows the relationship between the correlation coefficient r_{pq} of the two normalized acceleration responses and the covariance of the acceleration UIR vectors. Using the Euclidean distance d_{pq} to evaluate the independence between two normalized acceleration $\hat{\ddot{z}}_p$ and $\hat{\ddot{z}}_q$ yields

$$d_{\mathrm{pq}} = \sqrt{\sum_{i=0}^{n-1} [\hat{\ddot{z}}_p(t_i) - \hat{\ddot{z}}_q(t_i)]^2} = \sqrt{\sum_{i=0}^{n-1} [\hat{\ddot{z}}_p(t_i)]^2 + \sum_{i=0}^{n-1} [\hat{\ddot{z}}_q(t_i)]^2 - 2\sum_{i=0}^{n-1} [\hat{\ddot{z}}_p(t_i)\hat{\ddot{z}}_q(t_i)]} \tag{4.14}$$

Eq. (22) can be further simplified as

$$d_{\mathrm{pq}}{}^2 = \sum_{i=0}^{n-1} [\hat{\ddot{z}}_p(t_i)]^2 + \sum_{i=0}^{n-1} [\hat{\ddot{z}}_q(t_i)]^2 - 2\sum_{i=0}^{n-1} [\hat{\ddot{z}}_p(t_i)\hat{\ddot{z}}_q(t_i)] \approx n\sigma_{\hat{\ddot{z}}_p} + n\sigma_{\hat{\ddot{z}}_q} - 2nr_{\mathrm{pq}} \tag{4.15}$$

where $\sigma_{\hat{\ddot{z}}_p} = \sigma_{\hat{\ddot{z}}_q} = 1$ are the standard deviation of the normalized acceleration responses $\hat{\ddot{z}}_p$ and $\hat{\ddot{z}}_q$, respectively. The relationship between the correlation coefficient r_{pq} and the Euclidean distance d_{pq} of the two normalized accelerations is

$$r_{\mathrm{pq}} \approx \frac{\sigma_{\hat{\hat{z}}_p} + \sigma_{\hat{\hat{z}}_q}}{2} - \frac{{d_{\mathrm{pq}}}^2}{2n} = 1 - \frac{{d_{\mathrm{pq}}}^2}{2n} \tag{4.16}$$

Note that a larger d_{pq} results in a smaller correlation coefficient r_{pq}, which indicates a higher degree of independence between the two normalized acceleration responses. Thus, r_{pq} can be an index to represent the independence of acceleration responses. The correlation matrix for different acceleration responses is formed as

$$\mathbf{R} = \begin{bmatrix} r_{\mathrm{p_1q_1}} & r_{\mathrm{p_1q_2}} & \cdots & r_{\mathrm{p_1q}_k} & \cdots & r_{\mathrm{p_1q}_s} \\ r_{\mathrm{p_2q_1}} & r_{\mathrm{p_2q_2}} & \cdots & r_{\mathrm{p_2q}_k} & \cdots & r_{\mathrm{p_2q}_s} \\ \vdots & \vdots & \ddots & \vdots & \cdots & \vdots \\ r_{\mathrm{p}_l\mathrm{q_1}} & r_{\mathrm{p}_l q_2} & \cdots & r_{\mathrm{p}_l\mathrm{q}_k} & \cdots & r_{\mathrm{p}_l\mathrm{q}_s} \\ \vdots & \vdots & \vdots & \vdots & \ddots & \vdots \\ r_{\mathrm{p}_s\mathrm{q_1}} & r_{\mathrm{p}_s\mathrm{q_2}} & \cdots & r_{\mathrm{p}_s\mathrm{q}_k} & \cdots & r_{\mathrm{p}_s\mathrm{q}_s} \end{bmatrix} \tag{4.17}$$

where the symmetric matrix $\mathbf{R}$ is the correlation coefficient matrix computed from the interested acceleration responses with prescribed number of sensors; $\mathrm{p}_l \in [\mathrm{p}_1, \mathrm{p}_s]$ and $\mathrm{q}_k \in [\mathrm{q}_1, \mathrm{q}_s]$; and the correlation coefficient $r_{\mathrm{p}_l\mathrm{q}_k}$ is computed from the responses recorded by the sensors p_l and q_k. The second objective function f_{CA} formed by the matrix $\mathbf{R}$ for optimal sensor placement is then given by

$$f_{\mathrm{CA}}(\boldsymbol{\theta}) = \sqrt{\mathbf{trace}\left[\mathbf{R}^{\mathrm{T}}\mathbf{R}\right]} = \sqrt{\sum_{l=1}^{s}\sum_{k=1}^{s} r_{\mathrm{p}_l\mathrm{q}_k}^2} \tag{4.18}$$

To evaluate the independence of responses within a selected sensor configuration, all the correlation coefficients between any two acceleration responses are computed by Eq. (4.17). Then, the minimization of the second objective function of Eq. (4.18) leads to the largest independence of responses from different measurement locations. For a civil engineering structure, if only a few sensors are selected, these sensors may be distributed evenly to fully capture the dynamic responses with more spatial information of the structure through minimization of the objective function f_{CA}. The smaller correlation coefficients then mean larger independence between the measured responses.

The possibility of successful damage identification may be maximized with high response covariance sensitivity to the local damages. The limited number of measured acceleration responses can also be evenly distributed to fully capture the structural dynamic properties and reduce the possible overlapped information. However, a typical optimal solution with one design objective (such as response covariance sensitivity) may not match the requirement of other significant design objectives (such as response independence) simultaneously. Therefore, a sensitivity and correlation analysis based (SCA) sensor optimal placement, integrating the two objectives, is proposed in this study.

The weighted sum method (Marler and Arora 2004) is adopted to develop this integrated objective function for OSP in the form of a linear (weighted) combination of different objective functions as follows:

$$\underset{\boldsymbol{\theta}}{\text{Minimize}}\, I_{\text{SCA}}(\boldsymbol{\theta}) = w_{\text{SCA}}\left(\frac{f_{\text{SA}}(\boldsymbol{\theta})}{\max f_{\text{SA}}(\boldsymbol{\theta})}\right) + (1-w_{\text{SCA}})\left(\frac{f_{\text{CA}}(\boldsymbol{\theta})}{\max f_{\text{CA}}(\boldsymbol{\theta})}\right); w_{\text{SCA}} \in [0,1] \quad (4.19)$$

where I_{SCA} is the SCA index developed for optimal sensor placement, which can optimize both response covariance sensitivity and independence simultaneously; and w_{SCA} is the weighting factor. Because the two proposed objective functions have different units and amplitudes, they shall be normalized to become non-dimensional functions. In this regard, they are normalized by the factors $\max f_{\text{SA}}(\boldsymbol{\theta})$ and $\max f_{\text{CA}}(\boldsymbol{\theta})$, respectively, as shown in Eq. (4.19). The normalization factors are the maximum objective function values calculated in each iteration of the backward sequential sensor placement (BSSP) algorithm (Papadimitriou 2004). The normalization factors ensure that each objective function in bracket will not be greater than unity such that they can be combined without bias to represent their contributions in the sensor placement.

After giving the weighting factor w_{SCA}, the proposed optimal sensor placement index I_{SCA} can select the optimal sensor configuration by balancing the contribution between the two proposed objectives. The candidate locations are ranked based on their combined contribution from the f_{SA} and f_{CA}. Finally, the locations with less contribution are removed from the candidate set iteratively.

4.2.3 Implementation of Optimal Sensor Placement

Most of the optimal sensor placement approaches involve computation and rank on many different combinations of candidate sensor locations. An exhaustive search over all possible sensor configurations is required to obtain the exact optimal sensor configuration for these optimal sensor placement approaches. This could be time-consuming, particularly when a large number of candidate combinations of sensor locations are considered. Alternatively, Papadimitriou (2004) proposed the BSSP algorithm to obtain a good sensor configuration by eliminating the least contribution sensor one by one, and the simulation results indicated that the approximate suboptimal configuration from the BSSP algorithm was close to the optimal sensor locations from exhaustive search. Since the BSSP can provide satisfactory accuracy with much less computation effort, it is implemented for the subsequent OSP.

The detailed procedure for an optimal sensor placement through the sensitivity analysis and correlation analysis is shown in Fig. 4.1.

Step 1: Calculate the acceleration UIR vectors $\ddot{\mathbf{h}}_{p,f_j}(\gamma)$ and $\ddot{\mathbf{h}}_{q,f_j}(\gamma+\tau)$ at the candidate locations installed with accelerometers and the corresponding variances ${c_{jj}}^2$ of the related excitations.

Step 2: Calculate the sensitivity matrix $\mathbf{S}$ of the covariance-based damage detection index from Eq. (4.7) corresponding to all the interested subsets of sensor combinations. The objective function f_{SA} for response covariance sensitivity is calculated from Eq. (4.12), and $\max f_{\mathrm{SA}}$ is calculated in each iteration.

Step 3: The correlation coefficient r_{pq} in Eq. (4.13) between different acceleration responses are computed using the weighted acceleration UIR vectors. The correlation matrix $\mathbf{R}$ in Eq. (4.17) is formed for all the interested subsets of sensor combinations and the second objective function f_{CA} for response independence is obtained by Eq. (4.18), and $\max f_{\mathrm{CA}}$ is calculated in each iteration.

Step 4: The proposed SCA optimal sensor placement index I_{SCA} is calculated from Eq. (4.19) with a prescribed weighting factor w_{SCA} which provides a weighting for the contribution between the objectives f_{SA} and f_{CA} in this study. By using the BSSP algorithm, one sensor is removed at a time in the candidate sensor configuration. The subset of sensor configuration producing the smallest value of the index I_{SCA} will be retained in the next iteration.

Step 5: By repeating Steps 2 to 4, the number of sensors in the initial candidate set is successively reduced to the required number of sensors by removing the sensor one by one using the BSSP algorithm. The final optimal sensor configuration is then obtained if the iteration criterion is satisfied.

4.3 Numerical Study

4.3.1 Description of the Frame Structure and Candidate Sensor Locations

A three-dimensional frame structure, as shown in Fig. 4.2, is employed in the numerical study to examine the feasibility and effectiveness of the proposed optimal sensor placement method for damage detection. The finite element model of the frame structure consists of 37 equal-length beam elements and 17 nodes. The structural properties are listed in Table 4.1. The structural damping is assumed to be Rayleigh damping with the first two damping ratios $\xi_1 = \xi_2 = 0.01$. In this study, the first eight modes are considered for computing the dynamic responses of the frame structure. The natural frequencies and types of modes for the first eight modes of the frame structure are listed in Table 4.2.

The frame structure is subjected to six independent white noise excitations with standard deviations of $20N$ and $60N$ in the lateral and vertical direction respectively at Nodes 15, 16 and 17. The structural responses are sampled at 500 Hz over the time duration of 60s. Measurement noise is simulated by adding normally distributed random number to the noise-free response, which is used for the damage detection study to investigate the effectiveness of optimal sensor locations. The root-mean-square (RMS) of the measurement noise is equal to 5% of the RMS value of the noise-free response in this study.

Theoretically, the minimum eight accelerometers are needed to identify eight target modes, and therefore the number of the accelerometers is set as eight in this numerical study. At the frame structure, 28 initial candidate locations of accelerometers are selected from 14 nodes (Nodes 4 -17, excluding the nodes at the supports) in the lateral (y-direction) and vertical (z-direction) degree-of-freedoms. So, there are total 28 accelerometers in the initial sensor set, which are named from 1 to 28 (sensor location number) according to the DOFs number of the node installed with the sensors in the finite element model. The initial candidate set of sensor locations is reduced by removing accelerometers one by one and the iteration is stopped when eight accelerometers are left.

After the initial number of candidate sensor locations $N_p = 28$ is selected, the computational effort between the exhaustive search algorithm and the BSSP algorithm can be compared quantificationally. When using the exhaustive search algorithm, the number of all distinct sensor configurations involving $N_o = 8$ sensors is $N_s = \dfrac{N_p!}{N_o!(N_p - N_o)!} = \dfrac{28!}{8!(28-8)!} = 3{,}108{,}105$. If the BSSP algorithm is adopted, only $N_s = N_p + (N_p - 1) + \cdots + (N_o + 1) = 370$ iterative steps are needed to achieve the suboptimal solutions. Therefore, the BSSP is used in this study as a suitable sensor placement algorithm to take less computational effort for practical application.

4.3.2 Optimal Sensor Placement and Damage Detection

The application of the proposed OSP method for damage detection is introduced in this section. The integrated OSP objective function I_{SCA} developed for damage detection is given by Eq. (4.19). The best weighting factor is determined through a parameter analysis and the performance of the OSP is assessed by damage detection accuracy to obtain the best sensor configuration for damage detection. This implementation includes three major steps as follows:

Step 1 is the binary search of a weighting factor for OSP. A weighting factor $w_{\text{SCA}} \in [0,1]$ for I_{SCA} is used to balance the contributions between the two objectives regarding the response covariance sensitivity and response independence. The binary search algorithm, also known as half-interval search, is used to find the best weighting factor in this study. This numerical searching algorithm repeatedly bisects an interval and then selects a subinterval in which an asymptotic solution lies for further processing.

Specifically, the weighting factors are initially selected between 0 and 1, and the binary search begins by comparing the middle point with two extreme values on the boundaries. Accordingly, the searching area of w_{SCA} is divided into two subintervals by $w_{\text{SCA}} = 1.0$, $w_{\text{SCA}} = 0.0$ and $w_{\text{SCA}} = 0.5$. The case with $w_{\text{SCA}} = 1.0$ or $w_{\text{SCA}} = 0.0$ is an extreme case corresponding to the situation where only the response covariance sensitivity or only the response independence is included as the OSP objective function. The case with $w_{\text{SCA}} = 0.5$ indicates that both objectives are equally important.

After prescribing a weighting factor, the BSSP algorithm governed by the I_{SCA} objective function is performed and the selected sensor locations for the above cases are graphically described in Fig. 4.3. Only 8 accelerometers are selected from 28 candidates for an optimal sensor configuration. Three optimal sensor configurations OSP1 ($w_{\mathrm{SCA}} = 1.0$), OSP2 ($w_{\mathrm{SCA}} = 0.0$) and OSP0 ($w_{\mathrm{SCA}} = 0.5$) are obtained corresponding to the three cases described above for the subsequent damage detection, and they are shown in Fig. 4.

For the OSP1 shown in Fig. 4.4(a), it is noted that most of the selected accelerometers are located at the free end of the cantilevered frame structure and some of the neighboring sensors may provide repeating information. This sensor placement may not help to identify damaged elements, which are far away from the selected sensors. For the OSP2 shown in Fig. 4.4(b), the sensors are distributed in each bay of the structure, which provide relatively independent responses. However, this placement may sacrifice sensors which are sensitive to the damage parameters. For the OSP0 shown in Fig. 4.4(c), it has many accelerometers (at Nodes 13-17) which are the same as those found in OSP1. The accelerometers are also evenly distributed on the structure.

Step 2 is the assessment of the OSP performance. The selected OSPs from Step 1 are evaluated via their effectiveness and accuracy in the damage detection of the structure. Two scenarios with multiple damage locations are considered. In the first scenario, damages are assumed to occur in two longitudinal members and one diagonal member near the support; the three damages are in Elements 6, 8 and 9 with 10%, 5% and 10% stiffness reduction, respectively. In the second scenario, damages are assumed to occur in three longitudinal members at mid-span of the structure; the three damages are in Elements 14, 17 and 18 with 10%, 5% and 10% stiffness reduction, respectively.

The effects of the three optimal sensor configurations OSP0, OSP1, and OSP2 for damage detection are compared. For the damage scenario one, the damage detection results are depicted in Fig. 4.5(a). When using sensor configuration OSP1 for damage detection, the damaged elements 6 and 9 are respectively identified with 9.9% and 8.4% stiffness reduction, but the identification of damaged element 8 fails.

This may be due to the small damage severity in Element 8 and most of the selected sensors are close to the free end which is far away for this element. When using sensor configurations OSP2, both the damage locations and severities can be satisfactorily identified. The damaged Elements 6, 8 and 9 are identified with 9.4%, 3.4% and 9.6% stiffness reduction, while two relatively large false alarms are observed in Elements 14 and 23 with 1.7% and 1.3% stiffness reduction. When using sensor configurations OSP0, the 10% damages on Elements 6 and 9 are identified very accurately, and the 5% damage on Element 8 is identified satisfactorily with 3% stiffness reduction.

For the damage scenario two, the damage detection results are depicted in Fig. 4.5(b). Both the damage locations and severities can be identified satisfactorily when using the three selected sensor configurations, and observations are similar to those of the first scenario with OPS0 yielding relatively better results than the other two configurations. The small damage ($\Delta\alpha_{17}$=5%) in Element 17 is successfully identified in this scenario using the OSP1.

The above results show that: (a) the placement OSP0 offers the best measurement information to yield the best damage detection result amongst the three sensor placements; (b) the placement OSP2 is little poorer than OSP0 for damage detection with some relatively large false alarms; (c) the placement OSP1 can only identify two damages when the selected sensors are far away from the damaged element although this sensor configuration is selected with the aim to optimize the response sensitivity to the damage parameters. All the above observations indicate that a suitable optimal sensor configuration may be sensitive to damage as well as evenly distributed to fully capture the structural dynamics.

Step 3 is the selection of a new weighting factor within a reduced searching half-interval and the performance assessment of the new OSP. According to the assessment results from Step 2, the damage detection performance achieved by using the OPS2 ($w_{\mathrm{SCA}} = 0.0$) and the OPS0 ($w_{\mathrm{SCA}} = 0.5$) is better than that by using the OPS1 ($w_{\mathrm{SCA}} = 1.0$), and the damage detection performance corresponding to $w_{\mathrm{SCA}} = 0.5$ is the best among the three cases. Therefore, a new weighting factor $w_{\mathrm{SCA}} = 0.3$ between 0.0 and 0.5 is selected. The new optimal sensor configuration, namely the OSP3, is plotted in Fig. 4 (d). The results of damage detection using the OSP3 are shown in Fig. 4.6.

It can be seen that the damage detection performance using the OSP3 has a minor improvement, compared with OSP0. This result indicates that the weighting factor $w_{\mathrm{SCA}} = 0.3$ is the best weighting factor for the best sensor placement.

4.3.3 Comparison with an Information Entropy-Based OSP Method

Many research efforts have been devoted to the study of OSP with different objectives, such as structural mode shape identification, model updating, response reconstruction, and damage detection. For damage detection, the proposed method is now compared with an information entropy (IE)-based method (Papadimitriou et al. 2000). The objective function of the IE-based OSP method is to Minimize $\exp\left[\frac{H - H_0}{N_a}\right]$, where H is the entropy information for a selected sensor configuration; H_0 is the entropy information for the reference sensor configuration including all the initial candidate sensors; and N_a is the number of the estimated parameters. The IE-based OSP method aims to obtain the measured data which are less sensitive to the uncertainty but sensitive to the estimated parameters.

The optimal sensor configuration (OSP4) is obtained by using the above IE-based objective function and the BSSP algorithm and shown in Fig. 4.4 (e). The measured acceleration responses from the OSP4 are used for damage detection. The damage detection results for the two damage scenarios are depicted in Fig. 4.6 and compared with those by using the OSP0 and the OSP3. For damage scenario one, the result obtained by using the OSP4 indicates the poorer damage quantification for the damaged elements 8 and 9 than those using OSP0 and OSP3. Meanwhile, there are four relatively large false alarms occurring in the undamaged elements 4, 10, 12 and

14. For damage scenario two, the result of damage detection using the OSP4 is much poorer than those using OSP0 and OSP3. The damaged elements 14 and 18 are identified with 4.6% and 8.0% stiffness reduction which are obviously smaller than the preset 10% damage. Meanwhile, the damaged element 17 identified with 6.8% stiffness reduction which is larger than the preset 5% damage. Moreover, three large false alarms are observed in the undamaged elements 6, 13 and 22. This comparison revealed that the proposed response covariance-based OSP method could lead to more accurate damage detection than the IE-based OSP method.

4.4 Summary

A response covariance-based sensor placement method based on the sensitivity and correlation analyses (SCA) has been developed in this chapter for better structural damage detection. First, the relationship between the covariance of acceleration responses and the covariance of unit impulse responses of a structure subjected to multiple white noise excitations has been derived. This relationship indicates that optimal sensor location is related to the location of excitation but not to the amplitude of excitation. Second, the optimal sensor placement (OSP) objectives in terms of the response covariance sensitivity and the response independence have been derived, respectively. The first objective indicates that the estimation error of parameters is inversely proportional to the Fisher information matrix with respect to the response covariance sensitivity, while the second objective indicates that a larger Euclidean distance between two normalized acceleration responses leads to a higher degree of independence between the two responses.

The two objective functions proposed in this study for optimal sensor placement (OSP) are conflicting. This has been confirmed by comparing the OSP1 with the OSP2 (see Fig. 4.4) and by comparing the damage identifiability of the OPS1 with that of the OPS2 (see Fig. 4.5) for the frame structure concerned. The OSP1 (the first objective function) aims to enhance the damage sensitivities of the measured responses and does not consider response independence. As a result, some sensors with similar sensitivity cluster at the free end of the frame structure and these sensors actually measure overlapping information. Also because of the clustered sensors, the damaged element 8 is far away from these sensors and the damage identification of this element thus failed. On the other hand, the OSP2 (the second objective function) aims to reduce redundant measured responses for a given number of sensors without considering the damage sensitivity of the measured response. It is thus noted from Fig. 4.5 that the damage detection using the OSP2 with larger false alarms occurring in the undamaged elements than the OSP1. Therefore, the integrated SCA objective function, which combines the two OSP objectives, has been developed in this study to obtain the OSP with better performance for damage detection.

Furthermore, the backward sequential sensor placement (BSSP) algorithm is used to solve the typical single objective OSP problem governed by the proposed SCA objective function, which can save more computation effort than advanced intelligent algorithms for sensor placement. The numerical study showed that the best weighting factor for the best damage detection of the frame structure is 0.3. The numerical study also demonstrated that the approach combining the response covariance-based damage detection method and the SCA optimal sensor placement method is feasible and effective for damage detection.

It is noted that for the response covariance-based OSP mentioned above, an integrated single objective function was formed by using a weighting factor to combine the two conflicting objective functions in this chapter. The best weighting factor was determined by using the binary search and the performance of each OSP must be assessed by the damage detection accuracy, so that the whole process of OSP and damage detection were repeatedly conducted until the best weighting factor was found. To avoid the difficulty in choosing weighting factors, multi-objective optimization algorithms for OSP are desirable, which will be investigated in the next chapter.

Table 4.1 The list of structural properties

Properties	Value
Young modulus $E\,(\mathrm{N/m^2})$	2.10×10^{11}
Sectional area $A\,(\mathrm{m^2})$	3.1416×10^{-4}
Density $\rho(\mathrm{Kg/m^8})$	1.2126×10^{4}
Moment of inertia $I_y\,(\mathrm{m^4})$	7.854×10^{-9}
Moment of inertia $I_z\,(\mathrm{m^4})$	7.854×10^{-9}
Moment of inertia $I_p\,(\mathrm{m^4})$	1.5708×10^{-8}

Table 4.2 The natural frequencies and mode types

No. of mode	Frequency (Hz)	Type of mode
1	7.76	torsional
2	23.97	torsional
3	40.42	bending
4	41.88	torsional
5	59.47	torsional
6	61.28	torsional
7	76.98	torsional
8	162.24	bending

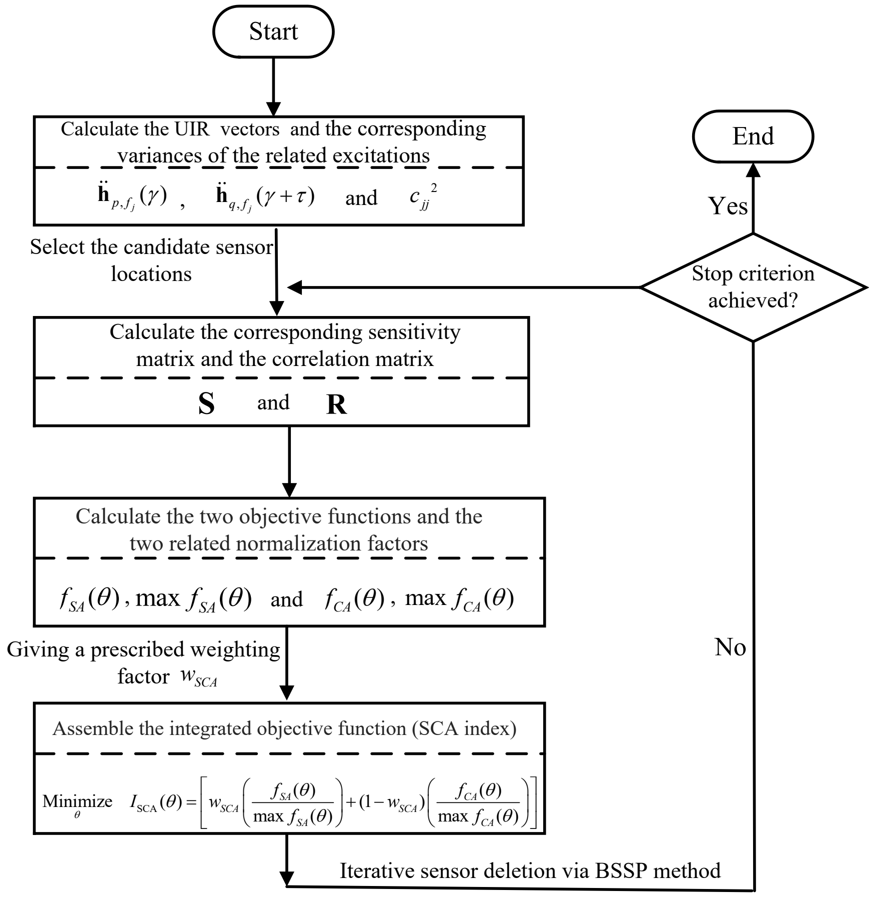

Fig. 4.1 Flowchart of response covariance based optimal sensor placement method

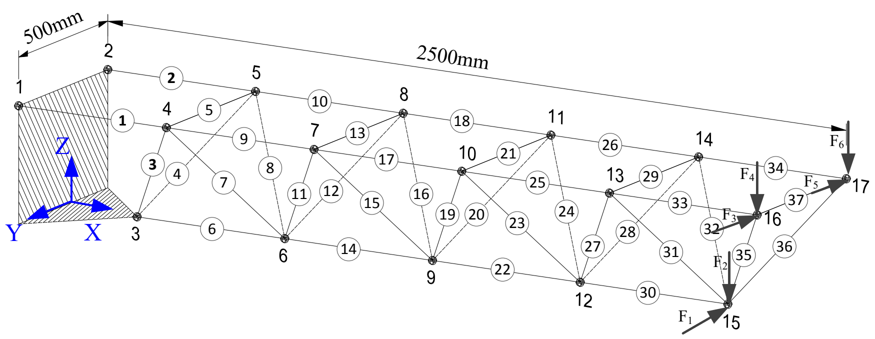

Fig. 4.2 The finite element model of a three-dimensional frame structure

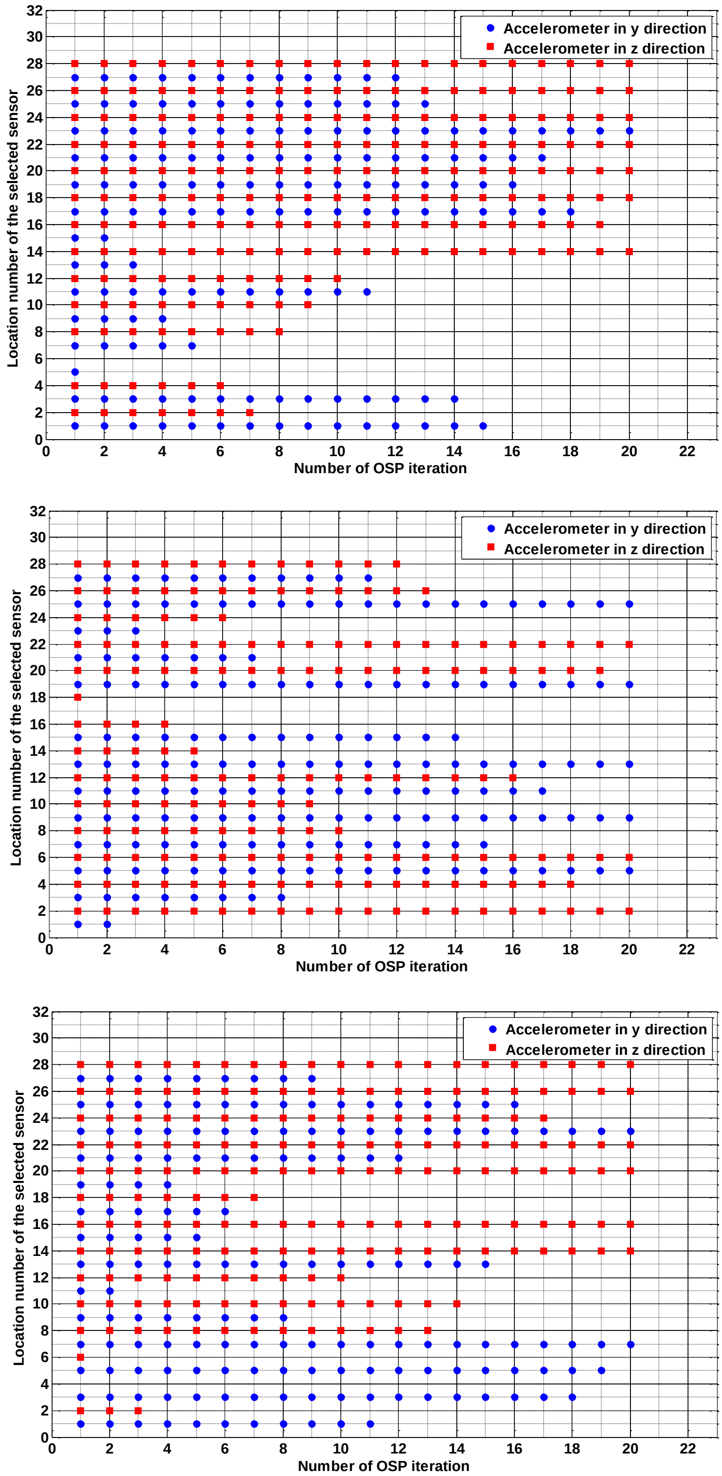

Fig. 4.3 The BSSP sensor placement using different weighting factors for the I_{SCA} index: (a) Using the weighting factor $w_{\mathrm{SCA}} = 1.0$; (b) Using the weighting factor $w_{\mathrm{SCA}} = 0.0$; (c) Using the weighting factor $w_{\mathrm{SCA}} = 0.5$.

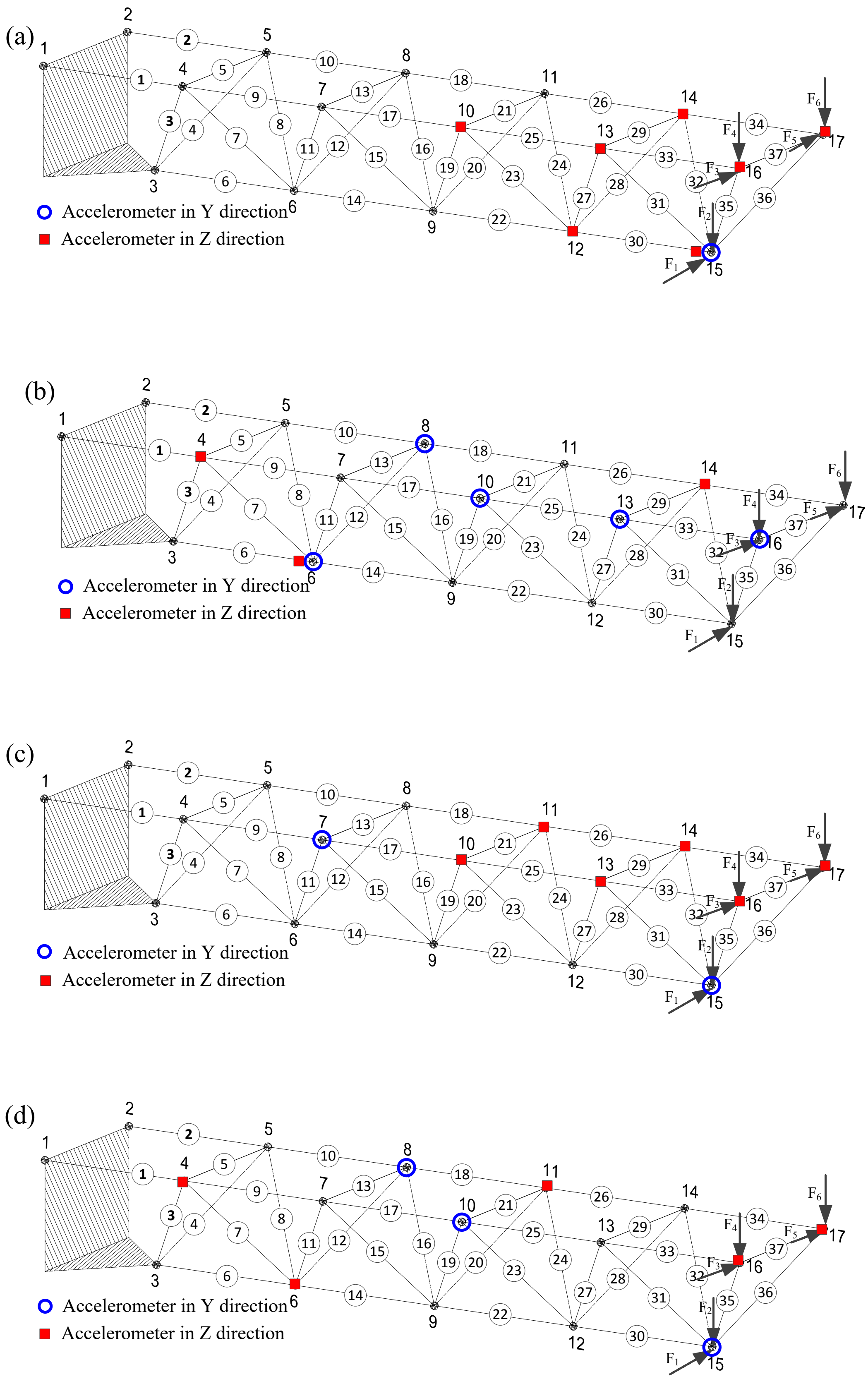
(a)
Accelerometer in Y direction
Accelerometer in Z direction
(b)
Accelerometer in Y direction
Accelerometer in Z direction
(c)
Accelerometer in Y direction
Accelerometer in Z direction
(d)
Accelerometer in Y direction
Accelerometer in Z direction

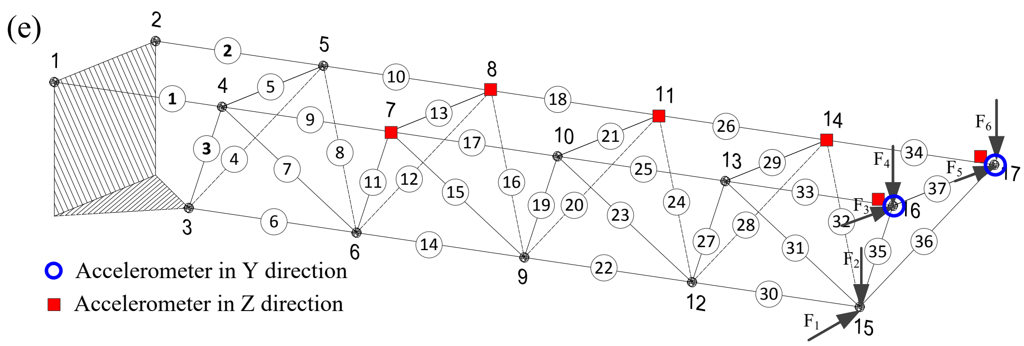

Fig. 4.4 The optimal sensor configurations with eight accelerometers : (a) OSP1 using the proposed SCA index with the weighting factor $w_{\mathrm{SCA}} = 1.0$; (b) OSP2 using the proposed SCA index with the weighting factor $w_{\mathrm{SCA}} = 0.0$; (c) OSP0 using the proposed SCA index with the weighting factor $w_{\mathrm{SCA}} = 0.5$; (d) OSP3 using the proposed SCA index with the weighting factor $w_{\mathrm{SCA}} = 0.3$; (e) OSP4 obtained by using the IE based OSP method.

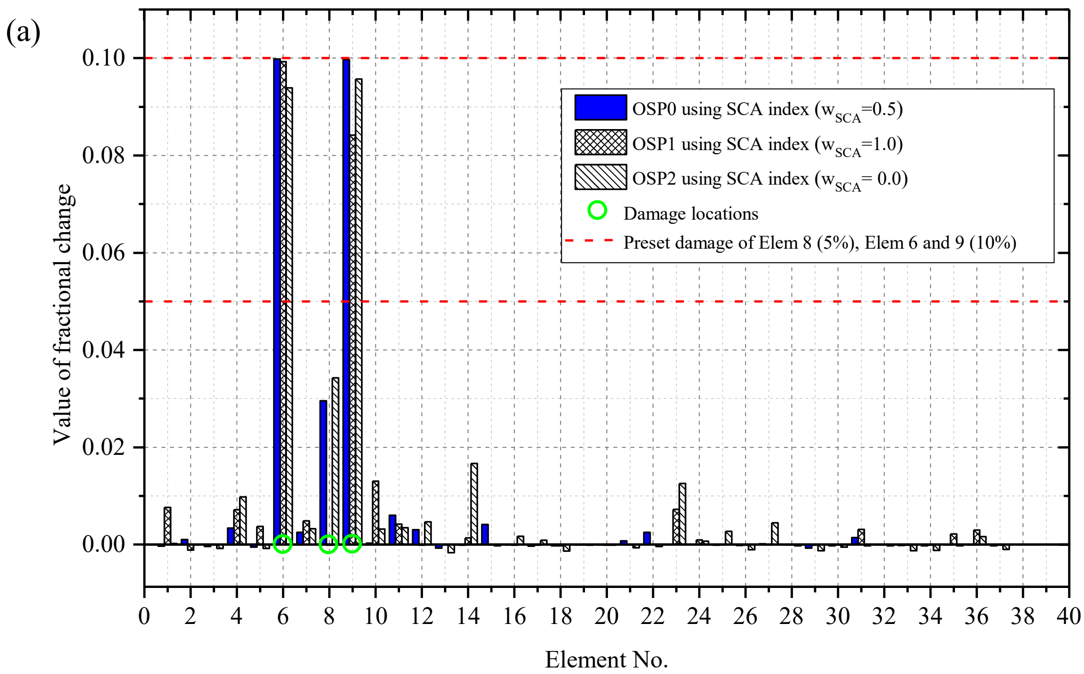

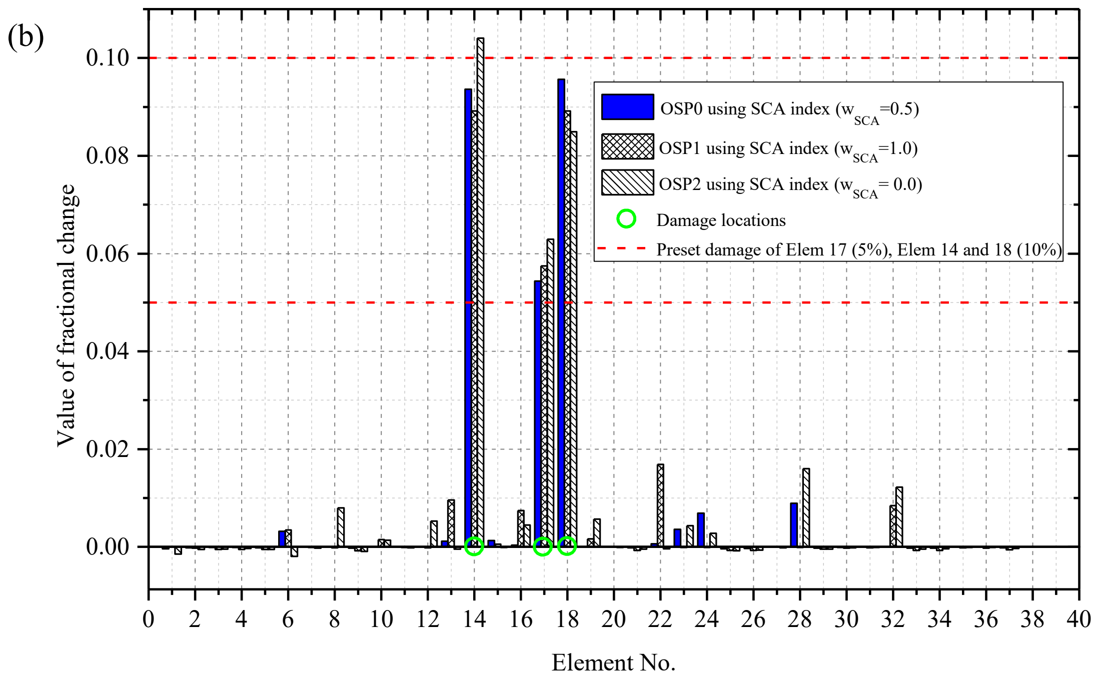

Fig. 4.5 Damage detection via OSP using the SCA indexes with different weighting factors: (a) Damage detection scenario 1; (b) Damage detection scenario 2.

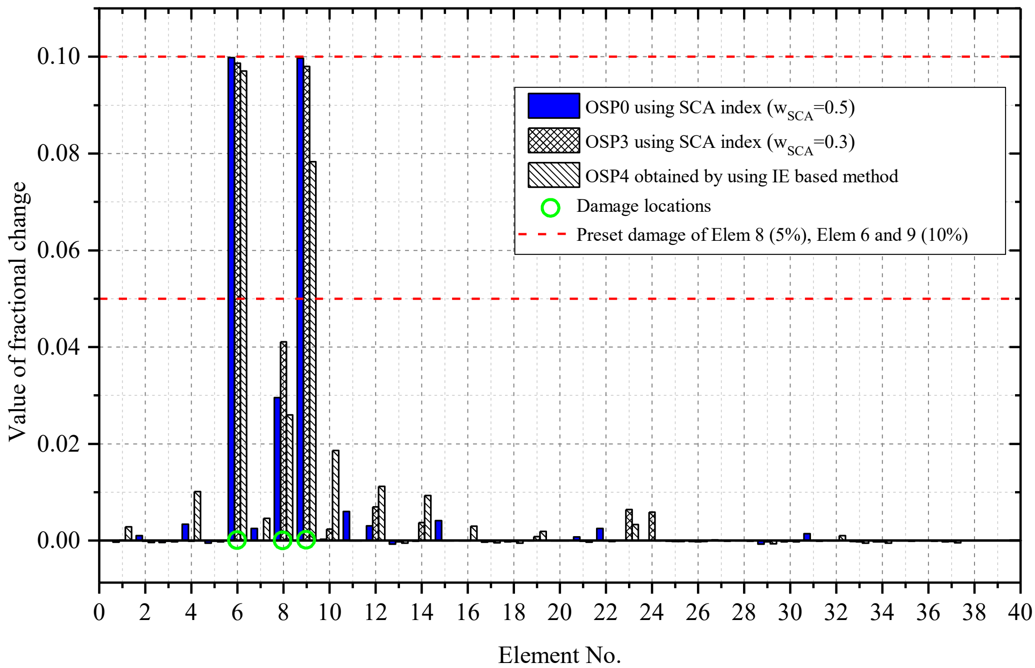

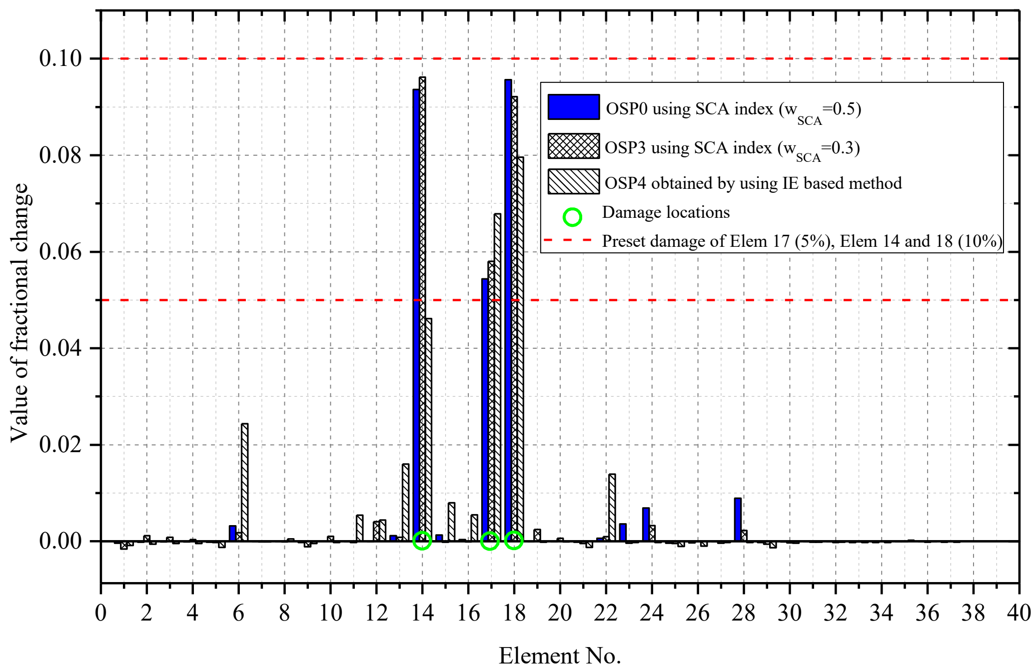

Fig. 4.6 Comparison of damage detection by using OSP0, OSP3 and OSP4:

(a) Damage detection scenario 1; (b) Damage detection scenario 2.

CHAPTER 5

STRUCTURAL DAMAGE DETECTION ORIENTED MULTI-TYPE SENSOR PLACEMENT WITH MULTI-OBJECTIVE OPTIMIZATION

5.1 Introduction

In Chapter 4, the two covariance-based OSP objectives in terms of response covariance sensitivity and response independence were proposed, and the multi-objective optimal sensor placement problem was transformed to the single-objective optimization by using the weighted sum method of combining the two objectives. The best weighting factor, however, shall be determined by trial and error in terms of the quality of damage detection. Moreover, only the accelerometer optimal placement was studied in Chapter 4.

In this chapter, the same objectives will be applied for multi-type sensor (accelerometer, displacement transducer, and strain gauge) optimal placement. To avoid the difficulty in choosing weighting factors, the multi-objective optimization algorithm for OSP will be developed so that the response covariance-based OSP method can be extended to multi-type sensor placement with multi-objective optimization in this chapter. The multi-objective optimization problem is formed by directly using the two covariance-related objective functions, and the non-dominated sorting genetic algorithm (NSGA)-II is adopted to find the solution for the optimal multi-type sensor placement to achieve the best structural damage detection. Section 5.2 will formulate the multi-objective multi-type sensor optimal placement problem and introduce the implementation of the proposed method. Section 5.3 is the numerical study by using a nine-bay three-dimensional frame structure to examine the feasibility and effectiveness of the proposed method, in which a utility-function-based method is first proposed to select the "best" OSP from the Pareto front considering the user's preferences. Section 5.4 will further propose the second method in terms of a knee point based method to find the "best" OSP from the Pareto front without any knowledge about the user's preferences. The proposed method will be compared with a Fisher information matrix based OSP method for traditional response sensitivity-based damage detection to demonstrate the merit of the proposed OSP. A summary of the works presented in this chapter is given in Section 5.5.

5.2 Methodology

5.2.1 Multi-Objective Multi-Type Sensor Placement Problem

The two OSP objectives in terms of response covariance sensitivity and response independence have been derived by the authors and applied for single-type sensor placement in Chapter 4 (Lin and Xu 2017), in which the multi-objective OSP problem was simplified to a single-objective OSP problem by using a weighted sum of the two objective functions. The weighting factors were solved by using binary search algorithm and accordingly the multiple runs of optimization were required with enormous computation cost. The same objectives are used in this chapter, but a new multi-objective function is formulated and a multi-objective optimization evolutionary algorithm is used to obtain the Pareto solutions of OSP.

To find optimal multi-type sensor placement fulfilling the two objective functions $f_{\mathrm{SA}}(\boldsymbol{\theta})$ in Eq. (4.12) and $f_{\mathrm{CA}}(\boldsymbol{\theta})$ in Eq. (4.18) at the same time, the multi-objective multi-type sensor placement problem can be formulated as

$$\begin{aligned} &\underset{\boldsymbol{\theta}}{\text{Minimize}} \quad \mathbf{F}(\boldsymbol{\theta}) = \left[\hat{f}_{\mathrm{SA}}(\boldsymbol{\theta}), \hat{f}_{\mathrm{CA}}(\boldsymbol{\theta}) \right] = \left[\frac{f_{\mathrm{SA}}(\boldsymbol{\theta})}{\max f_{\mathrm{SA}}(\boldsymbol{\theta})}, \frac{f_{\mathrm{CA}}(\boldsymbol{\theta})}{\max f_{\mathrm{CA}}(\boldsymbol{\theta})} \right]; \\ &\text{subject to} \begin{cases} N_{oi}^{L} \le N_{oi} \le N_{oi}^{U}; \\ \sum\limits_{i=1} N_{oi} \le N_{o} \end{cases} \end{aligned} \tag{5.1}$$

where $\mathbf{F}(\boldsymbol{\theta})$ is the multi-objective function based on the response covariance sensitivity and correlation analysis (SCA). $\hat{f}_{\mathrm{SA}}(\boldsymbol{\theta})$ and $\hat{f}_{\mathrm{CA}}(\boldsymbol{\theta})$ are the non-dimensional objective functions normalized by their maximum values $\max f_{\mathrm{SA}}(\boldsymbol{\theta})$ and $\max f_{\mathrm{CA}}(\boldsymbol{\theta})$, respectively; N_{oi} is the number of sensors of the i^{th} type; N_{oi}^{L}, N_{oi}^{U}, and N_{o} are respectively the lower and upper bounds of sensor number for the i^{th} type, and the total number of candidate locations. The multi-type sensor optimal placement can be obtained by solving Eq. (5.1). The implementation procedure is described in the following section.

5.2.2 Implementation Procedure of Multi-Objective Multi-Type Sensor Placement

The NSGA-II (Deb et al. 2002) is tailored to suit the specific multi-objective multi-type sensor placement problem in this study. The possible sensor locations are defined as the design variables of the optimization. Specifically, the decimal two-dimensional array coding system (Liu et al. 2008) is adopted for the representation of the design variables. Each possible sensor location is represented by an integer (the "gene"), and the optimal sensor configuration $\boldsymbol{\theta}$ is represented as an integer string (the "chromosome"). Moreover, a forced mutation is embedded to replace the repeated genes in the sensor placement problem. This is because each sensor is represented by a unique integer related to its location, and one location (e.g., a node of a structure) can accommodate different types of sensors (e.g., a displacement transducer and/or an accelerometer).

Since s sensors are selected from N_o candidate locations in this study, each chromosome consists of s genes. A gene pool of N_p (population size) chromosomes is explored in every generation. The tailored NSGA-II is conducted to solve the multi-objective multi-type sensor placement problem governed by the proposed SCA objective function and to find the Pareto-optimal solutions (the optimal sensor configurations) for structural damage detection. The flowchart of optimal sensor placement using the tailored NSGA-II for this study is shown in Fig.5.1. Detailed implementation procedure is described as follows:

Step 1: Initially, the sensor locations are assigned with uniformly distributed random integers between unity and N_o. Therefore, the NSGA-II starts with a collection of chromosomes $\mathbf{P}(\boldsymbol{\theta})^0$ that are strings of random integers uniformly distributed between unity and N_o.

Step 2: The same sensor may be placed more than once at the same location synchronously (e.g., the same integer may be repeatedly used for a chromosome $\boldsymbol{\theta}$) in newly generated chromosomes or chromosomes that will undergo crossover and mutation operations subsequently. A forced mutation is then applied to replace the repeated genes in each chromosome with unrepeated and uniformly distributed random integers from the set of difference obtained between the set $\boldsymbol{\theta}$ and the whole set of candidate sensor locations.

Step 3: Calculate the normalized objective functions $\hat{f}_{\mathrm{SA}}(\boldsymbol{\theta})$ and $\hat{f}_{\mathrm{CA}}(\boldsymbol{\theta})$ for each chromosome $\boldsymbol{\theta}$.

Step 4: Perform an elitist non-dominated sorting for all the chromosomes in the current generation and identify non-dominated fronts.

Step 5: Perform the GA operation including selection, crossover, and mutation to generate a new population $\mathbf{Q}(\boldsymbol{\theta})$. Thereafter, the forced mutation introduced in **Step 2** is conducted to replace the repeated genes in each chromosome, and values of the proposed normalized objective functions are computed as described in **Step 3.** The old population and new population are combined as $\mathbf{P}(\boldsymbol{\theta}) \cup \mathbf{Q}(\boldsymbol{\theta})$, and the elitist non-dominated sorting described in **Step 4** is conducted to produce the next population.

Step 6: **Step 5** is repeated until the maximum generation number is reached. Finally,

N_p Pareto solutions on different optimal sensor configurations are obtained for the multi-objective multi-type sensor optimal placement problem.

5.3 Numerical Study

5.3.1 Finite Element Model and Candidate Sensor Locations

A three-dimensional frame structure shown in Fig. 5.2 is used for the numerical case study to examine the feasibility and effectiveness of the proposed method. It consists of 69 equal-length beam elements and 29 nodes. The structural and material properties of the frame structure are listed in Table 5.1. The structural damping is assumed to be Rayleigh damping with the first two damping ratios, and they are assumed to be the same for the structure before and after damage. Other higher-order damping ratios are obtained from $\xi_i = \mathbf{\Phi}_i^{\mathrm{T}} \mathbf{C} \mathbf{\Phi}_i / 2\omega_i$, where $\mathbf{\Phi}_i$, $\mathbf{C}$, ω_i are the i^{th} mode shape, the Rayleigh damping matrix, and the i^{th} natural frequency, respectively.

The dynamic characteristics analysis of the frame structure is performed. The first twelve modes are selected in the modal superposition for the subsequent analysis and they are listed in Table 5.2. The two Gaussian white noise excitations with a standard deviation of 20 N and 40 N are applied to Node 27 of the frame structure in the lateral (y) direction and vertical (z) direction, respectively, as shown in Fig. 5.2. The excitation frequency is selected with a bandwidth of 0-100 Hz to cover the first twelve natural frequencies. The structural responses are sampled at 500 Hz over the time duration of 50s. Measurement noise is simulated by adding normally distributed random number to the noise-free response, which is used in damage detection study to investigate the effectiveness of optimal sensor configurations. The root-mean-square (RMS) of the measurement noise is equal to 5% of the RMS value of the noise-free response in this study.

The total number of candidate sensor locations is determined basing on the following considerations. The three-dimensional frame structure has 26 candidate node locations (excluding the supporting nodes) and the structure is symmetrical about the x-z plane. The even-number nodes are selected for the candidate sensor locations to measure dynamic displacement and acceleration responses in the lateral (y) direction, while the odd-number nodes are selected for the candidate sensor locations to measure dynamic displacement and acceleration responses in the vertical (z) direction. A strain gauge is placed on the surface and at mid-span of each beam element, and all 69 beam elements are selected as candidate sensor locations to measure longitudinal strains parallel to the axis of the beam element. As a result, the total number of candidate sensor locations is 26+26+69=121. For the sake of sensor placement encoding, the accelerometers and displacement transducers are labeled by 1-26 and 27-52, respectively, and distributed over the 4^{th}-29^{th} nodes of the finite element model. The strain gauges are labeled by 53-121 and distributed over 1^{st} - 69^{th} beam elements.

5.3.2 The Optimal Sensor Placement

To find the optimal sensor placement, Eq. (5.1) is solved by using the tailored NSGA-II with the parameters listed in Table 5.3. The determination of the parameters of NSGA-II can refer to the MATLAB help document (MathWorks 2017). The total number of sensors N_o=25 is selected based on the principle of using the minimum number of sensors but guaranteeing enough accuracy of structural damage detection. Thereafter, two cases of OSP with and without constraint are discussed successively. In the "unconstrained" case, there is no restriction on the number of each type of sensors, and the lower and upper bounds of each type of sensors are $N_{oi}^{L}=0$ and $N_{oi}^{U}=s$. In the "constrained" case, the numbers of each type of sensors are specified and the lower and upper bounds of each type of sensors are equal ($N_{oi}^{L}=N_{oi}^{U}$).

For the "unconstrained" case, the 25 sensors are selected from 121 candidate locations ($s=25$, $N_o=121$) without the constraint on the number of each type sensor.

After solving the multi-objective multi-type sensor placement problem expressed by Eq. (19), the Pareto front of this case is obtained and plotted in Fig. 5.3(a). This Pareto front includes 200 Pareto solutions and each Pareto solution corresponds to an OSP. The Pareto front is not the final solution of the OSP for damage detection, because the simultaneous optimization of two conflictive objectives leads to a set of compromised solutions known as the non-dominated or Pareto-optimal solutions. It is also noted from the Pareto front that the proposed response covariance sensitivity objective and the response independence objective are conflicting. To balance the trade-off between the two conflictive objectives, the best OSP as the final solution from the Pareto front is subsequently selected by the two proposed strategies in terms of the utility-function or knee-point based method. Once the best OSP is selected, the performance of the best OSP can be evaluated by damage detection of the frame structure under different damage scenarios. It is worth pointing out that the determination of the final OSP does not need the prior knowledge of the specific damage severities and locations, which is actually the main advantage of this proposed method.

To determine a “best” OSP, there is a need to accept some trade-off between two conflitive objectives for a specific application (Marler and Arora 2004). The following scalar utility function is firstly defined for this purpose.

$$I_{\mathrm{SCA}}(\boldsymbol{\theta}_{\mathrm{Pa}}) = w_{\mathrm{SCA}} \cdot \hat{f}_{\mathrm{SA}}(\boldsymbol{\theta}_{\mathrm{Pa}}) + (1 - w_{\mathrm{SCA}}) \cdot \hat{f}_{\mathrm{CA}}(\boldsymbol{\theta}_{\mathrm{Pa}}); \qquad w_{\mathrm{SCA}} \in [0,1] \tag{5.2}$$

where I_{SCA} is the utility function; $\boldsymbol{\theta}_{\mathrm{Pa}}$ is the Pareto solution with respect to an OSP; and w_{SCA} is a weighting factor which is usually chosen in proportion to the importance of the objectives.

The proposed method can offer multiple optimal solutions in the Pareto front, with different weighting factors on the objective functions. Any of these solutions is unique with a selected pair of weighting factors. To investigate the effect of different weighting factors on the OSP, three different weighting factors $w_{\mathrm{SCA}} = 0.5$, $w_{\mathrm{SCA}} = 1.0$, and $w_{\mathrm{SCA}} = 0.0$ are selected for comparison in this study. The weighting factor $w_{\text{SCA}} = 0.5$ means that equal importance is assigned to the two objectives. The weighting factor $w_{\text{SCA}} = 1.0$ or $w_{\text{SCA}} = 0.0$ represents two extreme conditions considering either the objective $\hat{f}_{\text{SA}}(\boldsymbol{\theta})$ or the objective $\hat{f}_{\text{CA}}(\boldsymbol{\theta})$ only. Afterward, the minimization of I_{SCA} with a specified weighting factor in Eq. (20) leads to the desirable Pareto solution corresponding to a unique OSP. Thus, three specific OSPs corresponding to the three prescribed weighting factors are selected from the Pareto front respectively. The resulting OSPs are shown in Fig. 5.4 and listed in Table 5.4. In these figures and table, OSP1, OSP2 and OSP0 represent the "unconstrained" cases with the weighting factors being 1.0, 0.0 and 0.5, respectively. The notation 4(y) denotes sensor placed at Node 4 in the y-direction.

Furthermore, the proposed OSP method is very flexible to include some engineering judgment on constraining the number of each type of sensors to obtain a preferable solution. As a comparison, the number of each type of sensors in the "constrained" case is determined by referring to those in the OSP0 with a minor adjustment. Specifically, there are 12 accelerometers, 3 displacement transducers, and 10 strain gauges. Accordingly, the 25 genes in the chromosome are partitioned into three segments. They include 12 genes for the accelerometers, 3 genes for the displacement transducers, and 10 genes for the strain gauges in sequence. Decimal array coding of the genes is then allocated to the three segments. Similarly, the Pareto front for the constrained case is obtained and plotted in Fig. 5.3(b). Three specific OSPs corresponding to the three prescribed weighting factors are selected from the Pareto front respectively. The resulting sensor locations are shown in Figs. 5.5 and listed in Table 5.4. In these figures and table, COSP1, COSP2 and COSP0 with "C" represent the constrained cases with the weighting factors being 1.0, 0.0 and 0.5, respectively. The discussion on these unconstrained or constrained OSPs is presented in the following paragraphs.

5.3.2.1 The Unconstrained Case

When only the objective function for response covariance sensitivity is considered, the OSP1 ($w_{\mathrm{SCA}} = 1.0$) selected from the Pareto front in Fig. 5.3(a) is embodied in Fig. 5.4(a). It is noted that most of the selected sensors are strain gauges because strain response usually has higher sensitivity to local damage than acceleration response or displacement response. However, most of the strain gauges are clustered around some parts of the structure with similar sensitivity to local damage. The neighboring sensors tend to provide redundant information and may not be beneficial to identify damaged elements which are far away from the clustered sensors.

When only the objective function for response independence is considered, the OSP2 ($w_{\mathrm{SCA}} = 0.0$) selected from the Pareto front in Fig. 5.3 (a) is embodied in Fig. 5.4(b). All three types of sensors are distributed evenly on the structure. Although this may help to enhance the response independence, there is no guarantee on the higher sensitivity of the measured responses to structural damage.

When the equal weighting is given to the two objectives, the OSP0 ($w_{\mathrm{SCA}} = 0.5$) selected from the Pareto front in Fig. 5.3(a) is embodied in Fig. 5.4(c). It is noted that this configuration also has three types of sensors evenly distributed on the structure, but the response covariance sensitivity and the response independence both are considered in the selection.

5.3.2.2 The Constrained Case

For the constrained case, three OSPs selected from the Pareto front in Fig. 5.3(b) are embodied in Fig. 5.5 corresponding to the weighting factor $w_{\mathrm{SCA}} = 1.0$, 0.5 and 0.0. It is noted that the selected OSPS in terms of the COSP0, COSP1 and COSP2 have many common sensors. For instance, they have three common displacement transducers at Nodes 15, 21 and 27, three common accelerometers at Nodes 9, 15 and 17, and one common strain gauge on Element 6.

The restriction on the number of each type of sensors helps to reduce the search space in the optimization. The number of all possible OSPs for the unconstrained case is $\frac{121!}{(121-25)!25!}=5.262\times10^{25}$, while the number of all possible OSPs for the constrained case is $\frac{26!}{(26-12)!12!}\cdot\frac{26!}{(26-3)!3!}\cdot\frac{69!}{(69-10)!10!}=8.538\times10^{21}$. In this study, the near-optimal solutions are obtained by using the NSGA-II method with the same maximum generation number specified in the computation. However, the constrained case has a smaller search space in the multi-objective optimization that may lead the near-optimal solutions closer to the global optimization solution.

5.3.3 Damage Detection Results

To examine the feasibility and effectiveness of the proposed method for structural damage detection, three multiple damage scenarios are considered and the details are listed in Table 5. In the first scenario, damages are assumed to occur in two longitudinal members. Element 17 near the support is of 15% stiffness reduction while element 33 at mid-span of the structure is of 10% stiffness reduction. In the second scenario, damages occur in two longitudinal members close to the support of the structure. Elements 17 and 18 have 15% and 10% stiffness reduction, respectively. In the third scenario, the damage occurs in a total of six elements: element 10 (longitudinal member), element 11 (diagonal member), element 13 (lateral member), element 22 (longitudinal member), element 41 (longitudinal member) and element 42 (longitudinal member) with 15% stiffness reduction respectively. These unknown damages are detected by solving the damage detection equation $\Delta\mathbf{V}_{\mathrm{pq}}{}^{k}=\mathbf{S}^{k}\Delta\boldsymbol{\alpha}^{k+1}$ in Eq. (3.18). The identified results using sensor configurations OSP0, OSP1 and OSP2 are shown in Fig. 5.6, while those using configurations COSP0, COSP1 and COSP2 are shown in Fig. 5.7. The identifiability of these three sensor configurations is discussed in the following paragraphs.

5.3.3.1 The Unconstrained Case

The damage detection results from the damage scenarios 1 and 2 using the OSP0, OSP1 and OSP2 are compared and plotted in Figs. 5.6(a) and (b), respectively. In the first damage scenario, the OSP0 leads to effective damage localization for elements 17 and 33, as shown in Fig. 5.6 (a). It also gives accurate identification of the damage severity for element 17 but a smaller damage severity than the actual stiffness reduction for element 33 (i.e., 8.54% < 10%) is identified. When using OSP1, the damage identification results are similar to those obtained by using OSP0 but the difference lies in its poorer estimation of stiffness in element 33 (6.14%) and the four big false alarms in elements 16, 20, 29 and 64 with incorrect stiffness reduction of 2.45%, 2.13%, 1.82%, and 1.89% respectively. Further examination on Fig. 5.4(a) reveals that OSP1 has only three accelerometers. This may give insufficient global information for damage detection leading to these false alarms. When using the OSP2, it also leads to a set of poorer identified results compared with the OSP0. The stiffness reductions in elements 17 and 33 are identified as 12.03% and 7.03% respectively. False alarms occur in several elements with the largest error of 4.84% in element 25. Further examination on Fig. 5.4(b) reveals that element 25 is closed to the damaged elements 17 and 33. This large false alarm may be caused by the influence of its two adjacent damage elements. Essentially, the poor damage identification and the large false alarm from the OSP2 results from only optimizing the response independence but ignoring the requirement of damage sensitivity. In the second damage scenario, observations are similar to those of the first scenario with OPS0 yielding better damage detection results than the other two configurations, as shown in Fig .5.6(b).

The damage detection results from the scenario 3 using the OSP0, OSP1 and OSP2 are compared and plotted in Fig. 5.6(c). When using the OSP0, satisfactory damage detection results are obtained for elements 10, 11, 13, 22, 41 and 42 with 14.06%, 10.94%, 13.60%, 15.01%, 14.40% and 13.83% stiffness reduction, and the maximum false alarm occurs in element 15 with 5.35% stiffness reduction. This error may be due to the presence of the neighboring damaged elements 11 and 13. When using the OSP1, only the damaged elements 10, 22, and 41 are acceptably identified with 13.90%, 14.21% and 9.98% stiffness reduction, but the identification of the damaged elements 11, 13 and 44 fails. Moreover, three large false alarms in elements 5, 26 and 49 with 4.64%, 5.33% and 4.65 % stiffness reduction are observed. Similar to the damage detection for scenario 1, the poor damage detection for scenario 3 also results from the lack of global structural information measured by OSP1 with only three accelerometers. When using OSP2, the damage detection results are similar to those using OSP0; 12.88%, 11.64%, 12.13%, 15%, 13.26% and 12.63% stiffness reduction are respectively detected for the damaged elements 10, 11, 13, 22, 41 and 42. However, more false alarms are identified in elements 8 (3.36%), 20 (3.34%), 21 (3.60%), 24 (4.84%), 28 (3.82%) and 32 (3.27%). These false alarms indicate that the measurements from the OSP2 are not sensitive enough to damage. The comparison of the damage detection results from OSP0 with those from OSP1 and OSP2 show that the OSP0, which considers the two objectives, can achieve a better sensor placement for better damage detection in the damage scenario 3.

5.3.3.2 The Constrained Case

The damage detection results from the damage scenarios 1 and 2 using the COSP0, COSP1 and COSP2 are compared and plotted in Figs. 5.7(a) and (b), respectively. In the first damage scenario, the COSP0 leads to accurate detection of the damage locations as well as severities in elements 17 and 33, as shown in Fig. 5.7(a). The damage detection results are similar to that using the OSP0. This is because both the COSP0 and OSP0 have 19 common sensors amongst the total 25 sensors. The common sensors are 11 accelerometers (at Nodes 5, 6, 9, 11, 12, 13, 15, 18, 19, 28 and 29), 3 displacement transducers (at Nodes 15,21 and 27) and 5 strain gauges (on elements 6, 7, 11, 14, 16 and 69). When using the COSP1, the identification results are a bit different to those obtained by using OSP1. The difference lies in the slightly worse estimate of stiffness reduction in element 17 and a slightly better estimate of stiffness reduction in element 33. When using the COSP2, it leads to a better identification result compared to OSP2 with the stiffness reduction in elements 17 and 33 identified as 14.09% and 8.25% respectively. Moreover, the number of false alarm is reduced when using the COSP1 and COSP2 compared to those using the OSP1 and OSP2. This may be due to the inclusion of more accelerometers in the constrained case. In the second damage scenario, the damage detection result is plotted in Fig. 5.7(b). Comparing with OSP0, OSP1 and OSP2, a similar pattern is observed for the COSP0, COSP1 and COSP2 for the damage detection, in which all the three optimal sensor configurations can identify the damage locations and damage severity well.

The damage detection results from the damage scenario 3 using the COSP0, COSP1 and COSP2 are also compared and plotted in Fig. 5.7(c). It is observed that all the damage locations are identified accurately and the corresponding damage severities are identified satisfactorily if the COSP0 is used. The COPS0 leads to the best damage identification, while only one big false alarm occurs in element 15 with 5.18% stiffness reduction. The COPS1 leads to a slightly poor damage identification results comparing with those using the COSP0, and three false alarms occur in elements 7, 15, and 20 with 3.20%, 5.53% and 3.40% stiffness reduction respectively. The COPS2 leads to the worst identification results, and several large false alarms occur in elements 20, 21, 24, 28, 32, 36 and 40 with 4.48%, 3.20%, 5.38%, 3.93%, 3.78%, 4.21% and 4.02% stiffness reduction respectively. As a comparison, the performance of the COSP0 and COPS2 are similar with those of the OSP0 and OSP2 respectively, but the performance of the COSP1 shows a better performance than that of OSP1. The COSP1 can outperform OSP1 because a sufficient number of accelerometers are included. This indicates that expert experience is helpful for specifying the numbers of each type of sensors in the constrained optimal placement to achieve a better OSP.

The final damage detection results show that the OSP0 among three sets of OSPs (OP0, OSP1 and OSP2) provides the best quality of damage detection, which demonstrates that the best OSP can be obtained by the utility function with a weighting factor of 0.5. Similar conclusion can be drawn from the constrained case with the other three sets of COSPs (COSP0, COSP1 and COSP2), in which the COSP0 is the best.

For a close inspection on the number of accelerometers, the COSP0, COSP1 or COSP2 has 12 accelerometers, which is more than that in the OSP0 (11) and OSP1 (3), but less than OSP2 (14). It may be concluded from the above observations that a sufficient number of accelerometers is necessary to capture more global structural information for damage detection of the three-dimensional frame structure. It is also noted that the above constrained optimal sensor configurations with a requirement on the number of each type of sensors would not have obvious disadvantages for structural damage detection.

5.4 Discussions

5.4.1 A Knee-Point based Method to Select a "Best" OSP without Prior Knowledge

The multi-objective optimization algorithm-based multi-type sensor placement method often achieves a set of Pareto solutions, and relies on a decision maker to finally select the most desirable solution. However, if the number of Pareto-optimal solutions is large, it may be difficult to pick the "best" solution out of the large set of alternatives. For a specific application, the utility function method may be one of the feasible ways to quantify a decision maker's preference to select a desirable OSP from the Pareto solutions. It is noted that the weighting factor associated with each objective within a utility function is ideal to include information or knowledge of experts. Typically, these weighting factors are not explicitly known or difficult to be assessed by decision makers.

On the other hand, without any knowledge about the user's preferences, the most interesting solutions are the "knees" of the Pareto-optimal front. The importance of the "knees" has been stressed by many researchers (Branke et al. 2004; Deb 2008; Rachmawati and Srinivasan 2009; Jin et al. 2014; Zhang et al. 2015). These knees are mainly characterized by the fact that a small improvement in one objective will cause a large deterioration in the other objective, which makes the movement of the solution in either direction not attractive.

To facilitate the application of the proposed OSP method, the selection of the "best" OSP by identifying the knee of the Pareto front is further investigated here. As a demonstration, the Pareto front in Fig. 5.3 (b) with respect to the constrained OSP case is considered. In the case of only two objectives, the trade-offs in either direction can be approximately estimated through the curvature of the fitting curve of the Pareto front. The fitting curve is plotted in Fig. 5.8 (a). The curvature of each Pareto solution can then be computed through the function of the fitting curve, which is plotted in Fig. 5.8(b). Mathematically, a knee point is a solution located in the Pareto front with the maximum curvature. Thereafter, a sensor configuration named COSP3 with respect to the knee point is determined, showed in Fig. 5.9 (a), and listed in Table 5.4. Compared COSP3 with COSP0, it is found that the COSP3 only has two different sensors. They are an accelerometer at Node 24 in the y-direction and a strain gauge on element 50. The damage detection results using the COSP3 for three damage scenarios are respectively compared with those using COSP0, as shown in Fig. 5.10. The comparative results indicate that both the COSP0 and COSP3 can satisfactorily produce similar damage detection results. Therefore, either the COSP0 determined by the utility function with equal weighting factor or the COSP3 determined through the knee-point-based method is a "best" OSP achieving for better damage detection. Besides, the knee-point-based method for selecting the "best" OSP is more practicable since it does not need any prior information from users.

5.4.2 Comparison with a Fisher information matrix-based OSP Method

Many research efforts have been devoted to the study of OSP for structural damage detection (Shi et al. 2000; Xia and Hao 2000; Zhou et al. 2013; Li et al. 2015), and the Fisher information matrix corresponding to a specific damage index is widely used in determining OSP. In most previous studies, only acceleration responses were measured for the response sensitivity-based damage detection methods. Therefore, the proposed method will be compared with the Fisher information matrix based OSP method for the response sensitive-based damage detection. The Fisher information matrix is defined as $\mathbf{F} = \mathbf{S}_d{}^{\mathrm{T}}\mathbf{S}_d$, where $\mathbf{S}_d = \sum_{i=1}^{\mathrm{n}} \frac{\partial \ddot{\mathbf{z}}(\mathrm{t}_i)}{\partial \boldsymbol{\alpha}}$ is the sensitivity matrix of acceleration responses $\ddot{\mathbf{z}}$ with respect to the damage parameter $\boldsymbol{\alpha}$, t_i denotes a time instant and n is the total number of sampling points in the acceleration time history. To account for the contribution from different DOFs to the Fisher information matrix, an effective independence matrix (Kammer 1991) is defined as $\mathbf{EI} = \mathbf{S}_d \left[\mathbf{S}_d{}^{\mathrm{T}}\mathbf{S}_d\right]^{-1} \mathbf{S}_d{}^{\mathrm{T}}$. The terms on the diagonal elements of the matrix $\mathbf{EI}$ represent the contributions of the corresponding DOFs. For a fair comparison, the same number (25) of accelerometers is used, and the obtained OSP (named as COSP4) is shown in Fig. 5.9 (b) and Table 4. It is noted that many accelerometers with high sensitivity tend to be clustered around the free end of the frame structure.

The measured acceleration responses from the COSP4 are then used for damage detection. The damage detection results for the three damage scenarios are depicted in Fig. 5.11 and compared with those by using the COSP3 which is obtained by the proposed method with the knee-point. For damage scenario 1, the results from the COSP4 show poorer damage quantification of the damaged element 17 (12.18%) compared with that of damaged element 17 (14.85%) using the COSP3, although the identified severities of damaged element 33 are similar by using either the COSP4 or the COSP3. Moreover, one big false alarm occurs in element 25 with 3.16% stiffness reduction when using the COSP4. For damage scenario 2, the result of damage detection using the COSP4 shows poor damage quantification of damaged element 17 (11.43%) compared with that of damaged element 17 (14.62%) using the COSP3, although the identified severities of damaged element 18 are similar by using either the COSP4 or the COSP3. It is also observed that one big false alarm occurs in element 13 with 2.35% stiffness reduction when using the COSP4. For damage scenario 3, the result of damage detection using the COSP4 is significantly worse than that using the COSP3. The damaged elements 10, 11, 13, 22, 41 and 44 are identified with 13.18%, 6.16%, 8.20%, 6.74%, 13.69% and 14.23% stiffness reduction by using the COSP4, where the identified damage severities for the damaged elements 11, 13 and 22 are obviously smaller than the preset 15% stiffness reduction. Moreover, some large false alarms are observed in the undamaged elements 3 (5.64%), 7 (3.91%), 14 (3.85%) and 15 (4.23%). When using the COSP4, the poor identification results from the clustering sensors, and therefore the sensors cannot sufficiently capture the spatial information of the frame structure. This comparison reveals that the proposed OSP method with multi-type sensors could lead to more accurate damage detection than a typical Fisher information matrix based OSP method with single- type of sensor.

5.5 Summary

A new response covariance-based multi-objective multi-type sensor placement method has been proposed in this chapter for damage detection of a structure. It is based on the simultaneous optimization of the response covariance sensitivity and the response independence. An efficient NSGA-II method has been adopted and tailored to solve the multi-objective multi-type sensor optimal placement problem. The feasibility and effectiveness of the proposed method are examined numerically with a three-dimensional frame structure. The numerical results show that the optimization of the proposed SCA-based multi-objective function with the NSGA-II approach can give optimized locations for different types of sensors based on the Pareto-optimal solutions. Satisfactory damage detection results are obtained by using optimal sensor configurations for both the unconstrained and constrained cases. The configurations with the specified number for each type of sensors yield relatively more accurate results in the damage detection. Besides, the selection of a most desirable OSP from the Pareto solutions via the utility function method and the knee-point-based method is investigated. The numerical results indicate that OSP0, COSP0 and COSP3 considering the two objectives can achieve accurate damage detection results. The proposed SCA-based multi-type sensor placement method is feasible and efficient for structural damage detection.

The response covariance-based OSP method proposed in Chapter 4 has been successfully extended for multi-type sensor placement with multi-objective optimization in this chapter. The feasibility and accuracy of the theoretical framework of response covariance-based OSP method and the associated damage detection method have been also assessed through numerical studies. Nevertheless, the experimental studies on the topic are important because the new OSP method and damage detection method should be validated before they are applied to real structures.

Table 5.1 List of structural and material properties

Properties	Value
Young modulus $E\,(\mathrm{N/m^2})$	2.10×10^{11}
Sectional area $A\,(\mathrm{m^2})$	6.597×10^{-5}
Density $\rho\,(Kg/\mathrm{m^3})$	7850
Poisson ratio ν	0.30
Moment of inertia $I_y\,(\mathrm{m^4})$	3.645×10^{-9}
Moment of inertia $I_z\,(\mathrm{m^4})$	3.645×10^{-9}
Moment of inertia $I_p\,(\mathrm{m^4})$	7.290×10^{-9}

Table 5.2 Natural frequencies of the frame structure

Mode number	Frequency (Hz)
1	5.29
2	11.42
3	15.45
4	19.46
5	28.11
6	40.39
7	53.11
8	63.14
9	66.41
10	79.67
11	87.92
12	91.72

Table 5.3 Parameters used in the NSGA-II method

Parameters	Values / operators
Population size of each generation	200
Maximum Number of generation	1000
Selection	Tournament algorithm
Probability of crossover	0.2
Probability of mutation	0.2

Table 5.4 Optimal sensor configurations of the unconstrained and constrain cases

Configuration	Sensor installation location		
	Accelerometers	Displacement transducers	Strain gauges (Element No.)
OSP1	6(y),10(y),29(z)	15(z),21(z), 27(z)	1,6,8,11,14,16,19, 21,27,30,32,39, 43,48,51,60,64, 67,68
OSP2	4(y),6(y),7(z),9(z),11(z),12(y), 13(z),15(z),17(z),18(y),20(y), 26(y),27(z), 29(z)	10(y),15(z), 21(z),24(y), 28(y)	1,6,7,23,37,69
OSP0	5(z),6(y),9(z),11(z),12(y),13(z) ,15(z),18(y),19(z),28(y),29(z)	15(z),21(z), 27(z)	6,7,11,14,15,16, 22,23,27,36,69
COSP1	4(y),9(z),10(y),15(z),17(z), 19(z),20(y),21(z),23(z),25(z), 27(z),29(z)	15(z),21(z), 27(z)	6,7,8,11,14,15,16, 20,22,56
COSP2	5(z),6(y),7(z),9(z),11(z),12(y), 13(z),15(z),17(z),20(y),26(y), 28(y)	15(z),21(z), 27(z)	1,6,13,29,34,44, 45,53,67,69
COSP0	5(z),6(y),9(z),11(z),12(y),13(z) ,15(z),17(z),18(y),19(z),28(y), 29(z)	15(z),21(z), 27(z)	1,6,7,11,14,16,19, 25, 55,69
COSP3	5(z),9(z),11(z),12(y),13(z), 15(z),17(z),18(y),19(z),24(y), 28(y), 29(z)	15(z),21(z), 27(z)	1,6,7,11,14,16,19, 25,50,55
COSP4	7(z),10(z),13(y),13(z),14(y), 16(y),16(z),17(y),18(y),18(z), 19(y),19(z),20(y),21(z),22(y), 22(z),23(y),24(z),25(y),25(z), 26(y),27(z),28(y),28(z),29(y)	null	null

Table 5.5 Parameters for numerical damage detection studies

Damage detection scenario	Scenario 1	Scenario 2	Scenario 3
Damage locations	Elements 17 and 33	Elements 17 and 18	Elements 10,11,13,22,41 and 42
Damage severities	15% and 10%	15% and 10%	15%
Measurement noise	5%	5%	5%
Optimal sensor placement configurations	OSP0, OSP1, OSP2, COSP0, COSP1, COSP2, COSP3 and COSP4		

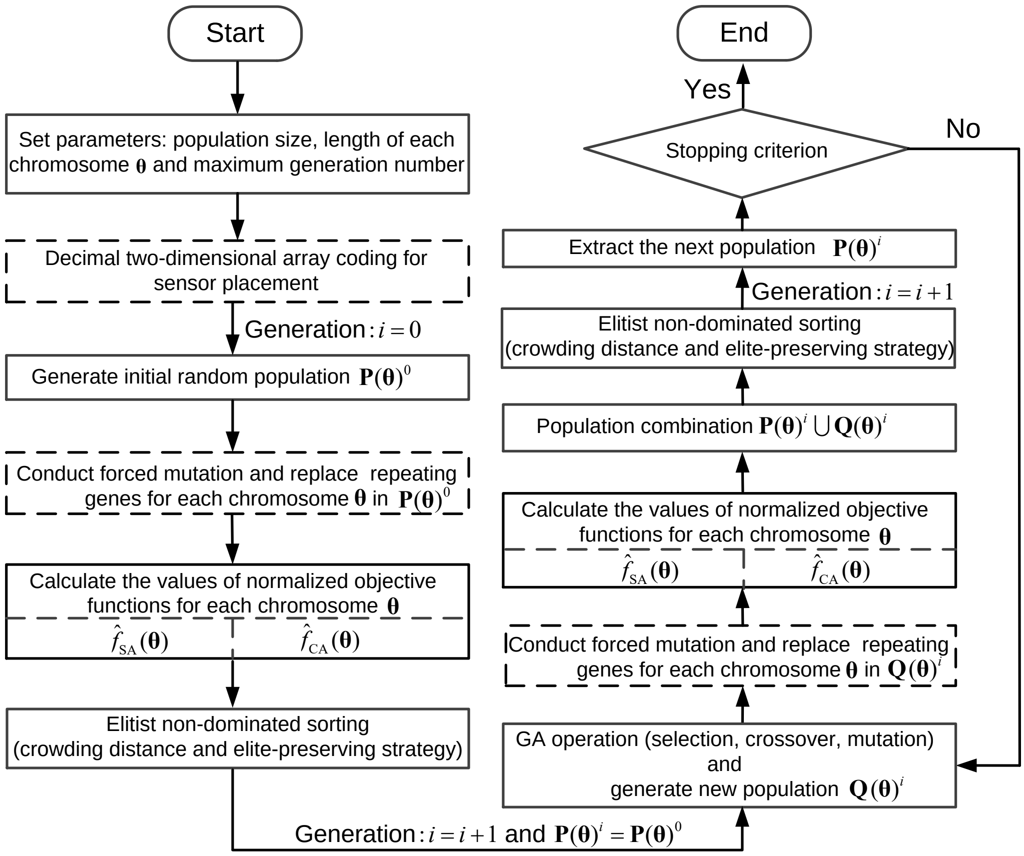

Fig. 5.1 Flowchart of multi-objective multi-type sensor placement using the tailored NSGA-II method

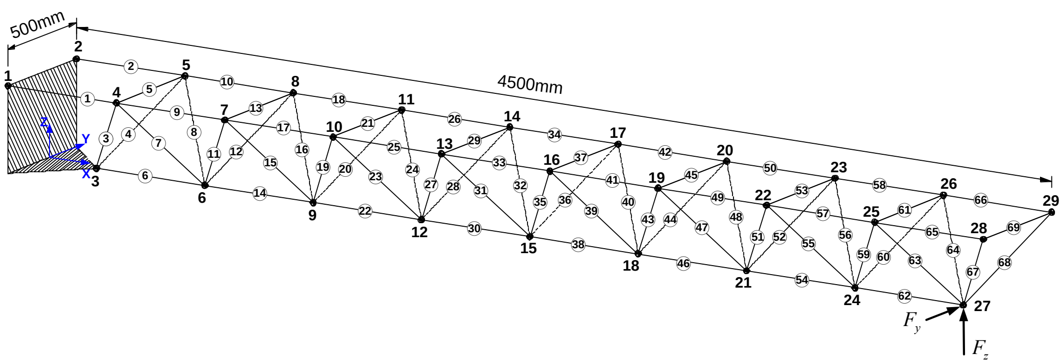

Fig. 5.2 The finite element model of a 9 bays three-dimensional frame structure

(a)

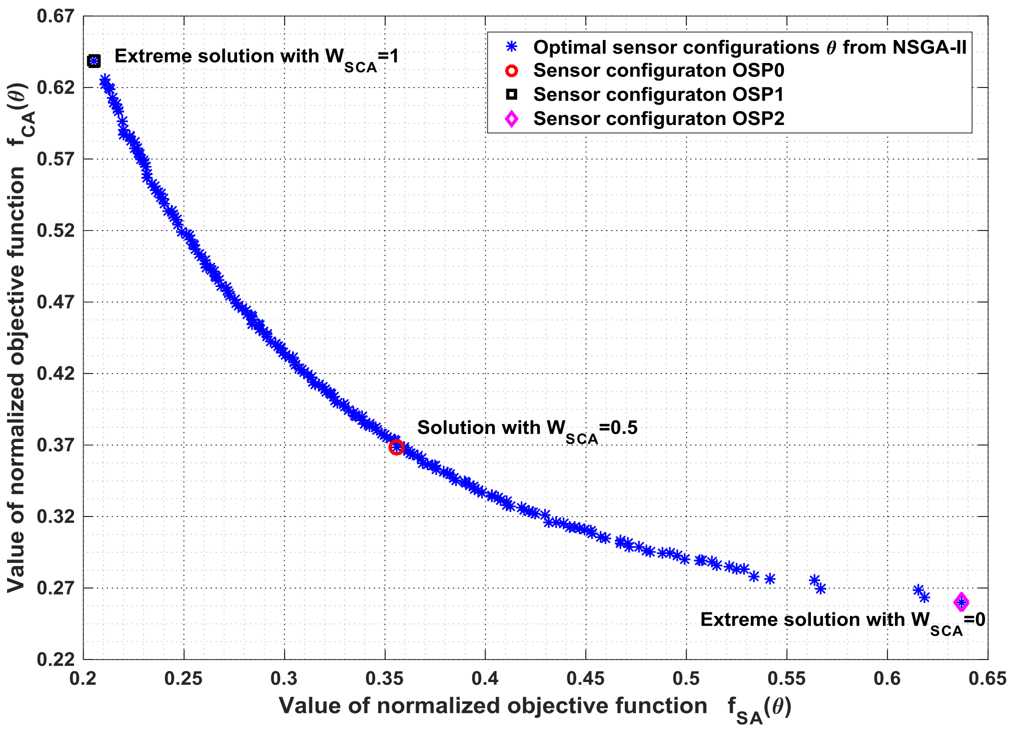

(b)

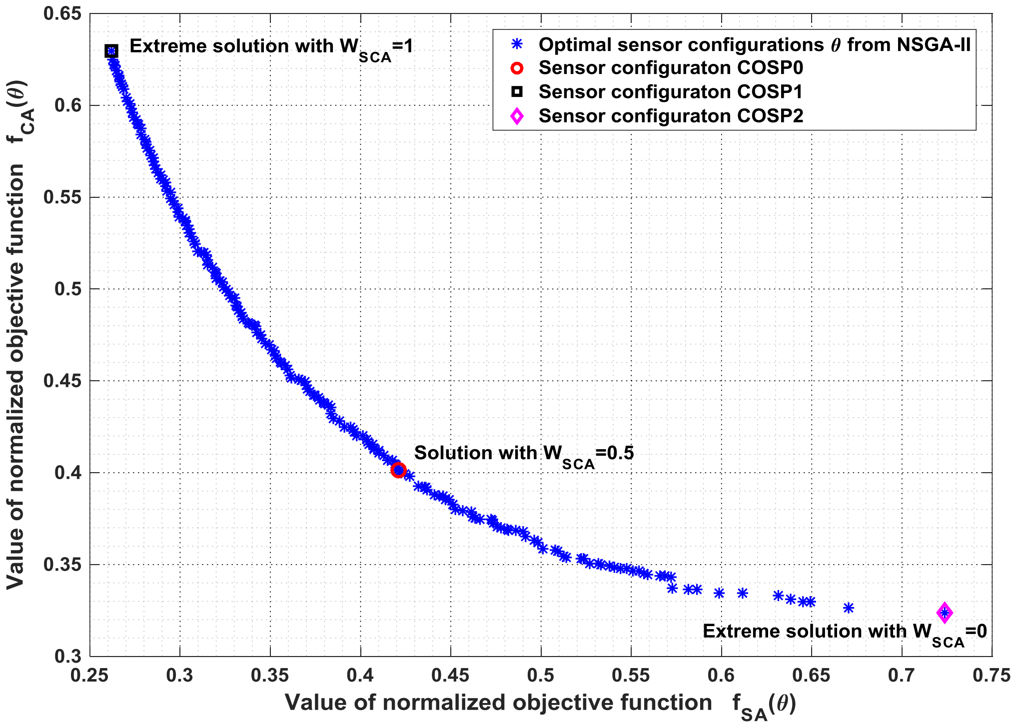

Fig. 5.3 Pareto front of optimal sensor configurations when using the tailored NSGA-II method: (a) optimal sensor placement without constraint; (b) optimal sensor placement with constraint.

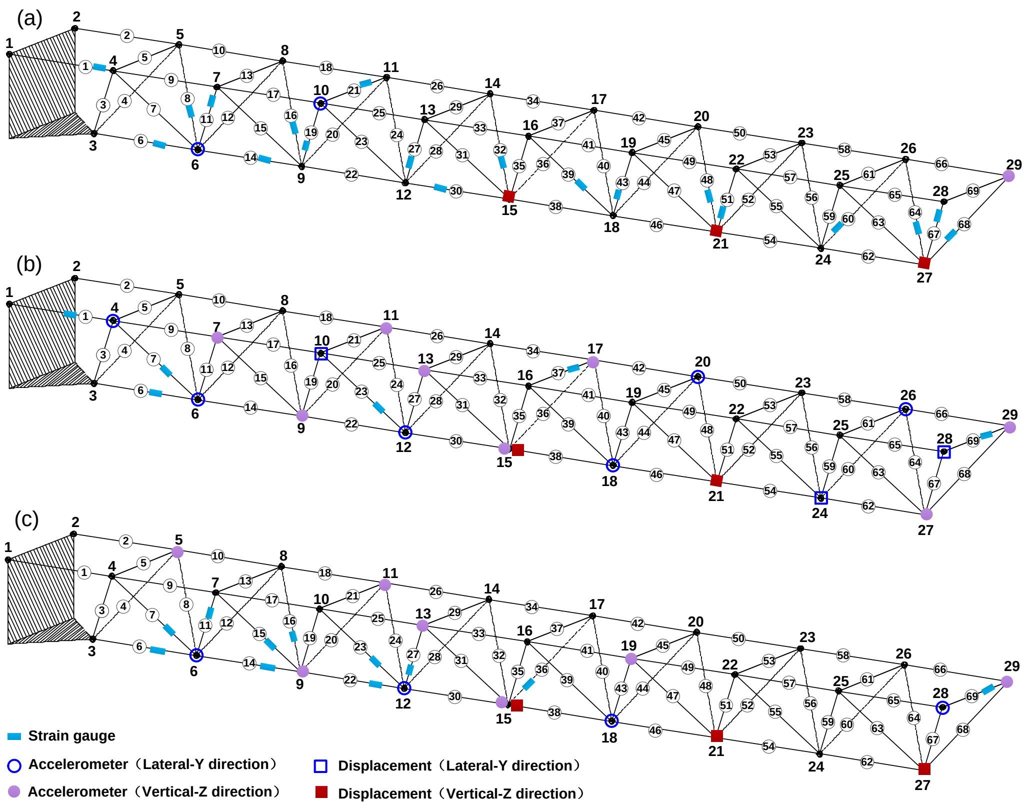

Fig. 5.4 Unconstrained sensor configurations from Pareto front with different weighting factors: (a) OSP1 with weighting factor $w_{\mathrm{SCA}} = 1.0$; (b) OSP2 with weighting factor $w_{\mathrm{SCA}} = 0.0$; (c) OSP0 with weighting factor $w_{\mathrm{SCA}} = 0.5$.

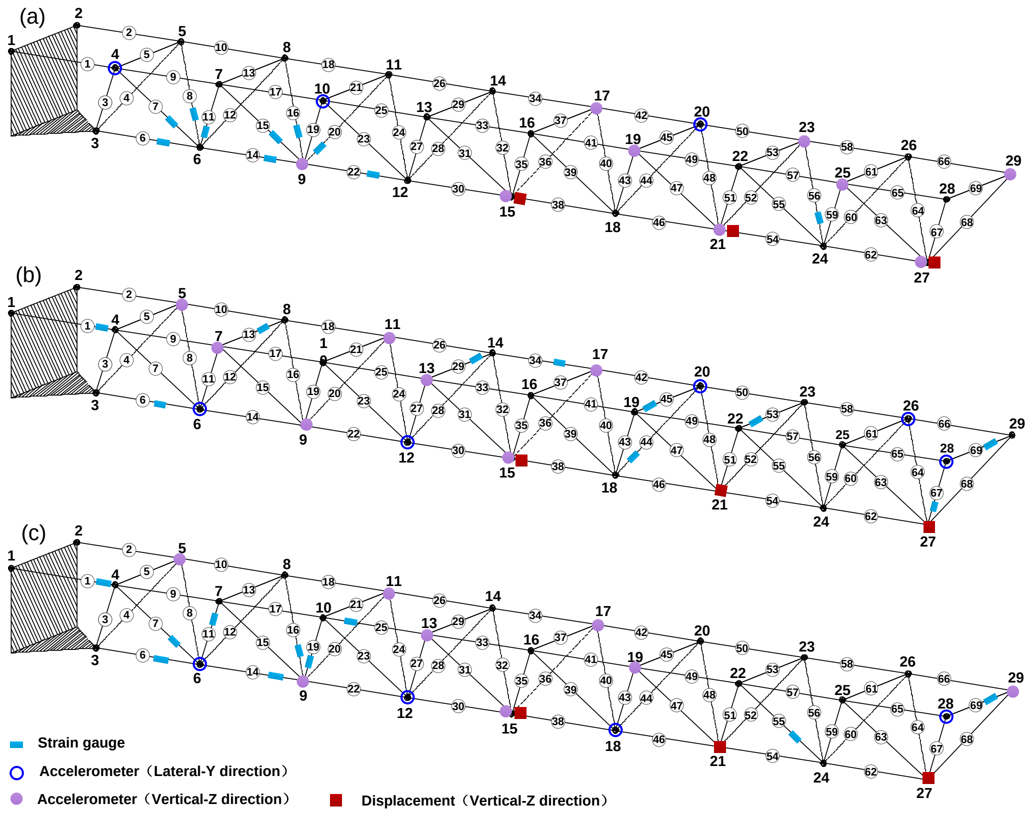

Fig. 5.5 Constrained sensor configurations from Pareto front with different weighting factors: (a) COSP1 with weighting factor $w_{\mathrm{SCA}} = 1.0$; (b) COSP2 with weighting factor $w_{\mathrm{SCA}} = 0.0$; (c) COSP0 with weighting factor $w_{\mathrm{SCA}} = 0.5$.

(a)

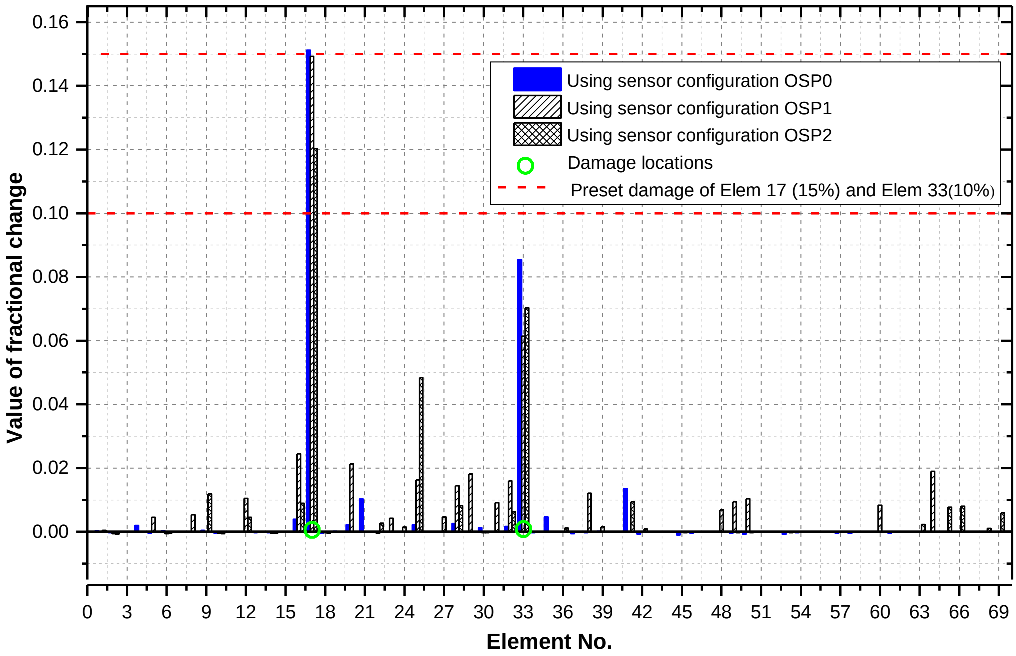
Using sensor configuration OSP0
Using sensor configuration OSP1
Using sensor configuration OSP2
Damage locations
Preset damage of Elem 17 (15%) and Elem 33(10%)
Value of fractional change
Element No.
0.16
0.14
0.12
0.10
0.08
0.06
0.04
0.02
0.00
0 3 6 9 12 15 18 21 24 27 30 33 36 39 42 45 48 51 54 57 60 63 66 69

(b)

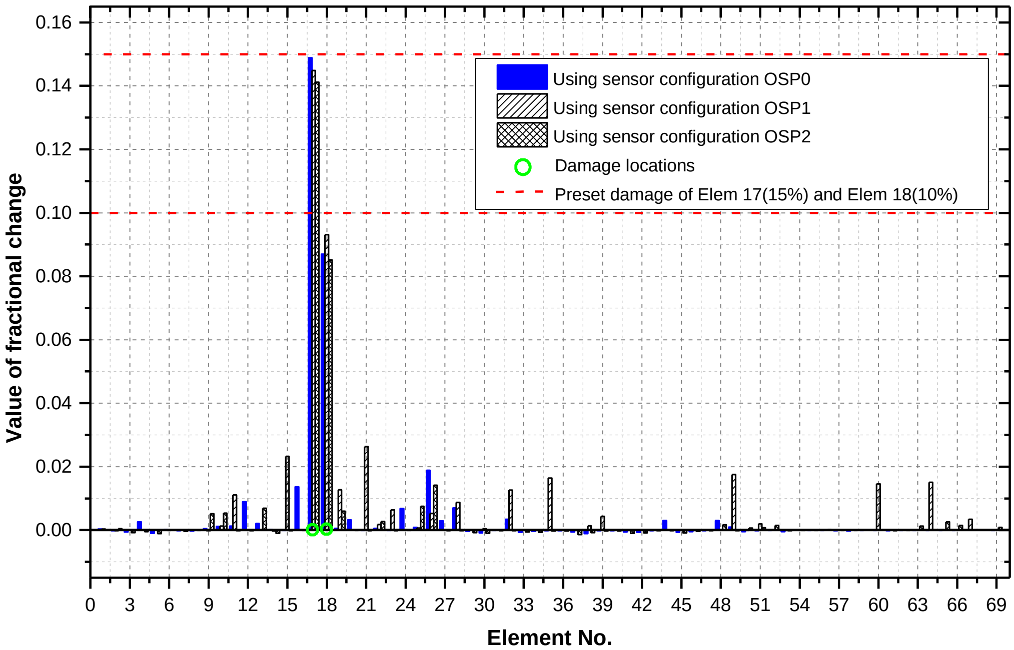
Using sensor configuration OSP0
Using sensor configuration OSP1
Using sensor configuration OSP2
Damage locations
Preset damage of Elem 17(15%) and Elem 18(10%)
Value of fractional change
Element No.
0.16
0.14
0.12
0.10
0.08
0.06
0.04
0.02
0.00
0 3 6 9 12 15 18 21 24 27 30 33 36 39 42 45 48 51 54 57 60 63 66 69

(c)

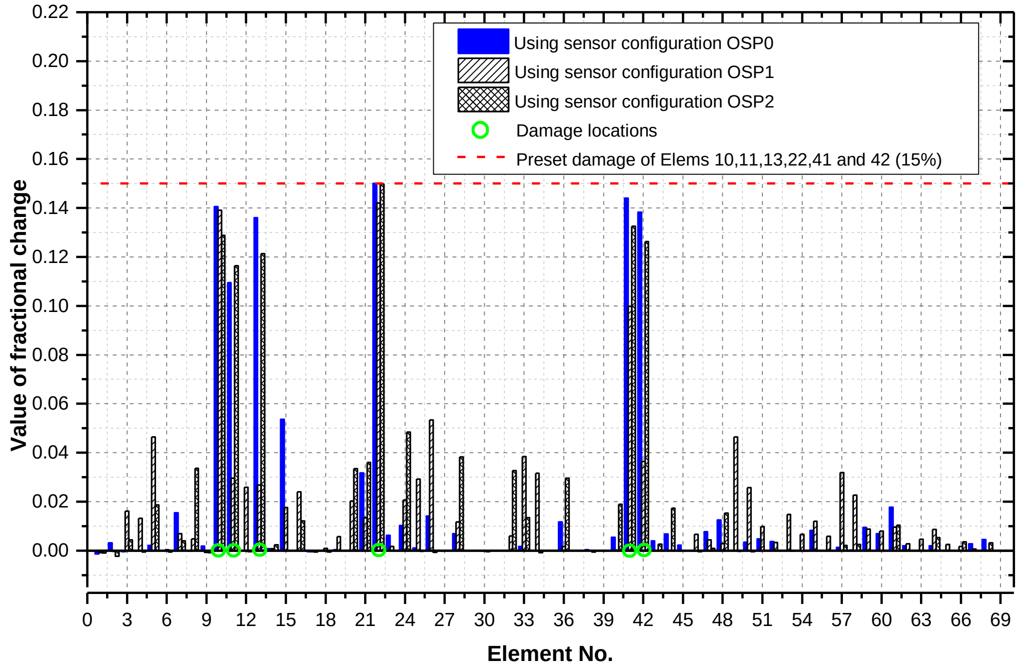

Fig. 5.6 Damage detection using unconstrained sensor configurations with different weighting factors: (a) damage scenario 1; (b) damage scenario 2; (c) damage scenario 3.

(a)

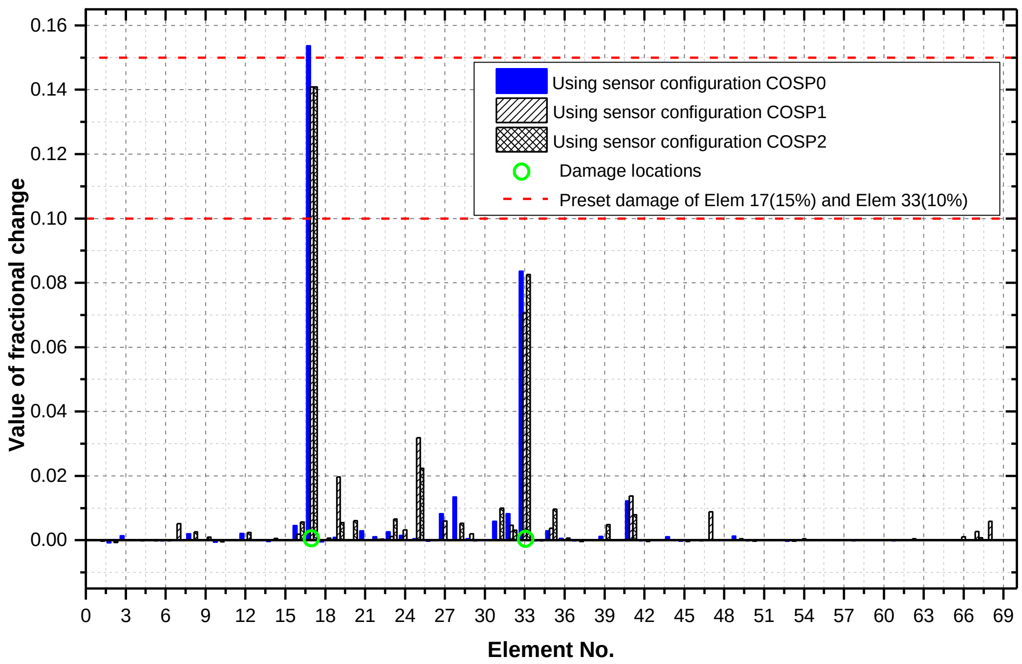
Value of fractional change
Element No.
Using sensor configuration COSP0
Using sensor configuration COSP1
Using sensor configuration COSP2
Damage locations
Preset damage of Elem 17(15%) and Elem 33(10%)

(b)

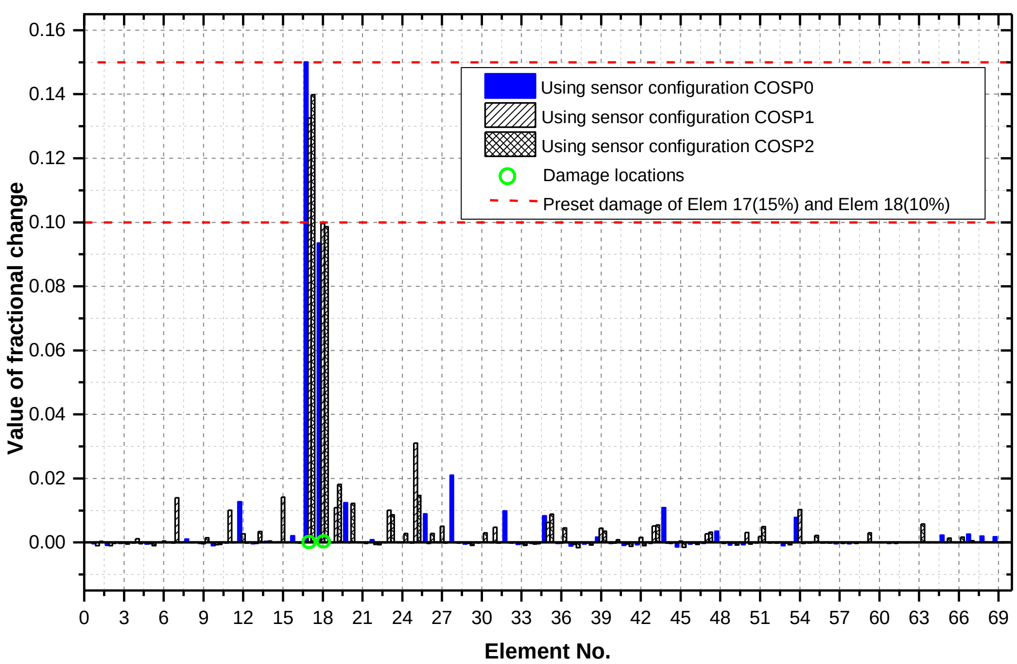
Value of fractional change
Element No.
Using sensor configuration COSP0
Using sensor configuration COSP1
Using sensor configuration COSP2
Damage locations
Preset damage of Elem 17(15%) and Elem 18(10%)

(c)

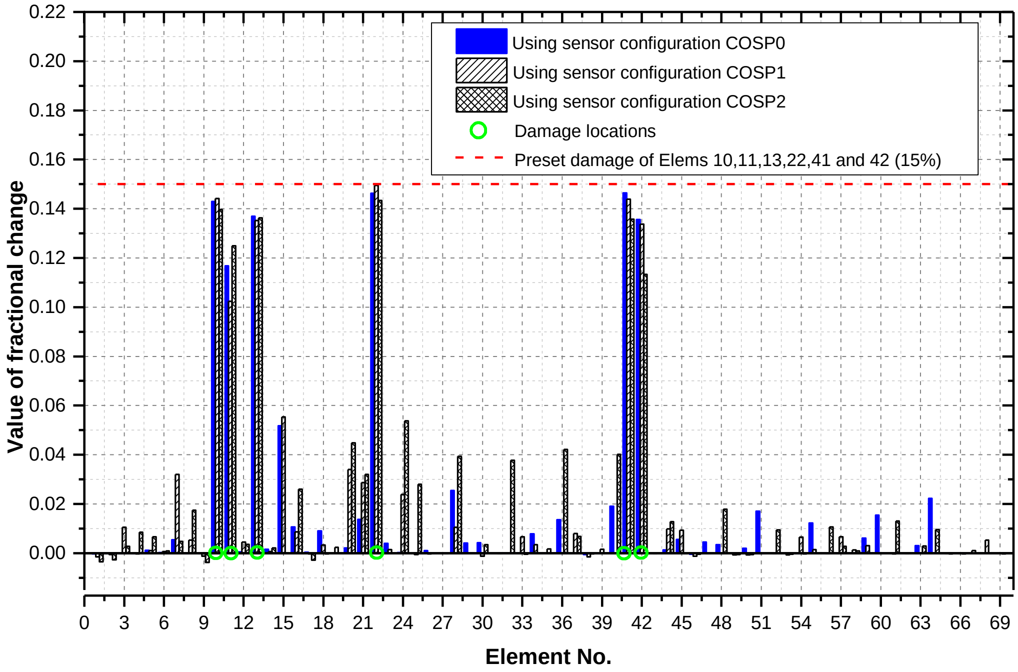

Fig. 5.7 Damage detection using constrained sensor configurations with different weighting factors: (a)damage scenario 1; (b)damage scenario 2; (c)damage scenario 3.

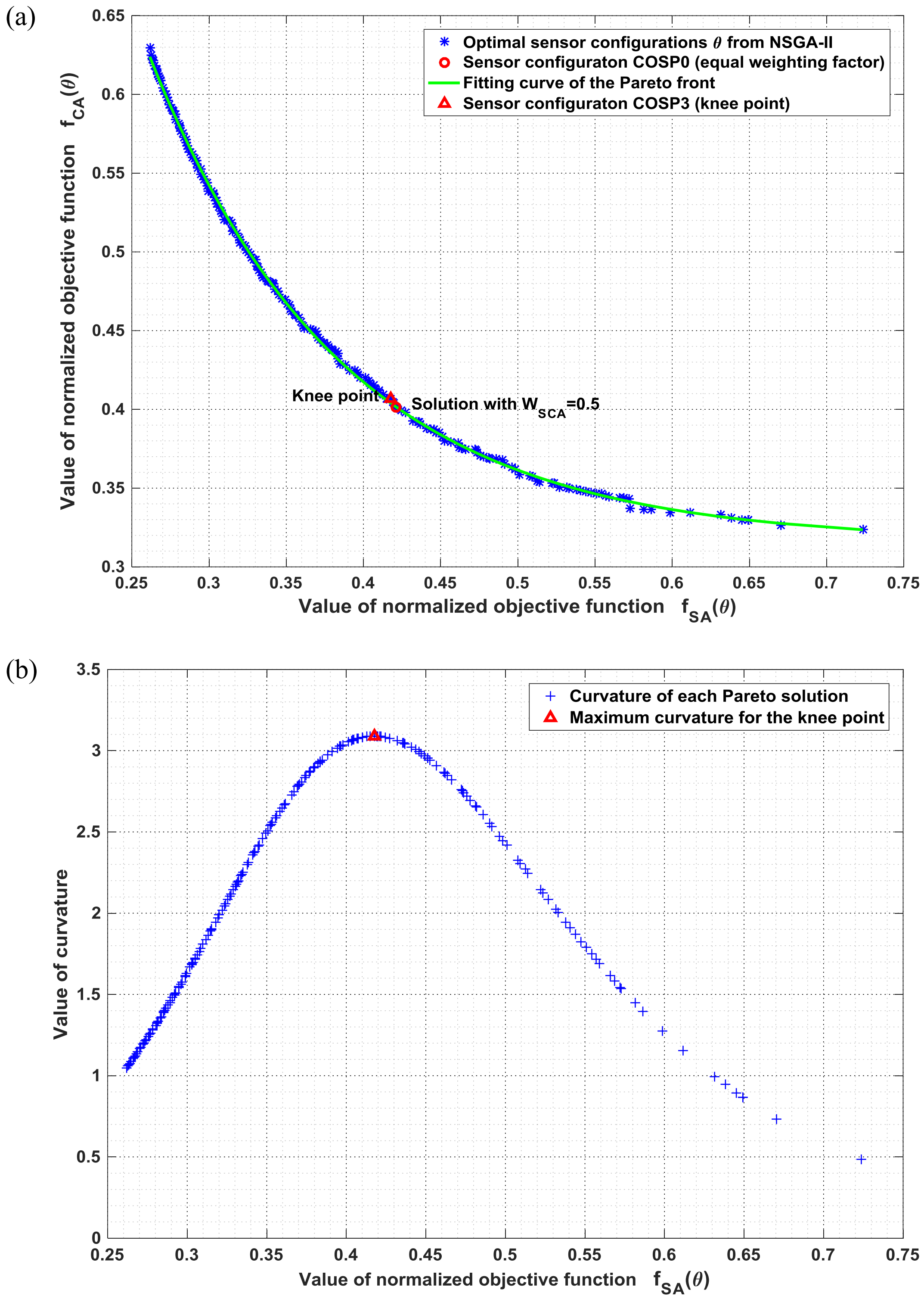

Fig. 5.8 The "best" OSP with respect to the knee point of the Pareto front: (a) the fitting curve of the Pareto front and the knee point; (b) the curvature of the Pareto solutions.

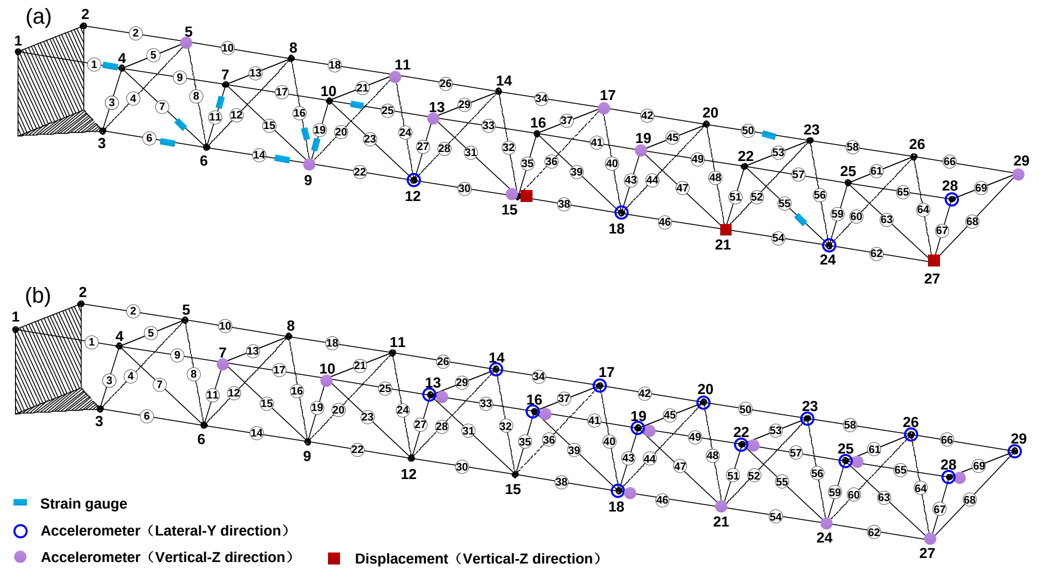

Fig. 5.9 The “best” optimal sensor configurations selected from different methods: (a) the configuration COSP3; (b) the configuration COSP4.

(a)

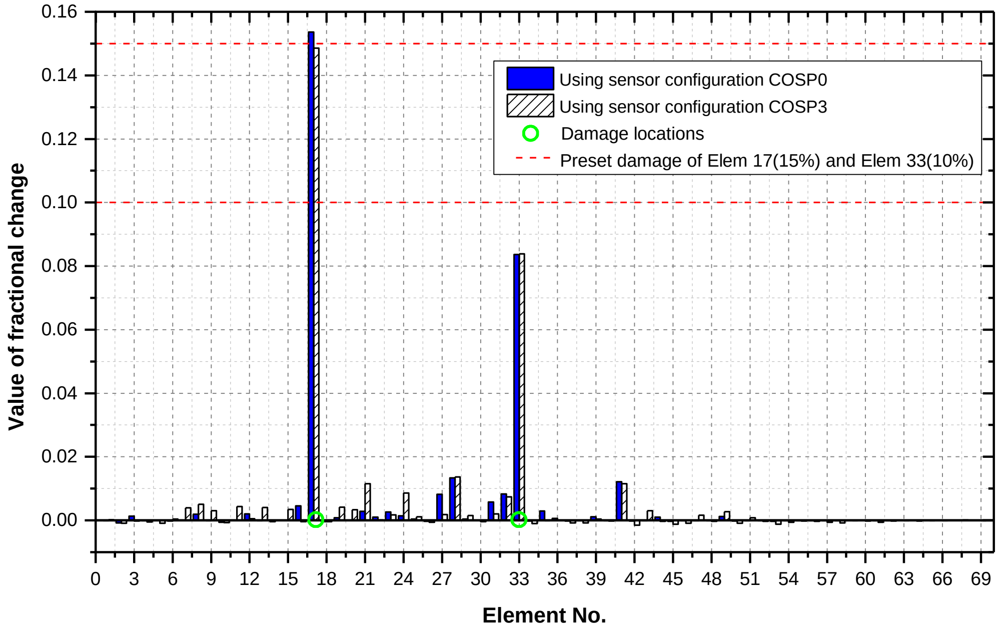

Using sensor configuration COSP0
Using sensor configuration COSP3
Damage locations
Preset damage of Elem 17(15%) and Elem 33(10%)
Value of fractional change
Element No.

(b)

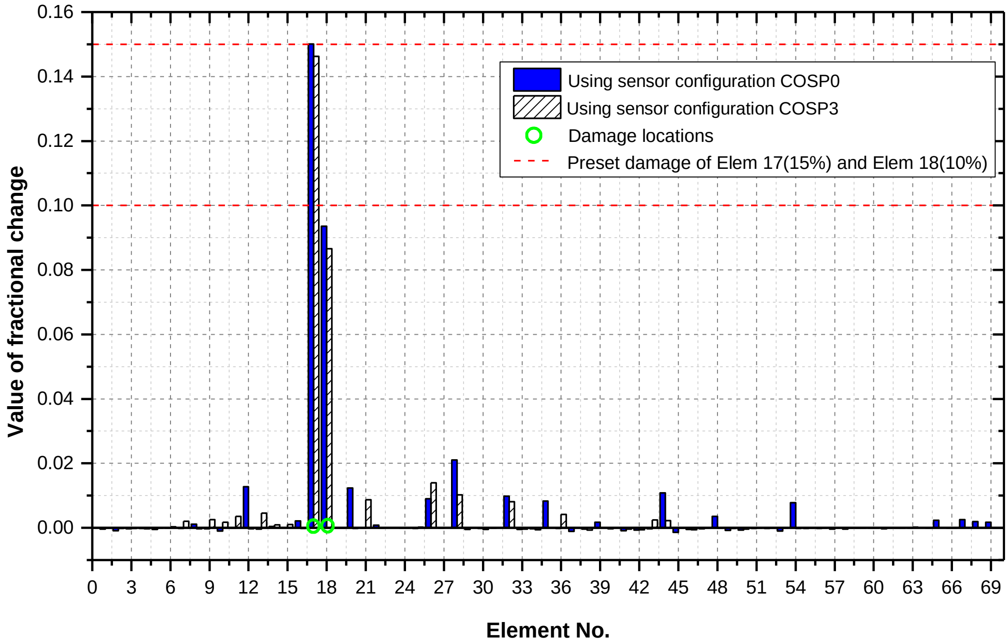

Using sensor configuration COSP0
Using sensor configuration COSP3
Damage locations
Preset damage of Elem 17(15%) and Elem 18(10%)
Value of fractional change
Element No.

(c)

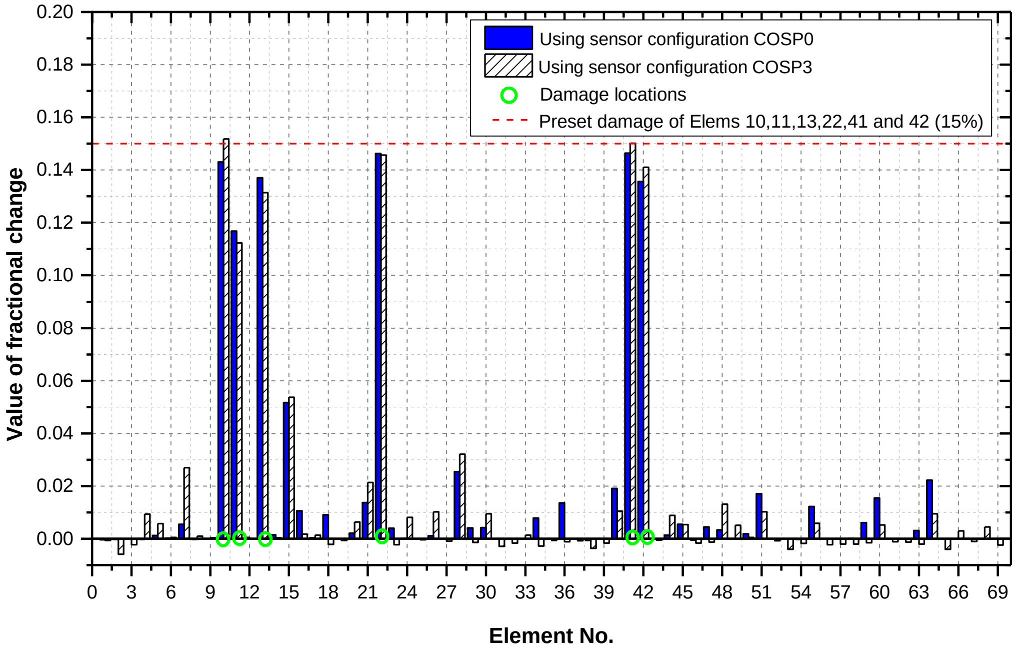

Fig. 5.10 Comparison of damage detection using optimal sensor configurations COSP0 and COSP3: (a) damage scenario 1; (b) damage scenario 2; (c) damage scenario 3.

(a)

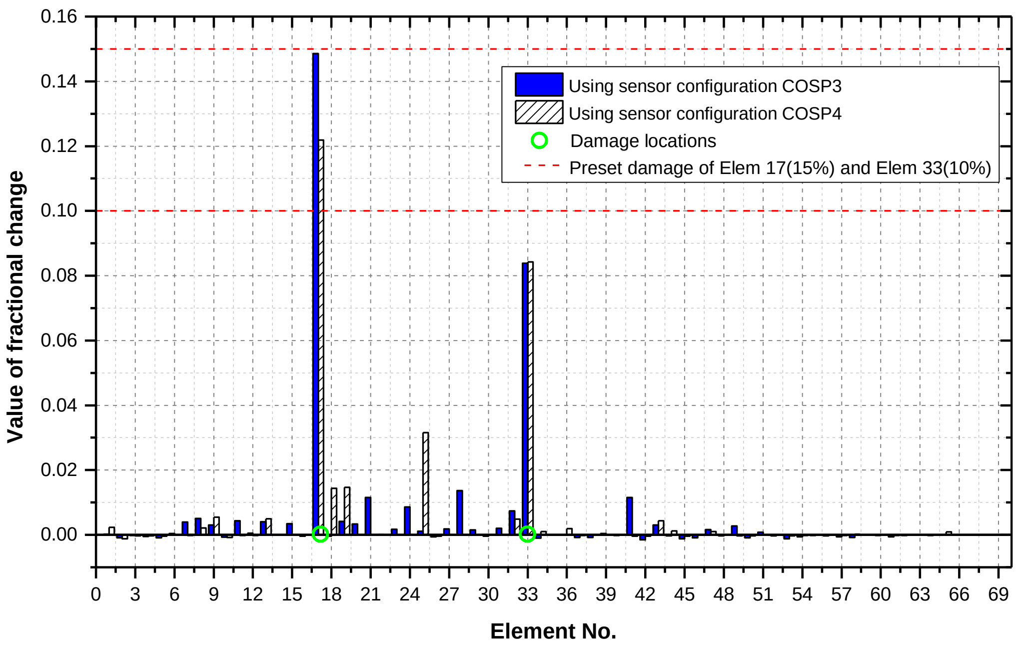

Value of fractional change
Element No.
Using sensor configuration COSP3
Using sensor configuration COSP4
Damage locations
Preset damage of Elem 17(15%) and Elem 33(10%)

(b)

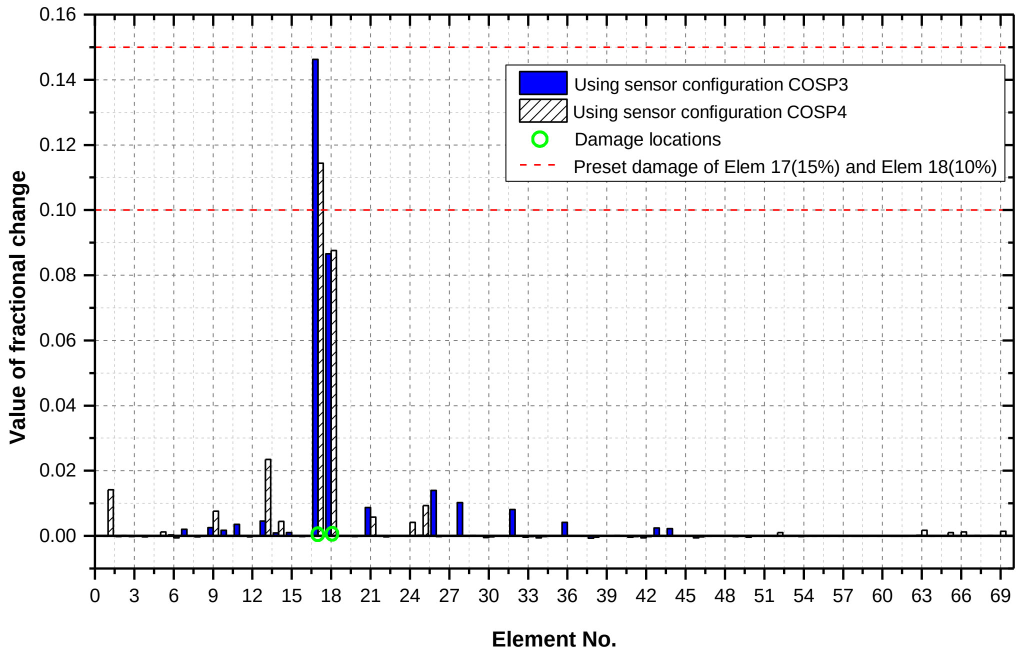

Value of fractional change
Element No.
Using sensor configuration COSP3
Using sensor configuration COSP4
Damage locations
Preset damage of Elem 17(15%) and Elem 18(10%)

(c)

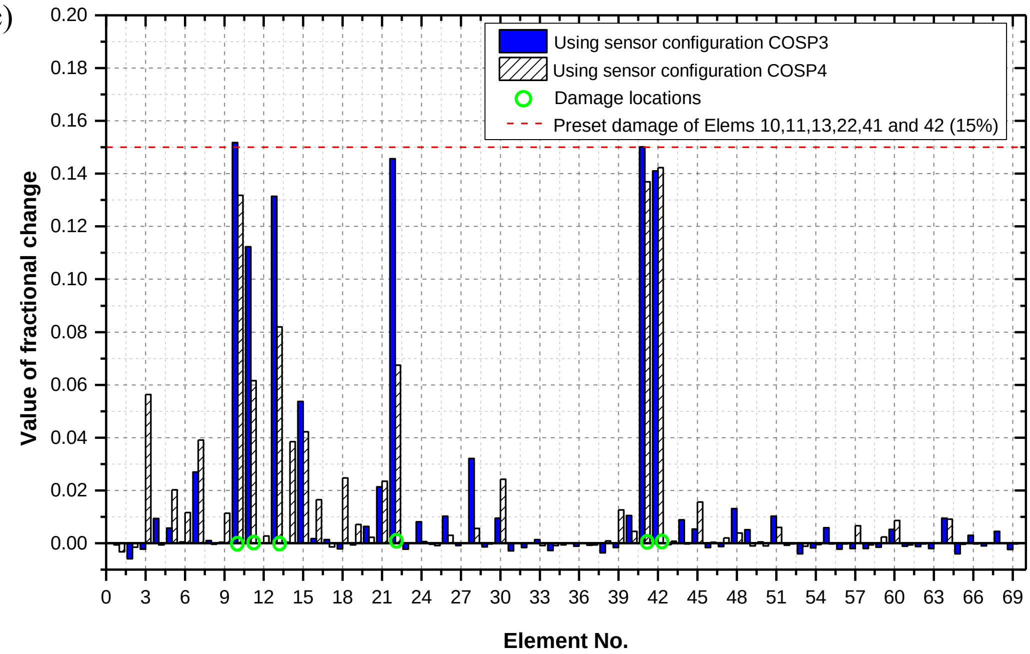

Fig. 5.11 Comparison of damage detection using optimal sensor configurations COSP3 and COSP4: (a) damage scenario 1; (b) damage scenario 2; (c) damage scenario 3.

CHAPTER 6

EXPERIMENTAL INVESTIGATION ON MULTI-OBJECTIVE MULTI-TYPE SENSOR OPTIMAL PLACEMENT FOR STRUCTURAL DAMAGE DETECTION

6.1 Introduction

This chapter is an extension of the theoretical study in Chapter 5 on the damage detection-oriented multi-type sensor placement with multi-objective optimization and the numerical study on a nine-bay three-dimensional frame structure. In the numerical study of the frame structure, the performance of damage detection was compared between optimal multi-type sensors configuration (denote as COSP3) and optimal accelerometer only configuration (denote as COSP4) with the same number of sensors under three different damage scenarios. The numerical results showed that the proposed OSP method with multi-type sensors could lead to more accurate damage detection than the Fisher information matrix-based OSP method with single-type of accelerometers. Nevertheless, most studies of OSP, including one in Chapter 5, are theoretical or numerical studies. Experimental studies on the topic are also important because the new OSP methods should be validated before they are applied to real structures. Therefore, this chapter aims to perform an experimental investigation using a nine-bay three-dimensional frame structure to validate the proposed response covariance-based multi-objective multi-type sensor optimal placement method for damage detection. Following this section, Section 6.2 describes the experimental set-up in detail. Section 6.3 presents the experimental results and discusses the feasibility and effectiveness of the proposed OSP method for structural damage detection. A summary of the works presented in this chapter is given in Section 6.4.

6.2 Experimental Set-Up

6.2.1 Laboratory Model of a Nine-Bay Steel-Frame Structure

A nine-bay three-dimensional frame structure was constructed in the Structural Dynamics Laboratory of The Hong Kong Polytechnic University using the Meroform M12 construction system. This physical model and the whole experimental setup are shown in Fig. 6.1(a). The structure orientates horizontally and is fixed to a rigid concrete support through its three end nodes (see Fig. 6.1 (b)). The concrete support is heavy and rigid compared with the frame structure, and it is held down to the strong floor of the laboratory with four steel bolts. The frame structure consists of 69 alloy steel tubes (500 mm length, 22 mm outer diameter, and 0.5 mm thickness) jointed by 29 standard Meroform ball nodes (see Fig. 6.1 (c)). Each tube is fitted with a screwed end connector which clamps the tube by means of an internal compression fitting. When these tubes are tightened into the nodes, all the connection bolts are tightened with the same torsional moment (30 Nm) to avoid asymmetry of the structure. The weight of the Meroform ball node and the screwed end connector are 234 g and 74 g, respectively.

Two input forces are applied at the free end of the frame structure in the lateral (y) direction and vertical (z) direction, respectively. These forces are generated by using two exciters as shown in Fig. 6.1(d). The exciter LDS V406 M4-CE applies the force in the y-direction, and the exciter JZK-5 applies the force in the z-direction. Each of the exciters is connected to the structure through a soft spring so that the exciter impacts force to the spring first and then to the structure. To measure the direct input forces to the structure (interface force between the spring and structure), two force transducers (B & K 8201) are attached between the structure and the spring, as shown in Fig. 6.1(e). The force transducer is a uniaxial transducer which can only measure the force in the axial direction. Therefore, the effect of additional stiffness from a spring only in the axial direction for the frame structure can be excluded in the measured interface force along the axis of the spring. Moreover, the additional stiffness from a spring in the lateral direction is often much smaller than that in the axial direction, which is neglected in this study.

6.2.2 Optimal Sensor Placement

To perform the proposed OSP, the finite element (FE) model of the frame structure described in Chapter 5 is established (see Fig. 5.2). Moreover, the proposed OSP needs to know the input forces and their acting locations on the structure (see, Fig. 6.1 (a)). In the current OSP study, the input forces are white noise excitations with the same acting locations as those in the experiment. Although the white noise excitations are not exactly consistent with the forces in the experiment, the locations of the inputs forces often determine the number of stimulated modes of a structure and affect the characteristic of the structural responses more significantly than the magnitude of the input forces. Under the white noise excitation assumption, the proposed method is used to determine OSP for experimental study of damage detection.

The total number of sensors installed on the frame structure is 25 which is sufficient for damage detection in this study. This conclusion comes from the companion numerical study presented in Chapter 5 and in the reference (Lin et al. 2018). In the numerical study, the total number of the sensors was decided based on the principle of using the minimum number of sensors but guaranteeing enough accuracy of structural damage detection. The 25 sensors are selected from 121 candidate locations when 12 accelerometers, 3 displacement transducers, and 10 strain gauges are allocated according to an optimal sensor configuration. By using the same FE model of the 3D frame structure, the proposed multi-objective multi-type sensor placement with constraint or without constraint on the number of each type of sensors was investigated numerically in Chapter 5. The numerical results showed that the appropriate constraint on the number of each type of sensors helps to reduce the search space in the optimization and therefore achieves the better performance for damage detection. The COSP0 (see Fig. 5.5 (c)) in Chapter 5 used in this chapter is the constrained case and the constraints are found based on the numbers of sensors in the unconstrained OSP0 case, which was obtained by using the utility function with an equal weighting factor.

6.2.3 Instrumentation and Implementation

The major instruments for the laboratory test are depicted in Fig. 6.2, and their arrangements are introduced here. Fig. 6.2 (a) and (b) show two damaged beam elements for the subsequent damage detection studies and a torque wrench used for the installation of the beams for the frame structure. According to the selected COSP0, three types of sensors (see, Fig. 6.2 (c) – 6.2 (e)) are installed to measure acceleration, displacement, and strain for the subsequent damage detection. They include twelve accelerometers (eight B & K 4370 accelerometers, three B & K 4382 accelerometers, and one KD 1010 accelerometer installed in structure with the sequence of No.1 to No.12), three LK-503 laser displacement transducers, and ten BFH120-3AA (23) strain gauges. To launch a vibration test, the signal generator (B & K 3160-B-022, see Fig. 6.2(f)) firstly offers a narrow-bandwidth (0 - 40 Hz) white noise excitation signal (signal level 300 mVrms). This signal is passed through a three-way connector (see Fig. 6.2(g)) and synchronously sent to two power amplifiers (LDS PA 500L and YE5871, see Fig. 6.2(h)). The power amplifiers work, respectively, with the two exciters to generate random forces together. To quantify a gain factor for each power amplifier, a gain factor label with 36 divisions in a circle (see Fig. 6.2(i)) is designed for the control of the magnitude of the force. Accordingly, the acceleration, displacement, strain responses of the excited frame structure, and input forces are measured, and then they are amplified by charge amplifiers (KD5008C, see Fig. 6.2(j)). Finally, all the measured responses and two input forces are collected by the data logger (Kyowa EXD-100A, see Fig. 6.2(k)). The responses and the input forces are sampled at 500 Hz over the time duration of 60 s with zero initial condition.

Additionally, the responses are passed through a band-pass filter of 2 - 40 Hz before the subsequent utilization, since the applied excitation bandwidth only covers the first six modes of the structure.

6.2.4 Finite Element Model Updating

The FE model of the frame structure established before is used to represent the intact state of the structure for the subsequent damage detection studies. However, some modeling errors may occur due to the uncertainties of the modeling parameters and some ideal assumptions (Friswell et al. 2001; Mottershead et al. 2011). In this study, the modeling errors may come from two sources: (1) The uncertainties of the material and geometric parameters of the steel tube; (2) The lump mass assumption at nodes for the weight of the Meroform balls, bolts, sensors and electric wires. The initial material properties and the total lump mass at each node are listed in the second column of Table 6.1. It is noticed that the additional weight of the sensors and electric wires and their locations are determined after the installation of sensors. Therefore, the model updating is conducted after OSP. These modeling errors usually lead to some discrepancy for the structure responses between analytical predictions and test results. The discrepancy due to the inaccurate FE model may, furthermore, result in the failure of damage detection or some false alarms. To refine the FE model, a two-step updating is successively conducted before damage detection. The objective functions for the two-step updating are the relative errors of the natural frequencies and the structural responses, and they are expressed as follows:

$$J_1 = \sum_{i=1}^{6} \frac{\left\| \omega_i^a - \omega_i^m \right\|_2}{\left\| \omega_i^m \right\|_2} \tag{6.1}$$

$$J_2 = \sum_{i=1}^{s} \frac{\left\| \mathbf{y}_i^a - \mathbf{y}_i^m \right\|_2}{\left\| \mathbf{y}_i^m \right\|_2} \tag{6.2}$$

where J_1 and J_2 are the objective functions in the first and second step of updating, respectively; the ω_i^a and ω_i^m are the i^{th} analytical and measured natural frequency;

$\mathbf{y}_i^a$ and $\mathbf{y}_i^m$ are the responses from the i^{th} sensor; and the operator $\|\bullet\|_2$ denotes the 2-norm of a vector.

In the first step of updating, 32 parameters are selected to be tuned, including the elastic modulus E, material density ρ, the outer diameter of the alloy steel tube D, and 29 lumped mass at all the nodes. With the use of Eq. (6.1), these selected parameters of the FE model are adjusted to reduce residuals of natural frequencies between the measurement set and the corresponding model predictions. In the second step of updating, the first six modal damping ratios $\xi_1 \sim \xi_6$ are tuned to refine the amplitudes of the calculated structural responses, by using Eq. (6.2). The parameters after being updated are listed in the third column of Table 6.1. As a result, the analytical frequencies and the structural responses computed by the FE model can achieve a good coincidence with those from experimental measurement. The measured and analytical natural frequencies (before and after updating) are compared in Table 6.2, which demonstrates a good agreement between them. The comparison between all measured and computed responses in the time domain and frequency domain is also conducted. In Figs. 6.3 – 6.4, three responses (acceleration, displacement, and strain) from three types of sensors are selected to graphically exhibit the consistency between the measured and computed responses. A similar observation can be found for other responses except for the strain response of Element 69. Further investigation found that the amplitude of this strain response is small (the maximum amplitude is about 2 $\mu\varepsilon$) with poor signal-to-noise ratio, which is easily contaminated by the environmental interruption. So, the measured strain response of Element 69 is excluded in the damage detection studies. The updated FE model now could be more accurate to represent the intact structure for the subsequent damage detection.

6.2.5 Damage Scenarios

The structural damage detection will be performed using the optimal sensor placement. Before the introduction of the damage scenarios, the manufacture of damaged beam elements and the calculation of equivalent damage severity are described. In this study, the mock-up damage is a weakened segment in the middle of a beam, which is produced by grinding away a layer of material from the surface of the beam, as shown in Fig. 6.5. The damage level, quantified by a certain percentage of equivalent stiffness reduction, is embodied by the geometric dimension change of a beam. An algorithm is provided in Appendix B for relating the geometric dimension change of a beam to a certain percentage of equivalent stiffness reduction. For a prescribed percentage of tensile stiffness reduction and bending stiffness reduction, the outer diameter and length of a weakened part can be designed by using Eq. (B3) in Appendix B in two steps: (1) a suitable reduction in outer diameter is selected and fixed as a constant (such as, 0.5mm); (2) the grinding length works as a variable which is selected to yield an equivalent stiffness reduction close to the prescribed value. Specifically, an approximate 10% stiffness reduction is equivalent to a reduction of 0.5 mm in outer diameter of a beam and a grinding length of 150 mm along the beam; an approximate 15% stiffness reduction is equivalent to a reduction of 0.5 mm in outer diameter of a beam and a grinding length of 250 mm along the beam. The 10% and 15% stiffness reductions and the calculated geometric changes are summarized in Table 6.4. To verify the feasibility and effectiveness of the proposed method, three damage scenarios are designed and introduced to the frame structure, namely, (1) one beam damaged, (2) two paralleled beams with different levels of damage, and (3) two longitudinally aligned beams with different levels of damage. The two damaged beams are shown in Fig. 6.2 (a). The one with larger damage is used in Scenario (1), and both are used in Scenarios (2) - (3).

The three damage scenarios characterized by the above damage levels and the specific locations in the experiment are listed in Table 6.5. In the first scenario, the defect with 15% stiffness reduction happens to a longitudinal beam near the support

(Element 17). In the second scenario, defects happen to two paralleled beams close to the support of the structure (Elements 17 and 18). Elements 17 and 18 have 15% and 10% stiffness reduction, respectively. In the third scenario, defects happen to two longitudinally aligned beams (Elements 17 and 33). The Element 17 is 15% stiffness reduction while the damaged Element 33 at mid-span of the structure is 10% stiffness reduction. For the above three damage scenarios, the local damages are introduced into the test structure by replacing the related intact members with the damaged ones. After the replacement, all the connection bolts should be tightened with the same torsional moment (30 Nm) by using the torque wrench (see Fig. 6.2(b)) such that the connection of the structure keeps the same condition before and after damaged. Considering the safety of the structure, the power amplifiers take different gain factors for different damage scenarios. In each scenario, two suitable gain factors (Gain factor 1 and 2) are specifically tuned for the related power amplifiers, and their values can refer to Table 6.5. The damage detection results for the above three damage scenarios will be presented in the next section.

6.3 Experimental Results and Discussions

6.3.1 Results Using the Optimal Sensor Placement

The damage detection studies on the frame structure under the prescribed three damage scenarios are conducted by using the sensor configuration COSP0. The input forces are measured for damage detection. As an example, the two input forces measured from the 7^{th} to 17^{th} seconds for the damage scenario one are plotted in Figs. 6.6 and 6.7, which are measured in the lateral (y) and vertical (z) directions respectively. Since the input forces are the interface forces between the structure and the springs, some peaks are observed in their spectrums as shown in Fig. 6.6(b) and Fig. 6.7(b). In other word, these forces are not the ideal white noise excitations. For other damage scenarios, the signal generator offers the same random excitation signal (signal level 300 mVrms) but the amplitudes of the two forces are tuned by two gain factors of the power amplifiers. Therefore, the measured forces for other damage scenarios are similar, and they are not shown one by one here.

After the damage occurs, three types of recorded responses from the 7^{th} to 17^{th} seconds are used for damage detection. The unknown damages are detected by solving Eq. (4), and the identified results are presented in Fig. 6.8. The damage detection results of the first scenario are illustrated in Fig. 6.8(a). The use of sensor placement COSP0 leads to the accurate detection of the damage location and severity in Element 17. The identified damage severity of Element 17 is 14.6 % which is close to the preset 15% equivalent damage. Meanwhile, two relatively large false alarms are also identified in Elements 9 and 26 with incorrect stiffness reduction of 4.5% and 3.6%, respectively. Further examination on Fig. 6.5 reveals that the false alarm in Elements 9 is because it is adjacent to the damaged element. The false alarm in Element 26 may result from the model error and the measurement noise. The damage detection results of the second scenario are illustrated in Fig. 6.8(b). Both the damage locations for Elements 17 and 18 are accurately detected. The stiffness reduction in Elements 17 and 18 are satisfactorily identified as 16.6% (i.e. 16.6% > 15%) and 8.2% (i.e. 8.2% < 10%) with minor discrepancies from the preset values. These discrepancies could be caused by the manufacturing error of damages or the computation error of the damage detection algorithm. Additionally, some relatively large false alarms are observed in Elements 9, 10, 26, and 38 with the maximum one occurring in Element 9 (4.6% incorrect stiffness reduction). The identification errors may also be induced by the model error as well as the measurement noise. Finally, the damage detection results of the third scenario are illustrated in Fig. 6.8(c), which are still acceptable. The damaged Elements 17 and 33 are identified with 16.1% and 7.6% stiffness reduction, while the largest false alarm is 6.2% stiffness reduction occurring in Element 9. Under different damage scenarios with different damage locations and severities, the damage detection results have demonstrated that the proposed method not only can identify the damage locations accurately, but also can estimate the damage severities satisfactorily. Although several false alarms are found, their identified damage severities are obviously smaller than those of real damages. Therefore, it could be concluded that the proposed method is feasible and effective for damage detection when using the optimal sensor configuration COSP0.

6.3.2 Results Using the Non-optimal Sensor Placement

As a comparison, two non-optimal sensor configurations are used for damage detection to verify the effectiveness of the optimal sensor placement. The two non-optimal sensor configurations are Non-OSP1 (see, Fig. 6.9(a)) and Non-OSP2 (see Fig. 6.9(b)). Non-OSP1 is obtained on the basis of COSP0 by relocating two displacement transducers. They are moved from Nodes 15 and 21 to Nodes 9 and 18 respectively without changing measurement direction. Non-OSP2 is obtained on the basis of Non-OSP1 by changing four more accelerometers for their measurement location and/or direction: the accelerometers at Nodes 13 and 17 are, respectively, moved to Nodes 16 and 14, and their measurement direction are also changed from vertical to lateral direction; the measurement direction of the accelerometer at Node 15 is changed from vertical to lateral direction; one accelerometer is moved from Node 29 to Node 23.

The damage detectability of the COSP0, Non-OSP1 and Non-OSP2 is compared in the third damage scenario, and the corresponding damage detection results are shown in Fig. 6.10. When using the Non-OSP1, the stiffness reductions in Elements 17 and 33 are identified as 15.5% and 5.5% respectively. Compared with the detection result using COSP0, the difference lies in the worse estimate of stiffness reduction in Element 33 and three new large false alarms occurred in Elements 18, 19 and 22. The adoption of placement Non-OSP2 leads to the worst identification results among the three sensor placements. Although the stiffness reduction in Elements 17 is still identified as 11.8%, but the identification of stiffness reduction in Elements 33 fails. Meanwhile many large false alarms are observed, and the largest one is found in Element 22 with 32.9% incorrect stiffness reduction. The poor damage identification and the large false alarms result from the non-optimal sensor placement which is less sensitive to the local damages. The comparison revealed that arbitrary sensor placement cannot provide reliable damage detection results and even may lead to the failure of damage identification.

6.4 Summary

The proposed multi-objective multi-type sensor optimal placement method for damage detection has been experimentally investigated in this chapter. This OSP simultaneously optimizes the response covariance sensitivity and response independence to ensure the identifiability of local damage in a structure. Three different damage scenarios have been designed to examine the proposed OSP method on a three-dimensional frame structure. The experimental results showed that accurate damage localization and satisfactory damage quantification could be yielded by using the selected optimal multi-type sensor placement (COSP0). It can be concluded that the proposed OSP is feasible and effective for damage detection. Furthermore, the optimal and non-optimal sensor placements (COSP0, Non-OSP1 and Non-OSP2) for damage detection are also compared. The comparison revealed that the various types of sensors with optimal placement are essential to provide most informative data on a structure and guarantee the success of damage detection.

The proposed covariance-based multi-type sensor placement method and the associated damage detection methods have been successfully applied to a three-dimensional frame structure experimentally in this chapter. However, when they are applied to large civil structures, a few major difficulties will be encountered. The global stiffness matrix, modal parameters, and dynamic responses are less sensitive to local damage of a large structure compared with a small structure. The one-stage damage detection in Chapters 3 and 4 is inaccurate and sometimes impossible due to too many unknown damage parameters and seriously ill-conditioned inversed problem for a large structure. Therefore, a covariance-based multi-stage damage detection strategy incorporating with a multi-scale finite element (FE) model for the damage detection of a large structure will be further investigated in Chapter 7.

Table 6.1 Initial and updated parameters of the frame structure

Updating Parameters	Initial value	Updated value
Young modulus E (Pa)	2.10×10^{11}	2.11×10^{11}
Density $\rho(Kg/\mathrm{m}^3)$	7850	7860
Outer diameter D (mm)	22	22
Added lump mass at the nodes from 1~ 29 (g)	282.1, 282.1, 378.3, 474.5,545.1, 593.2, 474.5, 474.5, 593.2,474.5, 545.1, 593.2, 545.1, 474.5,593.2, 474.5, 545.1, 558.6, 510.5,474.5; 522.6, 474.5, 474.5, 522.6,474.5, 474.5, 614.2, 414.3, 420.6	282.1, 282.1, 378.3, 474.5,545.1, 593.2, 654.5, 654.5, 593.2, 704.5, 775.1, 593.2, 755.1, 684.5, 593.2, 704.5, 775.1, 558.6, 690.5, 654.5; 542.6, 474.5, 474.5, 522.6, 324.5, 324.5, 364.2, 264.3, 270.6
Damping ratios $\xi_1 \sim \xi_6$ (%)	0.35, 0.23, 0.38, 0.13, 0.34, 0.14	0.35, 0.92, 0.38, 0.26, 0.17, 0.56

Table 6.2 Measured and analytical natural frequencies

Mode number	Measured (Hz)	Before updating		After updating	
		Analytical (Hz)	Error (%)	Analytical (Hz)	Error (%)
1	5.20	5.29	1.73	5.27	1.35
2	11.84	11.42	-3.55	11.81	-0.25
3	15.16	15.45	1.91	15.13	-0.20
4	20.0	19.46	-2.70	19.96	-0.20
5	27.22	28.11	3.27	27.13	-0.33
6	39.24	40.39	2.93	39.27	0.08

Fig. 6.1 The physical model of the nine-bay frame structure and experimental setup: (a) The nine-bay frame installed with two exciters; (b) The rigid concrete support; (c) The alloy steel tube and Meroform ball; (d) Two exciters LDS V406 M4-CE & JZK-5; (e) The springs and B & K force transducers.

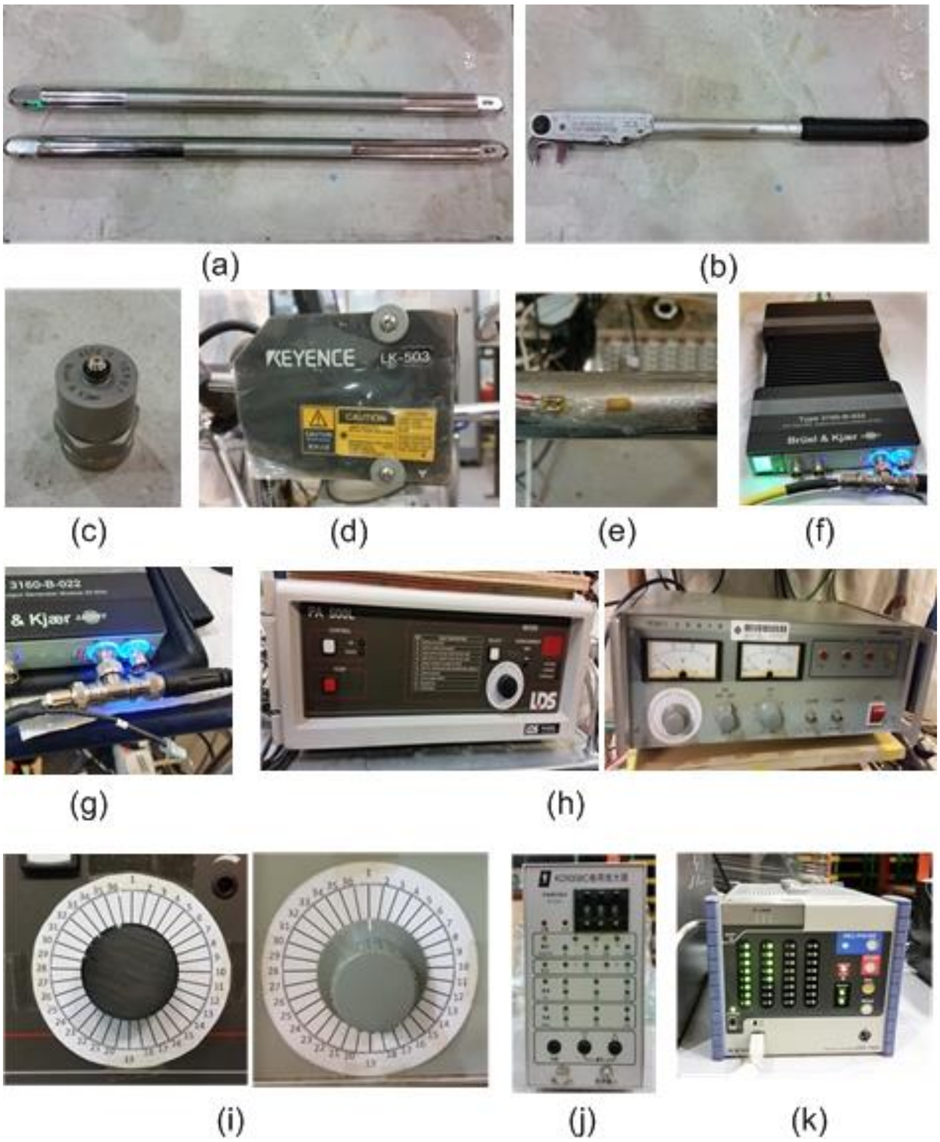

Fig. 6.2 The damaged beams and experimental instruments: (a) The damaged beam elements; (b) Torque wrench; (c) Accelerometer; (d) Laser displacement transducer; (e) Strain gauge; (f) B & K signal generator; (g) Three-way connector; (h) Power amplifiers LDS PA 500L and YE5871; (i) Gain factor labels for the power amplifiers; (j) Charge amplifier; (k) Kyowa data logger.

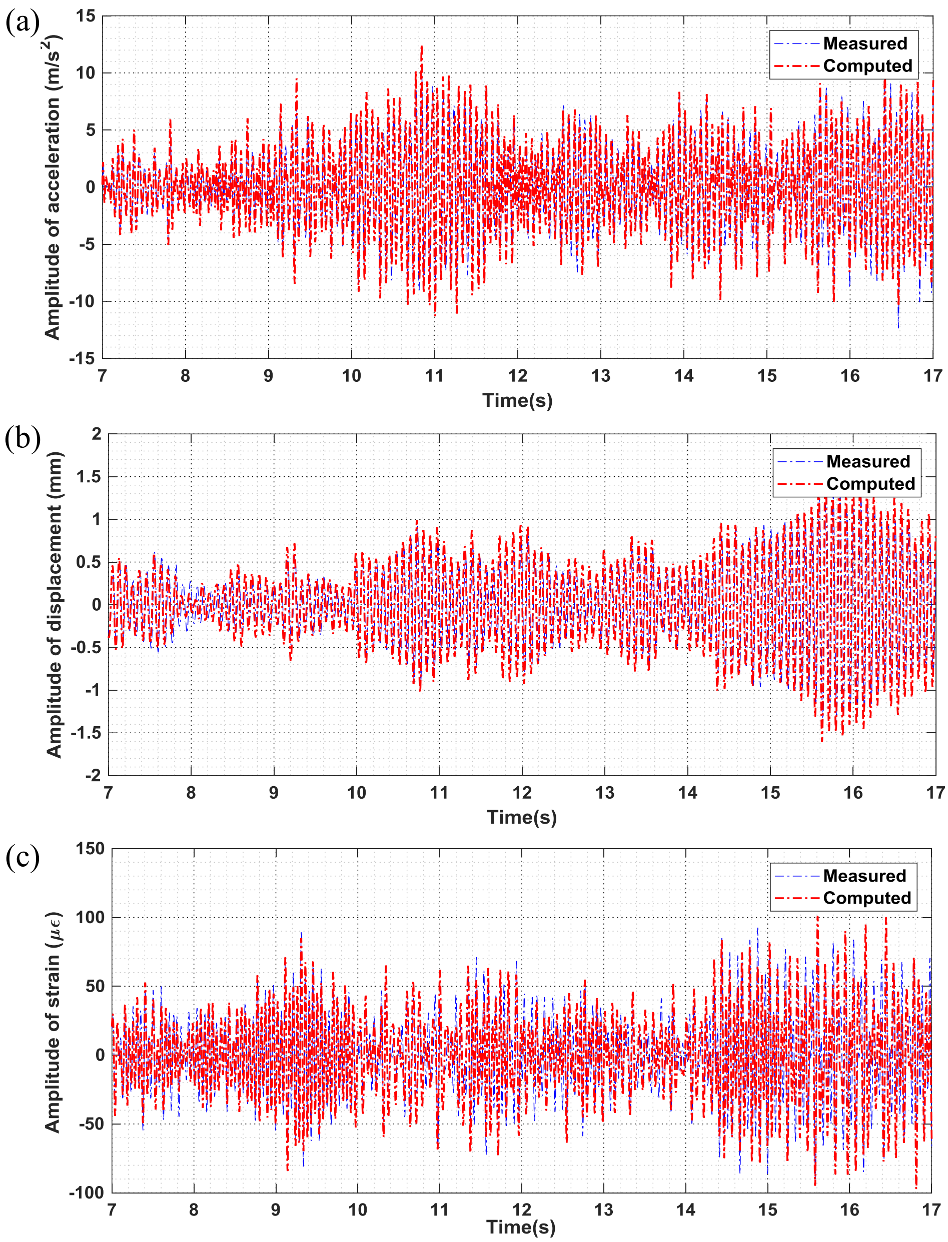

Fig. 6.3 The comparison of measured and computed responses of the structure after model updating: (a) The acceleration response at Node 28 in y-direction; (b) The displacement response at Node 21 in z-direction; (c)The strain response on Element 1.

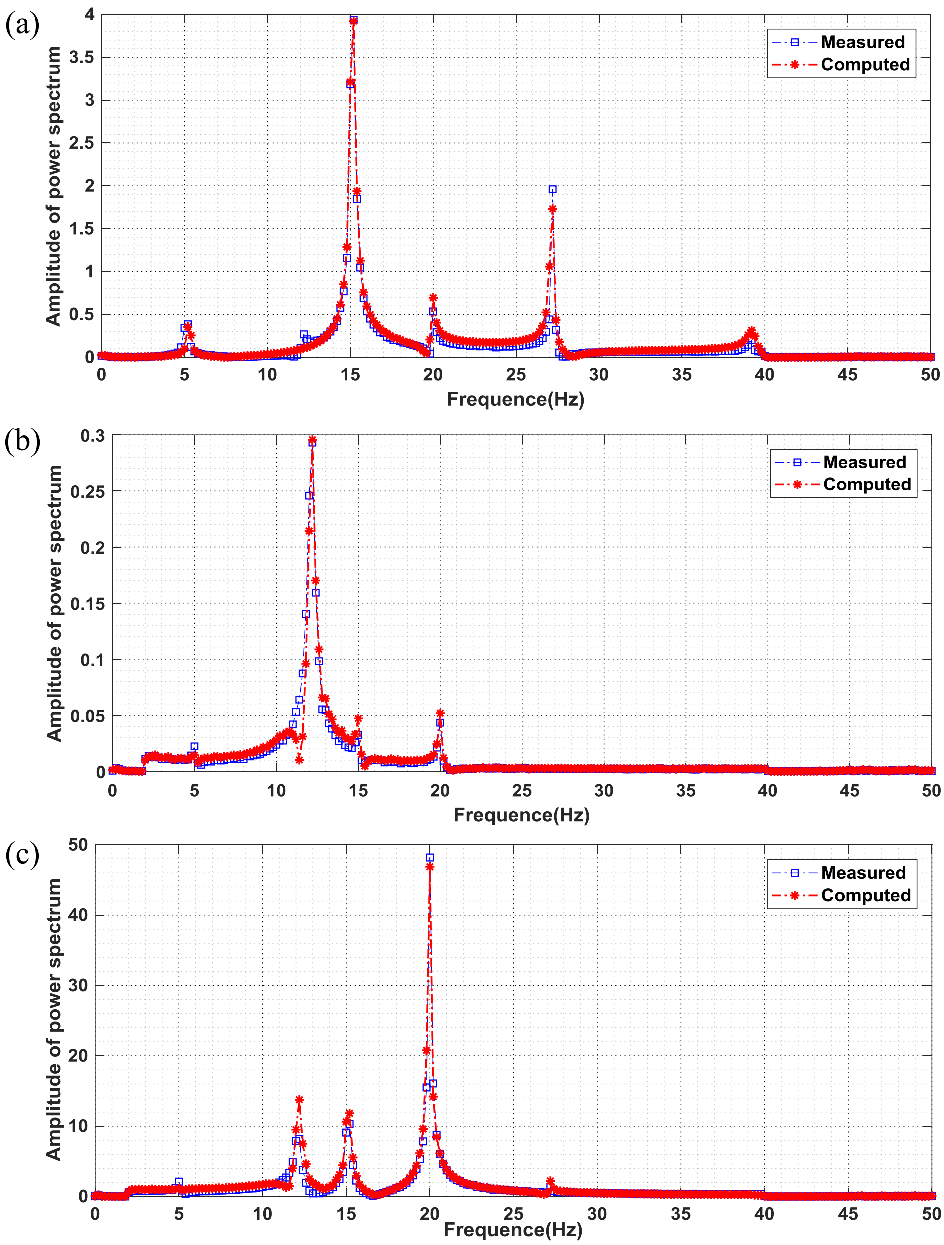

Fig. 6.4 The comparison of power spectrums of measured and computed responses after model updating: (a) The acceleration response at Node 28 in y-direction; (b)The displacement response at Node 21 in z-direction; (c)The strain response on Element 1.

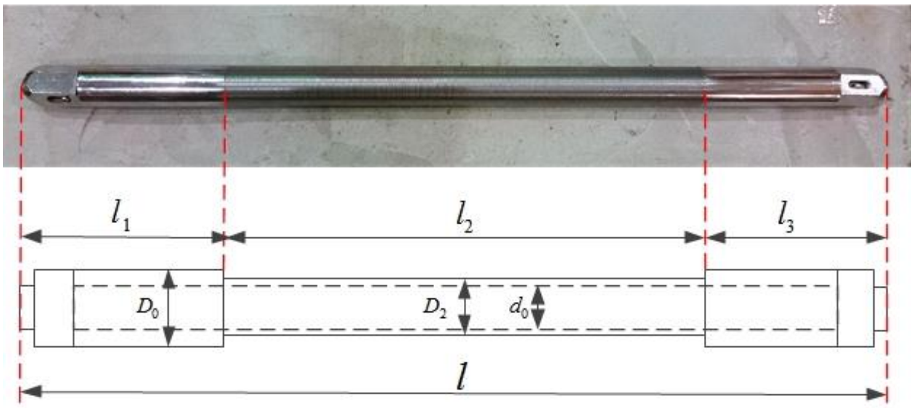

Fig. 6.5 The damaged beam element of the frame structure for damage detection

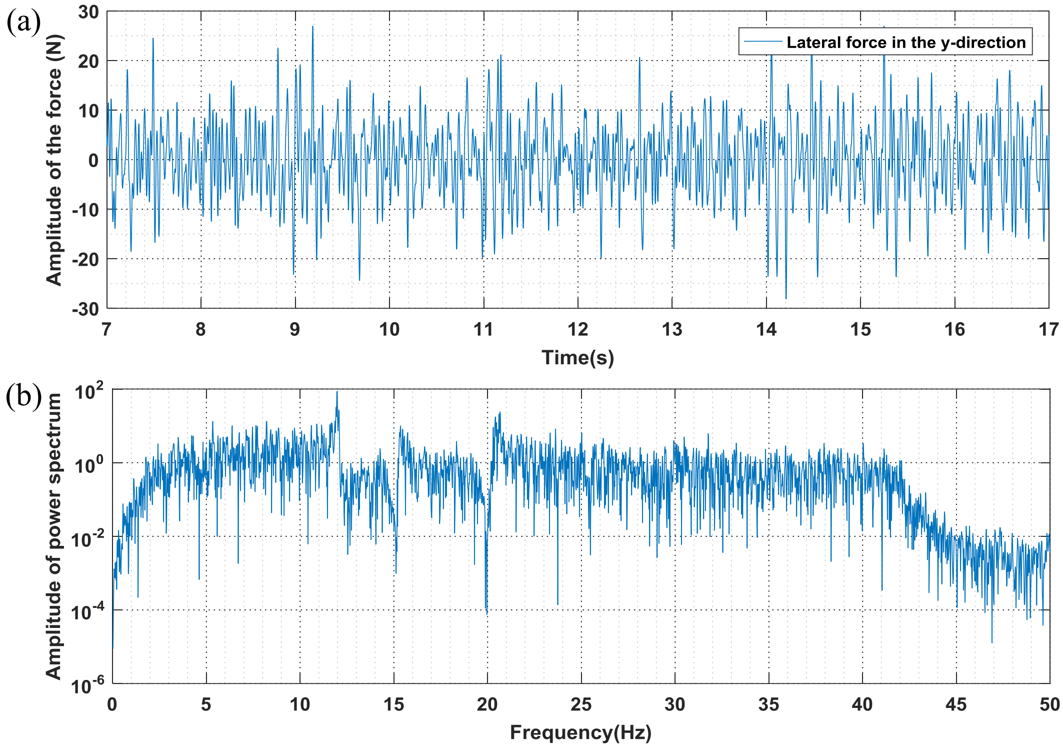

Fig. 6.6 The lateral excitation force in the y-direction for the damage scenario one: (a) In time domain; (b) In frequency domain.

(a)

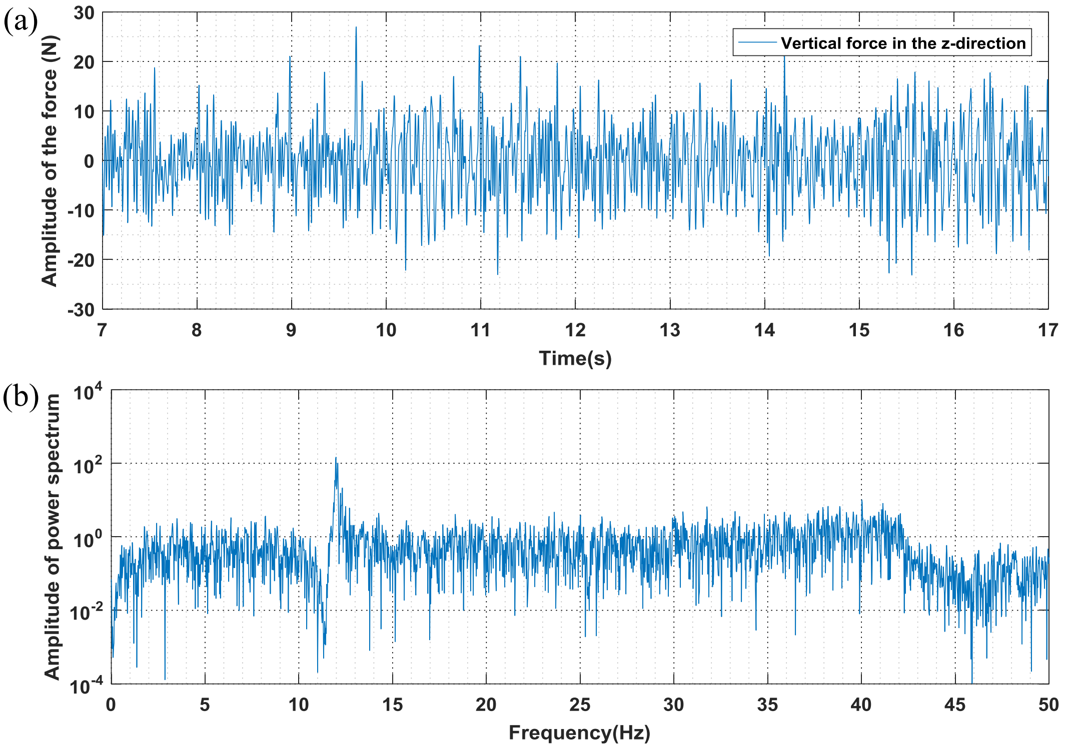

Fig. 6.7 The vertical excitation force in the z-direction for the damage scenario one: (a) In time domain; (b) In frequency domain.

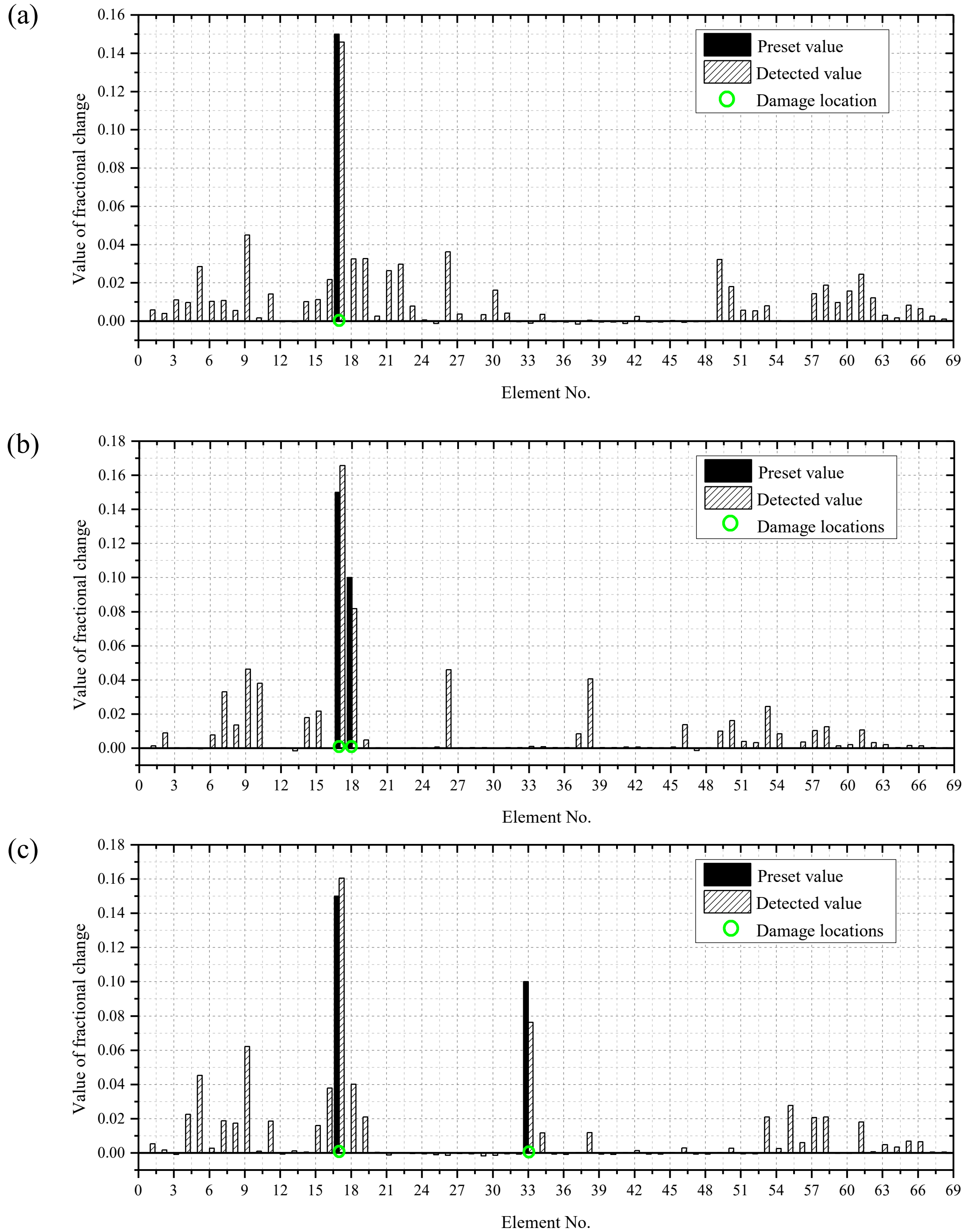

Fig. 6.8 The results of damage detection for three different damage scenarios: (a) Damage scenario one with one damage in Element 17; (b) Damage scenario two with two damages in Element 17 and Element 18; (c) Damage scenario three with two damages in Element 17 and Element 33.

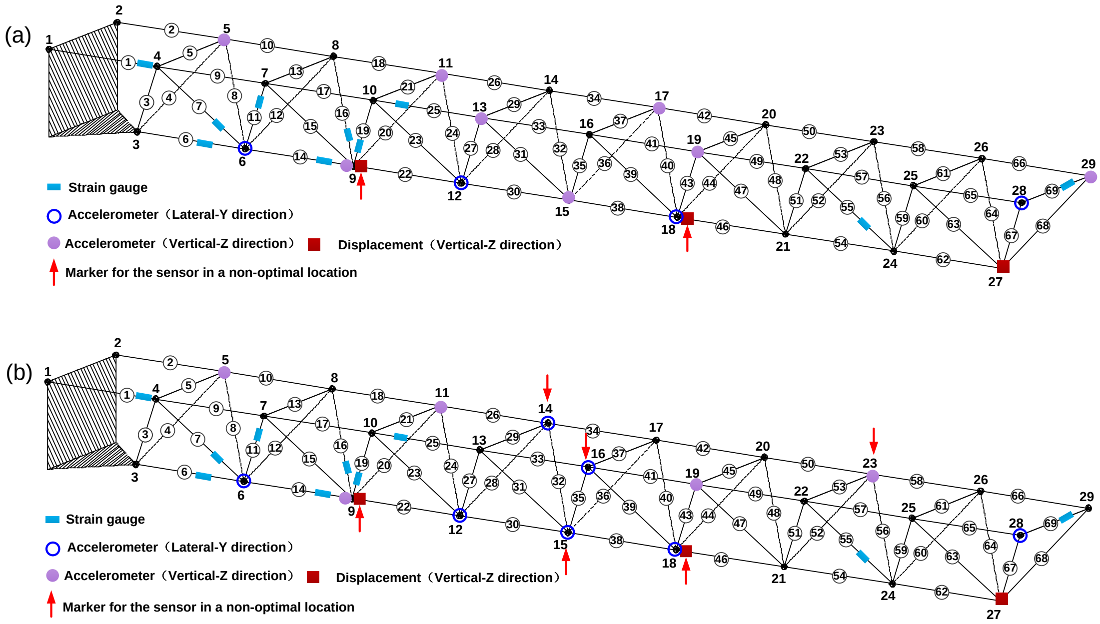

Fig. 6.9 Two non-optimal sensor placements :(a) Sensor configuration Non-OSP1; (b) Sensor configuration Non-OSP2.

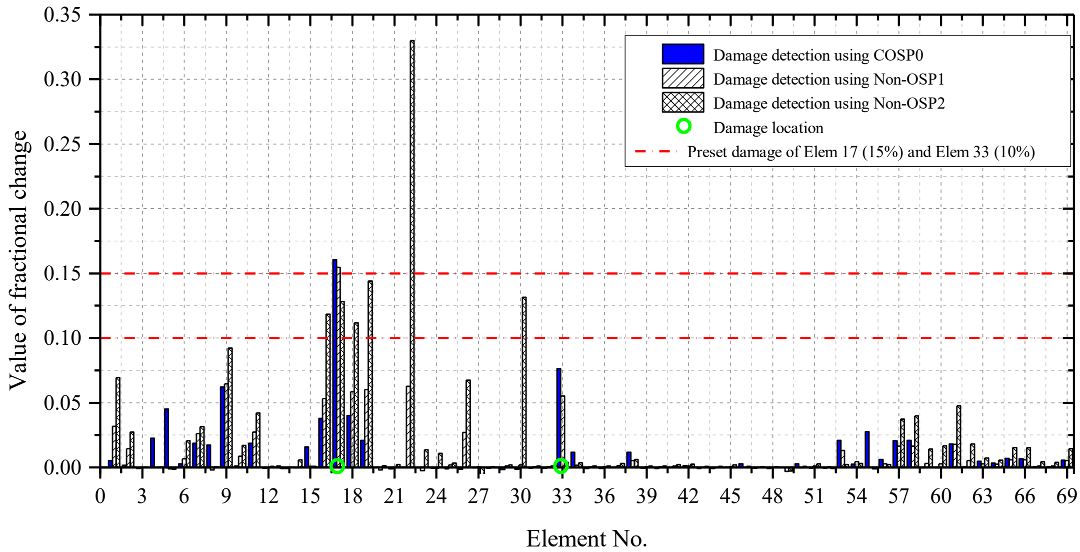

Fig. 6.10 Comparison of damage detection by using the optimal and non-optimal sensor placements

CHAPTER 7

MULTI-STAGE DAMAGE DETECTION OF A TRANSMISSION TOWER: NUMERICAL INVESTIGATION

7.1 Introduction

When the covariance-based multi-type sensor placement method and the associated damage detection methods proposed in the previous chapters are applied to a large transmission tower for damage detection of loosened bolts, a number of obstacles exhibit. The global stiffness matrix, modal parameters, and dynamic responses are less sensitive to local damage (loosened bolts) of a large transmission tower compared with small structures investigated in previous chapters. The one-stage damage detection is inaccurate and sometimes impossible due to too many unknown damage parameters and seriously ill-conditioned inversed problem for a large transmission tower. The two-stage damage detection strategy used in Chapter 3 is also not suitable for a large transmission tower because two types of sensors were separately installed in two stages in Chapter 3, which is impractical for a large transmission tower. Therefore, a new multi-stage damage detection incorporating with a multi-scale finite element (FE) model is proposed for the damage detection of loosened bolts of a large transmission tower in this chapter. Section 7.2 will describe the problem encountered for damage detection of loosened bolts at a joint of a large transmission tower. Section 7.3 will introduce the methodology of the multi-stage damage detection method, in which a multi-scale FE model of the transmission tower is introduced. Section 7.4 is the numerical study to demonstrate the feasibility and accuracy of the multi-stage detection method. A summary of the works done in this chapter is given in Section 7.5.

7.2 Problem Description

Lattice structures with bolted joints have been popularly used in different structural forms. The high-voltage power transmission (HVPT) tower is one form of these lattice structures in large size with a number of structural members connected through a series of bolted joints (see Fig.7.1). The HVPT towers are usually metallic structures. According to the code of lattice towers and masts from British Standard Institution (BSI) (Institution 2001), the three major composition members of the HVPT tower are leg members, primary bracing members, and secondary members. Leg members form the main load-bearing chords of the structure; primary bracing members other than legs carry the shear force due to imposed loads on the structure; secondary members are used to reducing the effective length of the main legs and sometimes that of the bracing, which are normally considered unstressed and are only loaded due to deformation of the structure. Thus, leg and primary bracing members are main load-bearing components and form critical load-bearing regions at joints with a series of bolts.

Previous studies (Albermani et al. 2009; Klinger et al. 2011; Hathout et al. 2013; Jiang et al. 2017; Valeti and Pakzad) revealed that the typical damages of the HVPT towers include (see Fig. 7.2): (a) corrosion of members or bolts at a joint near a support; (b) breaking of components at a critical joint; (c) fracture of a member at the joint; (d) loosened bolts at a joint; (e) bolted joint slippage; (f) cracking at a nut in the joint; and (g) global bucking and collapse. Clearly, apart from global bucking and collapse, all others are local damage occurring near or at a joint. Moreover, the global bucking and collapse sometime are also due to the structural deterioration caused by local damage at joints when the degraded tower suffers from extreme conditions such as strong winds and severe earthquakes. Therefore, the bolted joints in the transmission tower are vulnerable components and the bolted joints in the critical load-bearing regions should be prioritized for monitoring and damage detection. Moreover, for a transmission tower constructed with bolted joints, the gusset plates are often designed strongly enough to avoid damage. Therefore, the damage of a bolted joint is most likely from bolts. This chapter thus mainly concerns loosened bolts at a joint of a large transmission tower.

However, the local defects of joints are difficult to be identified because of the inaccessibility of visual inspection for some damage components in a large transmission tower. The transmission towers are often located in remote areas such that frequently visual inspection by experts is also impossible. Fortunately, damage detection technology has been developed as a cutting-edge technology to provide possible solutions (Xu and Xia 2012). Detecting local damage of a transmission tower at the earliest possible stage can provide useful information for decision makers to perform a cost-effective maintenance and repair such that serious damage can be avoided (Yin et al. 2009; Lam and Yin 2011; Hathout et al. 2013; Kong et al. 2017; Valeti and Pakzad).

The damage (loosened bolts) occurring at a joint is very local damage for a large transmission tower, which only induces small change in the structural system of the transmission tower. Identifying the local damage of loosened bolts at joints of the transmission tower is thus a very challenging issue. This chapter takes the straight-line type 5A-ZB2 HVPT tower model (see Fig. 7.1) as an example to illustrate the problem concerned and find the way forward. First, the number of the bolted joints in the transmission tower is large, leading to many unknown parameters for damage detection and a seriously ill-conditioned inversed problem. Secondly, a bolted joint has a complex geometric composition, constructed of angle members, gusset plates, and bolts. The accurate modelling of the bolted joints using shell/solid elements is necessary but the traditional FE model established by beam elements could not accommodate. On the other hand, if the entire tower is modelled using shell/solid elements, it will be very difficult to apply the proposed response covariance-based damage detection method due to computational prohibition. Therefore, this chapter will propose a response covariance-based multi-stage damage detection strategy incorporating with a multi-scale finite element (FE) model for the damage detection of loosened bolts at a joint of a transmission tower. In a multi-scale FE model of a transmission tower, the local detailed FE models using solid elements and a global FE model using beam elements are integrated. The damage detection strategy proposed in this chapter involves three stages. The first stage damage detection is to locate the damaged joints using the traditional beam model of the tower. This damage location detection is based on the fact that any change in the physical property of bolts in a joint will affect the stiffness of the connected members and then affect the related local region of the joint. In this stage, the suspicious rigid joints will be selected and the locations of the damaged joints will be identified by using the response covariance-based multi-sensing damage detection method introduced in the previous chapters. Because a joint often consists of a number of angle members and these angle members may be connected in series or parallel, the second stage is therefore to find out which members at the damaged joint are suspicious to loosened bolts. This stage detection is conducted also using the traditional beam model of the tower. In the third stage, the multi-scale FE model of the tower is used, in which the detailed local models of the damaged joints are embedded and the actual connections of all members in the joint are modelled. By taking the damage detection results from the second stage as initial damage results, the location and severity of the loosened bolts in the joint are finally determined in the third stage. The methodology of the proposed multi-stage damage detection will be further elaborated in the next section.

7.3 Multi-Stage Damage Detection Method

The multi-stage damage detection is characterized by a few stages of different damage detection levels (Sohn et al. 2002). For the problem concerned in this chapter, the three-stage damage detection strategy is used. The first stage is to detect the existence of damaged joints and the locations of damaged joints based on the traditional beam model of the tower. The second stage is to detect the possibly damaged members with loosened bolts in the identified damaged joint based on the traditional beam model of the tower. The final stage is to identify the loosened bolts and quantify the damage severity based on the multi-scale FE model of the tower. Fig.7.3 shows the damage model for each stage and Fig.7.4 exhibits the flow chart of the multi-stage damage detection. It can be seen that a high-level stage requires the knowledge of low-level stage(s) to start further detection.

7.3.1 Localization of Damaged Joints

In the first stage, the traditional beam model of the tower is used, in which a joint is characterized by one node with several beam elements rigidly connected. This joint can be seen as a substructure or a super-element in the beam model of the tower. The loosened bolts of some members connected to the joint will certainly affect the total stiffness of the joint contributed by all the members connected to the joint. This effect is actually accounted by introducing an equivalent damage parameter for a suspicious joint in the first stage damage detection based on the traditional beam model. That is, an equivalent damage parameter is assigned to the stiffness matrix of each suspicious super-element (joint). The stiffness matrices of all the suspicious super-elements with the equivalent damage parameters are then assembled to the total stiffness matrix of the tower. The response covariance-based multi-sensing damage detection method is then applied to the total stiffness matrix to find the locations of the damaged super-elements. The first-stage damage model, with the suspicious super-element as a basic unit, can be expressed as

$$\mathbf{K}^{\mathrm{d}}(\Delta\boldsymbol{\alpha}^{\mathrm{sub}}) = \mathbf{K}^{\mathrm{u}} + \sum_{r=1}^{\mathrm{Nr}} (\Delta\alpha_r^{\mathrm{sup}} \cdot \hat{\mathbf{K}}_r^{\mathrm{u,sup}}); \quad (-1 \le \Delta\boldsymbol{\alpha}^{\mathrm{sup}} \le 0) \tag{7.1}$$

in which the matrix $\mathbf{K}^{\mathrm{d}}$ ($\mathbf{K}^{\mathrm{u}}$) denotes the global stiffness matrix of the damaged (undamaged) tower structure; the matrix $\hat{\mathbf{K}}_r^{\mathrm{u,sup}}$ represents the stiffness matrix of the undamaged r^{th} super-element, and a hat (^) over the matrix denotes the super-element stiffness matrix assembled in the global coordinate; the vector $\Delta\boldsymbol{\alpha}^{\mathrm{sup}}$ is the equivalent damage parameter vector; $\Delta\alpha_r^{\mathrm{sup}}$ is the equivalent damage parameter assigned to the r^{th} super-element and it implies that every beam element in this super-element has the same stiffness reduction $\Delta\alpha_r^{\text{sup}}$; and Nr is the total number of the suspicious super-elements.

To alleviate the ill-conditioned inversed problem of damage detection, the adaptive Tikhonov regularization method (Li and Law 2010) is adopted. The damage detection problem based on the first-stage damage model and the response covariance-based multi-sensing (CBMS) damage detection method can be formulated as

$$\Delta\boldsymbol{\alpha}^{\text{sup}} = \underset{(\Delta\boldsymbol{\alpha}^{\text{sup}})^{k+1}}{\arg\min}\left[\|\mathbf{S}^k\cdot(\Delta\boldsymbol{\alpha}^{\text{sup}})^{k+1} - \Delta\mathbf{V}_{\text{pq}}{}^{k}\|_2^2 + \lambda^2\cdot\|(\Delta\boldsymbol{\alpha}^{\text{sup}})^{k+1} + \sum_{j=1}^{k}(\Delta\boldsymbol{\alpha}^{\text{sup}})^j - (\boldsymbol{\alpha}^{\text{sup}})^{k,*}\|_2^2\right];$$

(7.2)

with
$$\Delta\mathbf{V}_{\text{pq}}^k = \mathbf{V}_{\text{pq}}^m - \mathbf{V}_{\text{pq}}^c[(\Delta\boldsymbol{\alpha}^{\text{sup}})^k]; \tag{7.3}$$

where $\mathbf{V}_{\text{pq}}^m$ and $\mathbf{V}_{\text{pq}}^c$ are the CBMS index vectors computed by using the measured responses and the responses from the finite element model; the vector $\Delta\mathbf{V}_{\text{pq}}$ is the variance of $\mathbf{V}_{\text{pq}}^m$ and $\mathbf{V}_{\text{pq}}^c$; $\mathbf{S}$ is the sensitivity matrix of the CBMS index vector to the equivalent damage parameter vector $\Delta\boldsymbol{\alpha}^{\text{sup}}$; λ is the regularization parameter; the superscript k denotes the current iteration number; and the term $(\boldsymbol{\alpha}^{\text{sup}})^{k,*}$ is an adaptive adjustment factor (Li and Law 2010).

The CBMS index vectors $\mathbf{V}_{\text{pq}}^m$ and $\mathbf{V}_{\text{pq}}^c$ are computed using Eq. (3.13) with the measured and computed responses from the optimal sensor placement (OSP). For the first-stage damage model, the sensitivity matrix in Eq. (3.20) becomes $\mathbf{S} = \left[\frac{\partial\mathbf{V}_{\text{pq}}^c}{\partial\alpha_1^{\text{sup}}}, \frac{\partial\mathbf{V}_{\text{pq}}^c}{\partial\alpha_2^{\text{sup}}}, \cdots, \frac{\partial\mathbf{V}_{\text{pq}}^c}{\partial\alpha_r^{\text{sup}}}, \cdots, \frac{\partial\mathbf{V}_{\text{pq}}^c}{\partial\alpha_{\text{Nr}}^{\text{sup}}}\right]$. After computing $\mathbf{V}_{\text{pq}}^m$, $\mathbf{V}_{\text{pq}}^c$, and $\mathbf{S}$, the damage detection objective function Eq. (7.2) can be solved. Thereafter, the damage parameters $\Delta\boldsymbol{\alpha}^{\text{sup}} = \sum(\Delta\boldsymbol{\alpha}^{\text{sup}})^{k+1}$ are obtained and the locations of the damaged joints are qualitatively identified in the first stage damage detection.

7.3.2 Localization of Damage Suspicious Beams

After the locations of the damaged joints are identified, only the damaged joints will be focused on to localize damage suspicious members (beams) at these joints in the second-stage damage detection based on the beam model of the tower. In the second-stage damage detection, a damaged joint is not regarded as a super-element because damage suspicious members at the joint should be located. All the other undamaged joints are excluded from further investigation in the second-stage damage detection. In this way, the number of unknown parameters in the damage detection is reduced significantly. Furthermore, in the real tower structure, some members at the joint may be connected to its adjacent member other than directly connected to the joint, but in and due to the simple beam model, these members have to be directly connected to the joint. Therefore, the purpose of the second-stage damage detection is to locate damage suspicious members at the damaged joints. By using a new damage parameter vector $\Delta\boldsymbol{\alpha}^{\mathrm{ele}}$ that is assigned to the stiffness matrix of each member at the joint, the second-stage damage model is formulated as

$$\mathbf{K}^{\mathrm{d}}(\Delta\boldsymbol{\alpha}^{\mathrm{ele}}) = \mathbf{K}^{\mathrm{u}} + \sum_{h=1}^{\mathrm{Ne}} (\Delta\alpha_h^{\mathrm{ele}} \cdot \mathbf{K}_h^{\mathrm{u,ele}}); \quad (-1 \le \Delta\boldsymbol{\alpha}^{\mathrm{ele}} \le 0) \tag{7.4}$$

In the above equation, the global stiffness matrix $\mathbf{K}^{\mathrm{d}}$ of the damage affected tower structure is expressed as the superposition of the global stiffness matrix $\mathbf{K}^{\mathrm{u}}$ of the intact tower structure and the summation of individual stiffness matrix $\Delta\alpha_h^{\mathrm{ele}} \cdot \mathbf{K}_h^{\mathrm{u,ele}}$ of the beam element at the damage joints. The parameters $\Delta\alpha_h^{\mathrm{ele}}$ and $\mathbf{K}_h^{\mathrm{u,ele}}$ are the stiffness reduction factor (damage parameter) and the stiffness matrix of the h^{th} intact beam element (see Fig. 7.3(b)). Ne is the total number of beam elements in all the damaged joints. From the second term at the right-hand side of Eq. (7.4), it can be seen that only the beam elements of the damaged joints are scrutinized, thereby improving the damage identification accuracy within affordable computations.

Similar to the objective function in Eq. (7.2), the objective function for damage detection based on the second-stage damage model is expressed as

$$\Delta\boldsymbol{\alpha}^{\text{ele}} = \underset{(\Delta\boldsymbol{\alpha}^{\text{ele}})^{k+1}}{\arg\min}\left[\| \mathbf{S}^k \cdot (\Delta\boldsymbol{\alpha}^{\text{ele}})^{k+1} - \Delta\mathbf{V}_{\text{pq}}{}^k \|_2^2 + \lambda^2 \cdot \| (\Delta\boldsymbol{\alpha}^{\text{ele}})^{k+1} + \sum_{j=1}^{k} (\Delta\boldsymbol{\alpha}^{\text{ele}})^j - (\boldsymbol{\alpha}^{\text{ele}})^{k,*} \|_2^2 \right];$$

(7.5)

where the variance of the CBMS index vector, $\Delta\mathbf{V}_{\text{pq}}$, has an expression $\Delta\mathbf{V}_{\text{pq}}^k = \mathbf{V}_{\text{pq}}^m - \mathbf{V}_{\text{pq}}^c[(\Delta\boldsymbol{\alpha}^{\text{ele}})^k]$; and the sensitivity matrix in Eq. (3.20) is computed as $\mathbf{S} = \left[\frac{\partial \mathbf{V}_{\text{pq}}^c}{\partial \alpha_1^{\text{ele}}}, \frac{\partial \mathbf{V}_{\text{pq}}^c}{\partial \alpha_2^{\text{ele}}}, \cdots, \frac{\partial \mathbf{V}_{\text{pq}}^c}{\partial \alpha_h^{\text{ele}}}, \cdots, \frac{\partial \mathbf{V}_{\text{pq}}^c}{\partial \alpha_{\text{Ne}}^{\text{ele}}} \right]$. After computing $\Delta\mathbf{V}_{\text{pq}}$ and $\mathbf{S}$, the damage detection objective function Eq. (7.5) can be solved. Thereafter, the damage parameters $\Delta\boldsymbol{\alpha}^{\text{ele}} = \sum (\Delta\boldsymbol{\alpha}^{\text{ele}})^{k+1}$ are obtained and the damage suspicious beams at the damaged joints are located.

7.3.3 Localization and Quantification of Loosened Bolts

Based on the identification results in Stage 2, the third stage damage detection aims to locate and quantify the locations and extents of loosened bolts, which connect the damage suspicious beams to the gusset plates, at the damaged joints. Since the bolts are not explicitly included in the beam FE models of the tower structure in the previous two stages, a detailed joint model with bolts explicitly modeled is demanded for the damage detection in this stage. The detailed joint model is established by using solid elements (see Fig. 7.3(c)), replacing the rigid joint model used in the previous two stages (see Fig. 7.3(a-b)). How to construct a multi-scale FE model by combining the detailed joint model with the global beam model will be explained in the numerical study in detail. With the multi-scale FE model and taking the identification results from the second stage as initial values, the third-stage damage model for damage identification of loosened bolts is formulated as

$$\mathbf{K}^{\text{d,hybrid}}(\Delta\boldsymbol{\alpha}^{\text{bol}}) = \mathbf{K}^{\text{u,hybrid}} + \sum_{n=1}^{\text{Nc}} (\Delta\alpha_n^{\text{bol}} \cdot \bar{\mathbf{K}}_n^{\text{u,bol}});$$
$$\text{subject to}: \begin{cases} (\Delta\alpha_n^{\text{bol}})^0 \triangleq \Delta\alpha_h^{\text{ele}}; \\ -1 \le \Delta\boldsymbol{\alpha}^{\text{bol}} \le 0 \end{cases} \tag{7.6}$$

where $\mathbf{K}^{\text{d,hybrid}}$ ($\mathbf{K}^{\text{u,hybrid}}$) is the hybrid global stiffness matrix of damaged (undamaged) tower structure represented by the multi-scale FE model; $\bar{\mathbf{K}}_n^{\text{u,bol}}$ is the stiffness matrix contributed by the n^{th} set of bolts in intact state; a new damage parameter $\Delta\alpha_n^{\text{bol}}$ is defined as a stiffness reduction factor assigned to the n^{th} set of bolts (see Fig. 7.3(c)) and the symbol $\triangleq$ denotes that its initial value is provided by $\Delta\alpha_h^{\text{ele}}$ obtained in the second stage; and Nc is the total number of the sets of bolts in the damaged joint, where one set of bolts includes all the bolts connecting one angle member to the gusset plate.

Similar to the objective functions in Eq. (7.2) and Eq. (7.5), the objective function for damage detection based on the third-stage damage model is expressed as

$$\Delta\boldsymbol{\alpha}^{\text{bol}} = \underset{(\Delta\boldsymbol{\alpha}^{\text{bol}})^{k+1}}{\arg\min} \left[\| \mathbf{S}^k \cdot (\Delta\boldsymbol{\alpha}^{\text{bol}})^{k+1} - \Delta\mathbf{V}_{\text{pq}}{}^k \|_2^2 + \lambda^2 \cdot \| (\Delta\boldsymbol{\alpha}^{\text{bol}})^{k+1} + \sum_{j=1}^{k} (\Delta\boldsymbol{\alpha}^{\text{bol}})^j - (\boldsymbol{\alpha}^{\text{bol}})^{k,*} \|_2^2 \right];$$
$$\text{subject to}: \begin{cases} (\Delta\boldsymbol{\alpha}^{\text{bol}})^0 \triangleq \Delta\boldsymbol{\alpha}^{\text{ele}} \\ (\mathbf{V}_{\text{pq}}^c)^0 = \mathbf{V}_{\text{pq}}^c[(\Delta\boldsymbol{\alpha}^{\text{bol}})^0 \triangleq \Delta\boldsymbol{\alpha}^{\text{ele}}] \end{cases}$$

(7.7)

where the variance of the CBMS index vector, $\Delta\mathbf{V}_{\text{pq}}$, has an expression of $\Delta\mathbf{V}_{\text{pq}}^k = \mathbf{V}_{\text{pq}}^m - \mathbf{V}_{\text{pq}}^c[(\Delta\boldsymbol{\alpha}^{\text{bol}})^k]$. The sensitivity matrix in Eq. (3.20) is computed as $\mathbf{S} = \left[\frac{\partial \mathbf{V}_{\text{pq}}^c}{\partial \alpha_1^{\text{bol}}}, \frac{\partial \mathbf{V}_{\text{pq}}^c}{\partial \alpha_2^{\text{bol}}}, \cdots, \frac{\partial \mathbf{V}_{\text{pq}}^c}{\partial \alpha_n^{\text{bol}}}, \cdots, \frac{\partial \mathbf{V}_{\text{pq}}^c}{\partial \alpha_{\text{Nc}}^{\text{bol}}} \right]$. It is worth mentioning that the initial values of $\Delta\boldsymbol{\alpha}^{\text{bol}}$ and $\Delta\mathbf{V}_{\text{pq}}$ come from the second stage damage detection. The identified damage severities in the second stage, $\Delta\boldsymbol{\alpha}^{\text{ele}}$, provide the initial values $(\Delta\boldsymbol{\alpha}^{\text{bol}})^0$ for the corresponding sets of bolts connecting the damage suspicious elements to the gusset plates. To make the problem manageable and to consider the companion experimental investigation, the damage severity (stiffness reduction) of the damage suspicious element obtained from the second stage is assigned as an initial damage value to all the bolts used to connect this suspicious element to the gusset plate. An extreme case of this assumption is that if all the bolts used to connect the suspicious element to the gusset plate are loosened, the damage severity of this set of bolts is zero. The initial value of the CBMS index $(\mathbf{V}_{\mathrm{pq}}^{c})^{0}$ is computed by $(\mathbf{V}_{\mathrm{pq}}^{c})^{0} = \mathbf{V}_{\mathrm{pq}}^{c}[(\Delta\boldsymbol{\alpha}^{\mathrm{bol}})^{0} \triangleq \Delta\boldsymbol{\alpha}^{\mathrm{ele}}]$. By using such initial values, the optimization search of the sets of loosened bolts is given a good starting point and the convergence is accelerated because of a narrow searching range. After computing $\Delta\mathbf{V}_{\mathrm{pq}}$ and $\mathbf{S}$, the damage detection objective function Eq. (7.7) can be solved. Thereafter, the damage parameters $\Delta\boldsymbol{\alpha}^{\mathrm{bol}}=\sum(\Delta\boldsymbol{\alpha}^{\mathrm{bol}})^{k+1}$ are obtained. The sets of loosened bolts are located at the damaged joints and the severities of the sets of loosened bolts are quantified.

7.4. Numerical Study

7.4.1 Finite Element Model of the Transmission Tower

The numerical investigation aims to examine the feasibility and accuracy of the proposed response covariance-based multi-stage damage method. The testbed model of a 5A-ZB2 HVPT tower (see Fig. 7.5(a)) in the Structural Dynamics Laboratory of The Hong Kong Polytechnic University is selected for the numerical study. The structural and material properties of the tower structure are listed in Table 7.1. According to the testbed model, a finite element model of the tower (see Fig. 7.5(b)) is built using the commercial software ANSYS with 1722 Beam188 elements for the angle members and 245 Mass21 elements for additional lump masses considering bolts and gusset plates in some joints which cannot be ignored. The four nodes of the tower at the ground level are fixed, and all joints in the beam model are modeled as rigid joints without considering joint eccentricities for the first and second stage damage detection. The first ten natural frequencies of the beam FE model of the tower are 16.45, 16.57, 23.36, 33.17, 44.89, 44.93, 45.73, 52.55, 53.44, 56.42 Hz. The first ten modes of vibration are selected for response computation using the mode superposition technique. The Rayleigh damping is assumed in this study for the computation.

For a transmission tower, the longitudinal loading is one of its major loadings, which may be induced by the longitudinal imbalances of wire tensions produced by wind and/or ice loading on adjacent spans or from temperature extremes on unequal spans. Therefore, the longitudinal eccentrical loading condition is simulated in the numerical study. Specifically, two Gaussian white noise excitations with a standard deviation of 3 N are applied to two nodes of the testbed model in the longitudinal (y) direction respectively, as shown in Fig. 7.5. The excitation frequency is selected with a bandwidth of 0-50 Hz to cover the first ten natural frequencies. The structural responses are sampled at 300 Hz over the time duration of 20s. Measurement noise is simulated by adding normally distributed random number to the noise-free response for the numerical study. The root-mean-square (RMS) of the measurement noise is equal to 5% of the RMS value of the noise-free response in this study.

The effectiveness of the proposed damage detection method will be numerically examined. After considering the tower is a mono-symmetric structure, only one of the four tower legs from the top to the bottom of the tower is selected for the performance demonstration of the proposed method so that the computational time and cost can be reduced significantly. Furthermore, some joints are damage-prone because they carry large forces and stresses but some joints are not. According to initial stress analysis, twelve joints are finally selected as damage-prone joints within the selected tower leg, and they are depicted in Fig. 7.6. The beam elements in each joint are renamed as E1, E2, … in sequence for the easy identification in the subsequent multi-stage damage detection. For example, 89(E2) of Joint 1 in Fig. 7.6 (a) means that the original element No. 89 in the entire structure is renamed as E2 when we scrutinize the specific joint.

7.4.2 Multi-Type Sensor Optimal Placement

To achieve better damage detection, accelerometers and strain gauges are optimally placed before the first stage of damage detection based on the beam FE model. The optimal sensors are deployed in the selected tower leg region, which includes 24 candidate accelerometer sensor locations at the 12 nodes with respect to the selected joints and 37 candidate strain sensor locations at the mid-spans of the beam elements of the tower leg. For the sake of sensor placement encoding, the accelerometers are labeled by 1 to 24, distributed over the 1st to 12th nodes in the x- (lateral-) direction and the y- (longitudinal-) direction. The strain gauges are labeled by 25 to 61 and distributed over the 1st to 37th beam elements in the tower leg. The total number of optimal sensors N_o=22 is finally determined based on the principle of using the minimum number of sensors but guaranteeing enough accuracy of structural damage detection. The multi-type sensor optimal placement is conducted by using the OSP method introduced in Chapter 5, and the parameters used in the NSGA-II are listed in Table 7.2.

After solving the multi-objective multi-type sensor placement problem expressed by Eq. (5.1) in Chapter 5, the Pareto front is obtained and plotted in Fig. 7.7(a). This Pareto front includes 200 Pareto solutions and each Pareto solution corresponds to an OSP. The simultaneous optimization of two conflictive objectives leads to a set of compromised solutions known as the non-dominated or Pareto-optimal solutions. Thus, a knee-point based method proposed in the reference (Lin et al. 2018) is adopted to determine the final OSP for application. First, the trade-offs in either direction can be approximately estimated through the curvature of the fitting curve (see Fig.7.7 (a)) of the Pareto front. Then, the curvature of each Pareto solution is computed through the function of the fitting curve, which is plotted in Fig. 7.7(b). Mathematically, the most desirable knee point is a solution located in the convex region of the Pareto front with the maximum curvature of positive (Bechikh et al. 2010). Finally, the best OSP is determined by using the knee point-based method, in which the knee point carries the maximum curvature of the curve of the Pareto front. Moreover, the OSP obtained is displayed in Fig. 7.8, which includes 15 accelerometers named A1 to A15 and 7 strain gauges named S1 to S7.

7.4.3 Damage Sensitivity Analysis

The traditional damage detection strategy tends to conduct damage detection of all beam elements in the tower in one step. That is just to consider the second stage damage detection for all the beam elements other than only the damaged joints identified from the first-stage damage detection in this study. To demonstrate the necessity of the first-stage damage detection proposed in this study, the sensitivity analysis is conducted to show the feasibility of damage detection of the traditional strategy and the multi-stage strategy. For the traditional strategy, all the beam elements (totally 84 elements in this study) are considered, and the sensitivity matrix of the CBMS damage index to all the beam elements, $\mathbf{S}^{\mathrm{ele}} = \dfrac{\partial \mathbf{V}_{\mathrm{pq}}}{\partial \boldsymbol{\alpha}^{\mathrm{ele}}}$, is calculated. For the first stage damage detection of the multi-stage strategy, all the beam elements are grouped as several super-elements, and the sensitivity matrix of the CBMS damage index to all the super-elements $\mathbf{S}^{\mathrm{sup}} = \dfrac{\partial \mathbf{V}_{\mathrm{pq}}}{\partial \boldsymbol{\alpha}^{\mathrm{sup}}}$ (totally 12 super-elements in this study) is calculated.

By using the same OSP, the two sensitivity matrices (Eq. (3.20)) are computed and the column norms of them in terms of $\left\| \dfrac{\partial \mathbf{V}_{\mathrm{pq}}^{c}}{\partial \alpha_i} \right\|_2$ are plotted in Fig. 7.9 (a) and (b) respectively. Each column norm represents the damage sensitivity of each beam (Fig. 7.9 (a)) or each super-element (Fig. 7.9 (b)). The two sensitivity matrices are compared in terms of mean values of column norm, condition numbers and number of unknowns. The relevant comparison results are summarized in Table 7.3. As seen from Table 7.3, the mean value of column norm of $\mathbf{S}^{\mathrm{ele}}$ is 105.72 while that of $\mathbf{S}^{\mathrm{sup}}$ is 493.422, which implies the proposed method (the first stage) is much more sensitive than its counterpart. Looking back to Fig. 7.9(a), there are many beam elements with very small norm values. These less sensitive elements usually lead to false alarms or even divergent identification results. Also, the condition numbers of $\mathbf{S}^{\mathrm{ele}}$ and $\mathbf{S}^{\mathrm{sup}}$ are 4.80×10^{19} and 5.50×10^{2} respectively, as listed in Table 7.3. The drastically large condition number of $\mathbf{S}^{ele}$ indicates that the former method suffers from severe ill-condition problem when it concerns a large structure. The damage detection of the critical joints consisting of 84 beam elements by using the traditional strategy fails because of lower sensitivity and severer ill-condition. After grouping the 84 beam elements as 12 super-elements, the number of unknowns is reduced significantly. The damage detection succeeds because of the enhanced sensitivity and alleviated ill-condition. Therefore, the first stage of the multi-stage strategy is indispensable for damage detection of a large structure.

7.4.4 Multi-Stage Damage Detection

Two common causes of bolt damage in the HVPT tower are vibration-induced bolt loosening and environment-induced corrosion of bolts in joints. To examine the performance of the proposed multi-stage damage detection method, a damage scenario with loosened bolts in a critical position "Joint 9" (see Fig. 7.10) is designed for the case study. The critical position "Joint 9" and the enlarged illustration of its composition are shown in Fig. 7.10. The three stages for damage detection of loosened bolts at Joint 9 are illustrated in Fig. 7.11, and the procedure for implementing the multi-stage method can refer to Fig. 7.4. The detailed implementation procedure and results of damage detection are described in the following.

7.4.4.1 Localization of Damaged Joints in Stage One

In the first stage, the damage detection is started from the searching of damaged joints due to loosened bolts (see Fig. 7.11(a)) by using the first-stage damage model. In this stage, a rigid joint is composed by one node and several beam elements connected to the node, which is represented by a super-element in the beam FE model. The super-elements works as a basic unit to locate the damaged joint. As mentioned in Section 7.4.1, only one of the four tower legs from its top to its bottom in 1/4 tower is selected for performance demonstration of the proposed method, in which twelve joints are further selected as damage-prone candidates within the selected leg and their detailed compositions are depicted in Fig. 7.6. Accordingly, the beam FE model includes 12 super-elements (joints), and accordingly the first-stage damage model in Eq. (7.1) has 12 damage parameters to be determined. The damage parameters $\Delta\boldsymbol{\alpha}^{\mathrm{sup}}$ identified in the first stage are plotted in Fig. 7.12 (a). The highest bar, representing an equivalent stiffness reduction of 37.62%, is found at Joint 9. The equivalent stiffness reductions of other joints are incomparable with that of Joint 9. Therefore, Joint 9 is satisfactorily identified as the damaged joint, and other joints are identified as no damage.

7.4.4.2 Localization of Damage Suspicious Beams in Stage Two

Although the damaged joint is located at Joint 9, this joint is composed of several members and which members actually subject to loosened bolts are still unknown. Thus, the second-stage damage detection will focus on all the members at Joint 9 using the beam FE model (see Fig. 7.11(b)). As this joint consists of 9 beam elements, the second-stage damage model in Eq. (7.4) has 9 damage parameters to be determined. The damage parameters $\Delta\boldsymbol{\alpha}^{\mathrm{ele}}$ identified from the second stage are depicted in Fig. 7.12 (b). Two bars are found dominant in this figure, with stiffness reductions of 62.52 % and 89.78% for the beam elements E6 and E7 respectively. Therefore, the beam elements E6 and E7 are the two damage suspicious elements identified from the second-stage. The reason why these two elements are damage suspicious elements only shall refer to the detailed configuration of Joint 9. As shown in Fig.7.11 (c), the beam E6 at Joint 9 is actually connected to the beam E7 other than directly connected to the joint as modeled in the bean FE model. There is possibility that only the set of bolts for the beam E7 loosens while the set of bolts for the beam E6 is still in good condition. Such a dilemma cannot be solved by the second-stage damage detection using the beam FE model of the tower.

7.4.4.3 Localization and Quantification of Loosened Bolts in Stage Three

To solve the dilemma faced by the second stage, the model of Joint 9 which connects nine beam elements to a common joint is replaced by a detailed local model. The detailed local model constitutes angle members, bolts, and gusset plates (see Fig. 7.11(c)). It is built by using solid185 elements in ANSYS and composed of 13615 solid elements in total. The connection among angle members, bolts, and gusset plates is shown in Fig. 7.13(a). The bolts contribute to transfer forces by coupling those common nodes of the contact surfaces between bolts and angle members and the contact surfaces between nuts and gusset plates. The detailed local models using solid elements and the global FE model using beam elements are then integrated to form the multi-scale FE model. The interface between the detailed model of Joint 9 and the beam elements of the global model are coupled via the multipoint constraint (MPC) (see Fig. 7.13(b)).

As the detailed local model of Joint 9 contains 12 sets of bolts, the third-stage damage model in Eq. (7.6) has 12 damage parameters to be determined. For the easy manipulation of the subsequent damage detection, each set of bolts is assigned a unique name and their names are B1, B2, …, B12 (see Fig. 7.11 (c)). When damaged, the material and/or geometric characteristics of the bolts change. In this study, the stiffness reduction parameter $\Delta\boldsymbol{\alpha}^{\mathrm{bol}}$ is simulated by the change of the elastic modulus of all the solid elements included in each set of bolts. Solving damage parameters $\Delta\boldsymbol{\alpha}^{\mathrm{bol}}$ is much more complicated than those in the previous two stages. It needs to take into consideration the damage identification results from the second stage, in which the beams E6 and E7 are found to be damage suspicious elements. After examining the detailed local model of Joint 9 in Fig. 7.11 (c), it can be seen that the beam E6 is subordinately connected to the beam E7 through a gusset plate and using the bolt sets B1 and B2, and that the beam E7 is connected to another gusset plate by the bolt set B3. Thus, B3 is only damage source for the beam E7 but could influence the beam E6 subordinated to the beam E7. If the bolt set B3 is loosened and the beam E7 is separated from the Joint 9, the beam E6 will also be separated from Joint 9 no matter whether the bolt sets B1 and/or B2 are damaged or not. Thus, the bolt sets B1 and B2 are assumed unloosened to avoid the multiple-solution problem in the damage detection. The damage severities (stiffness reductions) of all the other beams identified in the second-stage are thus assigned to all the bolt sets attached to Joint 9 as their initial values. For example, the beam E1 in Fig.11(b) is connected by two sets of bolts B6 and B7. Thus, the identified severity of E1 with 1.61% stiffness reduction is assigned to B6 and B7 as the initial value. Specifically, the stiffness reductions for the beam elements, namely 0.8978 (E7), 0.0752 (E8), 0.0230 (E9), 0.0161(E1), 0.0161(E1), 0.0523 (E5), 0.0523(E5), 0.0175 (E2), 0.0083 (E3), and 0.0425 (E4), are used as the initial values of the damage parameters $(\Delta\boldsymbol{\alpha}^{\mathrm{bol}})^0$ for B3, B4, B5, B6, B7, B8, B9, B10, B11, and B12 respectively. The initial value of the CBMS damage index $(\mathbf{V}_{\mathrm{pq}}^{c})^0 = \mathbf{V}_{\mathrm{pq}}^{c}[(\Delta\boldsymbol{\alpha}^{\mathrm{bol}})^0 \triangleq \Delta\boldsymbol{\alpha}^{\mathrm{ele}}]$ in this stage is computed after the initial values of all the bolt sets have been assigned. The damage parameters $\Delta\boldsymbol{\alpha}^{\mathrm{bol}}$ are finally identified and depicted in Fig. 7.12 (c). The highest bar, standing for a stiffness reduction of 98.81%, is found at the 3rd bolt set B3. The stiffness reductions at other bolt sets are incomparable with that at B3. Therefore, the loosened bolt set B3 is successfully identified, which is close to the preset damage by removing the bolt set B3 with 100% damage.

7.5 Summary

This chapter has presented a response covariance-based multi-stage damage detection strategy incorporating with the multi-stage damage models and the multi-scale FE model for the damage detection of loosened bolts in a large transmission tower. The multi-stage damage detection is effective to progressively reduce the unknown parameters and alleviate the ill-condition problem so as to make the problem solvable. The numerical study has shown that the proposed multi-stage damage detection method for the transmission tower testbed can achieve highly accurate identification of loosened bolts in a transmission tower. The uses of a detailed local model for a joint and thus a multi-scale FE model are necessary.

The theoretical framework of the response covariance-based multi-stage damage detection strategy has been presented and assessed through a numerical study.

Although the measurement noise of the structural response is considered in the simulation and numerical studies, there are still some uncertainties in the numerical study compared with the real tower structure conditions. Therefore, before this method can be applied to real transmission towers, an experimental investigation will be conducted in the next chapter to validate the numerical study.

Table 7.1 List of structural and material properties

Properties	Value
Young modulus $E\,(\mathrm{N/m^2})$	1.96×10^{11}
Density $\rho\,(Kg/\mathrm{m}^3)$	7930
Poisson ratio ν	0.26

Table 7.2 Parameters used in the NSGA-II method

Parameters	Values / operators
Population size of each generation	200
Maximum Number of generation	1000
Selection	Tournament algorithm
Probability of crossover	0.8
Probability of mutation	0.2

Table 7.3 Comparison of two sensitivity matrices

Analysis parameters	Sensitivity matrix	
	$\mathbf{S}^{ele}$	$\mathbf{S}^{sup}$
Mean value of sensitivity	105.72	493.422
Condition number	4.80×10^{19}	5.50×10^{2}
Number of unknowns	84	12

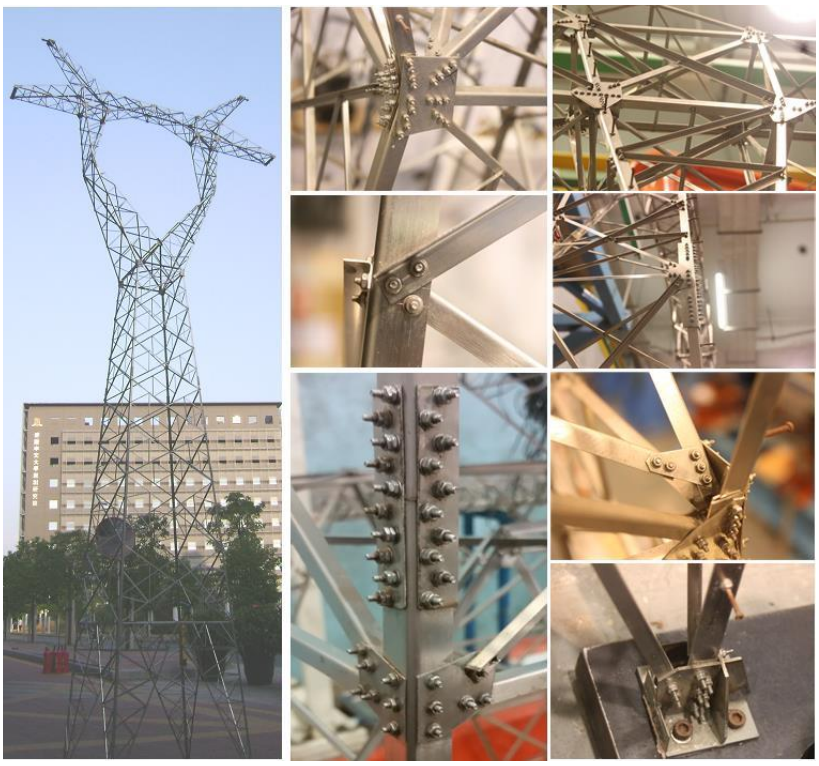

Fig. 7.1 The straight-line type 5A-ZB2 HVPT tower and its bolted joints

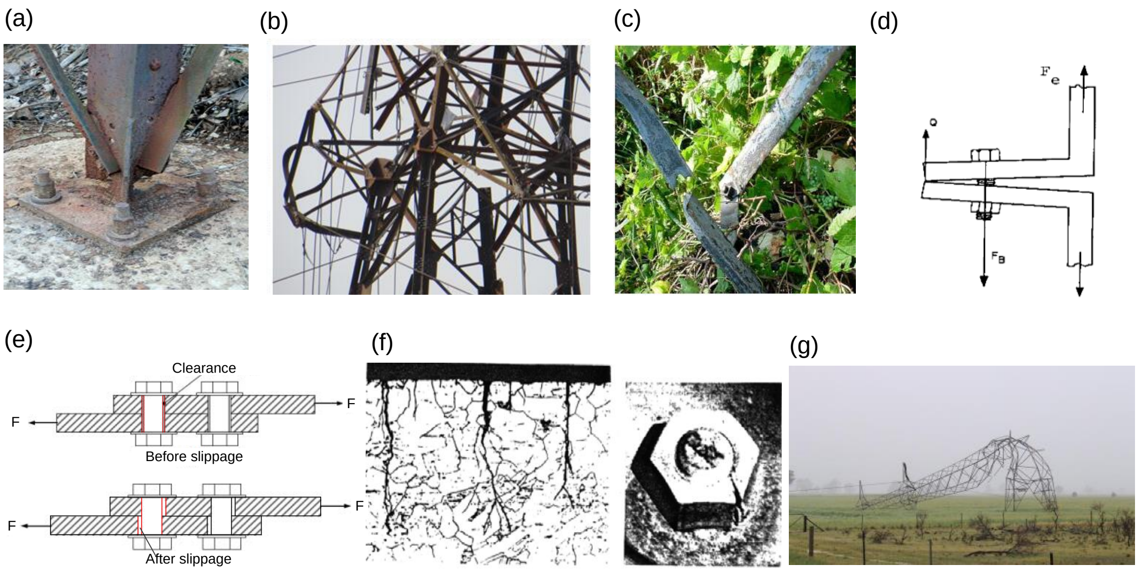

Fig. 7.2 Typical damage for a steel power transmission tower: (a) corrosion of beam or bolts at a joint near a support; (b) breaking of components at a critical joint; (c) fracture of a beam at the joint; (d) loosened bolts at a joint; (e) bolted joint slippage; (f) cracking at a nut in the joint; (g) global bucking and collapse.

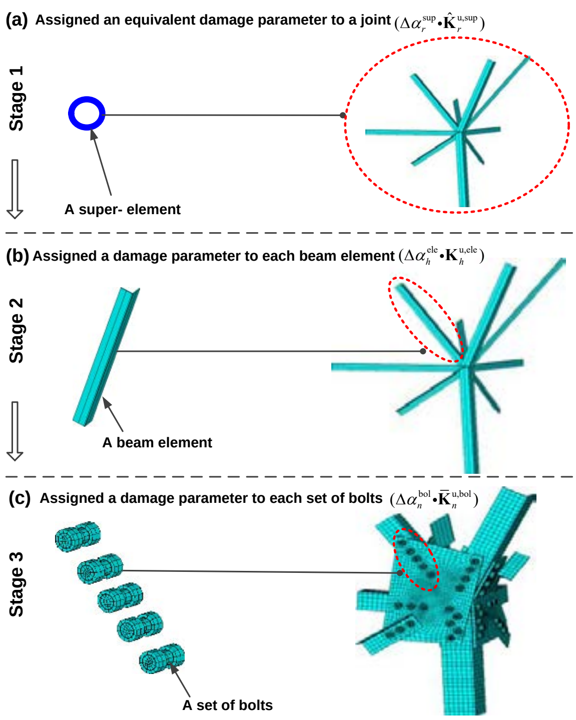

Fig. 7.3 The multi-stage damage model: (a) the first-stage damage model; (b) the second-stage damage model; (c) the third-stage damage model.

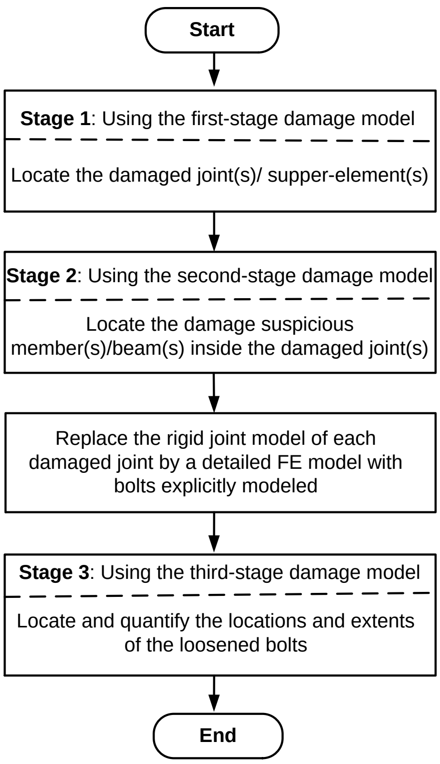

Fig. 7.4 Flowchart of multi-stage damage detection

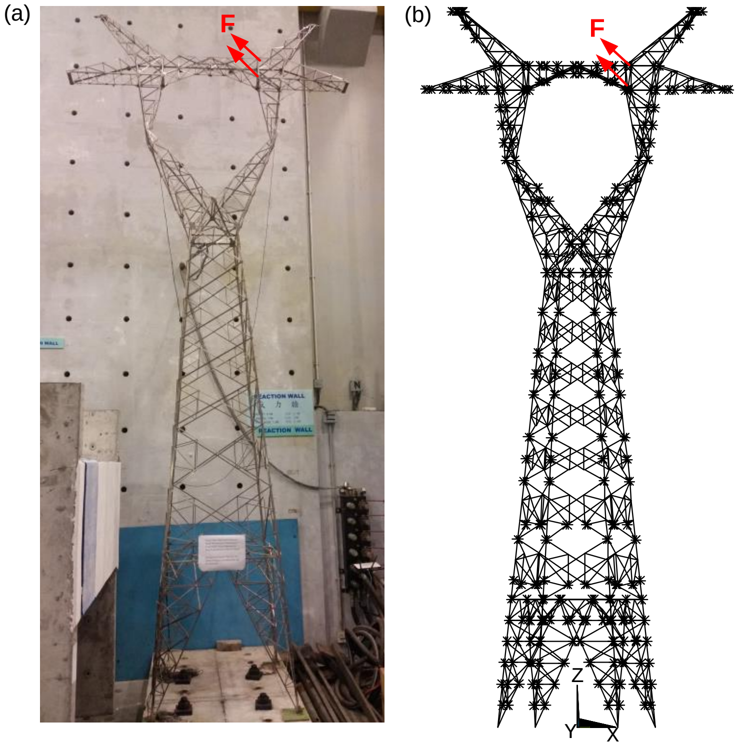

Fig. 7.5 The high-voltage power transmission tower model: (a) the physical model; (b) the finite element model.

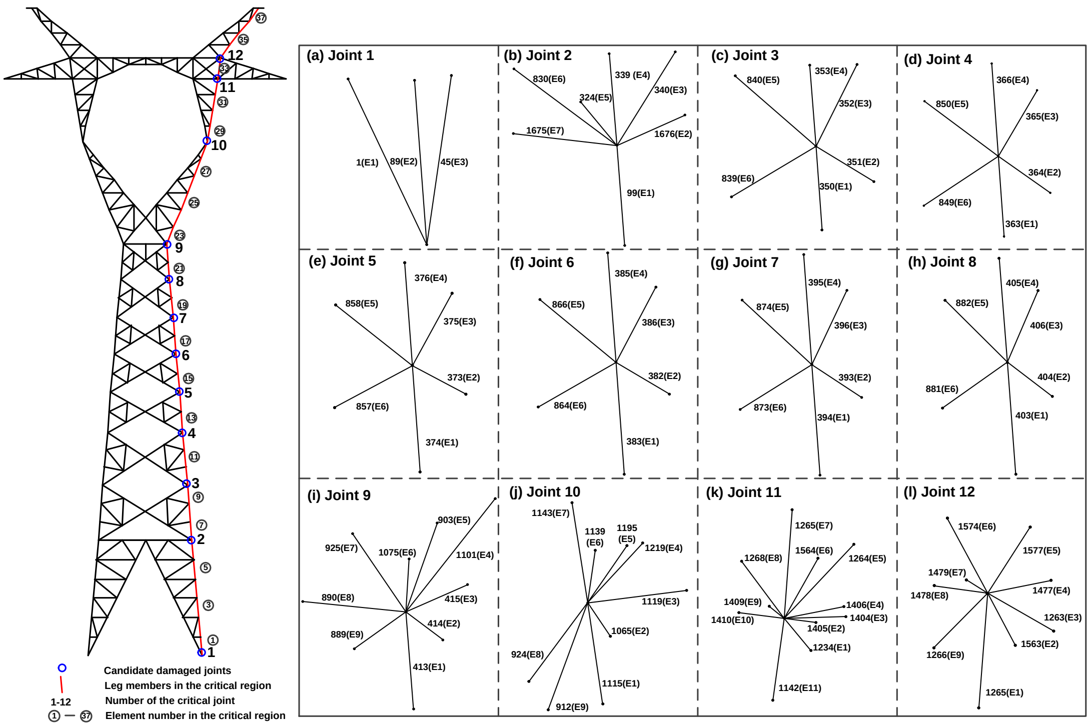

Fig. 7.6 The locations of the selected joints and their detailed compositions in the transmission tower

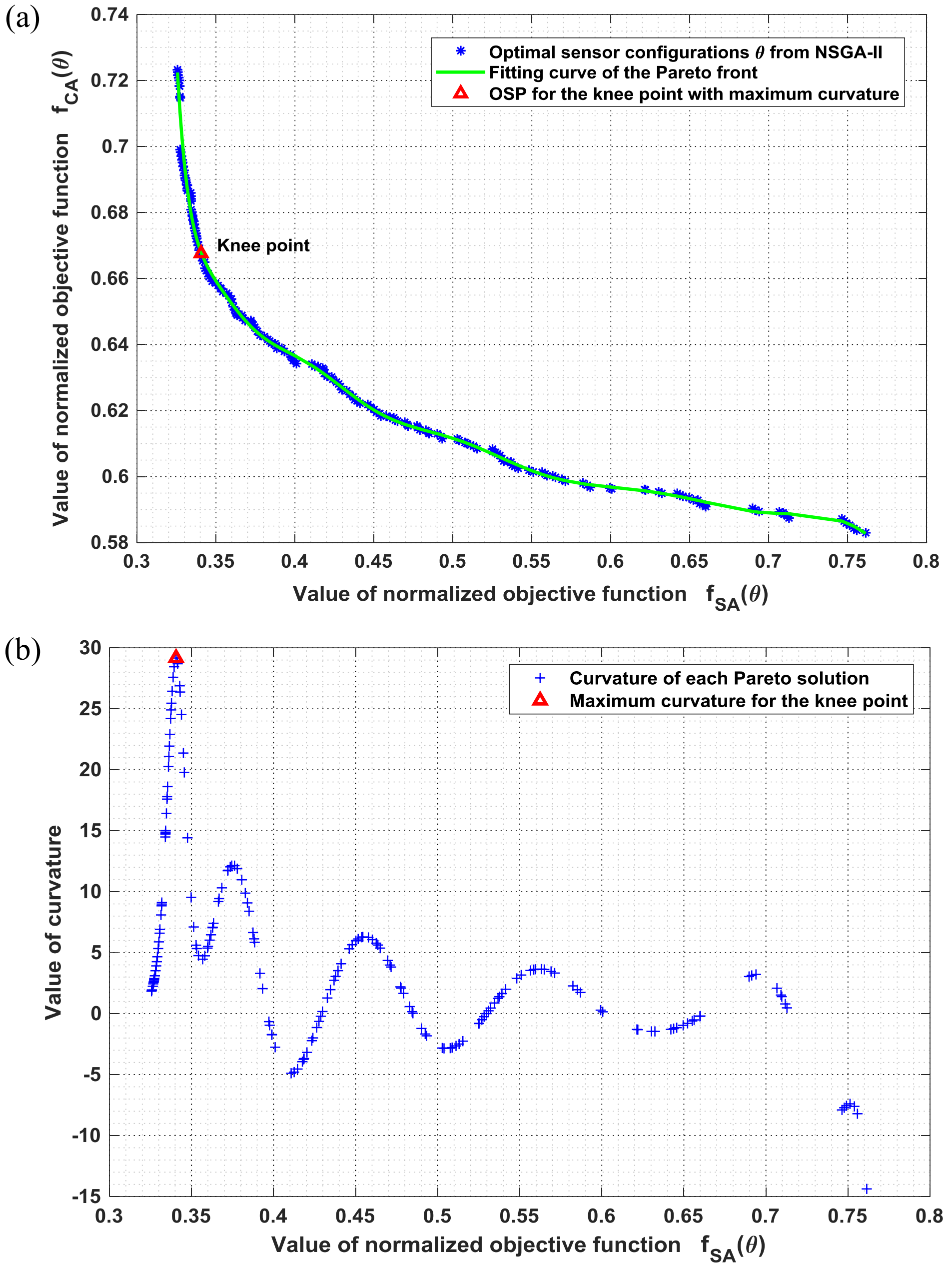

Fig. 7.7 The best OSP determined by the knee-point based method: (a) the fitting curve of the Pareto-front and the knee point of the Pareto-front; (b) the curvature of the fitting curve with respect to the Pareto solutions.

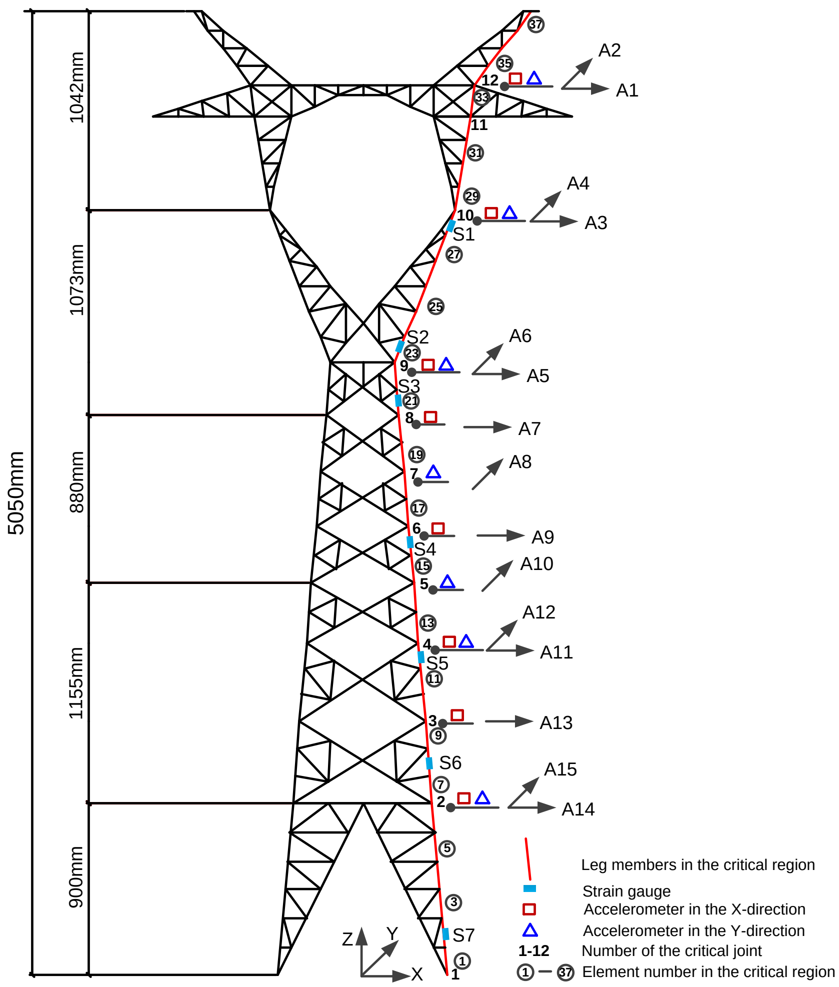

Fig. 7.8 The optimal sensor placement referring to the knee-point in the Pareto front

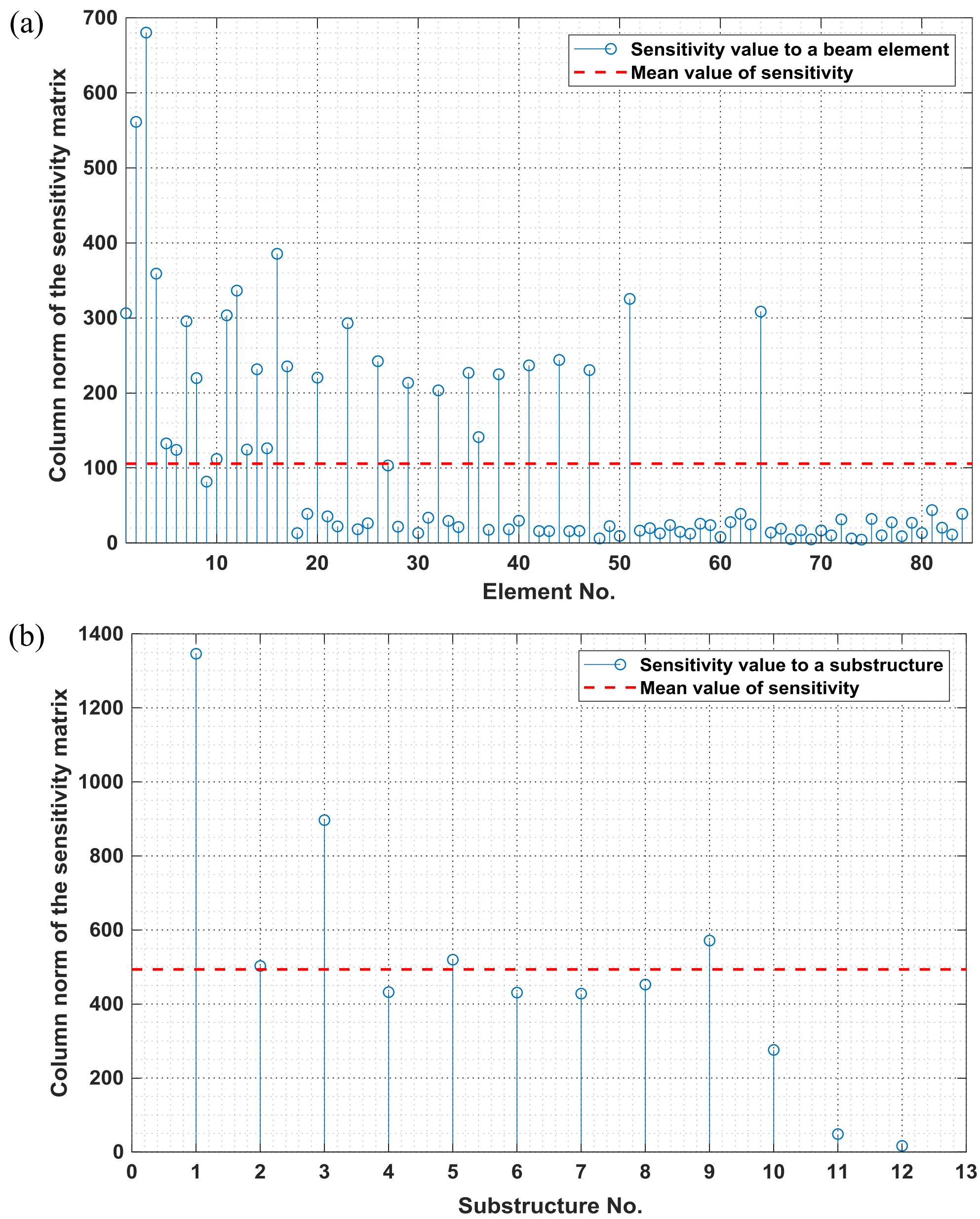

Fig. 7.9 Comparison of damage sensitivity in the beam-element-level and the super-elements-level: (a) damage sensitivity analysis to the 84 beam elements; (b) damage sensitivity analysis to the super-elements of 12 joints.

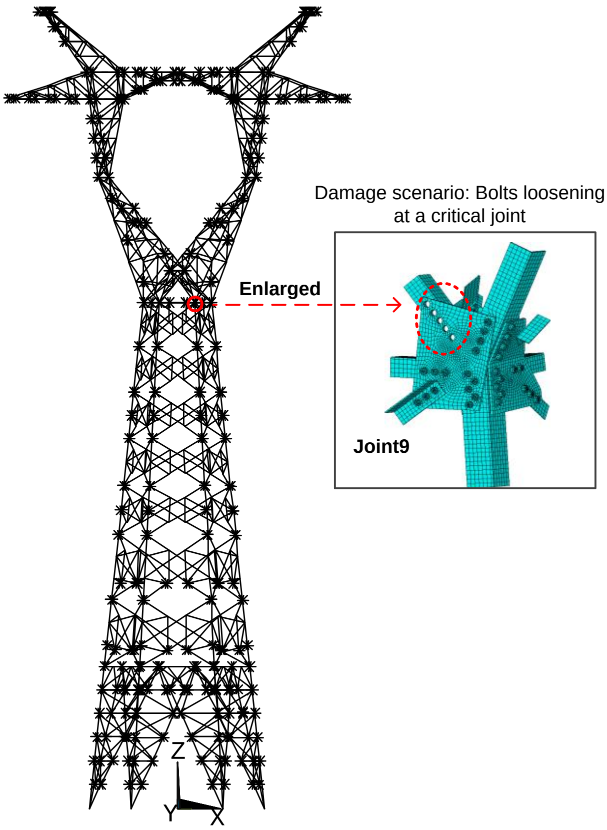

Fig. 7.10 The damage scenario of the transmission tower for damage detection study

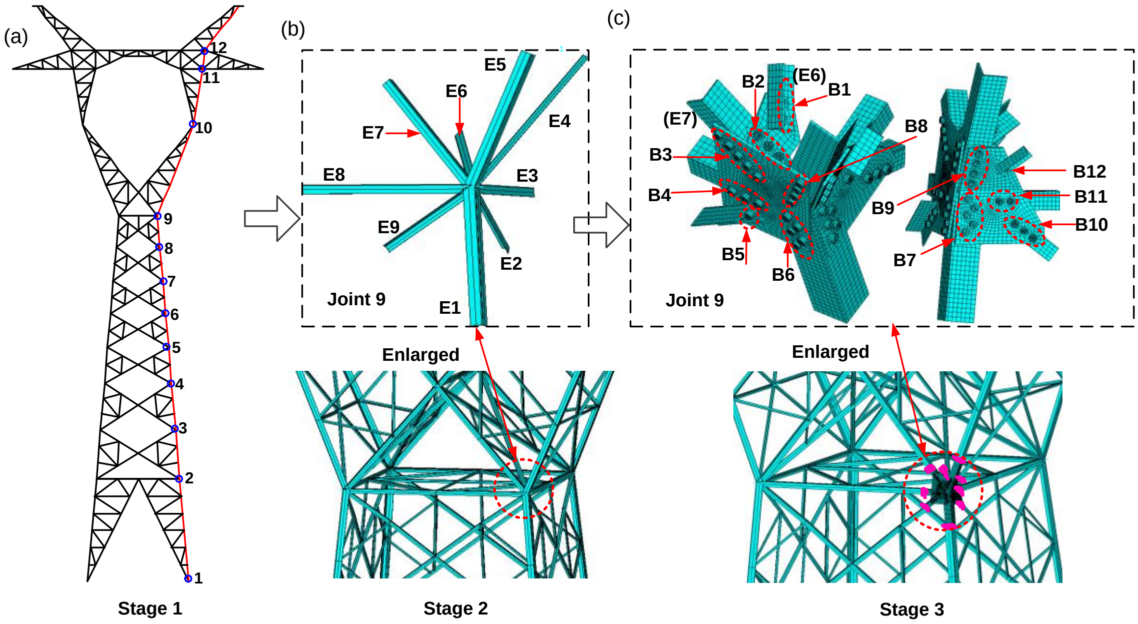

Fig. 7.11 Damage detection procedure: (a) Stage 1 based on the first-stage damage model; (b) Stage 2 based on the second-stage damage model; (c) Stage 3 based on the third-stage damage model.

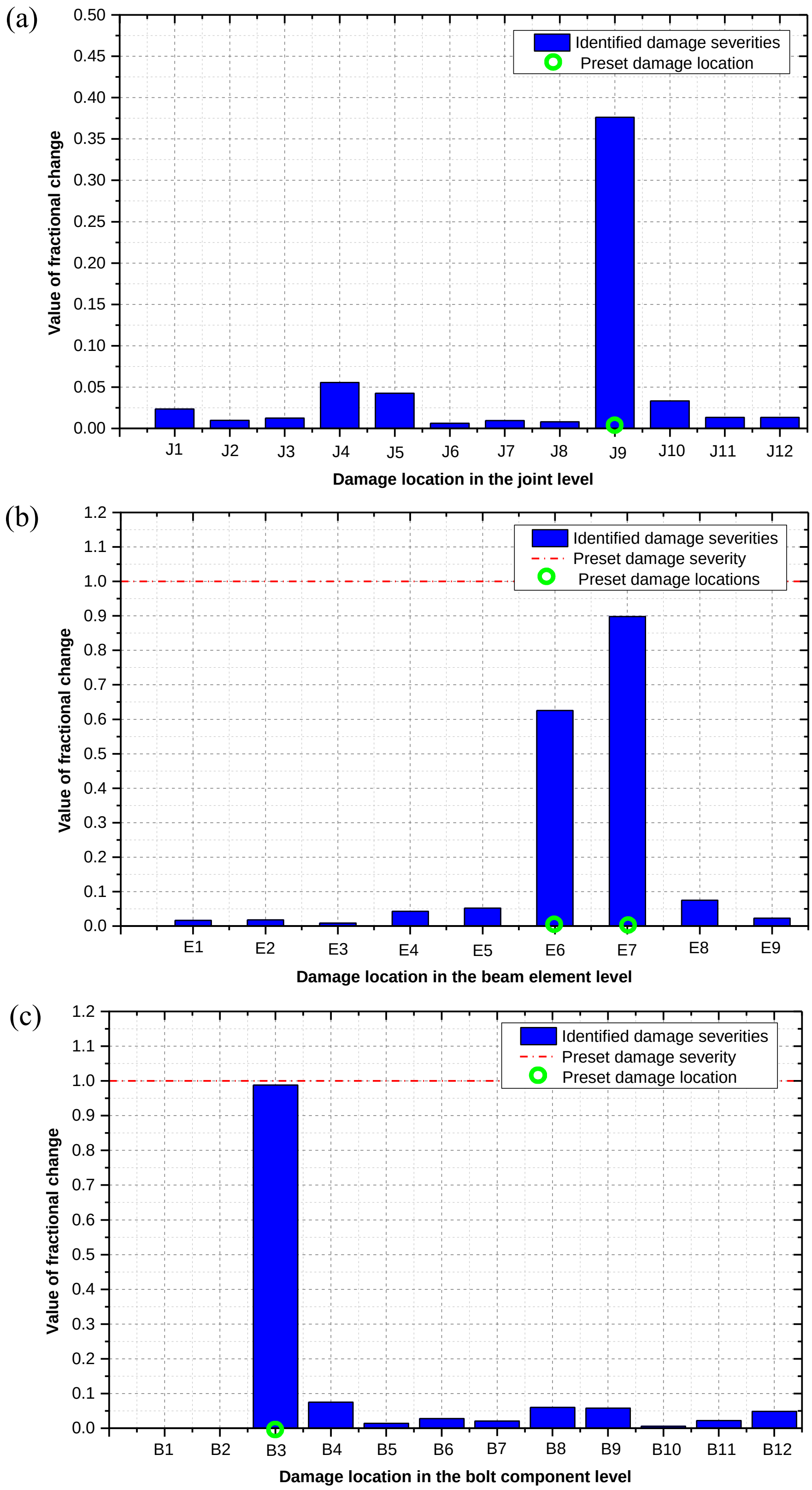

Fig. 7.12 Damage detection results: (a) Stage 1 based on the first-stage damage model; (b) Stage 2 based on the second-stage damage model; (c) Stage 3 based on the third-stage damage model.

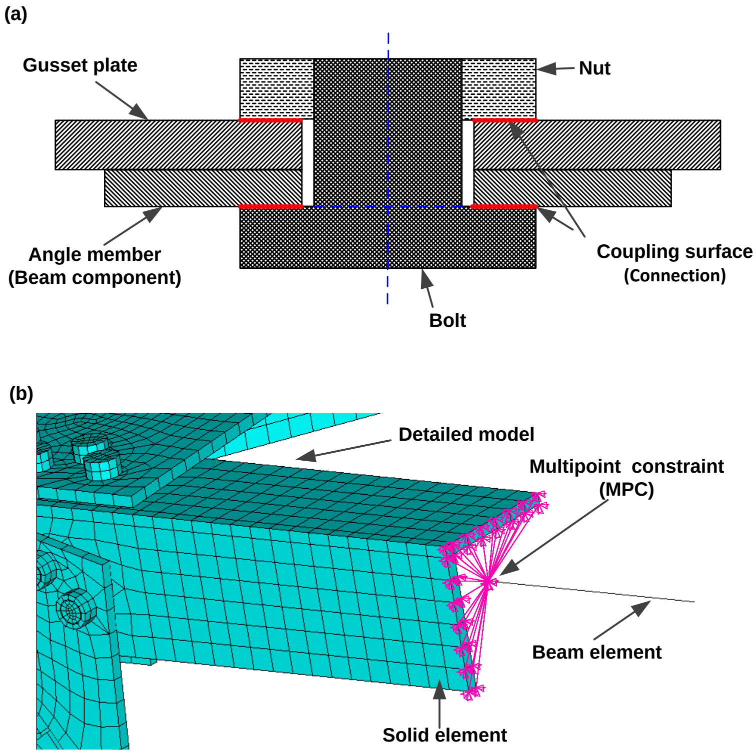

Fig. 7.13 Connections in the detailed joint model: (a) connection among bolt, angle member, and gusset plate by coupling the common nodes in interfaces; (b) connection between the solid185 and beam188 elements by MPC.

CHAPTER 8

MULTI-STAGE DAMAGE DETECTION OF A TRANSMISSION TOWER: EXPERIMENTAL VALIDATION

8.1 Introduction

In Chapter 7, the theoretical framework of a multi-stage damage detection strategy in cooperation with a multi-scale FE model has been proposed for damage detection of loosened bolts in a transmission tower. The numerical study has also been conducted, and the results showed that the proposed method could achieve satisfactory damage detection. However, before this method can be applied to real transmission towers, the experimental validation is necessary to ascertain the effects of uncertainties involved in the numerical study on the damage detection results. The uncertainties in the numerical study include uncertainties in input, modelling and measurement, which will be naturally involved in the experimental tests.

This chapter therefore presents an experimental investigation to validate the proposed method in Chapter 7. A physical scaled model of a large transmission tower was manufactured and installed in the laboratory. The beam FE model and the multi-scale model of the physical tower model have been introduced in Chapter 7. Section 8.2 will describe the experimental set-up and instrumentation in detail. The optimal sensor configuration, including 15 accelerometers and 7 strain gauges determined by the damage detection-oriented multi-type sensor placement method with multi-objective optimization in Chapter 7, will be installed on the physical tower model. An excitation system to generate proper external random loading to the tower will be introduced. Because of the installation of the excitation system to the physical tower model, the two FE models established in Chapter 7 have to be modified. Section 8.3

will introduce the two modified FE models as well as the model updating of the FE models to make the models more close to the intact state of the tower for the subsequent damage detection. The damage scenario of loosened bolts at Joint 9 discussed in Chapter 7 will be created in the physical tower model. Section 8.4 will then present the experimental damage detection results compared with the numerical damage detection results presented in Chapter 7. A summary of the works presented in this chapter is finally given in Section 8.5.

8.2 Experimental Set-up and Instrumentation

8.2.1 Physical Tower Model

In consideration of the space of the laboratory available, a 1:10 scaled physical model of the 5A-ZB2 HVPT tower (see Fig. 7.5(a)) was designed, manufactured, and installed in the Structural Dynamics Laboratory of The Hong Kong Polytechnic University. The 5A-ZB2 HVPT tower is designed by the State Grid Corporation of China (SGCC) and used in a 500 KV power grid. The prototype of the tower is 50.50m high and 22.02m wide. The physical tower model was designed according to the geometric similarity law (Ramu et al. 2011). The angle members and gusset plates were all fabricated according to the geometric ratio of 1:10. The physical tower model was constructed with 930 angle members, 402 gusset plates, 3649 bolts, and 779 joints. The further details on the physical model can be found in the references (Wang et al. 2016; Wang et al. 2017). It is noted that many of the bolted joints in the tower have a complex geometric composition and are composed by several angle members of different sizes with a series of bolts connected to gusset plates of different shapes. Fig, 8.1 shows the physical tower model, the experimental set-up and instrumentation. It can be seen that the four legs of the tower were firmly fixed on the strong floor of the laboratory through a series of bolts (see Fig. 8.1 (k)).

8.2.2 Excitation System

The 5A-ZB2 HVPT tower is commonly used in the transmission line system in China (Wong and Miller 2009). The longitudinal loading is one of its major loadings, which could be induced by the longitudinal imbalance of wire tensions produced by wind and/or ice loading on adjacent spans or from temperature difference on unequal spans (Ostendorp 1998). The real forces transmitted from the wires to the tower are complicated in the operation condition (Lam and Yin 2011). In the laboratory, only a simplified longitudinal loading was applied to the transmission tower at the wire position with some eccentricity in the horizontal direction so that the single force can generate both the longitudinal and torsional vibration of the tower. An exciter JZK-5 was therefore fixed on a steel frame and the steel frame was hanged by three steel wires, as shown in Fig.8.1 (a). The reason why the exciter and the steel frame were hanged is to provide least additional stiffness to the tower. The installation detail of the exciter is shown in Fig.8.1 (b), and the exciter was connected to the tower model through a soft spring (see Fig. 8.1 (d)) at the wire position with some eccentricity in the horizontal direction. To directly measure the excitation force acting on the tower, a force transducers B & K 8201 (see Fig. 8.1 (e)) was installed between the tower and the spring, as shown in Fig. 8.1 (c). The force transducer is a uniaxial transducer, which can measure the force in the axial direction only. The installation of a soft spring aims to reduce additional stiffness by the exciter connection to the tower. The schematic diagram of the installation of the exciter is illustrated in Fig. 8.2. The steel frame designed to install the exciter is shown in Fig.8.2 (b) and Fig. 8.2 (c). Because of the additional stiffness from the spring and the suspended steel frame in the longitudinal direction to the tower, the two FE models established in Chapter 7 shall be modified slightly. Such an additional stiffness is simulated by using a spring element Matrix 27 in ANSYS and added to the two FE models established in Chapter 7, as shown in Fig. 8.3.

8.2.3 Optimal Sensor Placement

The optimal sensor placement (OSP) has been performed in Section 7 .4.3 in Chapter 7 by using the damage detection-oriented multi-objective multi-type sensor placement method. The best OSP was determined by using the knee point-based method, which includes 15 accelerometers and 7 strain gauges. The 15 accelerometers (KD1010) with the sequence from A1 to A15 and the 7 strain gauges (BFH120-3AA (23)) with the sequence from S1 to S7 were accordingly installed in the physical tower model (Fig. 8.1 (f) and 8.1 (g)).

8.2.4 Measurement System and Test Cases

The measuring system for the damage detection of the transmission tower is illustrated in Fig.8.4. To start a dynamic test, the signal generator (B & K 3160-B-022), as shown in Fig. 8.1 (h), first generates a narrow-bandwidth white noise excitation signal. This signal is then sent to a power amplifier (YE5871), as shown in Fig.8.1 (i). The power amplifier works with the exciter to generate a random force to the tower through the spring. The random force recorded by the force sensor is amplified by the charge amplifier KD5008C, as shown in Fig.8.1 (j). At the same time, the acceleration responses of the excited tower are recorded by the accelerometers and amplified by the charge amplifier (KD5008C). The strain responses of the tower are recorded by the strain gauges and transmitted to the data acquisition system (KYOWA DB-120T-8), as shown in Fig. 8.1 (l). Finally, all the measured responses and the excitation force are transmitted to the computer through the data acquisition system (Kyowa EXD-100A) shown in Fig. 8.1 (m).

In the experimental investigation, the measurement system was calibrated and the two narrow-banded random excitations were generated. The first excitation with a bandwidth of 5 - 55 Hz was used to excite the transmission tower for the modal identification before and after damage. The second excitation with a bandwidth of 10 - 35 Hz was used to excite the transmission tower for damage detection of loosened bolts at Joint 9. All the input forces and corresponding responses before and after the damage were recorded with a sampling frequency of 512 Hz and a time duration of 60s.

8.3 Finite Elemental Models and Model Updating

The proposed multi-stage damage detection method involves the two FE models: the traditional beam FE model (see Fig 8.3 (a)) and the multi-scale FE model (see Fig 8.3 (b)) of the transmission tower. The FE models of the tower structure shall represent the actual tower structure as close as possible. Since the physical tower used in the experimental investigation involves an exciter connected to the tower through a soft spring and a suspended steel frame (see Fig. 8.1 (c) and Fig. 8.2), the FE models used in Chapter 7 shall have some minor modification. In this regard, a spring element Matrix 27 and a mass element MASS21 in ANSYS are added to the tower at the location of the exciter to represent the additional stiffness from the soft spring and the suspended steel frame and the additional mass from the force sensor and the shaft of the exciter, as shown in Fig.8.3. The initial stiffness of the spring element is set as $3N/mm$ and subject to modal updating. The additional mass is estimated as 134.5g and subject to modal updating. Furthermore, the weight of accelerometer (1.2 g per sensor) installed in the tower is also added to the node according to its locations, as shown in Fig. 8.5(a).

The modal analysis of the modified beam FE model is then carried out. The first six natural frequencies of the tower are listed in Table 8.2. The first three modes of vibration of the tower structure are global vibration-dominated mode shapes, as shown in Fig. 8.6. The higher order mode shapes are mainly the local vibration-dominated mode shapes for the primary bracing members of the tower. The modified bean FE model used for the subsequent damage detection needs to be updated in consideration of uncertainties in the modeling. The modified beam FE model (see Fig 8.3 (a)) is first updated by updating seven groups of parameters. The seven groups of parameters are listed in Table 8.1 and their locations are shown in Fig. 8.5(b). A two-step modal updating is successively conducted. The first step is to update the six groups of parameters in terms of the measured natural frequencies in the frequency domain. The six groups of parameters involve the five groups of additional masses and one group of additional stiffness. The second step is to update the modal damping ratios (the seventh group of the parameters) in terms of the measured structural responses in the time domain.

To obtain the measured natural frequencies of the physical tower, the first excitation with a bandwidth from 5 to 55Hz was used to excite the tower structure. The first six natural frequencies were identified and listed in the second column of Table 8.2. The first three modal damping ratios were identified and taken as initial values for the further updating in the time domain because the identification of modal damping ratio always involves uncertainties. The first objective function for the first step updating is the minimization of the relative errors of the first six natural frequencies $J_1 = \sum_{i=1}^{6} \frac{\left\| \omega_i^a - \omega_i^m \right\|_2}{\left\| \omega_i^m \right\|_2}$, where the ω_i^a and ω_i^m are the i^{th} analytical and measured natural frequency. The results of the updated parameters are listed in the rows 2 to 7 of Table 8.1. The computed natural frequencies of the beam FE model before and after updating are listed in Table 8.2 together with the measured frequencies. As indicated by the relative error in the sixth column of Table 8.2, the first six analytical frequencies computed from the updated beam FE model match the measured frequencies well with the maximum relative error less than 1%.

For the second step updating of the modal damping ratios in the time domain, the first three global modes (see Fig. 8.6) and accordingly the first three modal damping ratios are considered. The bandwidth of the excitation is further narrowed to 10 - 35 Hz for the second step model updating (see Fig. 8.7 (a)) and the subsequent damage detection (see Fig. 8.7 (b)). Within this excitation bandwidth, the first three modal damping ratios are selected as the updating parameters because the identified damping ratios often have relatively large uncertainties which will affect the structural response prediction significantly. The initial damping ratios for the first three modes of the physical tower were identified through the frequency response function (FRF). Therefore, the objective function for the second step updating is the minimization of the difference of the amplitudes of the structural responses $J_2 = \sum_{i=1}^{17} \frac{\left\| \mathbf{y}_i^a - \mathbf{y}_i^m \right\|_2}{\left\| \mathbf{y}_i^m \right\|_2}$ by updating the damping ratios, where $\mathbf{y}_i^a$ and $\mathbf{y}_i^m$ are the analytical and measured responses from the i^{th} sensor. Since the third measured natural frequency is 22.344 Hz, the measured responses are passed through a low-pass filter of 0 - 25 Hz for a better comparison. Accordingly, the first three modes of vibration of the beam FE model with the first step updating are used to compute the accelerations and strain responses through the modal superposition method as introduced in Chapter 3. The first three damping ratios of the tower before and after updating are listed in the eighth row of Table 8.1. To show the accuracy of the second step updating, the responses of two accelerometers, A5 in the x-direction and A6 in the y-direction installed at Joint 9, and a strain gauge S2 installed in an element close to Joint 9 are selected for comparison with the computed responses. The locations of the above three sensors are shown in Fig. 8.8. The measured responses and computed response from the updated model in their first five seconds are compared with each other and shown in Fig. 8.9. It can be seen that both the computed acceleration and strain responses can match well with their counterparts. Similar observations can be found for other responses.

For the multi-scale FE model used in Chapter 7, a local detailed FE model using solid elements and a global FE model using beam elements are integrated. The updated parameters listed in Table 8.1 from the beam FE model can be directly applied to the modified multi-scale FE model. Moreover, the multi-scale FE model of the transmission tower without installing an exciter has been updated by Wang et al. (2016) by using a Kriging meta-method. A total of 13 updating parameters were selected through a parameter sensitivity analysis, in which 11 updated parameters refer to the global beam model and 2 updated parameters refer to the local detailed model. The updated two parameters are directly used in this study. The modal analysis is then carried out on the modified multi-scale FE model with the updated global parameters and local parameters. The first six natural frequencies computed are listed in the seventh column of Table 8.2. As indicated in Table 8.2, the modal frequencies of the multi-scale FE model have minor increment after embedding the local detail joint model. The first six computed natural frequencies of the multi-scale model can also match with the measured natural frequencies with the maximum relative error of 1.948% in the fifth modes. Since only the first three modes will be considered in the subsequent damage detection, the modified multi-scale FE model is accurate enough as far as the first three natural frequencies concerned. Thus, the modified multi-scale FE model does not need further model updating in this study.

As discussed in Chapter 7, the updated beam FE model of the transmission tower will be used for the first and second stage damage detection, while the modified multi-scale FE model will be used for the third-stage damage detection.

8.4 Experimental Results and Comparison

The damage (loosened bolts) occurring at a joint is common local damage for a large transmission tower, and the identification of such local damage of loosened bolts at joints of the transmission tower is a very challenging issue. In this experimental investigation, the damage scenario used in Chapter 7, with a set of loosened bolts of the member E7at a critical Joint 9, is considered so that the experimental results can be compared with the computed results directly. To this point, the set of bolts denoted as B3 in Chapter 7 is totally removed to simulate the bolt loosening damage (see Fig. 8.10 (b)). The damage detection of loosened bolts of the transmission tower under the preset damage scenario is then conducted by using the structural responses recorded by the sensors at their optimal sensor placements. In the experimental investigation, the first excitation with a bandwidth from 5 to 55 Hz is used for natural frequency identification before and after damage, and the second excitation with a bandwidth from 10 to 35Hz is used for the proposed response covariance-based multi-stage damage detection.

The proposed damage detection method is based on the fact that any change in the physical property of a structure will alter its natural frequencies and dynamic responses. The variance of the first six frequencies before and after the bolt loosening at Joint 9 are first identified and listed in Table 8.3. Noted that the first three frequencies have a relatively large change due to the damage. However, as indicated in Table 8.2 and Table 8.3, the relative change of the natural frequencies of the 4th and 5th modes are 0.322% and 0.950% only. These small changes are larger than the variances of the frequencies 0.095% and 0.576% induced by damage in the 4th and 5th modes. Thus, to reduce the effect of modeling uncertainties, only the information from the first three modes (16.283, 16.935, and 22.339 Hz) are considered in the experimental damage detection. The input force was measured and the time history of the force from the 6.5th to 16.5th seconds, as plotted in Fig. 8.7 (b), is used for the following multi-stage damage detection. The acceleration and strain responses from the 6.5th to 16.5th seconds are according recorded and used for the subsequent damage detection. By taking the sensors A5, A6 and S2 as example, the measured responses of the tower with loosened bolts and the computed responses from the updated beam model without damage are compared in Fig. 8.11. It is clearly observed that there are the discrepancies in the measured and computed responses, which indicates that the bolt loosening really affects the dynamic responses. Therefore, damage detection of this local damage is possible by using the proposed method. The three-stage damage detection method proposed in Chapter 7 is now applied to the physical tower model and the identified results for each damage detection stage will be described in the following and compared with those from the numerical studies.

8.4.1 The First Stage Damage Detection

In the first stage, twelve suspicious rigid joints as used in Chapter 7 (see Fig. 7.6) are selected and the locations of the damaged joints will be identified by using the response covariance-based multi-sensing damage detection method introduced in the previous chapters. In this stage, the traditional beam model of the tower is used, in which a joint is composed by one node with several beam elements connected. This joint can be seen as a substructure or a super-element (see Fig. 8.12 (a)) in the beam model of the tower. The loosened bolts of the members connected to the joint will certainly affect the total stiffness of the joint contributed by all the members connected to the joint. This effect is actually accounted by introducing an equivalent damage parameter for a suspicious joint in the first stage damage detection based on the traditional beam model. That is, an equivalent damage parameter is assigned to the stiffness matrix of each suspicious super-element (joint). Therefore, damage detection is now started from searching damaged joints. As the beam FE model includes 12 super-elements (joints), there are 12 equivalent damage parameters to be identified. The equivalent damage parameters $\Delta\boldsymbol{\alpha}^{sup}$ identified in the first stage are plotted in Fig. 8.13 (a). The damaged Joint 9 is satisfactorily identified with 32.97% stiffness reduction, because the equivalent stiffness reductions at other joints are incomparable with that at Joint 9. As compared with Fig. 8.13 (a), the identified damage severity 32.97% in the experiment is slightly smaller than that of 37.76% stiffness reduction from the numerical study. When comparing the false alarms in the experiment and numerical studies, there are three large false alarms are observed at Joint 7, Joint 8 and Joint 11 due to the effect of the neighboring damaged joint 9 as well as the uncertainties from the measurement and the FE model.

8.4.2 The Second Stage Damage Detection

The damaged region is located at Joint 9 after the first stage damage detection, while the other joints are excluded from further investigation in this stage. Because a joint often consists of a number of angle members and these angle members may be connected in series or parallel, the second stage is therefore to find out which members at the damaged joint are suspicious to loosened bolts. This stage detection is conducted also using the traditional beam model (see Fig. 8.12 (b)) of the tower. In Stage 2, the super-element of Joint 9 is restored to nine ungrouped beam elements. As this joint consists of 9 beam elements, there are nine damage parameters to be identified. For the easy recognition in the subsequent detection, each beam is assigned a unique name as E1, E2, …, E9 (see Fig. 7.11 (b)). The damage parameters $\Delta\boldsymbol{\alpha}^{\text{ele}}$ identified in the second stage are depicted in Fig. 8.13 (b). Both the damage location and the severity are successfully identified in the beam E7 with 91.85% stiffness reduction, which is similar to the numerical identification result with 89.78% stiffness reduction. The damage location in the beam E6 is also identified but only 24.85% stiffness reduction is identified, which is smaller than the numerical identification result with 62.52% stiffness reduction. As shown in Fig. 7.11(c) and Fig. 8.10, the beam E6 is a subordinate component connected to the beam E7, and the stiffness reduction of the tower structure due to the damage of the beam E6 is actually much smaller than that due to the beam E7, based on the analysis of the natural frequency of the FE model. Accordingly, the measured responses are less sensitive to the beam E6. Furthermore, the uncertainties in the measurement and the FE model are inevitable, which is a possible reason for the poorer identification result of the beam E6 found in the experimental investigation.

8.4.3 The Third Stage Damage Detection

The bolted joint (Joint 9) has a complex geometric composition, constructed of angle members, gusset plates, and bolts. The accurate modelling of the bolt joints using solid elements (see Fig. 8.12 (c)) is necessary but the traditional FE model established by beam elements (Fig. 8.12 (b)) could not accommodate. In Stage 3, the local detailed FE model of Joint 9 using solid elements and the global FE model using beam elements are integrated. As the detailed model of Joint 9 includes 12 sets of bolts, there should be 12 damage parameters for identification, in which each set of bolts is assigned a unique name as B1, B2, …, B12 (see Fig. 7.11 (c)). As demonstrated by numerical study in Chapter 7, solving damage parameters $\Delta\boldsymbol{\alpha}^{\text{bol}}$ is much more complicated than that in the first and second stages. It needs to take into consideration the damage identification results of Stage 2, in which the beams E7 and E6 are identified as two suspicious elements. According to the composition of Joint 9 in the detailed model, as shown in Fig. 7.11 (c) and Fig. 8.10, the set of bolts B3 is the only damage source for the beam E7 but it is able to influence the beam E6 which is directly concerted to the beam E7. If the bolt set B3 is damaged, the beam E7 and the beam E6 will be separated from Joint 9 no matter whether the bolt sets B1 and/or B2 are loosened or not. Similar with the numerical study in Chapter 7, B1 and B2 are assumed unloosened to avoid the multiple-solution problem in damage detection and accordingly the reductions of stiffness of B1 and B2 are set as zeros. The damage severities (stiffness reductions) of all the other beams identified in the second-stage are thus assigned to all the bolt sets attached to Joint 9 as their initial values. Specifically, the stiffness reductions for the beam elements, namely 0.9185 (E7), 0.1470 (E8), 0.1256 (E9), 0.1063(E1), 0.1063(E1), 0.1329 (E5), 0.1329(E5), 0.0470 (E2), 0.1705 (E3), and 0.0845 (E4), are used as the initial values of damage parameters $(\Delta\boldsymbol{\alpha}^{\text{bol}})^0$ for B3, B4, B5, B6, B7, B8, B9, B10, B11, and B12 respectively. The initial values of the CBMS damage index $(\mathbf{V}_{\text{pq}}^{c})^0 = \mathbf{V}_{\text{pq}}^{c}[(\Delta\boldsymbol{\alpha}^{\text{bol}})^0 \triangleq \Delta\boldsymbol{\alpha}^{\text{ele}}]$ in this stage are then computed after the initial values of the stiffness reductions of all the bolt sets are assigned. The damage parameters $\Delta\boldsymbol{\alpha}^{\text{bol}}$ are finally identified and depicted in Fig. 8.13 (c). The damage severity of B3 is accurately identified, which is increased from the initial 91.85% stiffness reduction to the 96.51% stiffness reduction. When compared with the numerical identification, the identified damage severity of B3 from the experimental study is slightly smaller than that from the numerical study, and the false alarms are relatively larger from the experimental study due to some uncertainties in the measurement and the FE model. After three-stage damage detection, the loosened bolt set B3 is successfully identified, which is close to the preset damage of totally removing the bolt set B3 with 100% stiffness reduction.

After successful damage detection in the above three stages, the multi-scale FE model is updated to the damaged state to represent the damaged physical tower. The computed responses of the tower after damage are then compared with the directly measured responses. By taking the sensors A5, A6 and S2 as example again, the measured responses of the tower with loosened bolts and the computed responses from the damaged multi-scale FE model are compared in Fig. 8.14. It is clearly observed that the measured and computed responses are matched with each other much better than the comparative responses shown in Fig. 8.11 for the tower before damage. This result indicates that the damage detection really converges to the correct damage state with the preset loosened bolts in the physical tower. As indicated in Fig. 8.14, there are slight discrepancies between the computed and measured responses, which may result from for the falsely identified stiffness reduction in the undamaged bolt sets (See Fig. 8.13). Other possible reasons for the discrepancies may come from the ideal coupling of the bolt connection without considering their nonlinearity and from some modeling errors of the MPC connection for the global and local models used in the multi-scale FE model.

8.5 Summary

This chapter has experimentally validated the response covariance-based multi-stage damage detection strategy incorporating with the multi-stage damage models and the multi-scale FE model for the damage detection of loosened bolts in a large transmission tower testbed. The uncertainties in input, modelling and measurement are considered in the experimental tests. The model updating is first conducted, and the damage detection is then performed in three stages step by step. The experimental results of damage detection showed that accurate damage localization and satisfactory damage quantification could be yielded by using the proposed damage detection method and the optimal sensor configuration determined by the multi-objective multi-type sensor optimal placement method proposed in Chapter 5. Furthermore, the numerical and experimental damage detection results are compared with each other. The comparison revealed that similar identification result is achieved for successful damage detection. It can be concluded that the proposed damage detection method and the associated OSP method are feasible and effective for damage detection of a large transmission tower. Some conclusions and recommendations regarding the whole thesis will be given in the next chapter.

Table 8.1 Initial and updated parameters of the tower structure

Group of updating parameters	Number of Parameters	Initial value	Updated value
Lump mass-1(g)	2	16.736	7.763
Lump mass-2 (g)	4	49.478	76.478
Lump mass-3 (g)	8	8.895	13.950
Lump mass-4 (g)	16	0.858	6.858
Lump mass-5 (g)	2	62.250	52.252
Lateral stiffness (N/mm)	1	3	3.780
Damping ratio (%)	3	0.58, 0.18, 0.21	0.47, 0.10, 0.11

Table 8.2 Comparison of measured and analytical modal frequencies

Mode No.	Measured (Hz)	Beam model (Before updating)		Beam model (After updating)		Multi-scale model	
		Analytical (Hz)	Error (%)	Analytical (Hz)	Error (%)	Analytical (Hz)	Error (%)
1	16.281	16.220	-0.375	16.283	0.012	16.283	0.012
2	16.938	16.804	-0.791	16.935	-0.018	16.940	0.012
3	22.344	23.251	4.059	22.339	-0.022	22.390	0.206
4	32.656	33.169	1.571	32.761	0.322	33.016	1.102
5	43.375	44.876	3.461	43.787	0.950	44.220	1.948
6	43.875	44.921	2.384	44.003	0.292	44.430	1.265

Table 8.3 Comparison of the change of modal frequencies before and after damage

Mode No.	Modal frequencies		Variance of frequency (%)
	Before damage	After damage	
1	16.281	16.125	0.958
2	16.938	16.406	3.141
3	22.344	22.000	1.540
4	32.656	32.625	0.095
5	43.375	43.125	0.576
6	43.875	43.734	0.321

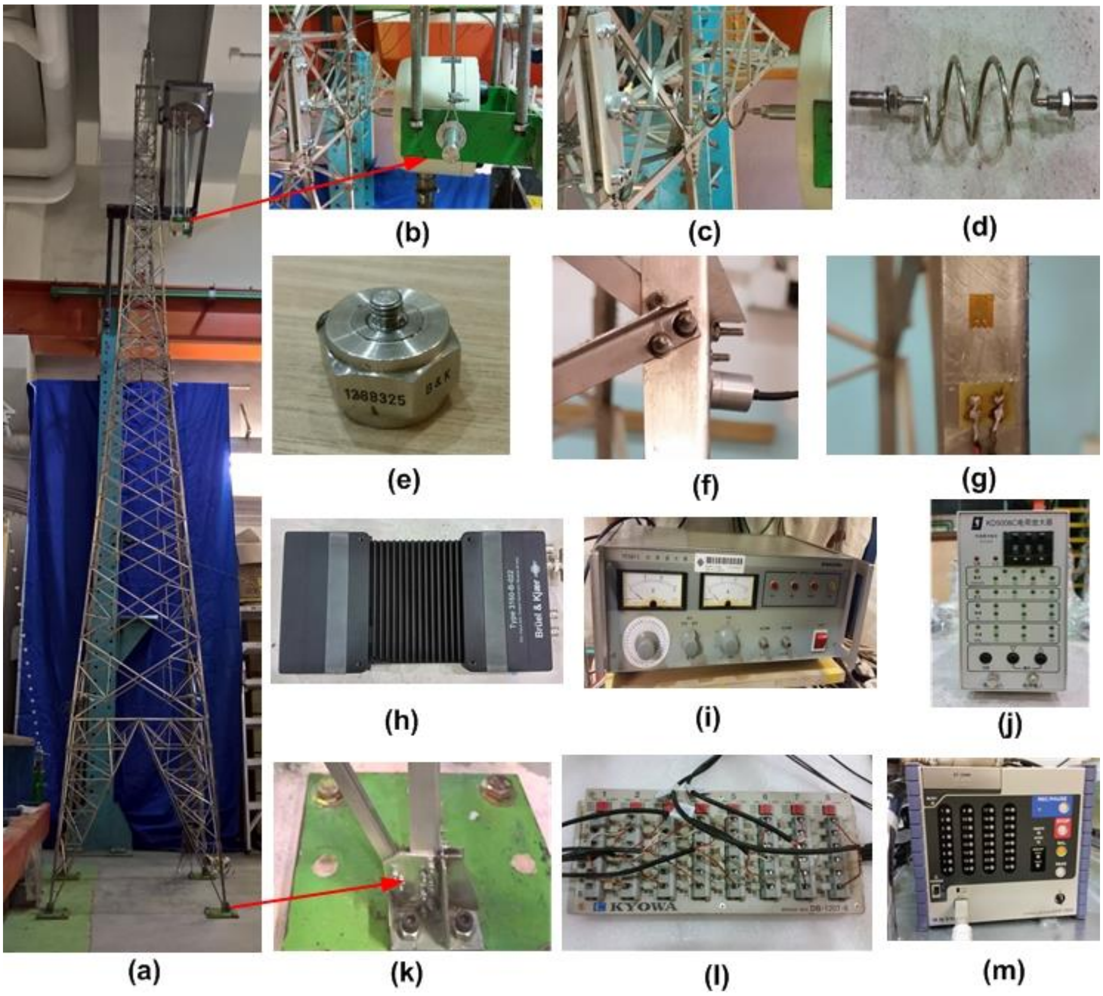

Fig. 8.1 The experimental set-up and instrumentation for transmission tower model: (a) the whole view of the set-up of the physical model; (b) the exciter JZK-5; (c) the connection between the tower and the exciter; (d) the soft spring; (e) the force transducers B & K 8201; (f) the accelerometer KD 1010; (g) the strain gauge BFH120-3AA (23); (h) the signal generator B & K 3160-B-022; (i) the power amplifier YE5871; (j) the charge amplifiers KD5008C; (k) a bolted joint support; (l) the bridge box KYOWA DB-120T-8; and (m) the data logger Kyowa EXD-100A.

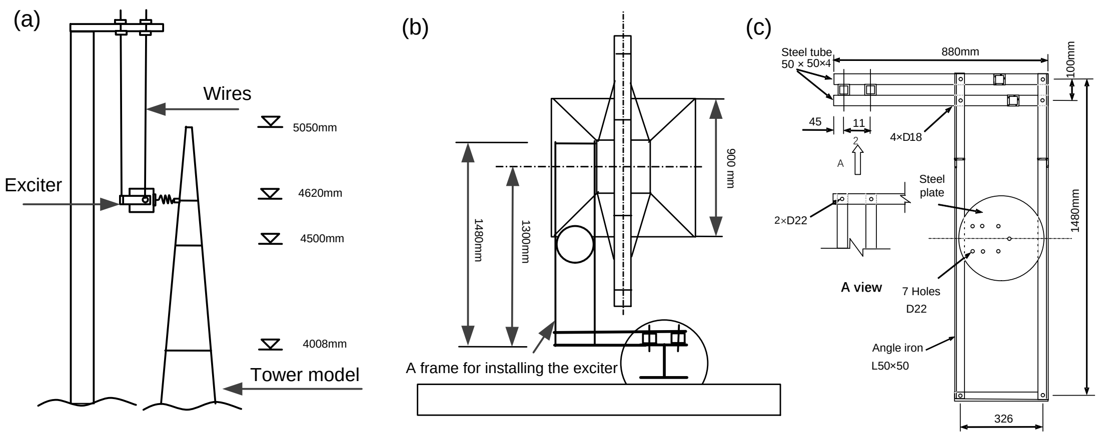

Fig. 8.2 The schematic diagram of the hanging exciter and the steel frame: (a) the side view of the exciter system and the transmission tower; (b) the top view of the suspended steel frame for installing the exciter and the transmission tower; and (c) the detailed drawing of the suspended steel frame.

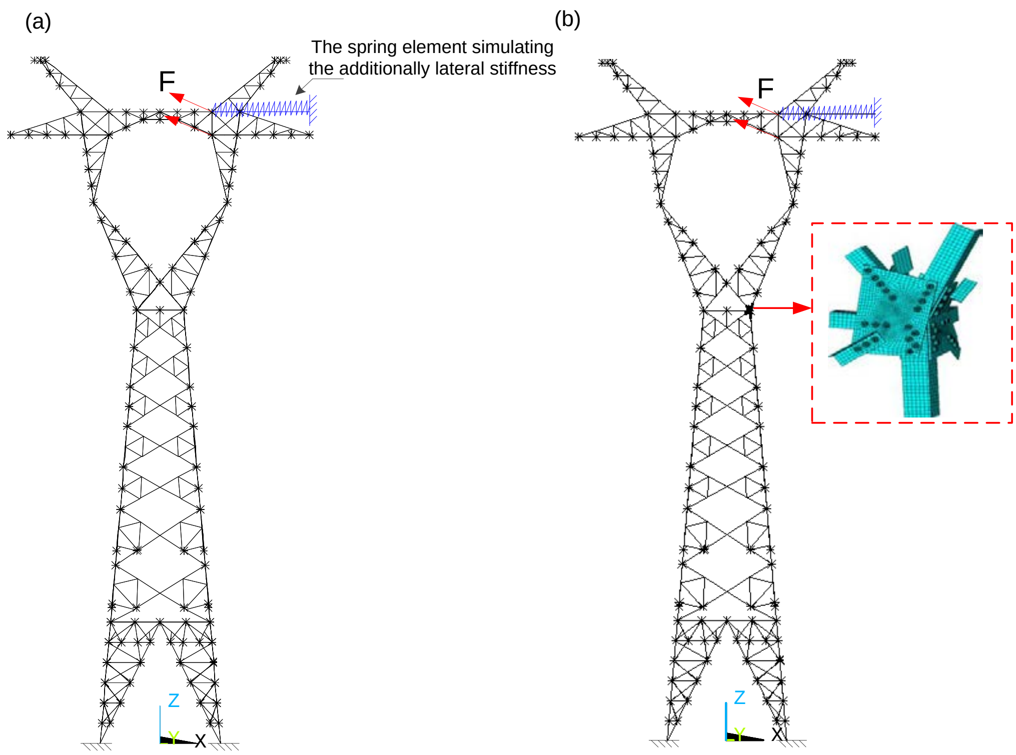

Fig. 8.3 The modified finite element models of the transmission tower considering the additionally lateral stiffness: (a) the modified beam FE model of the tower; and (b) the modified multi-scale FE model of the tower.

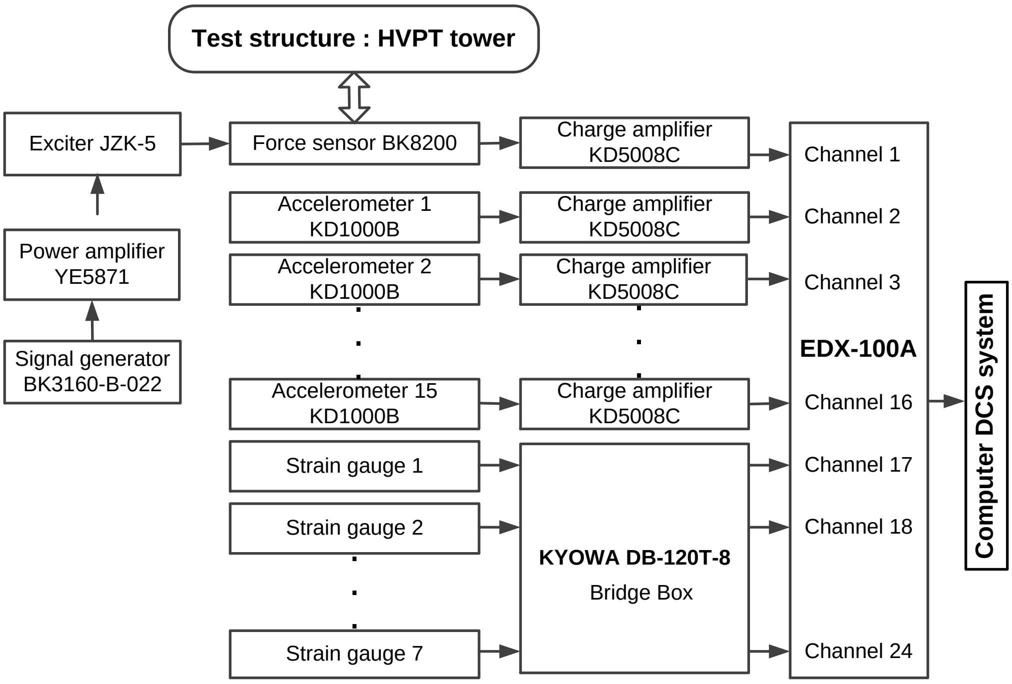

Fig. 8.4 Measurement system for the damage detection of the transmission tower

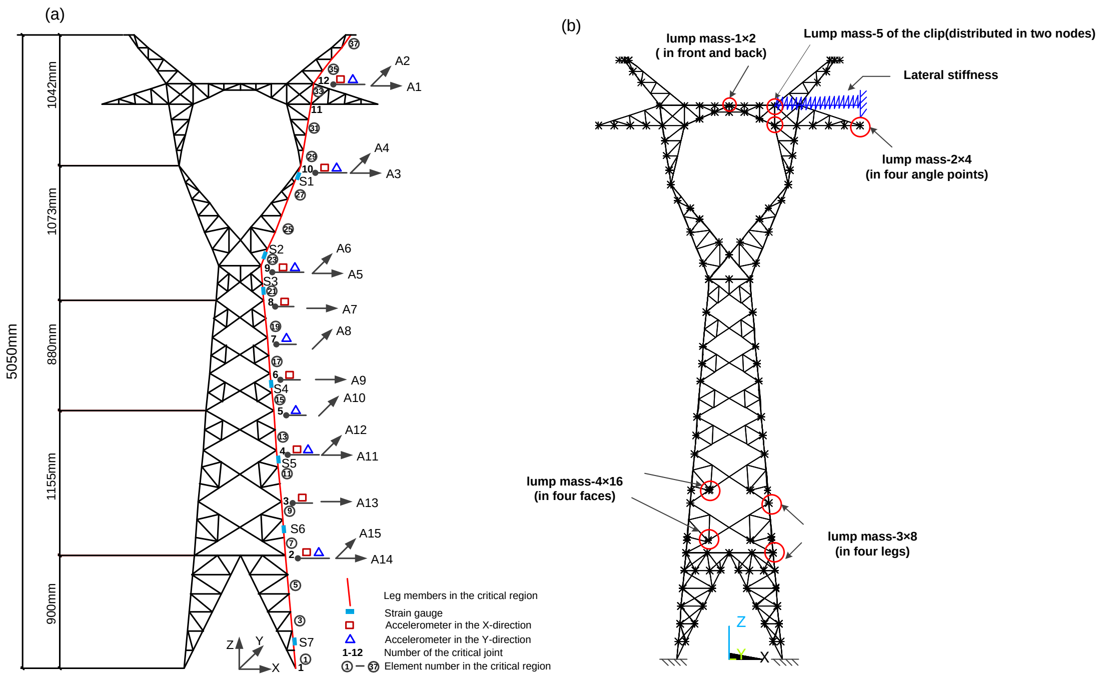

Fig. 8.5 The locations of sensors and the selected updating parameters: (a) the optimal sensor placement; and (b) the updating parameters for the modified beam FE model of the transmission tower.

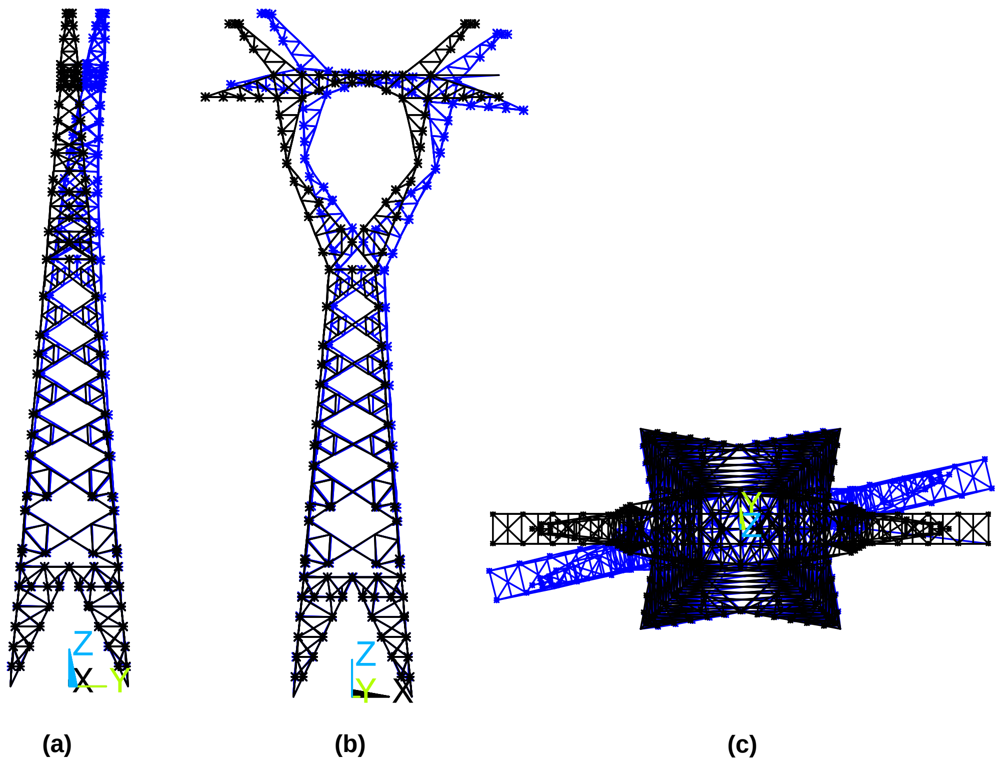

Fig. 8.6 The first three mode shapes of the transmission tower: (a) the first mode shape (view in x-direction); (b) the second mode shape (view in the y-direction); and (c) the third mode shape (view in z-direction).

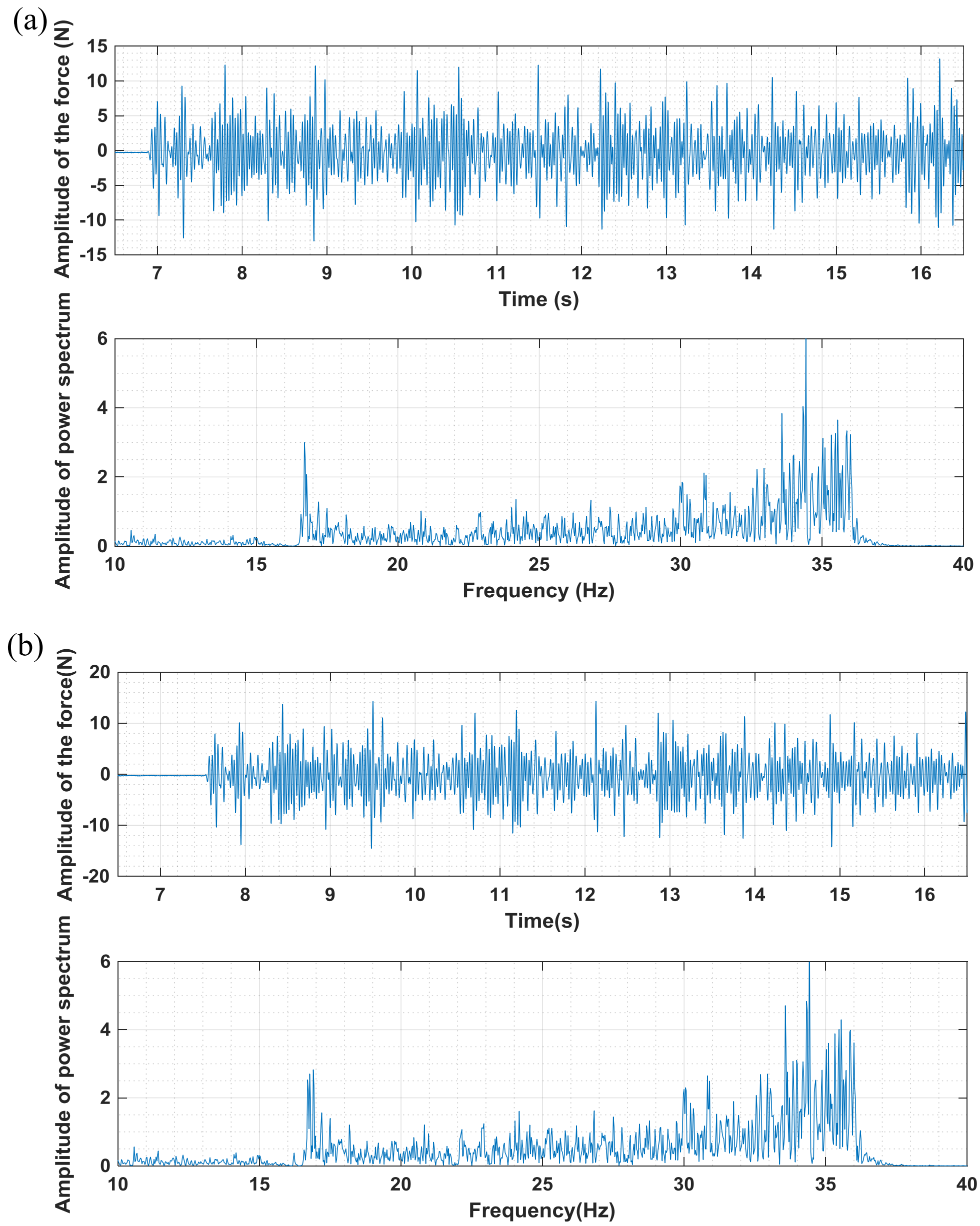

Fig. 8.7 The time histories and power spectrums of the measured longitudinal forces (10 - 35 Hz) in the y-direction: (a) the measured force before damage for the second step model updating; and (b) the measured force after damage for damage detection.

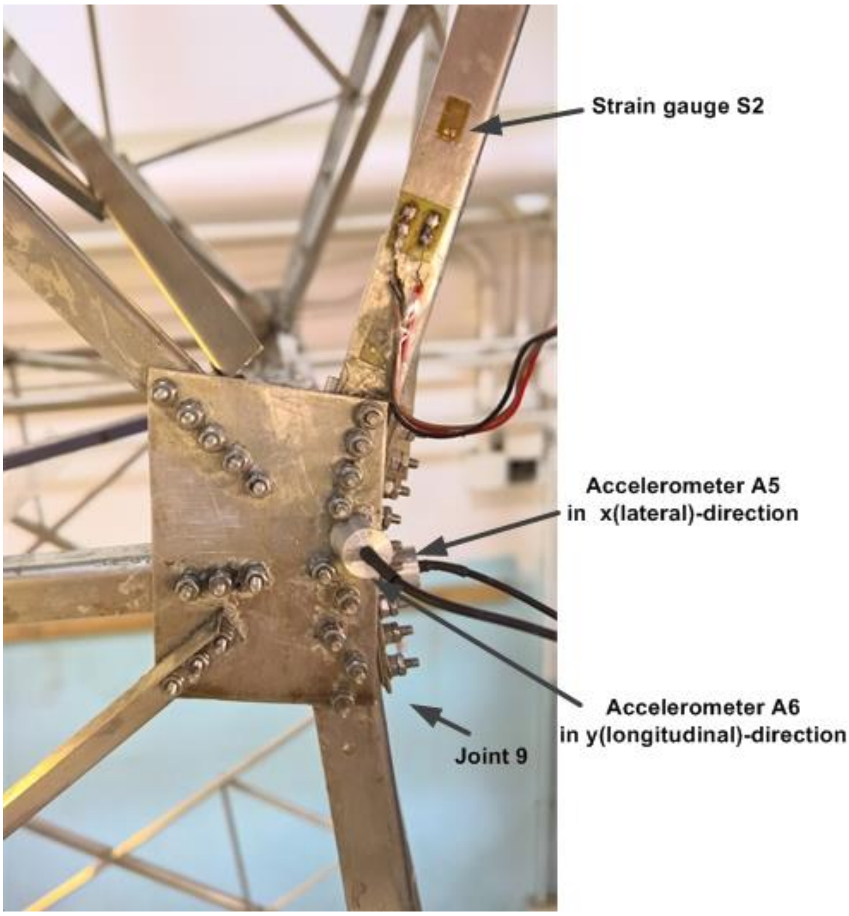

Fig. 8.8 The locations of two accelerometers (A5 and A6) installed at Joint 9 and the strain gauge (S2) installed on an angle member close to Joint 9.

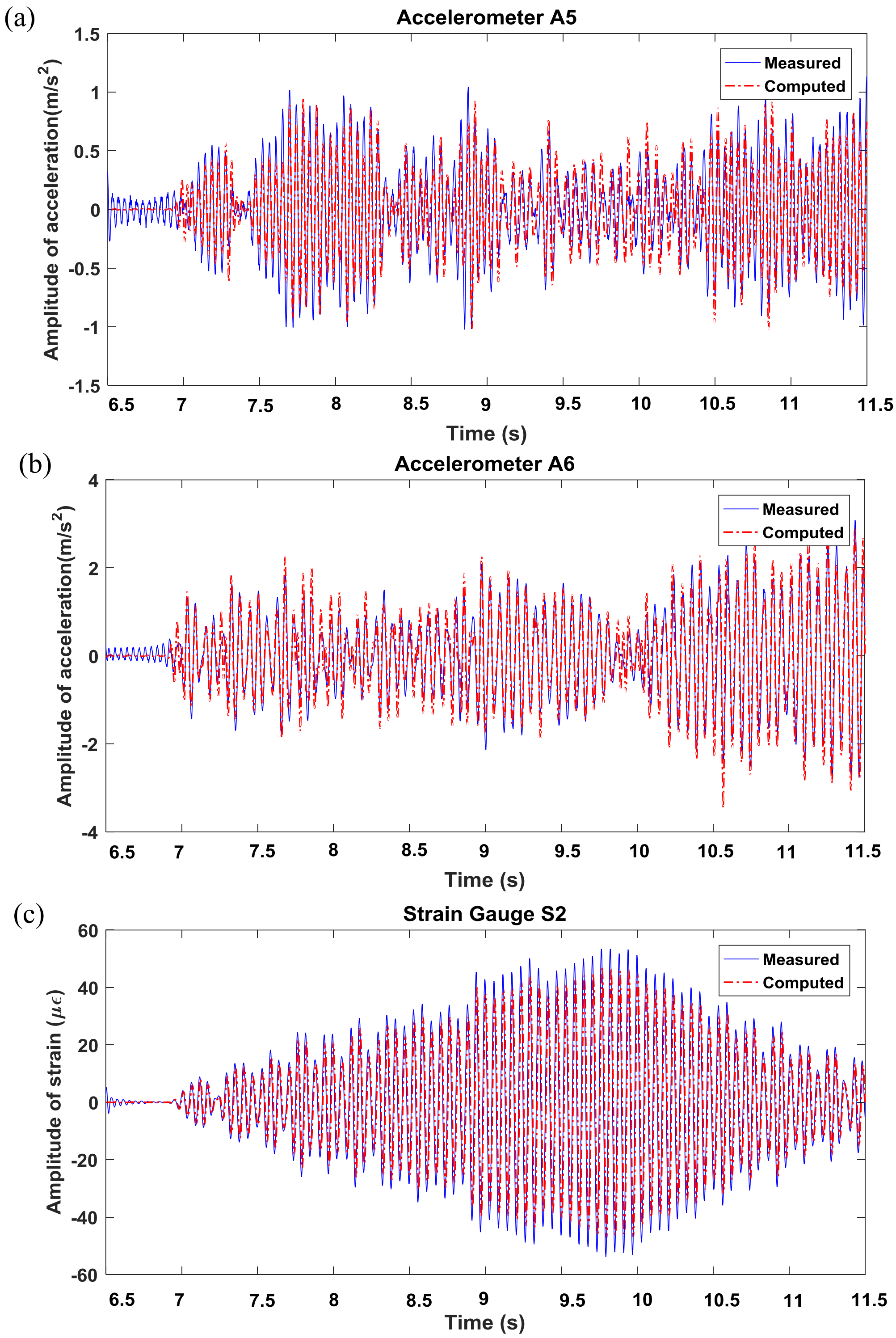

Fig. 8.9 Comparison of measured and computed responses of the tower after model updating: (a) the acceleration response (A5) at Joint 9 in x-direction; (b) the acceleration response (A6) at Joint 9 in y-direction; and (c) the strain response (S2) in an element closed to the Joint 9.

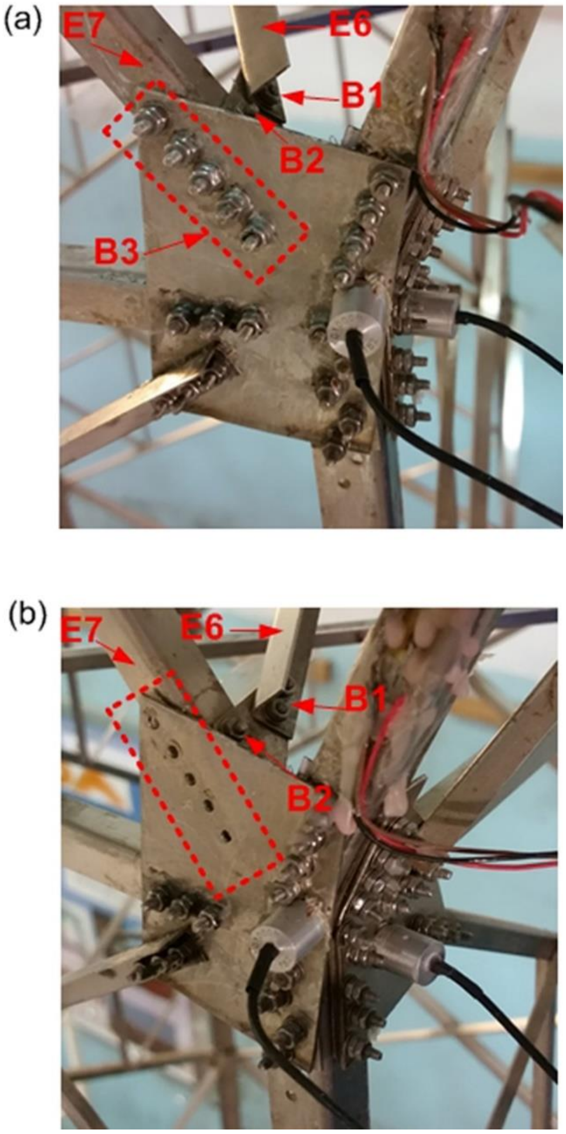

Fig. 8.10 The partial view for Joint 9 in the transmission tower before and after damage: (a) before the damage of loosened bolts; and (b) after the damage of loosened bolts.

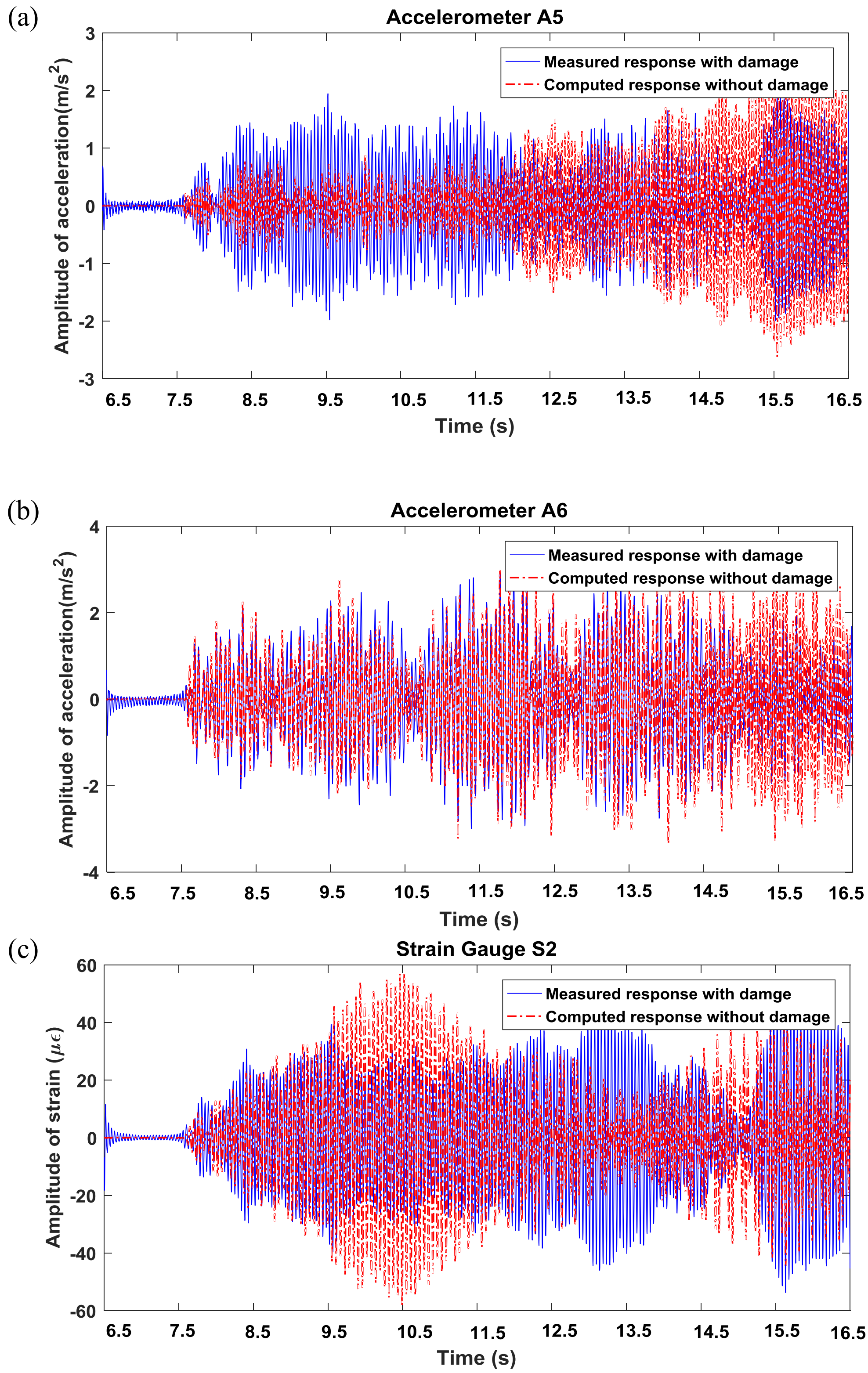

Fig. 8.11 Comparison of the measured responses with damage with the computed responses without damage from the intact beam FE model: (a) the acceleration response (A5) at Joint9 in x-direction; (b) the acceleration response (A6) at Joint 9 in y-direction; and (c) the strain response (S2) in an element closed to the Joint 9.

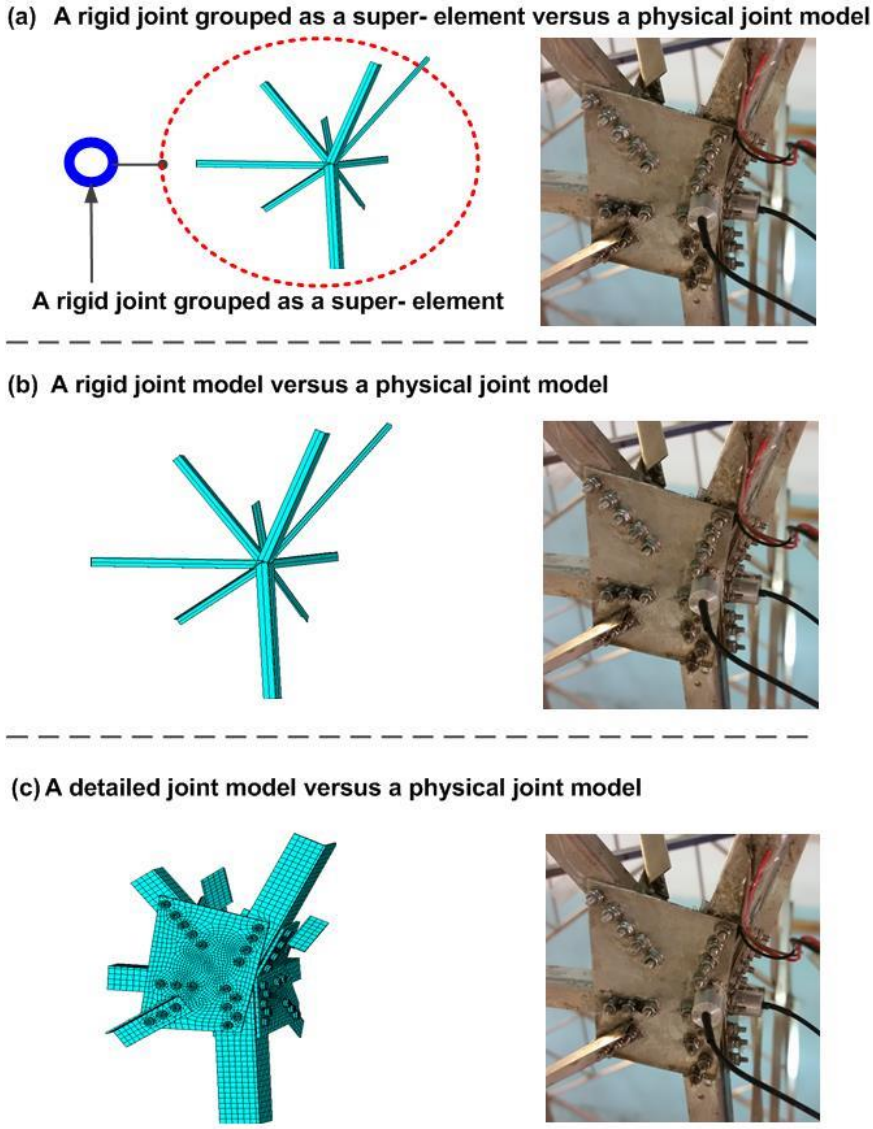

Fig. 8.12 Comparison of the FE model and the physical model of Joint 9 in three stages: (a) the super-element based model vs the physical model in stage one; (b) the rigid joint model consisted of several beam elements vs the physical model in stage two; and (c) the detailed joint model vs the physical model in stage three.

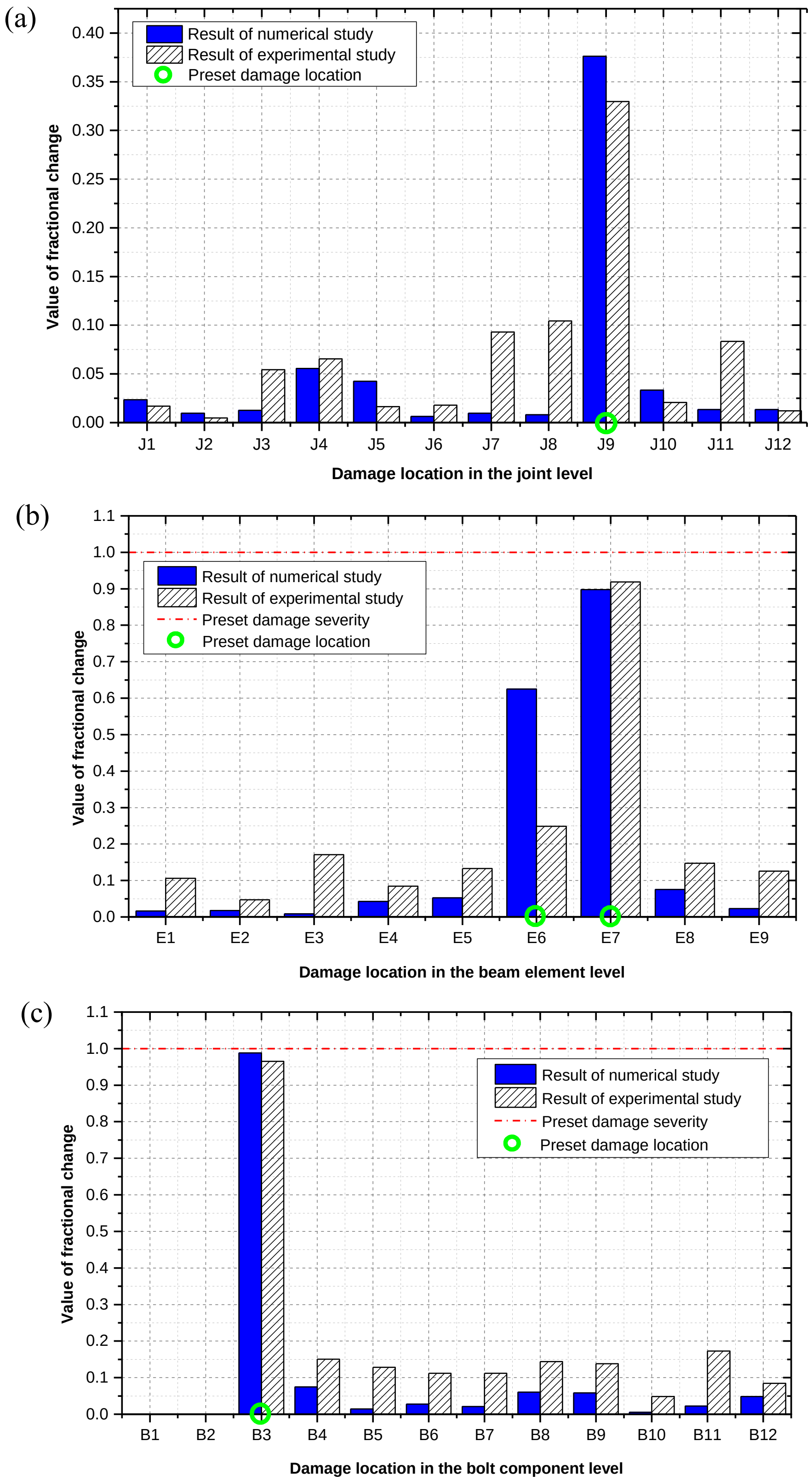

Fig. 8.13 Comparison of damage detection results between numerical and experimental studies: (a) using the first-stage damage model; (b) using the second-stage damage model; and (c) using the third-stage damage model.

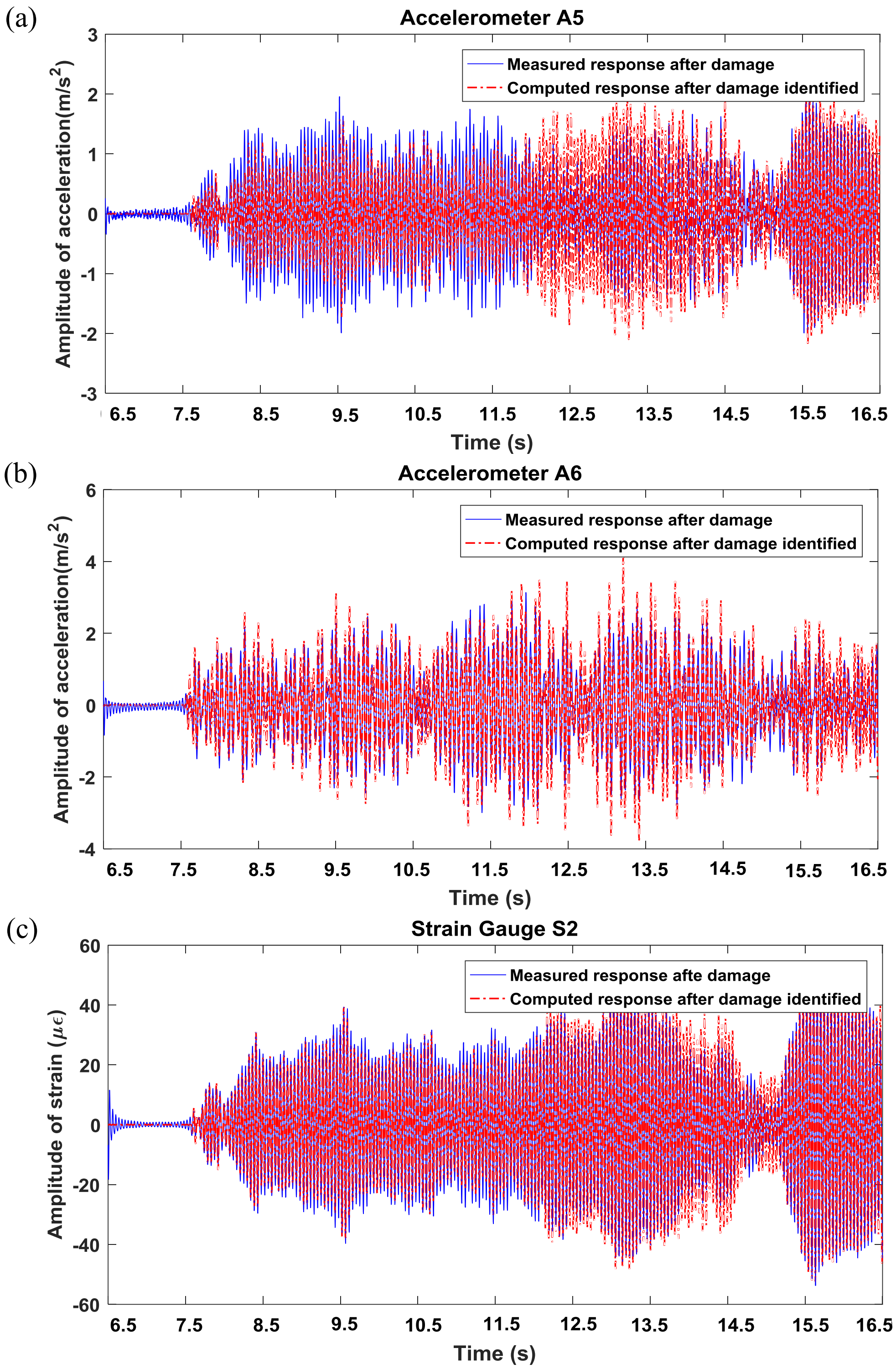

Fig. 8.14 Comparison of the measured responses of the tower with loosened bolts with the computed responses after damage identification based on the multi-scale FE model: (a) the acceleration response (A5) at Joint 9 in x-direction; (b) the acceleration response (A6) at Joint 9 in y-direction; and (c) the strain response (S2) in an element closed to the Joint 9.

CHAPTER 9

CONCLUSIONS AND RECOMMENDATIONS

9.1 Conclusions

This thesis focuses on vibration-based damage detection of civil structures with the new developments of a sensitive damage detection index, multi-objective optimal sensor placement, optimal multi-type sensor placement, and multi-stage damage detection. The originality of this study is attributed to: (1) the development of a response covariance-based multi-sensing damage detection index; (2) the advancement of two response covariance-based objective functions for optimal sensor placement (OSP); (3) the development of a structural damage detection-oriented multi-type sensor placement method with multi-objective optimization; (4) the extension of the response covariance-based damage detection method to the multi-stage damage detection method for large structures; and (5) the conduction of the experiments on a nine-bay three-dimensional frame structure and a transmission tower to validate the proposed methods. The major contributions and conclusions of this thesis could be summarized as follows:

1. A response covariance-based multi-sensing (CBMS) damage index in the time-domain and the associated sensitivity-based damage detection method has been proposed in this thesis. Heterogeneous data from multi-type sensors can be normalized and integrated into a united damage index such that the proposed damage detection method can effectively use multi-sensing information including both global and local responses (acceleration, displacement, and strain) for local damage detection. The feasibility of the new damage index has been confirmed through the numerical study by using an overhanging beam with multiple damaged elements. It can come to the conclusions that the CBMS vector is insensitive to the measurement noise but sensitive

to damage and that the dual-type sensor configuration (accelerometer and strain gauge) is better for damage detection with higher accuracy. Both the damage locations and severities are perfectly identified even with 10% measurement noise considered.

2. This thesis proposed a response covariance-based optimal sensor placement method for single type sensor optimal placement. First, the relationship between the covariance of acceleration responses and the covariance of unit impulse responses of a structure subjected to multiple white noise excitations has been derived. This relationship indicates that the optimal sensor location is related to the location of excitation but not to the amplitude of excitation. Second, the optimal sensor placement objectives in terms of the response covariance sensitivity and the response independence have been derived, respectively. The two OSP objectives aim to enhance the damage sensitivity to the sensor locations and reduce redundant sensors so that the limited number of sensors can be used for better damage detection. However, the two objective functions proposed in this thesis for OSP are conflicting, observed in the numerical studies by using a five-bays three-dimensional frame structure. Finally, an integrated single objective function is formed by using a weighting factor to combine the two objective functions. The numerical studies show that the best weighting factor in the OSP for the best damage detection of the frame structure is 0.3. The numerical studies also demonstrate that the approach combining the response covariance-based damage detection method and the optimal sensor placement is feasible and effective for damage detection. Comparing with an information-entropy-based OSP method, the proposed response covariance-based OSP method could lead to more accurate damage detection.

3. A structural damage detection-oriented multi-type sensor placement method with multi-objective optimization is further developed. The multi-objective optimization approach considers to directly use the two covariance-related objective functions, and the non-dominated sorting genetic algorithm (NSGA)-II is adopted to find the solution

for the optimal multi-type sensor placement to achieve the best structural damage detection. This method is advanced for simultaneously placing multi-type sensors in an optimal manner, which effectively balances the conflict of multi-objectives due to the limited number of sensors and the complex nature of the problem. Besides, the selection of a most desirable OSP from the Pareto solutions via the utility function method or the knee-point-based method is proposed for practical application. The proposed method is numerically validated by using a nine-bay three-dimensional frame structure model. Satisfactory damage detection results are obtained by using optimal sensor configurations for both the unconstrained and constrained cases on the number of each type of sensor. It is noted that the configurations with the specified number for each type of sensors yield relatively more accurate results in the damage detection. The proposed method is further compared with a Fisher-information matrix based OSP method. The comparison reveals that the proposed OSP method with multi-type sensors could lead to more accurate damage detection than a typical Fisher information matrix based OSP method with single- type of sensor.

4. To experimentally validate the proposed CBMS damage detection index and the damage detection-oriented multi-objective multi-type sensor optimal sensor placement method. A nine-bay three-dimensional frame structure was built in the laboratory and different damage scenarios were then generated on the frame structure. These damage scenarios covered single and multiple damage cases occurring at different locations with different damage severities. A series of experiments, including the optimal and non-optimal sensor placements, were finally carried out, and the measurement data (acceleration, displacement, and strain) were used together with the FE model to identify damage quantitatively. The identification results show that the optimal multi-type sensor placement determined by the proposed method could provide accurate damage localization and satisfactory damage quantitation and that the optimal sensor placement yielded better damage identification than the non-optimal sensor placement.

5. When the proposed covariance-based multi-type sensor placement method and the associated damage detection methods are applied to a large and complex civil structure, the obstacles exhibit. The global stiffness matrix, modal parameters, and dynamic responses are less sensitive to local damage of a large structure compared with a small structure. The one-stage damage detection is inaccurate and sometimes impossible due to too many unknown damage parameters and seriously ill-conditioned inversed problem for a large structure. Therefore, a covariance-based multi-stage damage detection strategy incorporating with a multi-scale finite element (FE) model is proposed for the damage detection of a large structure. The numerical study has shown that the proposed multi-stage damage detection for the HVPT tower testbed can achieve identification results with high accuracy. Noted that the proposed method is advantageous to divide difficulties of large structure damage detection into multiple stages. To accurately evaluate the effect of possible damage in critical components in terms of bolts, the usage of a detailed joint model is a meaningful exploration to provide sufficient information for maintenance of high-voltage power transmission towers.

6. To examine the performance of the proposed multi-stage damage detection method, a 5.5 m height power transmission tower testbed is established in the laboratory and a damage scenario with a set of bolts loosening in a critical joint is designed for damage detection study. The experimental results showed that accurate damage localization and satisfactory damage quantification could be yielded by using multi-stage damage detection method with the optimal sensor configuration. It can be concluded that the proposed multi-stage approach is feasible and effective for damage detection of a large structure.

9.2 Recommendations for Future Studies

Although progress has been made in this thesis in the development of a response covariance-based damage identification that is more applicable to civil structures, several important issues require further investigations.

1. The proposed damage detection method requires the input forces to be measured. In practice, some equipment (e.g. a shaker) can be used to generate appropriate input forces on real structures and these forces are adjustable and measurable. However, the artificial force generated by shaker sometimes may consume a large amount of power and energy. Natural environmental excitations may be preferable. To replace the requirement of input excitation measurement, the estimation or reconstruction of the unknown input excitations (such as, environmental excitations) is an important issue that deserves much more research efforts.

2. Theoretically, different types of excitation (random, harmonic, impulsive or others) can be used for the proposed response covariance-based damage detection method and the optimal sensor placement method. This thesis only investigated the most common excitation in terms of the narrow-banded excitation for the proposed methods. Since civil structures may service in more complicate loading conditions, it is worth to further study the effectiveness of the proposed methods under different excitations.

3. For the covariance-based multi-objective multi-type sensor placement method, the minimum number of the sensors are determined by numerical studies based on the principle of using the minimum number of sensors but guaranteeing enough accuracy of structural damage detection. This may require some professional knowledge to estimate the total number of sensors. Therefore, it is worth to further developing an effective objective function to select the total number of the sensor during the OSP procedure. Other objective functions, for instance taking the cost of each type sensor

into consideration, could also be useful in practical applications.

4. The proposed damage detection method relies on the availability of an FE model. The FE model is often available for a civil engineering structure even in the design stage. For the existing civil engineering structure, the model updating of the FE model used in the design stage may be conducted. It is worth pointing out that the proposed damage detection method often requires the FE model with relatively high accuracy, so model updating is a very important procedure to ensure the success of damage detection. Therefore, the uncertainty from the FE model that involved in the proposed method is also worth analyzing and quantifying.

5. In experimental damage detection studies, the structural damage can be modeled as a degradation of the stiffness the damaged region, such as grinding away a layer of material from the surface of the damaged beam for the three-dimensional frame structure and totally loosening one set of bolts in one connected beam for the damaged joint in the HVPT tower testbed in laboratory test. The main reason is that the severity of above-mentioned damage can be more easily controlled and quantified accurately. However, more elaborate damage models for some specific structural damages, such as bolt loosening or crack or corrosion, are demanded to capture more detailed damage characteristics.

6. Considering extensive computation required in the damage detection of the full HVPT tower, only the damage-prone joints in 1/4 tower are selected for the demonstration of the proposed multi-stage damage detection. The proposed response covariance-based damage detection method, applied to the whole structure, still needs further studies.

7. The structure is supposed to behave linearly under small elastic deformation before and after damage. For structural damage with large deformation, some structural nonlinearity may occur, which is not considered in this thesis.

8. Damage prognosis in terms of useful life estimation has not been touched in this thesis, which can provide some advising information for civil structure maintenance. Integrating the multi-scale FE model and response covariance-based damage detection results, structure operational lifetime prediction is a meaningful research topic.

APPENDIX A

DAMAGE MODEL OF THE 2D BEAM ELEMENT

For a beam element of rectangular section with 6 DOFs, the consistent element stiffness matrix $\mathbf{K}^e$ and element mass matrix $\mathbf{M}^e$ in a local coordinate are generally given as follows (Logan 2002):

$$\mathbf{K}^e = \begin{bmatrix} \frac{EA}{l} & 0 & 0 & -\frac{EA}{l} & 0 & 0 \\ & \frac{12EI}{l^3} & \frac{6EI}{l^2} & 0 & -\frac{12EI}{l^3} & \frac{6EI}{l^2} \\ & & \frac{4EI}{l} & 0 & -\frac{6EI}{l^2} & \frac{2EI}{l} \\ & & & \frac{EA}{l} & 0 & 0 \\ & SYM & & & \frac{12EI}{l^3} & -\frac{6EI}{l^2} \\ & & & & & \frac{4EI}{l} \end{bmatrix}$$

$$= b \cdot E \cdot \begin{bmatrix} \frac{h}{l} & 0 & 0 & -\frac{h}{l} & 0 & 0 \\ & \frac{h^3}{l^3} & \frac{h^3}{2l^2} & 0 & -\frac{h^3}{l^3} & \frac{h^3}{2l^2} \\ & & \frac{h^3}{3l} & 0 & -\frac{h^3}{2l^2} & \frac{h^3}{6l} \\ & & & \frac{h}{l} & 0 & 0 \\ & SYM & & & \frac{h^3}{l^3} & -\frac{h^3}{2l^2} \\ & & & & & \frac{h^3}{3l} \end{bmatrix} \tag{A1}$$

$$\mathbf{M}^e = \frac{\rho A l}{420} \cdot \begin{bmatrix} 140 & 0 & 0 & 70 & 0 & 0 \\ & 156 & 22l & 0 & 54 & -13l \\ & & 4l^2 & 0 & 13l & -3l^2 \\ & & & 140 & 0 & 0 \\ & SYM & & & 156 & -22l \\ & & & & & 4l^2 \end{bmatrix}$$
$$= b \cdot \frac{\rho h l}{420} \cdot \begin{bmatrix} 140 & 0 & 0 & 70 & 0 & 0 \\ & 156 & 22l & 0 & 54 & -13l \\ & & 4l^2 & 0 & 13l & -3l^2 \\ & & & 140 & 0 & 0 \\ & SYM & & & 156 & -22l \\ & & & & & 4l^2 \end{bmatrix} \tag{A2}$$

where ρ is the mass density; A is the area of beam cross-section; l is the element length; h is the element thickness; b is the element width; E is the elastic modulus; and I is the second moment of inertia of cross-section.

It is assumed that the i^{th} element has sustained damage as sketched in Fig.A1. The cross-sectional areas of the i^{th} element in the intact and damaged states are A_i and A_i^d respectively, and they can be calculated as:

$$\begin{cases} A_i = b \cdot h \\ A_i^d = (b - 2d) \cdot h \end{cases} \tag{A3}$$

where d is one side width reduction symmetrically arranged with respect to the beam axis.

The damaged global stiffness $\mathbf{K_d}$ and mass matrices $\mathbf{M_d}$ can then be calculated using Eq. (A4) in terms of the stiffness $\mathbf{K}_i$ and mass $\mathbf{M}_i$ matrices in its intact state together with their fractional changes $\Delta\alpha_{1,i}$ and $\Delta\alpha_{2,i}$, respectively. In this study, because the width b is reduced symmetrically in the damaged element, the fractional change of the i^{th} element's stiffness and mass matrix is of the same value and it can be calculated as:

$$\Delta\alpha_{1,i} = \Delta\alpha_{2,i} = \frac{A_i - A_i^d}{A_i} = \frac{2d}{b} \times 100\% \tag{A4}$$

The proposed damage model is just a subset of all available damage models although it is not the most advanced model of damage (Cattarius and Inman 1997). However, this model does provide a reasonable and convenient way to simplify the problem concerned. That is, the computed fractional change is for both the stiffness and mass matrices of the i^{th} element.

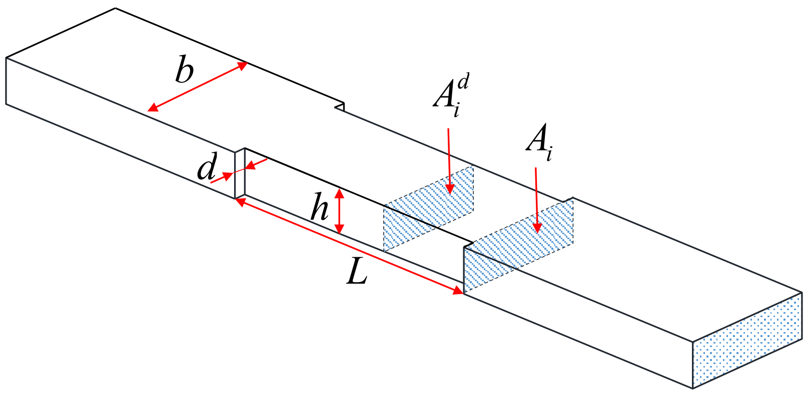

Fig. A.1 Beam with reduction in cross-sectional area

APPENDIX B

EQUIVALENT STIFFNESS REDUCTION

For a circle tube beam element, the elastic modulus, length, outer diameter, inner diameter, sectional area and moment of inertia of the undamaged beam are E, l, D_0, d_0, A_0 and I_0, respectively. The damage is simulated by grinding away a layer of material from the surface of the damaged beam in the middle segment. The mock-up damaged beam element (see Fig. 6.5) is divided into three segments with the lengths l_1, l_2 and l_3 from the left side to the right side. The A_1, A_2 and A_3 are the corresponding sectional areas of the three segments of the beam. The I_1, I_2 and I_3 are the corresponding moment of inertias of the three segments of the beam. For the damaged beam element, the length, outer diameter, sectional area and moment inertia of the weakened part are l_2, D_2, A_2 and I_2, meanwhile the geometric parameters of the undamaged parts are $l_1 = l_3 = \frac{l - l_2}{2}$, $A_1 = A_3 = A_0$, and $I_1 = I_3 = I_0$.

To estimate the equivalent reduction of tensile stiffness and bending stiffness of a damaged beam element, the damaged beam element is assumed with a uniform equivalent sectional area $\bar{A}_d$ and equivalent moment inertia $\bar{I}_d$. This assumption is based on the fact that the same tensile force F and bending moment M acting on a beam can yield, respectively, the equal increment of a tensile length Δl and a bending angle θ as follows:

$$\begin{cases} \Delta l = \dfrac{Fl}{E\bar{A}_d} = \sum_{i=1}^{3} \dfrac{Fl_i}{EA_i} \\ \theta = \dfrac{Ml}{E\bar{I}_d} = \sum_{i=1}^{3} \dfrac{Ml_i}{EI_i} \end{cases} \tag{B1}$$

where l_i, A_i and I_i are, respectively, the length, sectional area and moment inertia of i^{th} segment of the damaged beam. Then, the $\bar{A}_d$ and $\bar{I}_d$ can be computed from

Eq. (B1) as

$$\begin{cases} \overline{A}_d = \dfrac{l}{\dfrac{l_1}{A_1}+\dfrac{l_2}{A_2}+\dfrac{l_3}{A_3}} = \dfrac{A_0 l}{(l-l_2)+\dfrac{A_0}{A_2}l_2} \\ \overline{I}_d = \dfrac{l}{\dfrac{l_1}{I_1}+\dfrac{l_2}{I_2}+\dfrac{l_3}{I_3}} = \dfrac{I_0 l}{(l-l_2)+\dfrac{I_0}{I_2}l_2} \end{cases} \tag{B2}$$

Therefore, the fractional change of tensile stiffness α_t and the bending stiffness α_b can be approximately computed as

$$\begin{cases} \alpha_t = \dfrac{E(A_0-\overline{A}_d)}{EA_0}\times 100\% = (1-\dfrac{\overline{A}_d}{A_0})\times 100\% = \left[1-\dfrac{l}{(l-l_2)+\dfrac{A_0}{A_2}l_2}\right]\times 100\% \\ \alpha_b = \dfrac{E(I_0-\overline{I}_d)}{EI_0}\times 100\% = (1-\dfrac{\overline{I}_d}{I_0})\times 100\% = \left[1-\dfrac{l}{(l-l_2)+\dfrac{I_0}{I_2}l_2}\right]\times 100\% \end{cases} \tag{B3}$$

with

$$\begin{cases} A_0 = \dfrac{\pi(D_0^2-d_0^2)}{4}; \quad A_2 = \dfrac{\pi(D_2^2-d_0^2)}{4} \\ I_0 = \dfrac{\pi(D_0^4-d_0^4)}{64}; \quad I_2 = \dfrac{\pi(D_2^4-d_0^4)}{64} \end{cases} \tag{B4}$$

It is noted from Eqs. (B3) and (B4) that the equivalent stiffness reduction in terms of fractional change of tensile stiffness α_t and the bending stiffness α_b can be obtained when we provide the geometric dimension changes for the grinding length l_2 and the outer diameter D_2 of the weakened segment of the damaged beam.

REFERENCES

Aktan, A., Catbas, F., Grimmelsman, K., and Tsikos, C. (2000). "Issues in infrastructure health monitoring for management." *Journal of Engineering Mechanics*, 126(7), 711-724.

Aktan, A. E., Helmicki, A. J., and Hunt, V. J. (1998). "Issues in health monitoring intelligent infrastructure." *Smart Materials & Structures*, 7(5), 674-692.

Albermani, F., Kitipornchai, S., and Chan, R. W. K. (2009). "Failure analysis of transmission towers." *Engineering Failure Analysis*, 16(6), 1922-1928.

ANSYS® Academic Research, R. 2015. ANSYS,Inc., Pennsylvania, USA.

Au, S. K., Zhang, F.L., and Ni, Y. C. (2013). "Bayesian operational modal analysis: theory, computation, practice." *Computers & Structures*, 126, 3-14.

Barthorpe, R. J., and Worden, K. (2009). "Sensor placement optimization." *Encyclopedia of Structural Health Monitoring*, Wiley Interscience, Hoboken, USA.

Bechikh, S., Ben Said, L., and Ghédira, K. "Searching for knee regions in multi-objective optimization using mobile reference points."*, Proceedings of the 2010 ACM symposium on applied computing*, ACM, 1118-1125.

Bendat, J. S., and Piersol, A. G. (1993). *Engineering Applications of Correlation and Spectral Analysis*, Wiley, New York.

Bendat, J. S., and Piersol, A. G. (2010). *Random data: analysis and measurement procedures*, John Wiley & Sons.

Branke, J., Deb, K., Dierolf, H., and Osswald, M (2004). "Finding knees in multi-objective optimization." *Proc., PPSN*, 722-731.

Castro-Triguero, R., Garcia-Macias, E., Saavedra Flores, E., Friswell, M., and Gallego, R. (2017). "Multi-scale model updating of a timber footbridge using experimental vibration data." *Engineering Computations*, 34(3), 754-780.

Cattarius, J., and Inman, D. J. (1997). "Time domain analysis for damage detection in smart structrues." *Mechanical Systems and Signal Processing*, 11(3), 409-423.

Cawley, P., and Adams, R. D. (1979). "The location of defects in structures from measurements of natural frequencies." *The Journal of Strain Analysis for Engineering Design*, 14(2), 49-57.

Cha, Y.J., Kim, Y., Raich, A. M., and Agrawal, A. K. (2013). "Multi-objective optimization for actuator and sensor layouts of actively controlled 3D buildings." *Journal of Vibration and Control*, 19(6), 942-960.

Cha, Y.J., Raich, A., Barroso, L., and Agrawal, A. (2013). "Optimal placement of active control devices and sensors in frame structures using multi-objective genetic algorithms." *Structural Control and Health Monitoring*, 20(1), 16-44.

Cha, Y. J., Agrawal, A., Kim, Y., and Raich, A. (2012). "Multi-objective genetic algorithms for cost-effective distributions of actuators and sensors in large structures." *Expert Systems with Applications*, 39(9), 7822-7833.

Cha, Y. J., and Buyukozturk, O. (2015). "Structural damage detection using modal strain energy and hybrid multiobjective optimization." *Computer‐Aided Civil and Infrastructure Engineering*, 30(5), 347-358.

Chan, W. S., Xu, Y. L., Ding, X. L., and Dai, W. J. (2006). "An integrated GPS–accelerometer data processing technique for structural deformation monitoring." *Journal of Geodesy*, 80(12), 705-719.

Chance, J., Tomlinson, G. R., and Worden, K. (1994). "A simplified approach to the numerical and experimental modeling of the dynamics of a cracked beam." *Proceedings of the 12th International Modal Analysis Conference, Vols 1 and 2*, 2251, 778-785.

Choi, S., and Stubbs, N. (2004). "Damage identification in structures using the time-domain response." *Journal of Sound and Vibration*, 275(3-5), 577-590.

Coello, C. A. C. (1999). "A comprehensive survey of evolutionary-based multiobjective optimization techniques." *Knowledge and Information systems*, 1(3), 269-308.

Deb, K. (2001). *Multi-objective optimization using evolutionary algorithms*, John Wiley & Sons, Chichester, England.

Deb, K. "A robust evolutionary framework for multi-objective optimization.", *Proceedings of the 10th annual conference on Genetic and evolutionary computation*, ACM, 633-640.

Deb, K., Pratap, A., Agarwal, S., and Meyarivan, T. (2002). "A fast and elitist multiobjective genetic algorithm: NSGA-II." *IEEE Transactions on Evolutionary Computation*, 6(2), 182-197.

Doebling, S. W., Farrar, C. R., and Prime, M. B. (1998). "A summary review of vibration-based damage identification methods." *Shock and Vibration Digest*, 30(2), 91-105.

Doebling, S. W., Farrar, C. R., Prime, M. B., and Shevitz, D. W. (1996). "Damage identification and health monitoring of structural and mechanical systems from changes in their vibration characteristics: a literature review." Los Alamos National Lab., NM (United States).

Donoho, D. L. (2006). "For most large underdetermined systems of linear equations the minimal." *Communications on pure and applied mathematics*, 59(6), 797-829.

Fan, W., and Qiao, P. (2011). "Vibration-based damage identification methods: a review and comparative study." *Structural Health Monitoring*, 10(1), 83-111.

Farrar, C. R., Baker, W. E., Bell, T. M., Cone, K. M., Darling, T. W., Duffey, T. A., Eklund, A., and Migliori, A. (1994). "Dynamic characterization and damage detection in the I-40 bridge over the Rio Grande." Los Alamos National Lab, Los Alamos, NM,.

Farrar, C. R., and Doebling, S. W. (1997). "Lessons learned from applications of vibration-based damage identification methods to a large bridge structure."

International workshop on structural health monitoring, Stanford, CA (United States), 18-20.

Farrar, C. R., Doebling, S. W., and Nix, D. A. (2001). "Vibration-based structural damage identification." *Philosophical Transactions of the Royal Society of London Series A: Mathematical, Physical and Engineering Sciences*, 359(1778), 131-149.

Farrar, C. R., and Worden, K. (2007). "An introduction to structural health monitoring." *Philosophical Transactions of the Royal Society A: Mathematical, Physical and Engineering Sciences*, 365(1851), 303-315.

Farrar, C. R., and Worden, K. (2012). *Structural health monitoring: a machine learning perspective*, John Wiley & Sons, New York.

Figueiredo, E., Park, G., Farinholt, K. M., Farrar, C. R., and Lee, J. R. (2012). "Use of Time-Series Predictive Models for Piezoelectric Active-Sensing in Structural Health Monitoring Applications." *Journal of Vibration and Acoustics-Transactions of the ASME*, 134(4).

Figueiredo, E., Park, G., Farrar, C. R., Worden, K., and Figueiras, J. (2011). "Machine learning algorithms for damage detection under operational and environmental variability." *Structural Health Monitoring*, 10(6), 559-572.

Figueiredo, E., Radu, L., Worden, K., and Farrar, C. R. (2014). "A Bayesian approach based on a Markov-chain Monte Carlo method for damage detection under unknown sources of variability." *Engineering Structures*, 80, 1-10.

Figueiredo, E., Todd, M. D., Farrar, C. R., and Flynn, E. (2010). "Autoregressive modeling with state-space embedding vectors for damage detection under operational variability." *International Journal of Engineering Science*, 48(10), 822-834.

Friswell, M. I., Mottershead, J. E., and Ahmadian, H. (2001). "Finite–element model updating using experimental test data: parametrization and regularization." *Philosophical Transactions of the Royal Society of London A: Mathematical, Physical and Engineering Sciences*, 359(1778), 169-186.

Fugate, M. L., Sohn, H., and Farrar, C. R. (2001). "Vibration-based damage detection using statistical process control." *Mechanical Systems and Signal Processing*, 15(4), 707-721.

Guo, Y., Ni, Y., and Chen, S. (2016). "Optimal sensor placement for damage detection of bridges subject to ship collision." *Structural Control and Health Monitoring*.

Hansen, P. C., and O'Leary, D. P. (1993). "The use of the L-curve in the regularization of discrete ill-posed problems." *SIAM Journal on Scientific Computing*, 14(6), 1487-1503.

Hathout, I., Cheema, H., and Callery-Broomfield, K. (2013). "Damage Assessment of Existing Transmission Structures Using ANFIS (Adaptive Neuro-Fuzzy Inference) Model." *Journal of Energy and Power Engineering*, 7(12), 2363.

Hu, R. P., Xu, Y. L., and Zhan, S. (2018). "Multi-type sensor placement and response reconstruction for building structures: Experimental investigations." *Earthquake Engineering and Engineering Vibration*, 17(1), 29-46.

Huang, Q. D., Gardoni, P., and Hurlebaus, S. (2012). "A probabilistic damage detection approach using vibration-based nondestructive testing." *Structural Safety*, 38, 11-21.

Huston, D. (2010). *Structural sensing, health monitoring, and performance evaluation*, CRC Press, Boca Raton, Florida.

Institution, B. S. (2001). "Lattice tower and masts " *Part 3: Code of practice for strength assessment of members of lattice towers and masts*, BSI, London,UK.

Jiang, W. Q., Liu, Y. P., Chan, S. L., and Wang, Z. Q. (2017). "Direct analysis of an ultrahigh-voltage lattice transmission tower considering joint effects." *Journal of Structural Engineering*, 143(5), 04017009.

Jin, S.S., Cho, S., Jung, H.J., Lee, J.J., and Yun, C.-B. (2014). "A new multi-objective approach to finite element model updating." *Journal of Sound and Vibration*, 333(11), 2323-2338.

Kammer, D. C. (1991). "Sensor Placement for on-Orbit Modal Identification and Correlation of Large Space Structures." *Journal of Guidance Control and Dynamics*, 14(2), 251-259.

Khawsuk, W., and Pao, L. Y. "Decorrelated state estimation for distributed tracking of interacting targets in cluttered environments." *Proc., American Control Conference, 2002. Proceedings of the 2002*, IEEE, 899-904.

Kim, K., Murray, A. T., and Xiao, N. (2008). "A multiobjective evolutionary algorithm for surveillance sensor placement." *Environment and Planning B: Planning and Design*, 35(5), 935-948.

Klinger, C., Mehdianpour, M., Klingbeil, D., Bettge, D., Häcker, R., and Baer, W. (2011). "Failure analysis on collapsed towers of overhead electrical lines in the region Münsterland (Germany) 2005." *Engineering Failure Analysis*, 18(7), 1873-1883.

Koh, C., and Shankar, K. (2003). "Substructural identification method without interface measurement." *Journal of Engineering Mechanics*, 129(7), 769-776.

Koh, C. G., Hong, B., and Liaw, C. Y. (2003). "Substructural and progressive structural identification methods." *Engineering Structures*, 25(12), 1551-1563.

Koh, C. G., See, L. M., and Balendra, T. (1991). "Estimation of structural parameters in time domain: a substructure approach." *Earthquake Engineering & Structural Dynamics*, 20(8), 787-801.

Kohavi, R. "A study of cross-validation and bootstrap for accuracy estimation and model selection." *Proc., IJCAI*, 1137-1145.

Kong, X., Cai, C. S., and Hu, J. X. (2017). "The State-of-the-Art on Framework of Vibration-Based Structural Damage Identification for Decision Making." *Applied Sciences*, 7(5), 497.

Lam, H. F., and Yin, T. (2011). "Dynamic reduction-based structural damage detection of transmission towers: Practical issues and experimental verification." *Engineering Structures*, 33(5), 1459-1478.

Law, S. S., and Yong, D. (2011). "Substructure methods for structural condition assessment." *Journal of Sound and Vibration*, 330(15), 3606-3619.

Law, S. S., Zhang, K., and Duan, Z. D. (2010). "Structural damage detection from coupling forces between substructures under support excitation." *Engineering Structures*, 32(8), 2221-2228.

Law, S. S., Li, X. Y., Zhu, X. Q., and Chan, S. L. (2005). "Structural damage detection from wavelet packet sensitivity." *Engineering Structures*, 27(9), 1339-1348.

Law, S. S., Lin, J. F., and Li, X. Y. (2012). "Structural Condition Assessment from White Noise Excitation and Covariance of Covariance Matrix." *AIAA Journal*, 50(7), 1503-1512.

Lee, E. T., Rahmatalla, S., and Eun, H. C. (2013). "Damage detection by mixed measurements using accelerometers and strain gages." *Smart Materials and Structures*, 22(7), 075014.

Li, J., Hao, H., and Chen, Z. (2015). "Damage identification and optimal sensor placement for structures under unknown traffic-induced vibrations." *Journal of Aerospace Engineering*, 30(2), B4015001.

Li, J., Law, S.S., and Ding, Y. (2012). "Substructure damage identification based on response reconstruction in frequency domain and model updating." *Engineering Structures*, 41, 270-284.

Li, J., and Law, S. S. (2012). "Damage identification of a target substructure with moving load excitation." *Mechanical Systems and Signal Processing*, 30, 78-90.

Li, J., and Law, S. S. (2012). "Substructural damage detection with incomplete information of the structure." *Journal of Applied Mechanics, Transactions ASME*, 79(4).

Li, X. Y., and Law, S. S. (2010). "Adaptive Tikhonov regularization for damage detection based on nonlinear model updating." *Mechanical Systems and Signal Processing*, 24(6), 1646-1664.

Li, X. Y., and Law, S. S. (2010). "Matrix of the covariance of covariance of acceleration responses for damage detection from ambient vibration measurements." *Mechanical Systems and Signal Processing*, 24(4), 945-956.

Li, Z., Jiang, F., and Tang, Y. (2012). "Multi-scale analyses on seismic damage and progressive failure of steel structures." *Finite Elements in Analysis and Design*, 48(1), 1358-1369.

Li, Z., Zhou, T., Chan, T. H., and Yu, Y. (2007). "Multi-scale numerical analysis on dynamic response and local damage in long-span bridges." *Engineering Structures*, 29(7), 1507-1524.

Lin, J. F., and Xu, Y. L. (2017). "Response covariance-based sensor placement for structural damage detection." *Structure and Infrastructure Engineering*, 1-14.

Lin, J. F., and Xu, Y. L. (2017). "Two-Stage Covariance-Based Multisensing Damage Detection Method." *Journal of Engineering Mechanics*, 143(3), B4016003.

Lin, J. F., Xu, Y. L., and Law, S. S. (2018). "Structural damage detection-oriented multi-type sensor placement with multi-objective optimization." *Journal of Sound and Vibration*, 420, 1-22.

Liu, W., Gao, W. C., Sun, Y., and Xu, M. J. (2008). "Optimal sensor placement for spatial lattice structure based on genetic algorithms." *Journal of Sound and Vibration*, 317(1), 175-189.

Logan, D. L. (2002). *A First Course in the Finite Element Method*, Brooks/Cole, Pacific Grove.

Long, Q., Asad, E., and G., M. H. (2012). "Signal Pattern Recognition for Damage Diagnosis in Structures." *Computer-Aided Civil and Infrastructure Engineering*, 27(9), 699-710.

Lu, W., Wen, R., Teng, J., Li, X., and Li, C. (2016). "Data correlation analysis for optimal sensor placement using a bond energy algorithm." *Measurement*.

Lu, Z. R., and Law, S. S. (2007). "Features of dynamic response sensitivity and its application in damage detection." *Journal of Sound and Vibration*, 303(1-2), 305-329.

Marler, R. T., and Arora, J. S. (2004). "Survey of multi-objective optimization methods for engineering." *Structural and Multidisciplinary Optimization*, 26(6), 369-395.

Mathakari, S., Gardoni, P., Agarwal, P., Raich, A., and Haukaas, T. (2007). "Reliability‐Based Optimal Design of Electrical Transmission Towers Using Multi‐Objective Genetic Algorithms." *Computer‐Aided Civil and Infrastructure Engineering*, 22(4), 282-292.

MathWorks (2017). "Global Optimization Toolbox: User's Guide (R2017b)."

Meo, M., and Zumpano, G. (2005). "On the optimal sensor placement techniques for a bridge structure." *Engineering Structures*, 27(10), 1488-1497.

Mottershead, J. E., Link, M., and Friswell, M. I. (2011). "The sensitivity method in finite element model updating: A tutorial." *Mechanical Systems and Signal Processing*, 25(7), 2275-2296.

Neves, A. C., González, I., Leander, J., and Karoumi, R. (2017). "Structural health monitoring of bridges: a model-free ANN-based approach to damage detection." *Journal of Civil Structural Health Monitoring*, 7(5), 689-702.

Ni, Y. Q., Xia, Y., Liao, W. Y., and Ko, J. M. (2009). "Technology innovation in developing the structural health monitoring system for Guangzhou New TV Tower." *Structural Control and Health Monitoring*, 16(1), 73-98.

Ostendorp, M. "Longitudinal loading and cascading failure assessment for transmission line upgrades." *Proc., Transmission & Distribution Construction, Operation & Live-Line Maintenance Proceedings*, IEEE, 324-329.

Ottosen, N., Petersson, H., and Saabye, N. (1992). *Introduction to the finite element method*, Prentice Hall, New York.

Papadimitriou, C. (2004). "Optimal sensor placement methodology for parametric identification of structural systems." *Journal of Sound and Vibration*, 278(4-5), 923-947.

Papadimitriou, C. (2005). "Pareto optimal sensor locations for structural identification." *Computer Methods in Applied Mechanics and Engineering*, 194(12-16), 1655-1673.

Papadimitriou, C., Beck, J. L., and Au, S. K. (2000). "Entropy-based optimal sensor location for structural model updating." *Journal of Vibration and Control*, 6(5), 781-800.

Preis, A., and Ostfeld, A. (2008). "Multiobjective contaminant sensor network design for water distribution systems." *Journal of Water Resources Planning and Management*, 134(4), 366-377.

Rachmawati, L., and Srinivasan, D. (2009). "Multiobjective evolutionary algorithm with controllable focus on the knees of the Pareto front." *IEEE Transactions on Evolutionary Computation*, 13(4), 810-824.

Raghavan, A., and Cesnik, C. E. (2007). "Review of guided-wave structural health monitoring." *Shock and Vibration Digest*, 39(2), 91-116.

Ramu, M., Prabhu Raja, V., and Thyla, P. (2011). "Development of structural similitude and scaling laws for elastic models." *KSCE Journal of Civil Engineering*, 17(1), 139-144.

Santi, L. M., Sowers, T. S., and Aguilar, R. B. (2005). "Optimal sensor selection for health monitoring systems." *41st Joint Propulsion Conference and Exhibit*, National Aeronautics and Space Administration, Glenn Research Center, Tucson, Arizona.

Shi, Z. Y., Law, S. S., and Zhang, L. M. (2000). "Optimum sensor placement for structural damage detection." *Journal of Engineering Mechanics-ASCE*, 126(11), 1173-1179.

Sim, S. H., Spencer, B. F., and Nagayama, T. (2011). "Multimetric sensing for structural damage detection." *Journal of Engineering Mechanics*.

Sohn, H., Farrar, C. R., Hemez, F. M., and Czarnecki, J. J. (2002). "A Review of Structural Health Review of Structural Health Monitoring Literature 1996-2001." Los Alamos National Laboratory.

Sohn, H., and Law, K. H. (1997). "A Bayesian probabilistic approach for structure damage detection." *Earthquake Engineering & Structural Dynamics*, 26(12), 1259-1281.

Studer, M., and Peters, K. (2004). "Multi-scale sensing for damage identification." *Smart Materials and Structures*, 13(2), 283-294.

Sun, Z., and Chang, C. C. (2006). "Covariance-driven wavelet technique for structural damage assessment." *Smart Structures and Systems*, 2(2), 127-140.

Sung, S. H., Park, J. W., Nagayama, T., and Jung, H. J. (2014). "A multi-scale sensing and diagnosis system combining accelerometers and gyroscopes for bridge health monitoring." *Smart Materials and Structures*, 23(1).

Udwadia, F. E. (1994). "Methodology for Optimum Sensor Locations for Parameter Identification in Dynamic Systems." *Journal of Engineering Mechanics*, 120(2), 368-390.

Valeti, B., and Pakzad, S. "Automated Detection of Corrosion Damage in Power Transmission Lattice Towers Using Image Processing." *Proc., Structures Congress 2017*, 474-482.

Wang, F., Xu, Y., and Qu, W. (2017). "Multi-Scale Failure Analysis of Transmission Towers Under Downburst Loading." *International Journal of Structural Stability and Dynamics*, 1850029.

Wang, F. Y., Xu, Y. L., and Zhan, S. (2016). "Multi-scale model updating of a transmission tower structure using Kriging meta-method." *Structural Control and Health Monitoring*.

Wang, J., Liu, X. Z., and Ni, Y. Q. (2018). "A Bayesian Probabilistic Approach for Acoustic Emission - Based Rail Condition Assessment." *Computer - Aided Civil and Infrastructure Engineering*, 33(1), 21-34.

Wong, C. J., and Miller, M. D. (2009). "Guidelines for electrical transmission line structural loading." *ASCE Manuals and Reports on Engineering Practice No. 74*, Structural Engineering Institute of ASCE, Reston, Viginia, USA.

Wong, S. C., and Barhorst, A. A. (2007). "Stochastic analysis of Poisson impact series using discrete form, spectrum analysis and time correlation." *Mechanical Systems and Signal Processing*, 21(1), 151-164.

Worden, K., Farrar, C. R., Manson, G., and Park, G. (2007). "The fundamental axioms of structural health monitoring." *Proceedings of the Royal Society A: Mathematical, Physical and Engineering Science*, 463(2082), 1639-1664.

Xia, Y., and Hao, H. (2000). "Measurement Selection for Vibration-Based Structural Damage Identification." *Journal of Sound and Vibration*, 236(1), 89-104.

Xiang, J. W., and Liang, M. (2012). "A two-step approach to multi-damage detection for plate structures." *Engineering Fracture Mechanics*, 91, 73-86.

Xu, Y. L., and Xia, Y. (2012). *Structural health monitoring of long-span suspension bridges*, Spon Press, New York.

Xu, Y. L., Zhang, C. D., Zhan, S., and Spencer, B. F. (2018). "Multi-level damage identification of a bridge structure: a combined numerical and experimental investigation." *Engineering Structures*, 156, 53-67.

Xu, Y. L., Zhang, X. H., Zhu, S. Y., and Zhan, S. (2016). "Multi-type sensor placement and response reconstruction for structural health monitoring of long-span suspension bridges." *Science Bulletin*, 61(4), 313-329.

Yao, L., Sethares, W. A., and Kammer, D. C. (1992). "Sensor Placement for on-Orbit Modal Identification of Large Space Structure Via a Genetic Algorithm." *IEEE International Conference on Systems Engineering*, 332-335.

Yao, R., and Pakzad, S. N. (2012). "Autoregressive statistical pattern recognition algorithms for damage detection in civil structures." *Mechanical Systems and Signal Processing*, 31, 355-368.

Ye, S. Q., and Ni, Y. Q. (2012). "Information entropy based algorithm of sensor placement optimization for structural damage detection." *Smart Structures and Systems*, 10(4), 443-458.

Yi, T. H., and Li, H. N. (2012). "Methodology developments in sensor placement for health monitoring of civil infrastructures." *International Journal of Distributed Sensor Networks*, 2012.

Yin, T., Lam, H. F., Chow, H. M., and Zhu, H. P. (2009). "Dynamic reduction-based structural damage detection of transmission tower utilizing ambient vibration data." *Engineering Structures*, 31(9), 2009-2019.

Yoo, D. G., Chung, G., Sadollah, A., and Kim, J. H. (2015). "Applications of network analysis and multi-objective genetic algorithm for selecting optimal water quality sensor locations in water distribution networks." *KSCE Journal of Civil Engineering*, 19(7), 2333-2344.

Yuen, K. V., and Kuok, S. C. (2015). "Efficient Bayesian sensor placement algorithm for structural identification: a general approach for multi - type sensory systems." *Earthquake Engineering & Structural Dynamics*, 44(5), 757-774.

Yun, C.B., and Bahng, E. Y. (2000). "Substructural identification using neural networks." *Computers & Structures*, 77(1), 41-52.

Yun, C.B., and Lee, H.J. (1997). "Substructural identification for damage estimation of structures." *Structural Safety*, 19(1), 121-140.

Zhang, C. D., and Xu, Y. L. (2015). "Optimal multi-type sensor placement for response and excitation reconstruction." *Journal of Sound and Vibration*, 360, 112-128.

Zhang, C. D., and Xu, Y. L. (2016). "Structural damage identification via multi-type sensors and response reconstruction." *Structural Health Monitoring*, 1475921716659787.

Zhang, C. D., and Xu, Y. L. (2017). "Multi-level damage identification with response reconstruction." *Mechanical Systems and Signal Processing*, 95, 42-57.

Zhang, F. L., Au, S. K., and Lam, H. F. (2015). "Assessing uncertainty in operational modal analysis incorporating multiple setups using a Bayesian approach." *Structural Control and Health Monitoring*, 22(3), 395-416.

Zhang, J., Xu, Y. L., Xia, Y., and Li, J. (2008). "A new statistical moment-based structural damage detection method." *Structural Engineering and Mechanics*, 30(4), 445-466.

Zhang, X., Tian, Y., and Jin, Y. (2015). "A knee point-driven evolutionary algorithm for many-objective optimization." *IEEE Transactions on Evolutionary Computation*, 19(6), 761-776.

Zhang, X. H., Zhu, S. Y., Xu, Y. L., and Homg, X. J. (2011). "Integrated optimal placement of displacement transducers and strain gauges for better estimation of structural response." *International Journal of Structural Stability and Dynamics*, 11(03), 581-602.

Zhou, X.Q., Xia, Y., and Hao, H. (2013). "Sensor placement for structural damage detection considering measurement uncertainties." *Advances in Structural Engineering*, 16(5), 899-907.

Zhu, S. Y., Zhang, X. H., Xu, Y. L., and Zhan, S. (2013). "Multi-type sensor placement for multi-scale response reconstruction." *Advances in Structural Engineering*, 16(10), 1779-1798.

Zhu, W. D., Zheng, N. A., and Wong, C. N. (2007). "A stochastic model for the random impact series method in modal testing." *Journal of Vibration and Acoustics-Transactions of the ASME*, 129(3), 265-275.

Zou, H., and Hastie, T. (2005). "Regularization and variable selection via the elastic net." *Journal of the Royal Statistical Society: Series B (Statistical Methodology)*, 67(2), 301-320.